Preliminary sizing methodologies for regional aircraft with liquid hydrogen fuel and SOFC-GT-Battery hybrid-electric powertrain

MSc Thesis Aerospace Engineering

Pedro Garcia Gonzalez

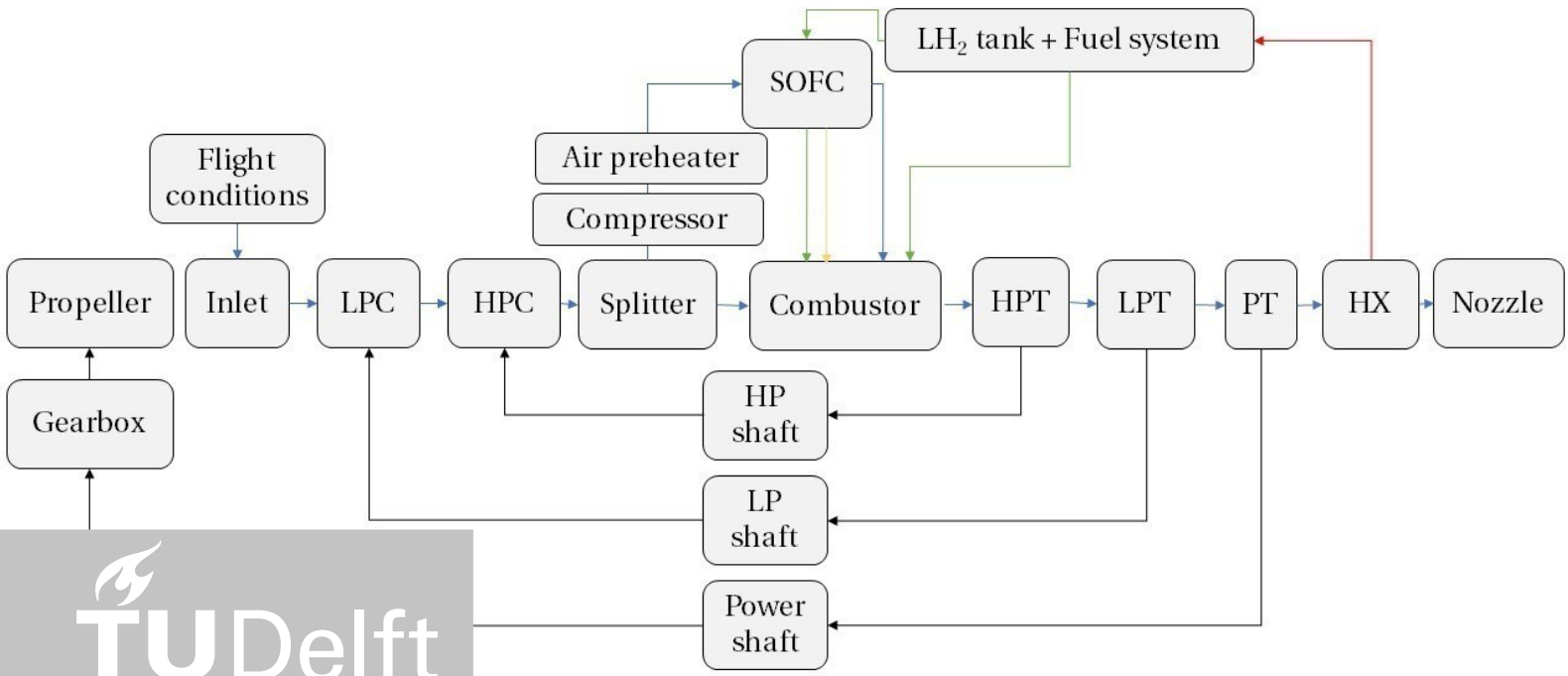

TU Delft

Preliminary sizing methodologies for regional aircraft with liquid hydrogen fuel and SOFC-GT-Battery hybrid-electric powertrain

by

Pedro García González

in partial fulfilment of the requirements for the degree of

Master of Science in Aerospace Engineering

at the **Delft University of Technology**,
to be defended publicly on
Thursday, December 15, 2022, at 11:00 CET

Student number:	5125030
Supervisors:	Dr. Carlo de Servi
	Mr. Carlos Mourao
Thesis committee:	**Chair**: Dr. Roelof Vos, TU Delft, Associate Professor, Flight Performance
	External Examiner: Dr. Woutijn Baars, TU Delft, Assistant Professor, Aerodynamics
	Daily supervisor: Dr. Carlo de Servi, TU Delft, Researcher, Propulsion and Power
	Additional Examiner: Dr. Fabrizio Oliviero, TU Delft, Lecturer, Flight Performance

An electronic version of this thesis is available at http://repository.tudelft.nl/

This research project has been done with the academic guidance of Dr. Carlo de Servi (TU Delft) and Mr. Carlos Mourao (Embraer).
Embraer does not own the copyright of the contents of this report or models developed for this research.

ABSTRACT

Hydrogen-powered aviation has been gaining momentum in the latest years. Research on the use of fuel cells and gas turbines fueled by hydrogen showcase the potential of this fuel for aviation applications. Solid Oxide Fuel Cell (SOFC) systems for aviation applications have been considered for their use as APUs or main power units, as standalone systems or in combination with gas turbines, and both fueled by reformed Jet-A or by hydrogen. Most of the existing studies focus on powertrain performance modelling. In this work, traditional tube-and-wing regional aircraft sizing methodologies are modified to account for liquid hydrogen fuel and SOFC-GT-Battery hybrid electric powertrains. Methodologies for powertrain modelling, power sizing, energy sizing, weight calculation and system integration have been derived, implemented, verified, validated when possible, and used to assess several case studies. Considering the adoption of state-of-the-art metal-supported planar ITSOFC technology aboard of a 50-seat regional aircraft as test case, it is concluded that current SOFC system power density is not sufficient to achieve MTOW values similar to those of conventional kerosene-powered regional aircraft. This work represents a first major step towards the integration of sizing methodologies for SOFC-GT-Battery powertrains into aircraft conceptual-to-preliminary design tools.

TABLE OF CONTENTS

LIST OF FIGURES

LIST OF TABLES

LIST OF ACRONYMS

Acronym	Meaning	Acronym	Meaning
APU	Auxiliary Power Unit	LPC	Low Pressure Compressor
ASR	Area-Specific Resistance	LPT	Low Pressure Turbine
BoP	Balance of Plant	LSC	Lanthanum Strontium Cobaltite
BPR	Bypass Ratio	LTSOFC	Low-Temperature Solid Oxide Fuel Cell
CS	Certification Specifications	MAWP	Maximum Allowable Working Pressure
CTE	Coefficient of Thermal Expansion	MLI	MultiLayer Insulation
DAM	Double Aluminized Mylar	MLW	Maximum Landing Weight
DSN	Double Silk Net	MTOW	Maximum Take-Off Weight
EASA	European Union Aviation Safety Agency	OCV	Open Cell Voltage
ECS	Environmental Control System	OEI	One Engine Inoperative
EIS	Entry Into Service	OEW	Operational Empty Weight
FAA	Federal Aviation Administration	OPR	Overall Pressure Ratio
FEM	Finite Element Method	ORR	Oxygen Reduction Reaction
GDC	Gadolinia-Doped ceria	PEMFC	Proton-Exchange Membrane Fuel Cell
GDL	Gas Diffusion Layer	ROC	Rate Of Climb
GT	Gas Turbine	SL	Sea Level
HALE	High Altitude Long Endurance	SOFC	Solid Oxide Fuel Cell
HOR	Hydrogen Oxidation Reaction	SUAVE	Stanford University Aerospace Vehicle Environment
HPC	High Pressure Compressor	TIT	Turbine Inlet Temperature
HPT	High Pressure Turbine	TO	Take-Off
HTSOFC	High-Temperature Solid Oxide Fuel Cell	TPB	Triple Phase Boundary
HX	Heat eXchanger	TRL	Technology Readiness Level
ITB	Interstage Turbine Burner	VTOL	Vertical Take-Off and Landing
ITSOFC	Intermediate-Temperature Solid Oxide Fuel Cell	YSZ	Yttrium-Stabilized Zirconia
LHV	Lower Heating Value		

NOMENCLATURE

Symbol	Meaning	Symbol	Meaning
W	Work, Weight	P_t	Total pressure
Δg	Change in Gibbs free energy	η	Efficiency
Δh	Change in enthalpy	ρ	Density
T	Temperature, Thrust	n_{cells}	Number of cells per stack
Δs	Change in entropy	A_{active}	Active area
E^0	Reversible voltage	M	Molar mass, Mach number
F	Faraday constant	$\dot{Q}$	Heat flow
R	Universal gas constant, Range	π	Pressure ratio
P	Pressure, Power	γ	Ratio of specific heat
f_u	Fuel utilization	LHV	Fuel lower heating value
λ	Excess air factor	V	Speed, Volume
V, v	Voltage	S	Wing area
I, i	Current	c_D	Drag coefficient
i_0	Exchange current density	k	Aerodynamic polar quadratic parameter
V_{act}	Activation voltage	c_L	Lift coefficient
α	Transfer coefficient	ξ	Maximum power ratio
i_{leak}	Leak current	ROC	Rate Of Climb
ASR	Area-Specific Resistance	$c_{gradient}$	Climb gradient
i_{lim}	Limiting current	N	Number of engines
δ	GDL thickness	Φ, Ψ, λ, Ω, β	Power management parameters
$\dot{W}$	Power	OEW	Operational Empty Weight
c_p	Specific heat at constant pressure	m	Mass
$\dot{m}$	Mass flow rate	$MTOW$	Maximum Take-Off Weight
T_t	Total temperature	t	Thickness, Time
ϕ	Porosity	D	Diameter
h	Convective heat transfer coefficient	σ_a	Allowable stress
e_w	Welding factor	L	Length
e_{bat}	Battery energy-to-mass ratio	y	Volume fraction
$MAWP$	Maximum Allowable Working Pressure	r	Radius
ν	Poisson ratio	SOC	State Of Charge
$\rho_{LH2\ storage}$	Liquid hydrogen storage density	$\frac{L}{D}$	Aerodynamic efficiency

1 INTRODUCTION

The McKinsey report on hydrogen-powered aviation [1] discusses the feasibility of using hydrogen as fuel for power and propulsion of aircraft, from the commuter segment to the long-range segment. Different powertrain configurations are recommended depending on the aircraft segment.

For commuter aircraft (19 passengers, ~500 km range) and regional aircraft (~80 passengers, ~1000 km range), a fuel cell system is proposed in the McKinsey report [1] as the optimal option for main aircraft propulsion and power. The fuel cell system provides power to electric motors and electric subsystems (e.g., Environmental Control System, de-icing system). Generally, to improve powertrain performance, a battery is installed in parallel to the fuel cell system, to improve the fuel cell transient response and to enable power peak shaving.

Several fuel cell types have been or are currently used for different market applications, as explained by Larminie et al. [2] and O'Hayre et al. [3]. These fuel cell types differ on characteristics such as electrode and electrolyte materials, charge carrier in the electrolyte, operating temperature range, fuel flexibility, and required Balance of Plant. The dominant fuel cell types and their characteristics are summarized in Table 1.

Table 1 – Characteristics of fuel cell types. Adapted from Larminie et al. [2] and O'Hayre et al. [3].

Fuel cell type	Acronym	Electrolyte	Charge carrier	Operating temperature	Power level	Use
Alkaline Fuel Cell	**AFC**	Immobilized liquid potassium hydroxide	OH^-	50-220°C	1 kW to 10 kW	Space vehicles
Proton Exchange Membrane Fuel Cell	**PEMFC**	Humidified polymer membrane	H^+	30-100°C	Up to 1 MW	Mobility, combined heat and power
Phosphoric Acid Fuel Cell	**PAFC**	Immobilized liquid phosphoric acid	H^+	200-220°C	10 kW to 1 MW	Combined heat and power
Molten Carbonate Fuel Cell	**MCFC**	Molten carbonate	CO_3^{2-}	650°C	1 MW to 100 MW	Combined heat and power
Solid Oxide Fuel Cell	**SOFC**	Ceramic	O^{2-}	500-1000°C	1 kW to 100 MW	Combined heat and power

Fuel cell systems require a set of subsystems that support stack power delivery and correct functioning. The ensemble of subsystems required for fuel cell stack operation is named Balance of Plant (BoP), as explained by Larminie et al. [2] and O'Hayre et al. [3]. The components that are part of the BoP are a function of the fuel cell type and target application of the fuel cell system. In general terms, the BoP includes an air/oxygen supply conditioning subsystem, a fuel supply conditioning subsystem, a thermal management subsystem, an electric power management and conditioning subsystem, and a control system.

Most recent studies on fuel cell systems for aviation (e.g., Juschus [4], Datta [5]) focus on the sizing and performance study of PEMFC systems for propulsion and power applications, due to the high stack-level power density of PEMFC compared to other fuel cell types, as well as the high Technology Readiness Level (TRL) of PEMFC systems for mobility applications. Nevertheless, the state-of-the-art system-level power density of PEMFCs (between 0.6-1.1 kW/kg estimated by Datta [5] for a 500-kW system) is substantially lower than that of existing gas turbine powertrains (in the order of 10 kW/kg). The low power density of PEMFC systems is mainly due to the complexity of the required BoP for operation of fuel cells within the aircraft operational envelope. Due to the low operating temperature of PEMFCs (< 100°C), stringent fuel cell cooling requirements arise, leading to high radiator area and coolant weight due to the low temperature difference with the heat sink (for aircraft, atmospheric air). Further, high radiator area leads to substantial increase in ram drag. Operation of the fuel cell system at high altitude implies that the pressure of the air supply needs to be increased from its value at high altitudes (~0.224 atm at FL360) to the fuel cell operating pressure (generally above 2 bar), leading

to bulky compressor arrangements. Additionally, humidifiers are required to humidify the air delivered to the fuel cell stack. Regarding efficiency, high-temperature fuel cells are capable of achieving higher efficiency values than PEMFCs, due to the substantial decrease of activation losses with increasing temperature.

An alternative fuel-cell-based powertrain concept which may overcome the disadvantages of PEMFC systems for aviation consists of integrating a Gas Turbine engine (GT) with a Solid Oxide Fuel Cell (SOFC) system. This concept, named SOFC-GT, has been widely studied for ground power generation applications, due to its high thermal efficiency. The SOFC-GT concept proposed in this thesis, considering a turboprop engine, is shown in a diagram in Figure 1. This concept presents several performance advantages:

- The SOFC operates at very high efficiency compared to other fuel cell types, due to its high operating temperature.
- The pressurized SOFC gas exhaust is used to produce work in the turbines.
- The unused fuel in the SOFC, which appears due to fuel utilization constraints, is injected into the gas turbine combustor, participating in the combustion process, hence releasing heat. This virtually enables for the utilization of all the fuel, either by the SOFC or by the gas turbine.
- The injection of water generated in the SOFC leads to benefits in system thermal efficiency, as demonstrated by Seitz et al. [6].
- Fuel cell cooling requirements are potentially eliminated, thanks to the use of the high-temperature SOFC heat, carried by the exhaust products and injected into the combustor, for production of work in the gas turbine.
- No fuel cell humidification required.

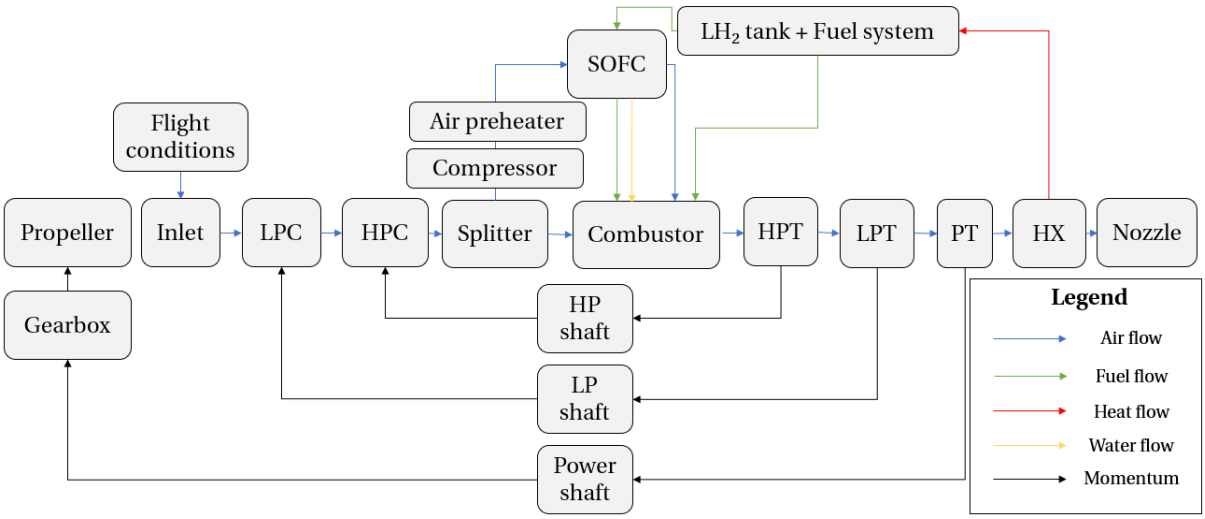

Figure 1 – SOFC-GT system architecture.

Hybridization of the SOFC-GT powertrain with batteries can be used to improve the transient performance of the system, and to obtain an extra degree of freedom for system design and performance optimization.

To study the implementation of liquid-hydrogen-fueled SOFC-GT-Battery hybrid electric powertrains into aircraft, novel aircraft design methodologies shall be derived. These methodologies are derived on the basis of traditional tube-and-wing aircraft design routines, accounting for the required modifications on weight estimation methods, power sizing routines, energy sizing expressions, and system integration requirements. These new methodologies will allow aircraft designers to understand the impact of including liquid-hydrogen-fueled SOFC-GT-Battery hybrid electric powertrains on aircraft, in terms of aircraft weight, performance, and architecture. The work outlined in this report covers the development, implementation, verification, validation, and assessment of these novel methodologies against several study cases.

This report is structured as follows:

- Chapter 2 outlines a literature review on SOFC technology, on academic studies on aircraft powertrains including SOFC systems, and on existing methodologies for hybrid electric aircraft design.
- The research objective of this work, together with a set of research questions, are presented in Chapter 3.

- Chapter 4 describes the selected aircraft design framework and definition of the target aircraft and powertrain for this work.
- The powertrain performance modelling methodologies derived in this work are described in Chapter 5.
- Power sizing and energy sizing methodologies for aircraft with liquid hydrogen fuel and SOFC-GT-Battery hybrid electric powertrains are outlined in Chapter 6.
- The methodology for calculation of aircraft weights (OEW, MTOW) and system integration is outlined in Chapter 7.
- Chapter 8 includes the implementation, verification, and validation of the methodologies derived in the previous chapters.
- Results from the implementation of the methodologies are presented in Chapter 9.
- Conclusions, recommendations, and proposed next steps are included in Chapter 10.

2 LITERATURE REVIEW

2.1 SOLID OXIDE FUEL CELLS

Solid Oxide Fuel Cells (SOFCs) are high-temperature fuel cells with a ceramic electrolyte [3]. The ionic charge carrier is O^{2-} ions. The operating temperature of SOFCs is between 500°C and 1000°C.

In these fuel cells, oxygen reacts with the electrons in the cathode to form O^{2-} ions. These ions travel through the membrane to the anode, where they react with the fuel to form the product. SOFCs are characterized by fuel flexibility, being capable of operating with fuels such as hydrogen, methane, and carbon monoxide.

The electrochemical reactions that occur in hydrogen-fueled SOFCs are the following:

$$O_2 + 4e^- \rightarrow 2O^{2-}$$

$$2H_2 + 2O^{2-} \rightarrow 2H_2O + 4e^-$$

SOFCs can be classified according to several criteria: operating temperature, architecture, type of support, and flow configuration. The types of SOFCs according to these criteria, with their description, advantages, and drawbacks, are presented in Table 2.

Table 2 – Classification of SOFCs as a function of operating temperature, architecture, support, and flow configuration. Source: Own elaboration, with format inspired in [7], completed with data from several sources [2] [3] [8] [9] [10].

Classification	Type	Description	Advantages	Drawbacks
Operating temperature	Low temperature (LTSOFC)	Operating temperature between 500-650°C.	Lower thermal cycling than ITSOFC and HTSOFC.	Lower efficiency than ITSOFC and HTSOFC. Catalysts with high electrochemical activity required. Lower quality heat than ITSOFC and HTSOFC for used in combined cycles.
	Intermediate temperature (ITSOFC)	Operating temperature between 650-800°C.	Intermediate solution between LTSOFC and HTSOFC.	
	High temperature (HTSOFC)	Operating temperature between 800-1000°C.	High efficiency. High quality heat available for bottoming cycles.	High material costs. High thermal cycling. High startup and shutdown time.
Architecture	Planar	Anode-electrolyte-cathode in a sandwich structure, with cells connected in series.	Simple design and manufacturing. High power density. Low ohmic and concentration losses.	Complex sealing. Low durability due to thermal cycling. Brittleness. Slow transient response.
	Tubular	Concentric anode-cathode-electrolyte assembly.	Simple sealing. Simple fuel and air manifolding. Improved resistance to thermal cycling compared to planar. Improved transient response compared to planar.	Low power density. High manufacturing cost. Complex current collection, leading to high ohmic losses. Lower efficiency than planar SOFC.

	Microtubular	Tubular SOFC stack formed by tubes of small diameter (< 5 mm).	Low startup time. Easy sealing. Low capital cost. High resistance to thermal cycling. High volumetric power density.	Complex manufacturing. Complex current collection. Complex manifolding. Portable applications, not yet scaled up to kW-order power.
Support	Anode-supported	Thick anode (300-800 µm) as support	High power density. Low manufacturing cost. Enables low operating temperature.	Lower power density than metal-supported.
	Cathode-supported	Thick cathode as support.	Low ohmic losses.	High concentration losses. Complex manufacturing. Low power density.
	Electrolyte-supported	Thick electrolyte (150-300 µm) as support.	High TRL. Low concentration losses.	High ohmic losses. High operating temperature needed.
	Interconnect-supported	Thick interconnect as support.	Simple sealing.	High weight of interconnect.
	Metal-supported	Thick metallic interconnect as support.	Very high power density.	Limited to operating temperature below 800°C.
Flow configuration	Co-flow	Air and fuel flows are parallel and in the same direction.	Uniform temperature profile along the channel.	Concentration effects due to depletion occur at the same location for air and fuel.
	Crossflow	Air and fuel flows are perpendicular.	Easy manufacturing, manifolding, and gas routing.	Unfavorable temperature profile, with high temperature gradient through the cells.
	Counter-flow	Air and fuel flows are parallel and in the opposite direction.	Low concentration losses due to depletion of air and fuel in opposite locations.	Non-uniform temperature profile.

There are several types of SOFC cell-level performance models, as reviewed by Wang et al. [11]. These are:

- **0D**: no spatial discretization of the fuel cell stack is considered. The SOFC performance is predicted using a lumped parameter equations based on general thermodynamic relations. 0D models are generally used for system simulation, especially when the system model encompasses the main components of the overall vehicle or power plant.
- **1D**: the fuel cell is discretized in one spatial direction, generally in the flow direction of the cathode and anode streams. An example of 1D SOFC model in the literature is the Modelica model developed by Salogni and Colonna [12]. 1D models are generally used for cell-level simulation, stack-level simulation, and system-level simulation when 0D models do not show the required accuracy.

- **2D**: used to characterize the property distribution of the two streams in the fuel cell channels. These models are generally used for cell-level simulations.
- **3D**: used for computation of the 3D distribution of thermo-physical properties within the SOFC geometry, generally using a finite volume discretization scheme. 3D models are used for SOFC cell-level simulations, to accurately characterize SOFC performance, and assess the thermal and mechanical design of the stack. These models are excessively complex, and simulations are excessively time-consuming, for their integration into conceptual and preliminary aircraft design tools.

2.2 SOFC AND SOFC-GT SYSTEMS FOR AVIATION APPLICATIONS

In the last two decades, several authors have published studies on the use of SOFC systems and SOFC-GT hybrid electric propulsion and power systems onboard aircraft. Fernandes et al. [13] present a thorough review of publications related to these systems. In this section, these studies are summarized. The schemes of system architectures selected by different authors are presented alongside the explanations.

Whyatt and Chick [14] performed in 2012 a study on the use of a lightweight SOFC system for electric power generation onboard commercial aircraft. The medium-range Boeing 787-8 aircraft is used as test case. Its maximum electric power demand is about 1 MW. The geometric arrangement of the SOFC system considered for this application is shown in Figure 2. The Gen4 Delphi planar SOFC [15] is considered as a baseline. Optimal fuel cell operating condition was characterized in terms of operating voltage and pressure. The authors conclude that SOFC stack-level power density needs to be increased by a factor higher than 2 (compared to 2012 levels, to approximately 1 kW/kg) for SOFC systems to lead to block mission fuel savings compared to using a standard APU.

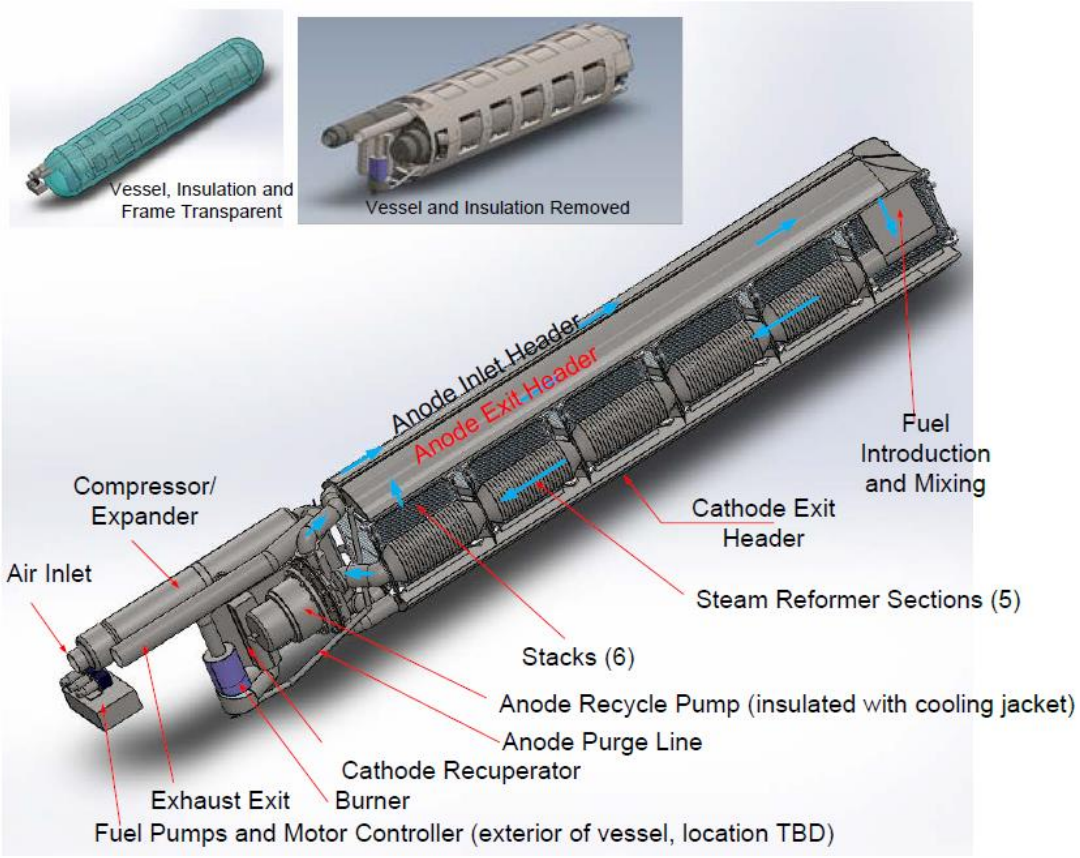

Figure 2 – SolidWorks model of the SOFC electric power generation system for application in the Boeing 787 aircraft, developed by Whyatt and Chick. Source: [14].

Braun, Gummalla and Yamanis [16] performed a study on system architectures for SOFC-based APUs for aircraft. These authors considered a system with a main turbofan powertrain and a Jet-A-fueled SOFC APU, as shown in Figure 3. In this system architecture, no direct performance coupling between the gas turbine and the SOFC exists. However, some functions overlap exist, such as the use of SOFC waste heat for fuel preheating, use of SOFC electric power for the starter generator, and substitution of the gas turbine alternator by the SOFC

to power ECS, anti-ice systems, and other electric and actuation loads. The comparison between performance of advanced gas turbine APUs with a hybrid SOFC APU system shows a decrease of aircraft fuel burn between 5-7% when using SOFC APU systems.

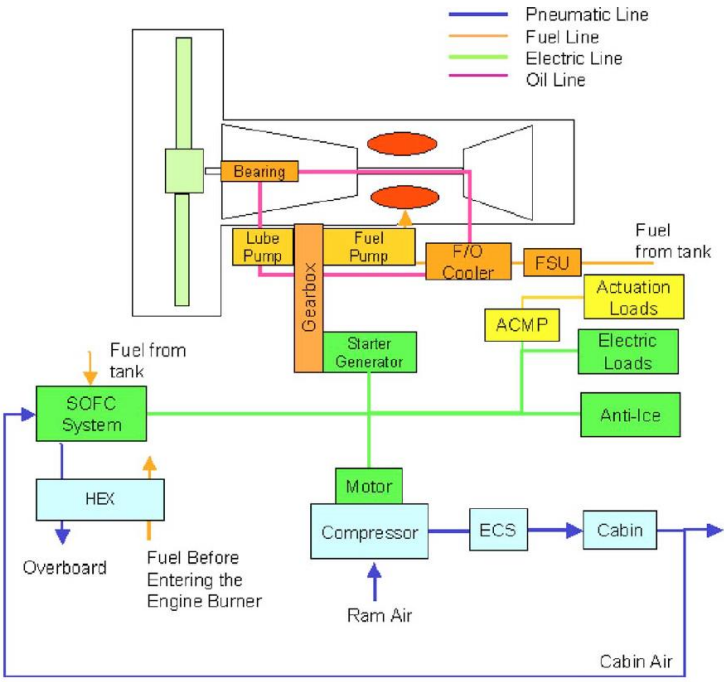

Figure 3 –System architecture for an aircraft with turbofan powertrain and SOFC APU. Source: [16].

Ji et al. [17] [18] developed a performance study of a SOFC-GT hybrid powertrain. The studied system consists of a SOFC integrated into a turbojet engine with Interstage Turbine Burner (ITB). The proposed system architecture is shown in Figure 4. Compared to performance of a turbojet engine for a commercial aircraft at transonic cruise, for SOFC operation at 800°C, 0.7 V per cell and 85% fuel utilization, results show that ~3% higher thermal efficiency and ~24% higher specific thrust are obtained for 10% electric power fraction with the integration of an ITB and a SOFC into the turbojet architecture.

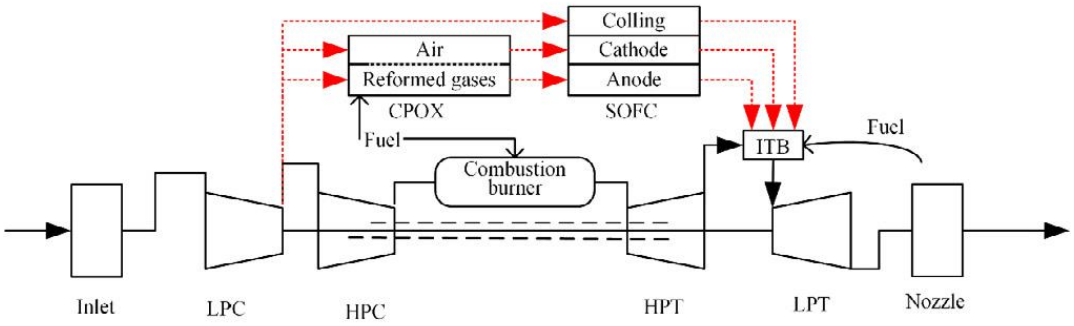

Figure 4 – Architecture of turbojet engine with ITB and SOFC. Source: [17].

Bahari et al. [19] performed a comparative study on hydrogen-fueled and methane-fueled SOFC-GT hybrid powertrains for supersonic UAVs, considering sensitivity to operating conditions. The studied system architecture is shown in Figure 5. The results show a cruise thermal efficiency of 48.7% for hydrogen fuel, and 67.9% for methane fuel.

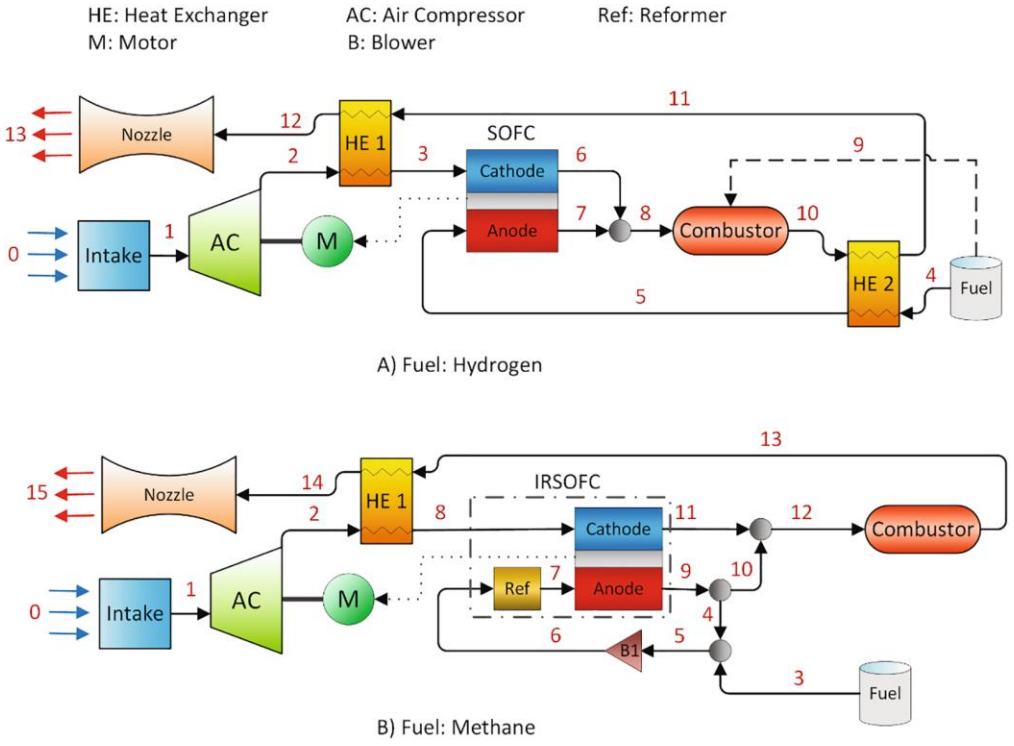

Figure 5 – SOFC-GT powertrain for supersonic UAVs using hydrogen and methane fuels. Source: [19]

Seyam et al. [20] performed a study on SOFC-GT systems coupled with a high bypass, 3-shaft turbofan engine. The proposed powertrain architecture is shown in Figure 6. 2 fuels are considered in this study: 100% Jet-A, and a blend of 75% methane and 25% hydrogen. Results show an increase of thermal efficiency from 43.4% for the turbofan to 52.8% for the hybrid system with methane-hydrogen fuel blend, with an increase of 18% of powertrain weight.

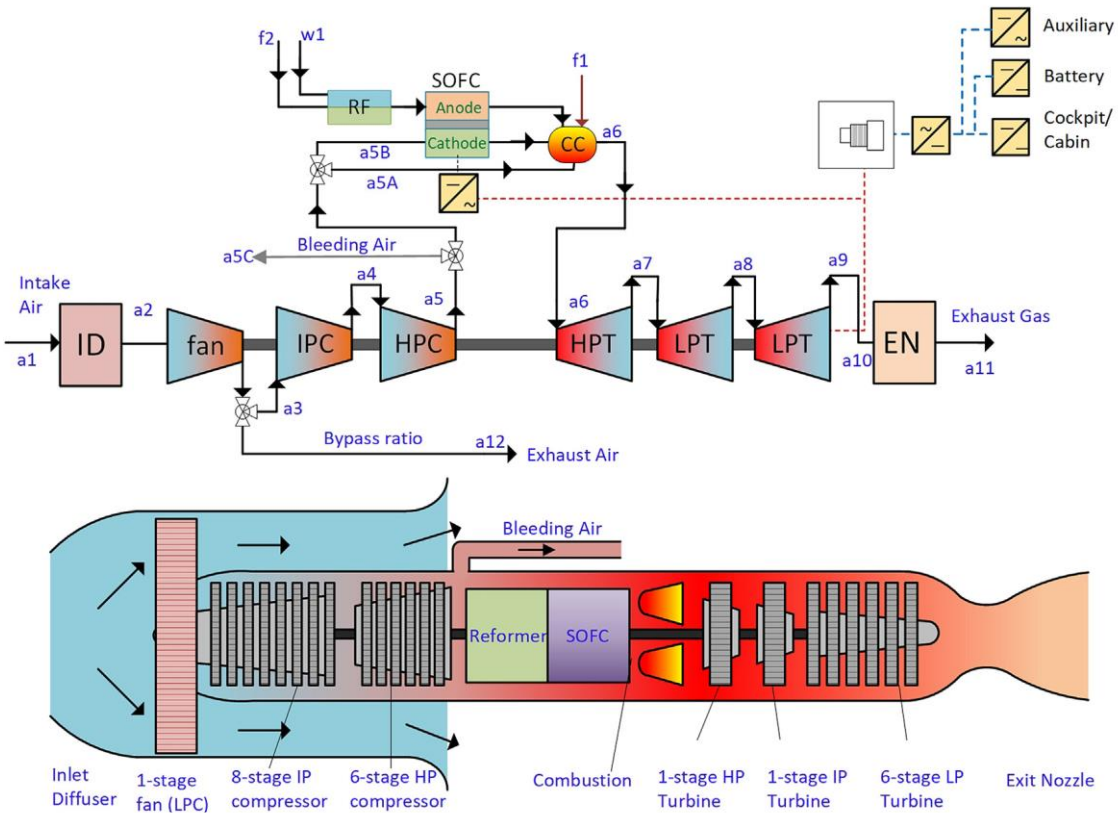

Figure 6 – Hybrid SOFC-Turbofan engine architecture. Source: [20]

Seitz et al. [6] performed an aircraft-level study of SOFC-GT powertrains, with system architecture shown in Figure 7. These authors modelled into detail the impact of SOFC exhaust water injection into the combustion chamber on GT performance. A short-medium range aircraft-level performance assessment was performed by the authors, obtaining 7.1% block fuel savings for the optimal SOFC-GT powertrain design.

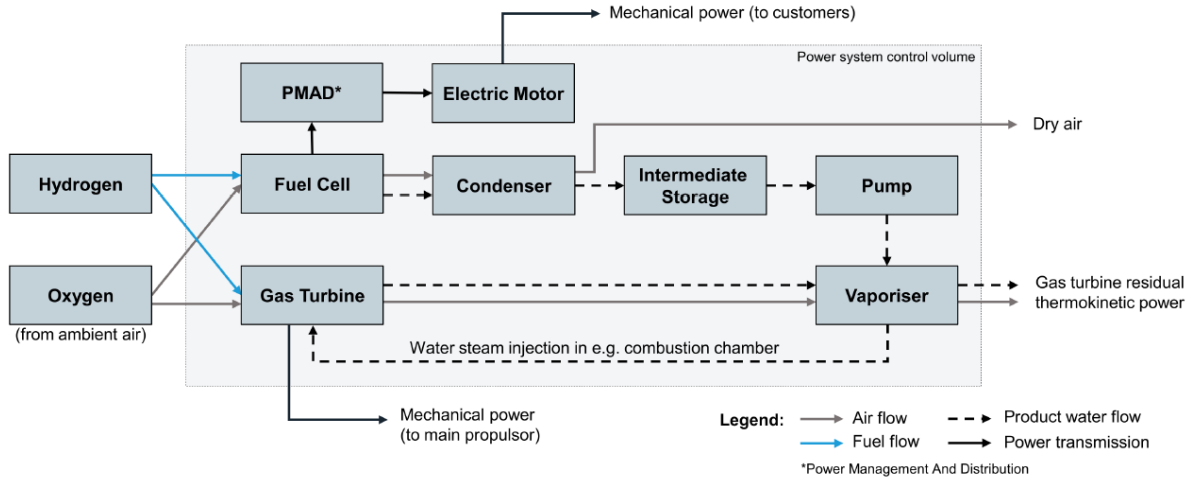

Figure 7 – Fuel cell-GT hybrid powertrain architecture proposed by Seitz et al., with a subsystem for fuel cell exhaust water management and injection into the gas turbine combustor. Source: [6].

Collins and McLarty [21] performed a design and performance analysis study for LH_2-fueled aircraft with all-electric SOFC-GT-Battery powertrains, including superconducting electric motors. A scheme of the proposed powertrain is shown in Figure 8. System optimization considering off-design component operation was undertaken, to obtain optimal component size. Studies for four modified commercial aircraft (Boeing 787-8, Airbus A380, Airbus A300, Fokker F70) were performed by the authors. The authors concluded that energy storage density above 7 kWh/kg and power density of 0.9 kW/kg at powertrain level can be obtained with optimal system sizing and hybridization. Optimal sizing leads to payload capabilities similar to state-of-the-art commercial jet aircraft.

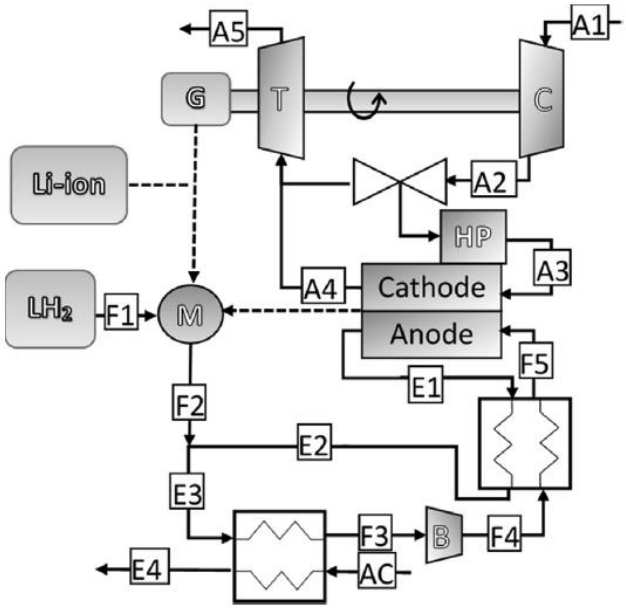

Figure 8 – All-electric SOFC-GT-Battery powertrain for aircraft proposed by Collins and McLarty. Source: [21].

Waters and Cadou [22] [23] performed a modeling study on Jet-A-fueled SOFC-GT propulsion and power systems for High-Altitude Long-Endurance (HALE) aircraft, including catalytic partial oxidation, with system architecture shown in the left of Figure 9 for a turbojet engine. An annular SOFC arrangement around the gas turbine is proposed, as shown in right of Figure 9. Studies considering turbojet, low-bypass-ratio turbofan and

high-bypass-ratio turbofan engines for different electric power demands up to 500 kW are performed. Their results show that fuel efficiency increases by 4% and 8% respectively for 50 kW and 90 kW electric power demand, with reductions of 8% and 13% respectively on powertrain power density. Further, the authors highlight that maximum electric power that the system can produce is substantially increased compared to turbofan engines, due to the lack of temperature limitations that appear in the gas turbine when high power needs to be extracted from an electric generator. Operating voltage, fuel utilization, and air stoichiometry factor are concluded to be the parameters that impact system performance the most.

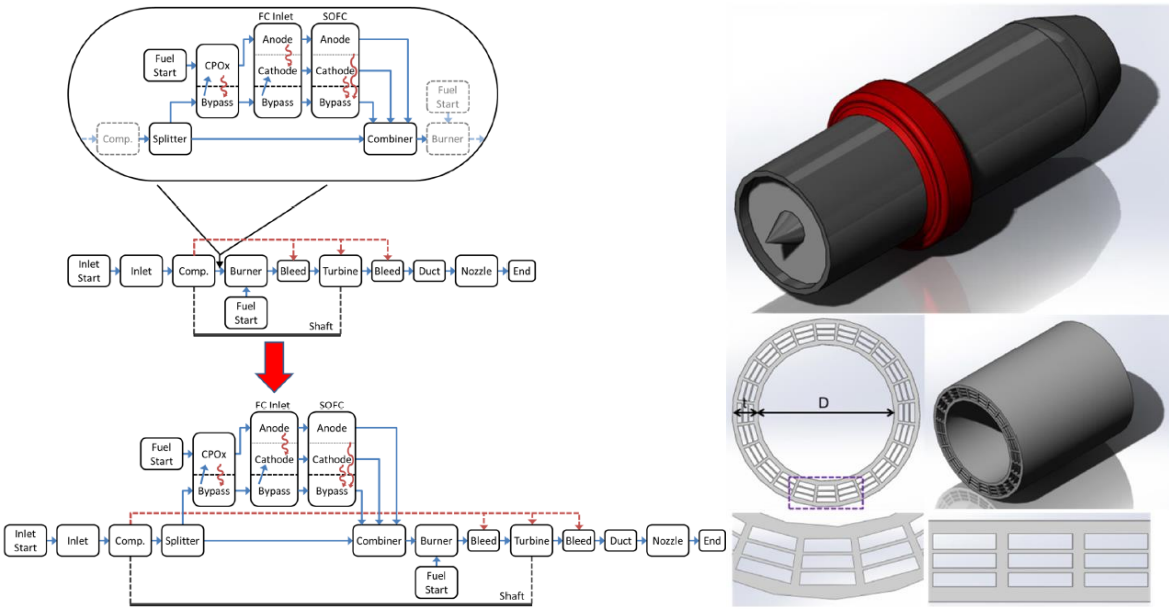

Figure 9 – Left: NPSS model architecture of SOFC-Turbojet system. Right: Annular SOFC integration into gas turbine engines, as proposed by Waters. Source: [22].

The installed performance of the SOFC-GT system proposed by Waters [22], as seen in the right of Figure 9, has also been studied by the author, as well as by Pratt [24]. A turbofan nacelle external aerodynamics model is developed, considering the SOFC housed in an annular ring at the engine hot section. From simulations, it is concluded that the SOFC installation drag cancels the benefits in terms of system energy consumption of the SOFC-GT system when compared to traditional electric generators powered by the gas turbine shaft. According to Waters, Pratt and Cadou [25], vehicle-level fuel consumption during cruise of HALE aircraft is reduced by 8% for fuselage-integrated SOFC systems, and by 4% for nacelle-integrated SOFC systems, considering tight integration with a high-bypass-ratio, high-pressure-ratio turbofan with optimal flowpath design. The authors highlight the need for research on less intrusive SOFC system integration for the hybrid system.

Regarding powertrain performance modelling, Freeh, Pratt and Brouwer [26] developed and validated a SOFC-GT model for aerospace applications. Chakravarthula [27] developed a transient model for a SOFC-GT powerplant for aircraft distributed electric propulsion. A startup time of 15 min is estimated for the SOFC.

2.3 HYBRID ELECTRIC AIRCRAFT DESIGN

The development of hybrid electric powertrain architectures for aircraft has been an increasing trend in the last years. Novel hybrid electric aircraft design methodologies have been developed by universities, research institutes and companies to study the conceptual and preliminary design requirements of low emission powertrains for aviation. These methodologies include the works by de Vries [28], Isikveren et al. [29], Brelje and Martins [30], and Finger [31].

In this work, the powertrain can count on two energy sources (liquid hydrogen and electric energy stored in batteries) and two mechanical power sources (gas turbine and electric motor). The design methodologies for hybrid electric aircraft described in this section will be adapted to tackle the specific requirements of the powertrain targeted in this work. This work, thus, represents a first contribution to the advancement of the state-of-the-art of design methodologies for fuel cell-gas turbine-battery hybrid powertrains for aircraft.

2.3.1 POWER SIZING FOR HYBRID ELECTRIC AIRCRAFT

de Vries [28] developed a methodology for obtaining the wing and power loading at the design point for generic hybrid electric aircraft with multiple energy sources and propulsion systems. The main steps of the methodology are:

- The aircraft performance constraint diagram, including failure conditions, is constructed.
- The hybrid electric powertrain architecture is selected. de Vries considered a general series/parallel partial hybrid architecture for the methodology derivation, including two energy sources (fuel, battery) and two power sources (gas turbine, battery). This general architecture is shown in the scheme reported in Figure 10.
- The design power control parameters of the powertrain configuration are defined. de Vries considers two parameters for the generic architecture shown in Figure 10. These are:
    - **Supplied power ratio (Φ)**: originally defined by Isikveren et al. [29] as the fraction of power provided by batteries.

$$\Phi = \frac{P_{bat}}{P_{bat} + P_f}$$

    - **Shaft power ratio (φ)**: fraction of shaft power produced by electrical machines.

$$\varphi = \frac{P_{s2}}{P_{s2} + P_{s1}}$$

- A set of power balance equations is defined based on the unknowns of the powertrain model (see Figure 10) and the selected power control parameters.
- The aircraft performance equations are modified to account for component failure conditions with the selected architecture.
- The performance constraints of the powertrain components are derived using the aircraft-level constraint diagram and the solution of the power balance system of equations.

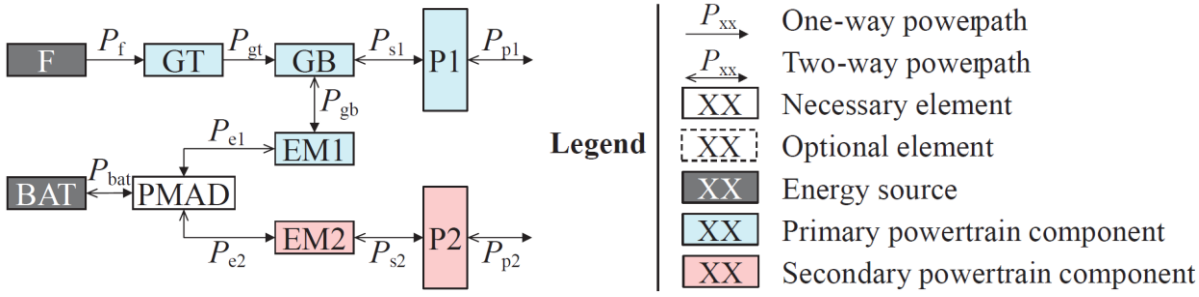

Figure 10 – Scheme of seriel/parallel partial hybrid electric powertrain architecture proposed by de Vries. Source: [28].

Brelje [32] uses the OpenConcept code for power sizing of powertrain components. This approach consists on the use of a Newton solver that matches the engine throttle with the power requirement at each flight condition.

In Chapter 6 of this work, the methodology proposed by de Vries [28] is adapted for liquid-hydrogen-fueled SOFC-GT-Battery hybrid electric aircraft.

2.3.2 ENERGY SIZING FOR HYBRID ELECTRIC AIRCRAFT

Methodologies to determine the energy carried onboard conventional aircraft have been modified for hybrid electric powertrains. The Breguet range equation is used in traditional aircraft design books (e.g., Raymer [33], Torenbeek [34] and Sadraey [35]) to compute the required fuel mass to fulfil the design mission. This equation is derived assuming a single energy source (fuel), which is consumed progressively during flight. Due to the dependency of range on aircraft mass, this equation needs to be derived again when considering batteries, as no mass reduction occurs for this energy source consumption during the mission. Hybrid electric powertrains are generally characterized by two energy sources: electric energy from batteries, and fuel. The equation to determine the energy required for the mission needs to account for the characteristics of both energy sources.

Hepperle [36] derived a modified Breguet equation to compute the range for battery-powered aircraft as a function of battery mass:

$$R = m_{bat} \frac{e_{bat} \eta_{total} \frac{L}{D}}{g\ MTOW}$$

The fact that the mass of the aircraft does not decrease as the energy of the batteries is depleted leads to a range penalty. This impact is especially relevant for long-range flights, where the fuel consumption effects lead to substantial range benefits.

Marwa et al. [37] derived a set of range equations for cruise flight of hybrid electric aircraft at (a) constant-airspeed and constant lift coefficient, (b) constant altitude and constant lift coefficient, and (c) constant airspeed and constant altitude. Ravishankar and Chakravarty [38] developed a range equation for series hybrid electric aircraft. Elmousadik et al. [39] proposed the use of two so-called hybridization ratios to parameterize the serial hybrid electric configuration, allowing for derivation of a range equation for hybrid-electric aircraft. de Vries, Hoogreef and Vos [40] developed, instead, a range equation for generalized hybrid electric aircraft.

de Vries [28] proposed a modification of the Breguet cruise range equation for general hybrid electric powertrains. First, the system architecture shown in Figure 10 is simplified, assuming no power losses at the nodes, and an overall transmission efficiency for each propulsive branch of the configuration. The simplified system architecture is shown in Figure 11. This implies that the supplied power ratio Φ is the only design parameter of the system, and it is not necessary to use the shaft power ratio φ in the range equation.

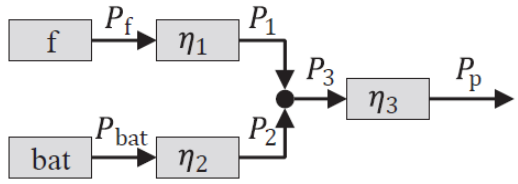

Simplified representation	Mechanical-node architectures	Electrical-node architectures
$\eta_1 =$	η_{GT}	$\eta_{GT}\eta_{GEN}$
$\eta_2 =$	η_{EM}	1
$\eta_3 =$	η_p	$\eta_{EM}\eta_p$

Figure 11 – Simplified generic representation of hybrid electric powertrains, and values of efficiency for mechanical nodes and electrical nodes. Source: [28].

For a given constant value of the power control parameter Φ during cruise, considering the system architecture and variables shown in Figure 10, the following expression is derived for the range equation, valid for conventional, serial, parallel, turboelectric, and fully electric aircraft:

$$R = \eta_{overall} \frac{LHV}{g} \frac{L}{D} \left(\eta_{GT,overall} + \eta_{electric.overall} \frac{\Phi}{1-\Phi} \right) \ln \left(\frac{\left(OEW + m_{payload} + \frac{g}{e_{bat}} E_{tot} \left(\Phi + \frac{e_{bat}}{LHV} (1-\Phi) \right) \right)}{OEW + m_{payload} + \frac{g}{e_{bat}} \Phi E_{tot}} \right)$$

Based on the work by Finger [31], de Vries recommends performing time-stepped mission analysis, considering instantaneous values of the power control parameters, to maximize the accuracy of the analysis, as the power / load distribution profile has a strong influence on mission energy requirements.

Waters [22] derived a modified Breguet range equation for SOFC-GT powertrain architectures. The used SOFC-Turbojet architecture is shown in Figure 9, considering both thrust and electric power production. Electric power fraction ζ is defined by Waters as the fraction between generated electric power and total system power:

$$\zeta = \frac{P_e}{P_e + P_p}$$

The derivation leads to the following expression, considering system thrust specific fuel consumption $TSFC$:

$$R = \frac{V}{g\ tsfc} \frac{L}{D} \ln \left(\frac{tsfc + \frac{V}{LHV\ \eta_{electric}} \left(\frac{\zeta}{1-\zeta} \right)}{\frac{tsfc}{\frac{m_{initial}}{m_{final}}} + \frac{V}{LHV\ \eta_{electric}} \left(\frac{\zeta}{1-\zeta} \right)} \right)$$

None of the previous derivations completely fulfils the requirements and the characteristics of LH_2-fuelled SOFC-GT-Battery hybrid electric powertrains. Therefore, a novel Breguet range equation for these systems is derived in Chapter 6 of this work.

2.3.3 WEIGHT ESTIMATION AND CALCULATION FOR HYBRID ELECTRIC AIRCRAFT

Aircraft Operational Empty Weight (OEW) is the result of different contributions, namely from the aircraft structure (wing, fuselage, tail, landing gear, nacelles, control surfaces), powertrain, and other systems and equipment [35].

Components weight estimation can be obtained via physics-based methods, published data, or empirical equations. Historically, conceptual-to-preliminary aircraft design methodologies have heavily relied on statistical methodologies for weight estimation, using data from previous aircraft with similar development year, mission, and configuration. Reference aircraft design books such as Raymer [33], Torenbeek [34] and Sadraey [35] report empirical equations for component weight calculation for aircraft.

For hydrogen-powered SOFC-GT-Battery hybrid-electric aircraft, statistical aircraft-level data are not available. Therefore, physics-based expressions and empirical component weight estimation methodologies shall be used.

de Vries [28] highlights the inapplicability and lack of an experimental database for Class I weight estimation methods for hybrid electric aircraft. A modified Class I statistical method, considering empirical data for the aircraft components that remain unchanged with respect to conventional aircraft, and using alternative component weight estimation methodologies for novel components, is proposed by the author:

$$OEW = OEW_{ref} - m_{wing,ref} - m_{powertrain,ref} + m_{wing} + m_{powertrain}$$

The work by Brewer [41] includes a dataset of component weight for hydrogen-powered aircraft, based on studies for supersonic civil transport aircraft (234 passengers, 4200 NM range, $M_{cruise} = 2.7$, 4 turbofan engines) and subsonic civil transport aircraft (400 passengers, 5500 NM range, $M_{cruise} = 0.85$, 4 turbofan engines) performed by Lockheed California in the 1970s.

The weight of fuel cell systems needs to be calculated to obtain an accurate estimation of the aircraft OEW. Literature on sizing and weight estimation of PEMFC systems for aviation applications has been gaining momentum in the last years. Juschus [4] developed, implemented, and validated a methodology for sizing and estimating the weight of PEMFC systems for CS-25 aviation applications. Datta [5] developed a model for sizing and weight estimation of PEMFC systems, based on a 0D model of PEMFC stacks, and physics-based and empirical models of BoP components. The purpose of the work of Datta was to determine the required technological development of PEMFC systems to make their use feasible for eVTOL applications. The baseline methodology proposed by Datta [5] for PEMFC system sizing and weight estimation is adapted in this work to deal with SOFC stacks and corresponding BoP.

Tornabene et al. [42] developed a set of parametric mass and volume estimation methods for SOFC-GT hybrid systems for aerospace applications, considering Jet A fuel. Steffen et al. [43] developed a Jet-A-fuelled SOFC-GT system weight estimation methodology for sizing of a 440 kW APU for a 300 passenger commercial transport aircraft. The use of hydrogen leads to a significantly different fuel system weight estimation methodology, as no reformer is used, and heat exchangers are needed to increase hydrogen temperature to that required for SOFC operation. Seitz et al. [6] developed a weight estimation methodology to determine SOFC weight for fuel cell-gas turbine hybrid propulsion systems for short-medium range aircraft. The authors considered a detailed model of the propulsion system accounting also for the impact of fuel cell exhaust water injection into the gas turbine. At the same time, the authors neglected the impact of operating conditions on SOFC system sizing. Waters and Cadou [23] estimate the mass of a SOFC system with catalytic partial oxidation by estimating the weight of each main component of the propulsion system.

The different fuel cell type and BoP requirements of the proposed SOFC-GT-Battery powertrain compared to the configurations studied in literature, as well as the different fuel chosen, made it necessary to implement significant modifications with respect to the sizing and weight estimation methodologies discussed in the literature. These modifications are presented in Chapter 7 of this work.

3 RESEARCH OBJECTIVE AND RESEARCH QUESTIONS

3.1 RESEARCH GAPS

The research gaps identified during the literature review, and how they are addressed in the present work, are summarized in Table 3.

Table 3 – Research gaps related to methodologies for liquid-hydrogen-fueled aircraft design with SOFC-GT-Battery hybrid electric propulsion and power systems, and how these are addressed in the present work.

Reference(s)	Year	Research focus	Research gaps	Present work
Waters, Cadou, Pratt [22] [23] [25] [24]	2015	Performance modeling of SOFC-GT integrated engine for UAVs with large electrical loads.	SOFC stack arranged in a tube around the gas turbine, thus causing high installation drag. Derivation of Breguet range equation for Jet-A-fueled SOFC-GT systems. No liquid hydrogen tank or battery is used.	SOFC integrated into fuselage to avoid additional drag. Derivation of range equation for LH_2-fuelled SOFC-GT-Battery hybrid electric powertrains, including impact of LH_2 tank and battery weight.
Collins and McLarty [21]	2020	Sizing procedure for aircraft with all-electric SOFC-GT-Battery powertrains.	No propulsion power directly generated by the gas turbine. MTOW is assumed constant, regardless of the power capacity chosen for the powertrain components.	The main engine is a turboprop that produces part of the propulsive power. Methodology to determine power of the powertrain components based on component-oriented constraint diagrams, as well as consistent estimation of aircraft MTOW.
Seitz et al. [6]	2022	Preliminary aircraft-level study of SOFC-GT powertrains for aviation, with detailed modelling of the impact of water injection from SOFC exhaust on GT performance.	Detailed component weight estimation is not included. No modification of Breguet equation to consider batteries. Constant power capacity assumed for the components of the powertrain.	Increased accuracy of OEW estimation methodologies. Breguet equation considering batteries. Power sizing methodology using component-oriented performance diagrams.
de Vries [28]	2022	Methods for energy sizing, power sizing, and weight estimation of hybrid electric powertrains.	No adaptation of derived methods to determine fuel weight, battery capacity, component power and powertrain weight of SOFC-GT-Battery hybrid-electric powertrains.	Derivation of component-oriented performance diagrams for power sizing of SOFC-GT-Battery hybrid electric powertrains. Physics-based and empirical equations for component weight estimation of LH_2-fuelled SOFC-GT-Battery hybrid electric powertrains. Derivation of range equation for LH_2-fuelled SOFC-GT-Battery hybrid electric powertrains.

3.2 RESEARCH OBJECTIVE AND SUB-GOALS

The main research objective of this work is to develop novel power sizing, energy sizing, weight estimation, and integration methodologies for regional aircraft with liquid-hydrogen-fueled SOFC-GT-Battery hybrid electric powertrains, and to use these methods to perform sensitivity analyses and assess possible applications of the technology. This goal is achieved by means of the following tasks:

- Implementation of thermodynamic cycle model of SOFC-GT hybrid electric powertrains.
- Development and validation of a novel, component-oriented power sizing methodology for SOFC-GT-Battery hybrid electric powertrains.
- Derivation of an equation analogous to the Breguet range equation to determine the hydrogen fuel mass and battery capacity needed on board of aircraft with SOFC-GT-Battery hybrid electric powertrains.
- Derivation of physics-based and empirical correlations for estimation of OEW of regional aircraft with liquid hydrogen fuel and SOFC-GT-Battery hybrid electric powertrains.
- Integration of the various methodologies to accurately estimate the MTOW of regional aircraft with liquid hydrogen fueled SOFC-GT-Battery hybrid electric powertrains.
- Implementation of a methodology to assess the requirements associated with the integration of liquid hydrogen tanks and SOFC-GT-Battery hybrid electric powertrains into the fuselage of regional aircraft.
- Application of the derived methodology to assess the sensitivity of SOFC-GT-Battery hybrid electric powertrain performance and size on the chosen system design variables.
- Application of the derived methodology to compute the MTOW and the corresponding weight breakdown of 50-seat regional aircraft adopting liquid hydrogen fueled SOFC-GT-Battery hybrid electric powertrains.

3.3 RESEARCH QUESTIONS

The following research questions are answered in the project:

1. What modifications are required to the traditional design methodologies of tube-and-wing aircraft for regional missions if a LH_2-fuelled SOFC-GT-Battery hybrid electric system is adopted for propulsion and power generation?
2. What is the effect on powertrain sizing and performance of varying the relative power capacity of the various components of a LH_2-fuelled SOFC-GT-Battery hybrid electric system?
3. What is the effect of the use of LH_2-fuelled SOFC-GT-Battery hybrid electric systems on regional aircraft weight and system integration?

4 AIRCRAFT DESIGN FRAMEWORK AND TARGET AIRCRAFT AND POWERTRAIN DEFINITION

4.1 AIRCRAFT DESIGN FRAMEWORK

To assess the feasibility of SOFC-GT-Battery powertrains for tube-and-wing regional aircraft, an ad-hoc aircraft preliminary design and performance analysis framework was implemented during the project. The framework consists of several sub-tools implemented in Python, whose interdependencies are as shown in Figure 12.

- Top level requirements are initially defined, based on the aircraft application defined in terms of payload, range, cruise speed, takeoff distance, landing distance, etc.
- Initial assumptions required for aircraft design are defined.
- Aircraft conceptual design is performed. This includes selection of wing location, number of engines, engine location, type of tail, control surfaces, high-lift devices…
- The estimate of the aerodynamic characteristics of the aircraft, together with a preliminary evaluation of the power and weight of the powertrain components, as well as of the fuel weight and MTOW, are obtained based on data from similar aircraft.
- The constraint analysis methodology is used to size the power of the components of the propulsion and power system and the wing area of the aircraft, given the MTOW.
- The weight and size of the components of the propulsion and power system are computed given the energy and power requirements identified through the constraint analysis.
- The OEW is estimated using a modified Class I method for hydrogen-powered aircraft with SOFC-GT-Battery hybrid electric propulsion and power systems.
- Using reference data for typical fuel consumption fractions during takeoff, climb, descent, and landing, and the Breguet equation for cruise operation, the fuel required for a reference mission is computed.
- The weight of the components that depends on the primary energy to carry out onboard, such as the LH_2 tank and fuel, is computed based on the results of the mission analysis.
- The results of the previous calculations are used to calculate a new estimate of the aircraft MTOW.
- The information regarding component power and weight, as well as MTOW is used to update the results of the constraint analysis and then subsequently of the sizing procedure adopted for the different components of the aircraft.
- The calculations are repeated for several iterations until convergence.
- After convergence, the size of each component is estimated, and an integration routine is run, to compute the required fuselage size to house the novel powertrain.

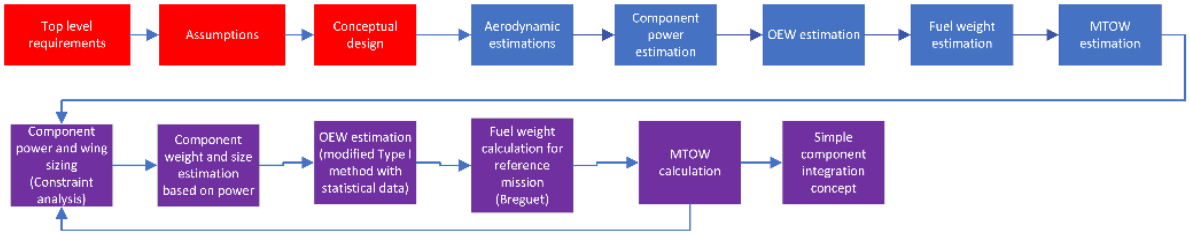

Figure 12 – Aircraft design framework implemented in this work.

4.2 TARGET AIRCRAFT DEFINITION

The focus of this work is the development of design methodologies for LH_2-fuelled regional aircraft with SOFC-GT-Battery hybrid electric powerplants. A 50-seat regional aircraft with 2 turboprop engines installed in the rear part of the fuselage and T-tail is considered as reference in this work. This aircraft will be hereafter referred to as the **target aircraft**.

The following conceptual design specifications for the target aircraft are considered:

- Tube-and-wing configuration.
- 2 aft turboprop engines.
- Low wing configuration.
- T-tail.

- Electric motor and fan installed in the lower part of the vertical tail.
- Liquid hydrogen fuel.
- SOFC-GT-Battery hybrid electric powerplant.

A market study on regional aircraft has been performed. The obtained data is presented in *APPENDIX I – Tables of market study of regional aircraft*, as reference. Table 20 lists the main characteristics of several regional aircraft in the market with 30-90 seats from different aircraft manufacturers. The corresponding weights and powerplant of these aircraft are presented in Table 21. The performance characteristics of these aircraft is shown in Table 22. The initial estimation on aerodynamic parameters for each aircraft, required for wing and power sizing, is presented in Table 23. Based on the data in the tables, the following conclusions can be drawn:

- The range of turbofan-powered aircraft is commonly between 2500-3500 km, while the range of turboprop-powered aircraft is between 1000-2000 km.
- Cruise Mach number of turbofan-powered aircraft is between 0.74-0.78, while cruise Mach number of turboprop-powered aircraft is between 0.45-0.6.
- Cruise altitude of turbofan-powered aircraft is 11,000 m, whereas for turboprop-powered aircraft is around 7,620 m (FL250).
- MTOW is 18-25 ton for 50-seater aircraft, with higher MTOW for aircraft with longer range (usually turbofan-powered).
- OEW is 12-14 ton for 50-seater aircraft.
- Maximum Mach number is around 0.78-0.82 for jet aircraft, while for turboprop aircraft it is between 0.45-0.6.
- Cruise ceiling is above the tropopause for jet aircraft, while it is at FL250 for turboprop aircraft.
- Takeoff distance is between 1800-2300 m for jet aircraft, while it is between 1000-1500 m for turboprop aircraft.
- Landing distance is between 1300-1700 m for jet aircraft, while it is between 800-1100 m for turboprop aircraft.
- In general, main performance data of the aircraft are publicly available. However, no public information on stall speed is usually available. The EASA CS-25 regulations [44] indicate that the approach speed for civil aircraft should be higher than or equal to 1.3 times the stall speed. According to Schaufele [45], the stall speed of regional turboprops is around 110 kt (56.6 m/s). Therefore, $V_{stall} \geq 43.5\ m/s$. The stall speed considered for the target aircraft is 45 m/s.

The performance requirements of the target aircraft are defined based on the data from Table 22. These requirements are summarized in Table 4.

Table 4 – Target aircraft performance requirements.

Pax	Range (km)	Max cruise Mach	Cruise ceiling (m)	ROC (ft/min)	Takeoff distance (m)	Landing distance (m)	Stall speed (m/s)
50	1500	0.60	9500	2000	1300	1000	45

The aerodynamic and weight parameter estimations required for application of the derived aircraft design methodologies to target aircraft are presented in Table 5.

Table 5 – Aerodynamic and weight estimations for the target aircraft.

Aspect ratio	Oswald efficiency factor	K polar	Zero-lift drag coefficient	$c_{L,cruise}$	Propeller propulsive efficiency at cruise	Propeller propulsive efficiency at takeoff and climb	μ	L/D max SL	$\frac{W_{landing}}{W_{TO}}$
12.0	0.8	0.0332	0.02	0.9	0.8	0.7	0.03	15	0.8

c_{D0LG}	$c_{D0HLD,TO}$	$c_{D0HLD,landing}$	$\Delta c_{L,HLD,TO}$	$\Delta c_{L,HLD,landing}$	Maximum c_L without flaps	Maximum c_L with TO flaps	Maximum c_L with landing flaps
0.010	0.008	0.035	0.8	1.0	1.7	2.5	2.7

4.3 LIQUID-HYDROGEN-FUELLED SOFC-GT-BATTERY HYBRID ELECTRIC POWERTRAIN ARCHITECTURE DEFINITION

The powerplant is formed by different systems, interconnected as shown in Figure 13:

- **Power generation system**.
  - **SOFC stack**. It is modeled as composed of four subcomponents, i.e., the anode, cathode, electrolyte, and bipolar plates.
  - **Gas turbine**. Its main components are the air inlet, low-pressure compressor (LPC), high-pressure compressor (HPC), combustor, high-pressure turbine (HPT), low-pressure turbine (LPT), power turbine, high-pressure shaft, low-pressure shaft, and power shaft.
- **Propulsion system**. It comprises the core nozzle, the propeller, and the electric fan.
- **Thermal management system**. It is composed of the oil tank, oil pump, and air pre-heater.
- **Fuel system**. It is composed of the LH2 tank and LH2 pumps.
- **Fuel cell air supply system**. It comprises the air compressor and pre-heater.
- **Electric system**. It includes the DC/DC converter, batteries, and the electric motor.

Different flows are used to model the system:

- **Hydrogen flow**. Starting at the liquid hydrogen tank, it is pumped using a booster pump, and divided into the SOFC stream and the GT stream. The SOFC stream is vaporized and heated in a heat exchanger, and then injected into the SOFC anode, where part of it is consumed, and part of it is re-injected into the combustor. The GT stream is compressed in a second, high-pressure pump, and passed through a heat exchanger for vaporization and temperature increase.
- **Air flow**. Air flow enters the system through the turboprop inlet. Then, it is compressed using 2 compressor stages (LPC and HPC). Afterwards, the stream is divided into the SOFC stream and the combustor stream. The SOFC stream is compressed and pre-heated before flowing through the SOFC cathode, where the oxygen is consumed to produce electricity. The exhaust, oxygen-depleted air is then injected into the combustor, together with the combustor air stream. After combination with the hydrogen stream and combustion, the mixture is expanded using 2 turbine stages (HPT and LPT), which power the LPC and HPC. After this, the mixture is further expanded in the power turbine, which provides mechanical power to the propeller via a power shaft. Finally, the air flow is expanded via a core nozzle, producing thrust.
- **Water flow**. Water is produced in the SOFC anode due to the electrochemical reaction of hydrogen and oxygen. This water is injected into the GT combustor.
- **Electric flow**. Electricity is produced by the electrochemical reaction within the SOFC and collected by the SOFC bipolar plates. This electricity is used to power electrical subsystems (e.g., oil pump, electric heater) and the electric propulsion system. A DC/DC converter is installed between the SOFC and the batteries, to allow for battery charging/discharging. Then, electricity flows through an electric inverter to the electric motor, that powers an electric fan.
- **Coolant flow**. Used to preheat the air before injection into the SOFC.

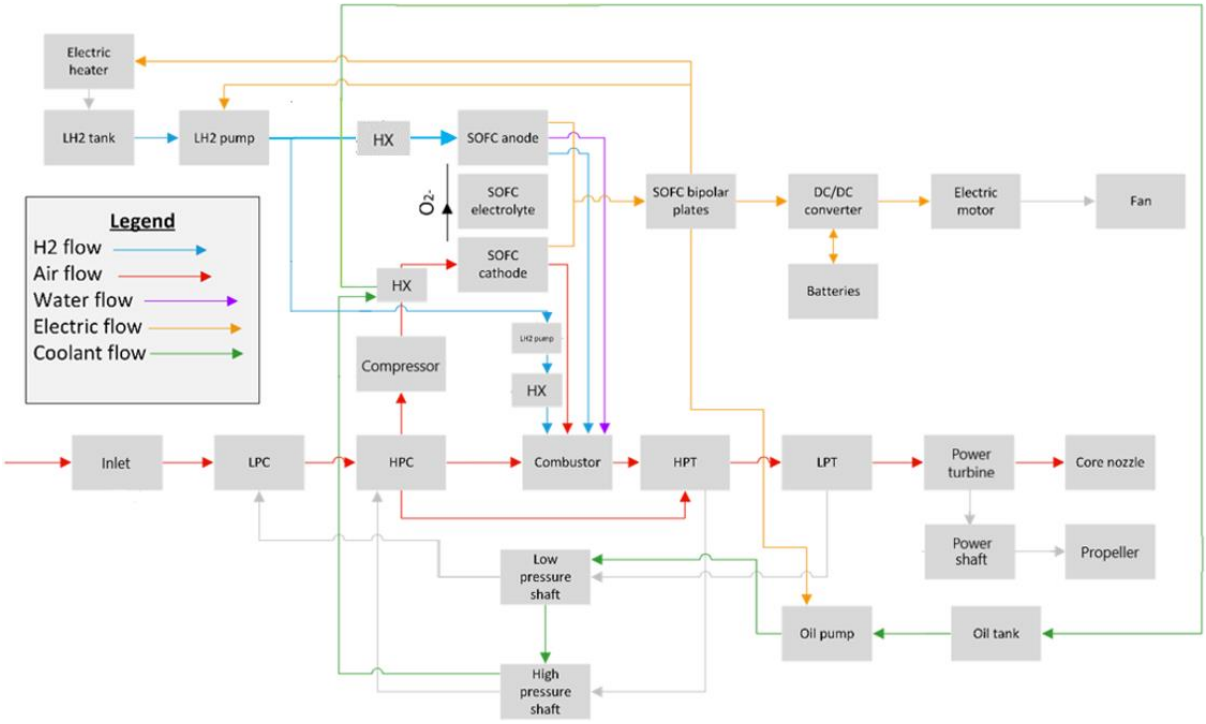

Figure 13 – Powertrain architecture for the target aircraft.

4.4 SOFC TYPE SELECTION

The selection of the type of SOFC technology strongly impacts the system design, sizing, and performance. In principle, the SOFC must feature high power density, high efficiency, low cost (non-expensive materials, simple design and manufacturing), operational compatibility with a gas turbine in terms of temperature and pressure level, adequate transient response, low startup and shutdown time, and low thermal cycling impact on durability.

NASA Glenn Research Center [46] developed in 2009 a structurally symmetrical bi-electrode-supported high-power-density SOFC, using a thin layer of electrically conductive LaCaCrO2 (LCC) for current collection instead of heavy metal interconnects, and thin YSZ electrolyte with two porous supports structures to maximize resistance to thermal cycling. A power density of 2.5 kW/kg and a volumetric power density of 7.5 kW/l at cell level is achieved with this concept.

Based on an extensive literature study, focusing on the state-of-the-art SOFC solutions developed for mobility in the last years, and following the recommendation on use of metal-supported SOFCs for aircraft applications by Braun, Gummalla and Yamanis [16], the most suitable technology for this work is the **high-power-density planar co-flow metal-supported ITSOFC** proposed by Udomsilp et al. in 2020 [47], originally developed as range extender for electric vehicles. The reasons of this selection are the high power density, high efficiency, fast dynamic response and quick start-up featured by the fuel cell[1], together with its mechanical robustness, resistance to thermal cycling and oxidation, as well as the relatively low cost given by the simple manufacturing process and the use of low-cost materials.

The selected metal-supported SOFC is formed by an yttrium-stabilized zirconia (YSZ) electrolyte, a gadolinia-doped ceria (GDC) diffusion barrier layer, a Ni/GDC cermet anode with Ni/YSZ interlayer and base layer, a LSC anode, and a highly porous 0.3-mm-thick ferritic oxide dispersion strengthened Fe-Cr alloy metal support. The microstructure of the SOFC is shown in Figure 14. This information about the SOFC microstructure will be used in later sections for weight and volume estimation.

[1] High thermal conductivity and mechanical stability of metal supports allows start-up in less than 15 min for 15 kW range extenders

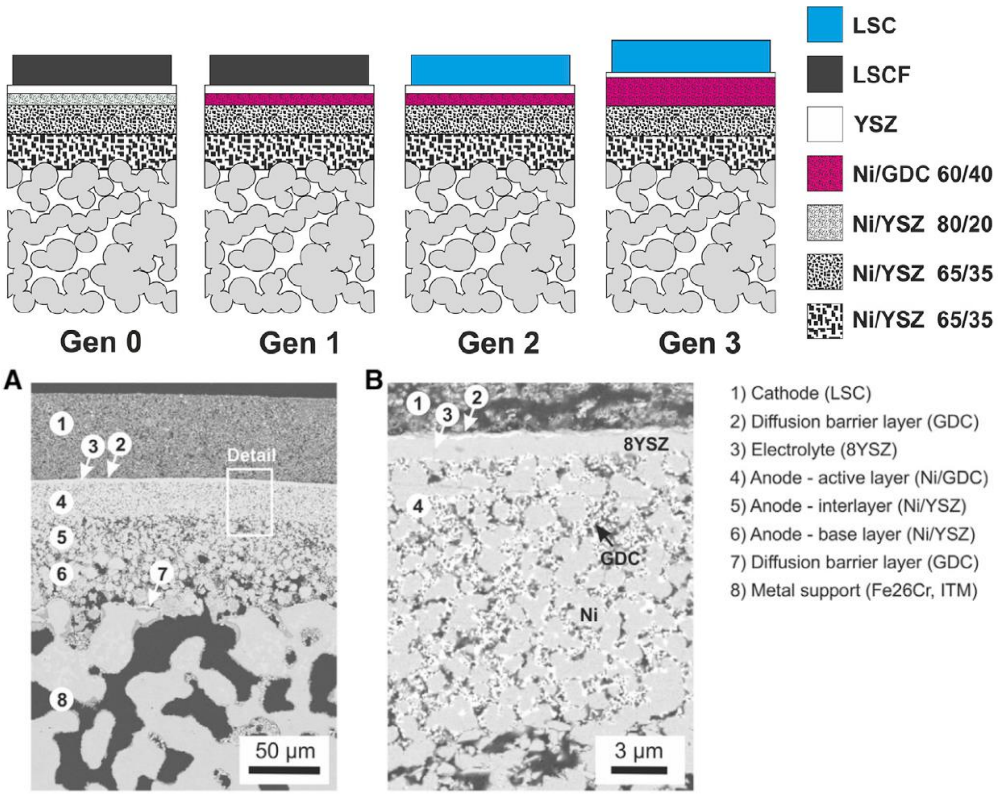

Figure 14 – Microstructure of the selected metal-supported SOFC [47].

The performance of this SOFC resulting from experimental tests is shown in Figure 15.

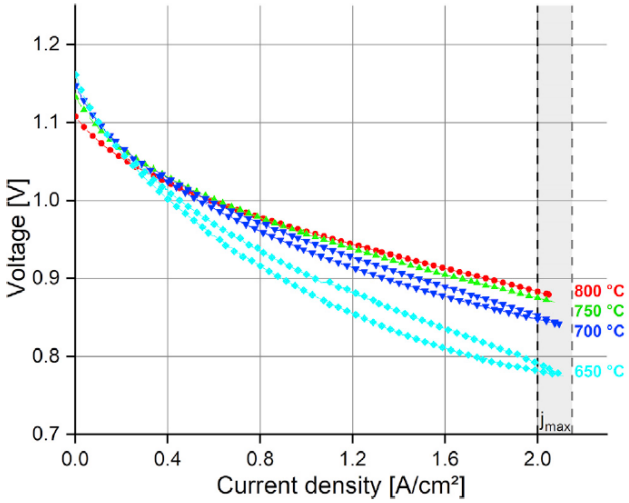

Figure 15 – Experimental performance of a prototype metal-supported SOFC (50 x 50 mm² cell with 16 cm² active cathode area) as a function of temperature, tested at 1,000 sccm H_2 (22% max fuel utilization at maximum current of 32 A, negligible concentration loss) and 2,000 sccm O_2. 2 curves are shown for each temperature, based on a hysteresis-like effect that appears when testing at increasing and decreasing current, respectively. Source: [47]

According to Udomsilp et al. [47], the volumetric power density of the metal-supported SOFC should exceed 1.2 kW/l at stack level. The objective of research and development efforts related to this SOFC technology is the achievement of a power density > 0.14 kW/kg and >0.12 kW/l at system level, as well as system-level efficiency in excess of 50%.

5 POWERTRAIN PERFORMANCE MODELLING

5.1 SOFC SYSTEM PERFORMANCE MODELLING

Given the objective of this work, that is the development of an aircraft design tool accounting for SOFC-GT-Battery hybrid electric powertrains, a 0D model of the fuel cell stack was deemed the most adequate. This model will be used to evaluate the performance of the fuel cell both in stack-level and system-level simulations and will be integrated in the aircraft design tool.

5.1.1 0D CELL-LEVEL SOFC PERFORMANCE MODEL

A 0D cell-level performance model to emulate the performance of the metal-supported SOFC by Udomsilp et al. [47] has been developed based on a combination of physics-based and empirical equations.

First, the reversible SOFC performance model is developed. Ideal fuel cell performance is obtained from the change of Gibbs free energy, which can be derived from thermodynamic tables for the H_2-O_2 reaction:

$$W = -\Delta g = -(\Delta h - T\Delta s)$$

Fuel cell reversible voltage at standard state conditions for a H_2-O_2 fuel cell is obtained using the following expression:

$$E^0 = -\frac{\Delta g^0}{2F}$$

Temperature, pressure, and concentration effects affect fuel cell reversible voltage. The Nernst equation is used to characterize the variation of reversible voltage with pressure and concentration. Further, temperature effects need to be included. The following expression is used to obtain the fuel cell reversible voltage:

$$E = E^0 + \frac{\Delta s}{2F}(T - T_0) + \frac{RT}{2F}\ln\left(\frac{P_{H2}\sqrt{P_{O2}}}{P_{H2O}}\right)$$

With $\frac{\Delta s}{2F} = -2.3 \cdot 10^{-4}\frac{V}{K}$ for hydrogen oxidation at ambient pressure and temperature.

The pressure terms represent the partial pressures of each species involved in the reaction, as indicated by Larminie and Dicks [2], namely:

$$P_{H2} = \alpha P;\ P_{O2} = \beta P;\ P_{H2O} = \delta P$$

For SOFC reactions involving air and pure hydrogen, $\alpha = 1$, $\beta = 0.2095$ and $\delta = 1$. With this consideration, the following expression is obtained, which accounts for the impact of temperature, pressure, and concentration on Open Cell Voltage (OCV, named E in the equations):

$$E = E^0 + \frac{\Delta s}{2F}(T - T_0) + \frac{RT}{2F}\ln\left(\frac{\alpha\sqrt{\beta}}{\delta}\right) + \frac{RT}{4F}\ln(P)$$

Further, the fuel utilization and air stoichiometry factor impact the OCV. Reactant activity is reduced as fuel utilization increases, leading to decrease in OCV. This is because the cell voltage is limited by the lowest local potential of the cell, due to the high conductivity and isopotential characteristics of electrodes that lead to uniform voltage [8] [9]. This impact is especially relevant in SOFCs, as the impact of local partial pressure is enhanced linearly by high temperatures (see Nernst equation). It results that the voltage decrease due to high utilization factors is 5 times higher at 1200°C compared to 25°C. From 80% fuel utilization to 20%, Nernst voltage increases quasi-linearly at an approximate rate of 0.0025V/%. The impact of excess air $\lambda = \frac{\dot{m}_{air,in}}{\dot{m}_{air,stoich}}$ and fuel utilization $f_u = \frac{\dot{m}_{H2,consumed}}{\dot{m}_{H2,in}}$ on OCV is characterized by the following expressions, proposed by Winkler [48], already including the partial pressure effect:

$$\Delta E = -\frac{RT}{2F}\ln(K)$$

$$K = \frac{f_u\sqrt{\frac{\lambda}{\beta} - f_u}}{(1 - f_u)\sqrt{P(\lambda - f_u)}}$$

$$E = E^0 + \frac{\Delta s^0}{2F}(T - T_0) + \frac{RT}{2F}\ln\left(\frac{(1-f_u)\sqrt{P(\lambda - f_u)}}{f_u\sqrt{\frac{\lambda}{\beta} - f_u}}\right)$$

Regarding process irreversibility, activation losses, ohmic losses, mass concentration losses and parasitic losses (leakage current, crossflow…) need to be modelled as a function of current density. The corresponding expression that describes the fuel cell voltage reads:

$$V(i) = E - V_{act} - V_{ohmic} - V_{concentration} - V_{parasitic}$$

The modelling of fuel cell performance irreversibilities is presented in several reference fuel cell textbooks (Larminie, Dicks and McDonald [2], O'Hayre [3], Singhal [8], U.S. Department of Energy [9]). The adopted approach to model irreversibilities is summarized in the following:

- **Activation losses** are the losses due to limitations on electrochemical kinetics. The activation loss is modelled by an activation overvoltage V_{act}, defined as the fuel cell voltage that is consumed to overcome the activation energy to start the reaction. The main parameter that characterizes activation losses is the exchange current density i_0, defined as the current density production to be reached to overcome the activation losses. High i_0 implies that activation losses are low, as apparent from the equations reported in the following. Further, the forward and reverse reactions can have different activation energies. This is quantified by the transfer coefficient α, with values between 0 and 1. If $\alpha = 0.5$, the reactions are called symmetric, namely the activation energy of the forward and reverse reaction is equal. For electrochemical reactions, values of α between 0.2-0.5 are typical. The Butler-Volmer equation describes the net current density as a function of the activation energy of the forward and reverse reactions:

  $$i = i_0\left(e^{\frac{2\alpha F V_{act}}{RT}} - e^{\frac{-2(1-\alpha)F V_{act}}{RT}}\right)$$

  The Butler-Volmer equation applies separately to the anode and cathode, each of them with their own exchange current density and transfer coefficient. For current density well above the exchange current density, the Tafel approximation of the Butler-Volmer equation can be used to characterize activation overvoltage from operating current density. The use of the Tafel approximation is usual for the prediction of activation losses for PEM fuel cells, as the exchange current density is low. For SOFCs, the exchange current density is usually in the same order of magnitude to the operating current. Therefore, the Tafel approximation cannot be used. In this work, the Butler-Volmer equation is solved numerically to model the activation losses. While activation losses are dominant in low temperature fuel cells (e.g., PEMFC), their effect is much smaller in high temperature fuel cells, such as ITSOFC and HTSOFC, due to the Arrhenius temperature dependence of the activation overvoltage.
- **Ohmic losses** are losses that appear due to the transport of electrons and ions within the fuel cell. As ionic conductivity of the electrolyte is several orders of magnitude lower than electronic conductivity of metallic bipolar plates, ionic transport generally dominates ohmic losses. These losses scale inversely with transport area. Therefore, the area-specific resistance ($ASR = \frac{L}{\sigma}, \Omega \cdot cm^2$) is the parameter that best models the ohmic losses. Ohm's equation is used to characterize ohmic overvoltage as a function of current density:

  $$V_{ohmic} = iASR$$

  Ohmic losses are the dominant losses in SOFC. They are minimized by decreasing electrolyte thickness. However, this poses some operational/design challenges such as SOFC mechanical integrity, electric shorting, fuel crossover and dielectric breakdown.
- **Concentration losses** appear due to limitations on species transport within the fuel cell. Fuel cell reactions occur at the contact point between the electrode, electrolyte, and reactant, named triple-phase-boundary. Effective transport of the reactants to the TPB is crucial to ensure effective fuel cell performance. Reactant transport through the fuel cell occurs mainly by convection (pressure difference), while transport across electrodes is governed by diffusion mechanisms (concentration gradient in the gas diffusion layer). Due to limitations in the diffusion transport, reactant local concentration at the reaction location is lower than in the bulk flow, while product local concentration

is higher. The higher the current density, the higher the diffusive reactant transport from bulk flow to the triple-phase-boundary, requiring higher concentration gradient. This implies lower reactant concentration at the triple-phase boundary. For this reason, concentration loss becomes dominant at high current density operation. Concentration losses can be sub-divided into two main loss mechanisms, as explained by O'Hayre [3]: Nernstian mechanism, and activation mechanism. These two effects can be modelled by introducing the limiting current density $i_{\lim}$ parameter. i_{lim} is defined as the current density at which the reactant concentration at the TPB is zero. Physically, $i_{\lim}$ is a function of effective diffusivity of the reactants (D_{eff}), electrode porosity ϵ, electrode tortuosity τ, reactant concentration in bulk flow c_R^0, and gas diffusion layer thickness δ ($i_{lim} = \frac{2FD_{eff}c_R^0}{\delta}$). Typical values range between 1-10 A/cm^2. Limiting current is translated into concentration overvoltage as follows, considering both the Nernstian and activation loss mechanisms:

$$V_{conc} = \frac{RT}{2F}\left(1 + \frac{1}{\alpha}\right)\ln\left(\frac{i_{lim}}{i_{lim} - (i + i_{leak})}\right)$$

Despite the theoretical validity of this expression, experimental data show that concentration losses are substantially higher than those predicted by theory. Therefore, an empirical constant c is introduced in the equation in place of the $\frac{RT}{2F}\left(1 + \frac{1}{\alpha}\right)$ parameter, i.e.:

$$V_{conc} = c\ln\left(\frac{i_{lim}}{i_{lim} - (i + i_{leak})}\right)$$

The value of *c* is calibrated with experimental data.

As concentration losses appear at high current density values, growing drastically at current density above the peak power density of the fuel cell performance curve, where operating efficiency is low, their significance for fuel cell performance simulation is low. The operating points that involve concentration losses are generally avoided during normal operation, being largely sub-optimal. Nevertheless, for operation close to the peak power density, namely during the high-power phases of the mission, concentration losses can become significant.

- **Parasitic losses** include current leakage, gas crossover and unwanted side reactions. They can be quantified using a leakage current i_{leak}, which affects activation and concentration losses, but not ohmic losses. Leakage current is obtained experimentally or calibrated empirically. Gross current produced by the fuel cell i_{gross} is the sum of useful current i and leakage current i_{leak}:

$$i_{gross} = i + i_{leak}$$

Overall, the H_2-O_2 fuel cell performance curve is described in this work using the following expression, where $V_{act,BV}$ is obtained by numerical solution of the Butler-Volmer equation:

$$\boldsymbol{V(i) = -\frac{\Delta g^0}{2F} + \frac{\Delta s}{2F}(T - T_0) + \frac{RT}{2F}\ln\left(\frac{(1 - f_u)\sqrt{P(\lambda_{air} - f_u)}}{f_u\sqrt{\frac{\lambda_{air}}{0.21} - f_u}}\right) - V_{act,BV}(i, \alpha_a, i_{0,a}, \alpha_c, i_{0,c}, i_{leak}) - iASR - c\ln\left(\frac{i_{lim}}{i_{lim} - (i + i_{leak})}\right)}$$

5.1.2 CALIBRATION OF BASELINE 0D CELL-LEVEL SOFC PERFORMANCE MODEL USING EXPERIMENTAL DATA

A calibration of the activation and ohmic losses of the baseline performance model is performed using least-squares fitting to the experimental performance data by Udomsilp et al. [47], shown in Figure 15. This work reports two curves for each temperature level, due to the Joule heating hysteresis effect, that leads to different measurements if the experimental campaign is performed increasing or decreasing current. In this work, only the upper curve for each temperature level is considered.

The ASR is obtained considering that, according to Udomsilp et al., the *i-V* curve shows linear behaviour when the current density is between 1.5-2 A/cm^2. This implies that the activation losses are nearly constant over this range. Further, in the experiments of Udomsilp et al., concentration losses are negligible due to the low fuel utilization ($f_u < 0.22$ for all operating conditions), and only ohmic losses lead to a decrease of operating voltage in the range of current density 1.5-2 A/cm^2. This allows to estimate the ASR using least-squares fitting on the experimental data, considering a linear behaviour of current as a function of voltage.

Regarding the activation losses, the fitting of the model parameters first required that the activation losses were isolated from the other loss sources. To this purpose, the OCV and the ohmic losses were subtracted to the voltage curve as a function of current. To avoid numerical problems in the least-squares method, anode activation losses are neglected, as their impact is foreseen to be negligible. This simplification is acceptable as proven by experimental data of SOFCs, as the exchange current density of the anode is ~2 orders of magnitude greater that of the cathode (according to O'Hayre [3], $i_{0,anode} = 10\frac{A}{cm^2}$ and $i_{0,cathode} = 0.1\frac{A}{cm^2}$ are typical values for SOFC). This means that the anode activation losses are negligible with respect to those occurring at the cathode. The resulting activation loss curve is used to perform a least-squares fitting of the cathode activation losses parameters.

In this thesis, fuel cell performance is modelled for operation at constant temperature, pressure, air stoichiometry factor and fuel utilization:

- Reference operating temperature is selected as 650°C.
- Reference operating pressure is 1 bar.
- Regarding $\lambda_{air,ref}$, in the paper by Udomsilp et al. [47], the experimental data is presented for constant air flow for all current densities (2,000 sccm air). For this reason, the experimental curves cannot be directly correlated to a single value of air stoichiometry. Considering that $f_u = 0.22$, for $i = 2\frac{A}{cm^2}$ the fuel consumed is 220 sccm and the corresponding oxygen consumption is 110 sccm, that in turns implies 524 sccm air consumption. The air requirement varies from 0 to 524 sccm from 0.0 to 2.0 A/cm^2. Therefore, $\lambda_{air} = \frac{\dot{m}_{air,inlet}}{\dot{m}_{air,consumed}}$ varies from 3.82 to ∞ in the graph. However, as the calibration of the nominal or baseline performance of the fuel cell model needs to be performed for a fixed stoichiometric factor, $\lambda_{air,ref} = 5.0$ is selected as reference value, as this represents to a first approximation the average operating condition of the fuel cell in the tests of Udomsilp et al.
- Regarding f_u, the paper [47] presents experimental data for constant fuel flow for all current densities (1,000 sccm H_2). For this reason, the experimental curves cannot be directly correlated to a single value of fuel utilization. 22% fuel utilization is assumed as reference value, as it is the maximum value reached in the tests of Udomsilp et al.

The operating conditions extrapolated from the paper by Udomsilp et al. [47] and considered as the reference ones for the modeling of the nominal performance of the fuel cell are included in Table 6.

Table 6 – Operating conditions for baseline performance of selected SOFC. Source: [47].

Parameter	T_{ref} **(°C)**	P_{ref} **(atm)**	$\lambda_{air,ref}$	$f_{u,ref}$
Value	650	1.0	5.0	0.22

The baseline performance of the SOFC predicted by the calibrated model is shown in Figure 16, compared with the experimental data from Udomsilp et al. [47]. The value of the calibrated parameters is shown in Table 7. Due to the low f_u and limitations in the experiments by Udomsilp et al., concentration losses cannot be calibrated using this source. The reference value of c is then derived based on information from O'Hayre [3], that indicates that $c = 0.1$ if $T = 1100\,K$. Correcting this value of c for the temperature effect as explained later, it results that $c_{ref} = 0.091$ at the reference temperature $T = 650°C$. The value of the limiting current is determined given the reference fuel utilization and assuming $i_{\text{lim,ref}} = 7.8\frac{A}{cm^2}$ according to data found in Singhal [8] and O'Hayre [3].

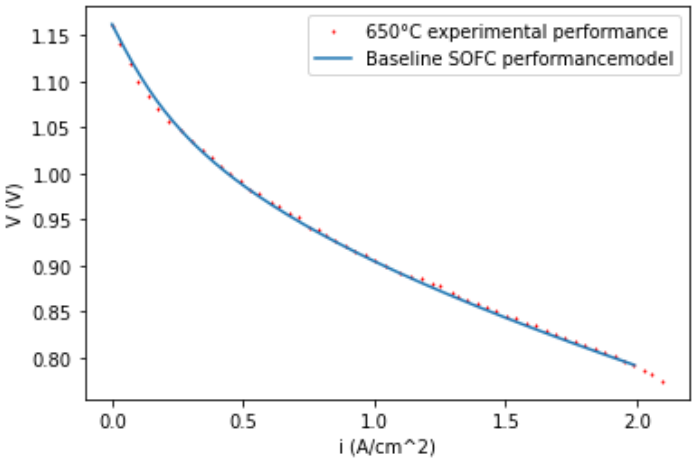

Figure 16 – Calibrated baseline SOFC performance, compared to experimental data. After [47].

5.1.3 CALIBRATION OF 0D CELL-LEVEL SOFC PERFORMANCE MODEL AS A FUNCTION OF OPERATING CONDITIONS

The general expression to characterize the cell performance curve, including the impact of operating conditions on performance, is the following:

$$\boldsymbol{V}(\boldsymbol{i}, \boldsymbol{P}, \boldsymbol{T}, \boldsymbol{\lambda_{air}}, \boldsymbol{f_u})$$
$$= -\frac{\boldsymbol{\Delta g^0}}{\boldsymbol{2F}} + \frac{\boldsymbol{\Delta s}}{\boldsymbol{2F}}(\boldsymbol{T} - \boldsymbol{T_0}) + \frac{\boldsymbol{RT}}{\boldsymbol{2F}}\ln\left(\frac{(\boldsymbol{1} - \boldsymbol{f_u})\sqrt{\boldsymbol{P}(\boldsymbol{\lambda_{air}} - \boldsymbol{f_u})}}{\boldsymbol{f_u}\sqrt{\frac{\boldsymbol{\lambda_{air}}}{\boldsymbol{0.21}} - \boldsymbol{f_u}}}\right)$$
$$- \boldsymbol{V_{act,BV}}(\boldsymbol{i}, \boldsymbol{\alpha_a}, \boldsymbol{i_{0,a}}, \boldsymbol{\alpha_c}, \boldsymbol{i_{0,c}}, \boldsymbol{i_{leak}}, \boldsymbol{P}, \boldsymbol{T}, \boldsymbol{\lambda_{air}}, \boldsymbol{f_u}) - \boldsymbol{iASR}(\boldsymbol{P}, \boldsymbol{T}, \boldsymbol{\lambda_{air}}, \boldsymbol{f_u})$$
$$- \boldsymbol{c}(\boldsymbol{P}, \boldsymbol{T}, \boldsymbol{\lambda_{air}}, \boldsymbol{f_u})\ln\left(\frac{\boldsymbol{i_{lim}}(\boldsymbol{P}, \boldsymbol{T}, \boldsymbol{\lambda_{air}}, \boldsymbol{f_u})}{\boldsymbol{i_{lim}}(\boldsymbol{P}, \boldsymbol{T}, \boldsymbol{\lambda_{air}}, \boldsymbol{f_u}) - (\boldsymbol{i} + \boldsymbol{i_{leak}}(\boldsymbol{P}, \boldsymbol{T}, \boldsymbol{\lambda_{air}}, \boldsymbol{f_u}))}\right)$$

The fuel cell performance depends on operating temperature T, pressure P, air stoichiometry factor λ_{air}, and fuel utilization f_u, marked in blue in the previous expression. Further, the fuel cell loss model is characterized by 8 empirically calibrated parameters marked in red in the previous expression: α_a, $i_{0,a}$, α_c, $i_{0,c}$, ASR, c, i_{lim} and i_{leak}. The impact of T, P, λ_{air}, f_u on the empirical parameters of the loss model also needs to be modelled.

The method for calibration of the performance model as a function of the operating conditions to realistically represent experimental SOFC performance is now presented. More in detail, Datta [5] developed a PEM fuel cell model for conceptual design of hydrogen fueled eVTOL aircraft. The same author proposed a modelling methodology to describe the relation between the operating conditions and the value of the model performance parameters. This methodology is here adapted to model SOFC performance. The variation of the loss parameters with temperature and pressure is modelled using polynomial relations whose calibration is based on SOFC experimental data found in the literature.

5.1.3.1 EFFECT OF TEMPERATURE

The model parameters at the temperature values at which there is experimental data from Udomsilp et al. [47] (700°C, 750°C and 800°C) are estimated via calibration to this experimental data using least-squares fitting. Then, the dependency of the SOFC model parameters with temperature is accounted with a 2nd order polynomial, as proposed by Datta [5] for PEMFC, of the form:

$$\Delta x(T) = a + b(T - T_{ref}) + c(T - T_{ref})^2$$

where Δx is a generic parameter of the model. Other references from the literature, such as Song et al. [49], are used for the verification and validation of the fitted polynomial. According to Udomsilp et al. [47], due to the low hydrogen utilization (<22%), concentration losses can be neglected until 2 A/cm^2. Therefore, the concentration losses for higher fuel utilization cannot be calibrated using the data from Udomsilp et al. [47]. An alternative procedure has been used to calibrate the activation losses. Recalling the expression for concentration losses:

$$V_{conc} = \frac{RT}{2F}\left(1+\frac{1}{\alpha}\right)\ln\left(\frac{i_{lim}}{i_{lim}-(i+i_{leak})}\right) = c\ln\left(\frac{i_{lim}}{i_{lim}-(i+i_{leak})}\right)$$

it has been demonstrated experimentally [50] that, as described by the equation above, concentration losses for a given operating current density increase with increasing temperature. Therefore, a linear model is used to characterize the increase in concentration losses with increasing temperature:

$$\Delta c(T) = \frac{R\left(1+\frac{1}{\alpha}\right)}{2F}(T - T_{ref})$$

Regarding the limiting current density i_{lim}, the variation of this parameter with temperature cannot be modeled using the data from Udomsilp et al. [47] either, due to the low fuel and air utilization of the experimental tests. On the contrary, the physics-based approach by O'Hayre [3] has been used to characterize the impact of temperature on i_{lim}. It is worth recalling the physics-based definition of limiting current density, which reads $i_{lim} = \frac{2FD_{eff}c_R^0}{\delta}$, where $D_{eff} = D_{ij}\frac{\epsilon}{\tau}$ for SOFC, c_R^0 accounts for the impact of f_u and λ_{air} on i_{lim}, while δ, ϵ and τ account for the impact of cell geometry on i_{lim}. The impact of temperature on i_{lim} can thus only be modeled through the gas diffusivity D_{ij}, whose value is, indeed, strongly dependent on temperature and pressure. More in detail, the following expression, from kinetic gas theory, can be used to compute D_{ij} [3]:

$$D_{ij} = a\left(\frac{T}{\sqrt{T_{ci}T_{cj}}}\right)^b \frac{\left(P_{ci}P_{cj}\right)^{\frac{1}{3}}}{P}\left(T_{ci}T_{cj}\right)^{\frac{5}{12}}\sqrt{\frac{1}{M_i}+\frac{1}{M_j}}$$

For $H_2 - O_2$ systems, this expression reads

$$D_{ij} = 0.06\left(\frac{T}{71.7}\right)^{1.823}\frac{1}{P}$$

where D_{ij} in cm^2/s, T in K, and P in atm

Finally, as this is the only term in the i_{lim} equation that accounts for temperature and pressure, it is possible to derive that to a first approximation

$$i_{lim} \propto 0.06\left(\frac{T}{71.7}\right)^{1.823}\frac{1}{P}$$

Once the model tuning for the reference or nominal operating conditions has been completed, the calibration of the variation of the model parameters as a function of temperature can be performed by a least squares fitting procedure considering the experimental data regarding OCV, activation losses, ohmic losses, and concentration losses. The results of this procedure are shown in Table 7.

Table 7 – Calibration of SOFC performance model for a planar metal-supported SOFC operated at 1 bar and <22% fuel utilization. (*) means assumption based on reference literature [3].

Parameter	Units	650°C (ref)	700°C	750°C	800°C
OCV	V	1.162	1.147	1.132	1.108
$\boldsymbol{i_{0,cathode}}$	$\frac{A}{cm^2}$	0.080	0.100	0.120	0.160
$\boldsymbol{\alpha_{cathode}}$	$-$	0.51	0.62	0.7	0.78
$\boldsymbol{ASR}$	Ωcm^2	0.06	0.045	0.04	0.035
$\boldsymbol{i_{leak}}$	$\frac{A}{cm^2}$	0.01*	0.01*	0.01*	0.01*
$\boldsymbol{i_{lim}}$	$\frac{A}{cm^2}$	7.8*	8.59	9.41	10.26
$\boldsymbol{c}$	V	0.006	0.012	0.018	0.024

The calibrated model is compared with the digitalized experimental data from Udomsilp et al. [47] in Figure 17. As shown in this figure, the calibrated model correctly predicts the performance of the reference SOFC.

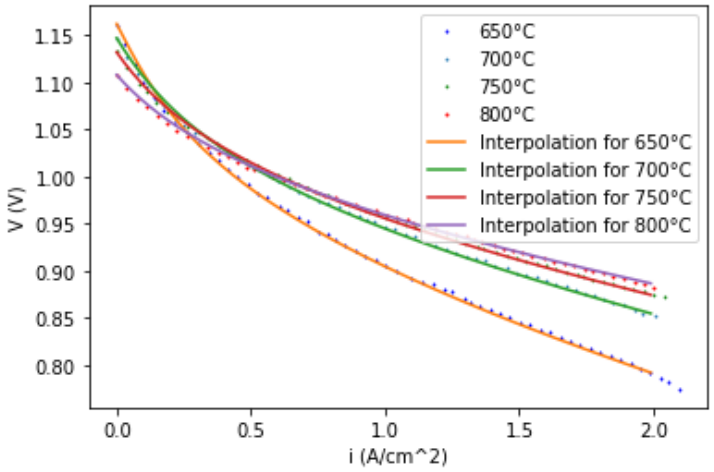

Figure 17 – Calibration of the SOFC performance model to fit the data by Udomsilp et al. (dots in the graph). After [47].

With the previous calibration, and including the physics-based methodology for concentration losses dependency with temperature, the following expressions can be used to model the SOFC performance as a function of temperature if SOFC operating temperature is between 650°C and 800°C:

$$\Delta i_0(T) = 0.000115(T - 923) + 2.5 \cdot 10^{-6}(T - 923)^2$$

$$\Delta \alpha(T) = 0.00244(T - 923) - 4 \cdot 10^{-6}(T - 923)^2$$

$$\Delta ASR(T) = -0.00065(T - 923) + 10^{-6}(T - 923)^2$$

$$\Delta c(T) = \frac{R\left(1 + \frac{1}{\alpha}\right)}{2F}\Delta T$$

$$i_{lim} \propto T^{1.823}$$

where T is in [K].

5.1.3.2 EFFECT OF PRESSURE

Based on the work by Datta [5], the effect of pressure on fuel cell performance can be modelled by varying the value of the model parameters according to an exponential relation of the type:

$$\Delta x(P) = a(P - P_{ref})^b$$

Where x is a generic parameter of the SOFC model, while a, b are calibration parameters.

The impact of the operating pressure is calibrated based on the works by Singhal et al. [8] (Figure 18), Zhou et al. [10], Seidler et al. [50] (Figure 19), Duan et al. [51], Willich et al. [52], Momma et al. [53], and Singhal, Virkar and Fung [54]. As shown in Figure 18, higher operating pressures lead to higher fuel cell voltage, thus higher efficiency. At the same time, the higher the pressure, the lower the extra improvement achievable by increasing further the operating pressure.

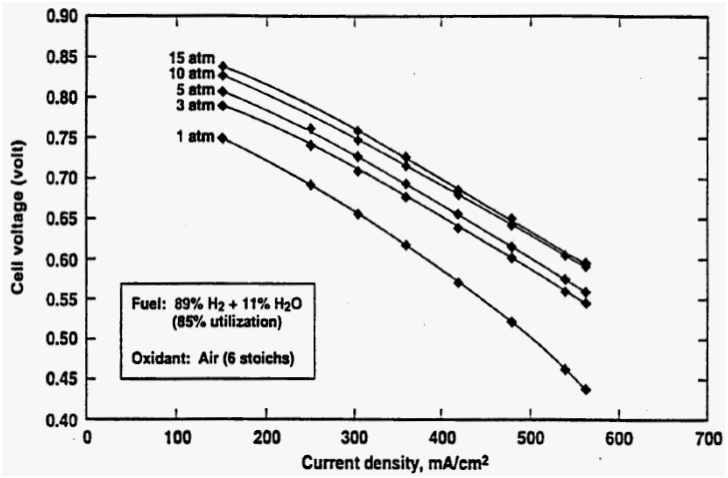

Figure 18 – Experimental results of performance of a cathode-supported tubular SOFC by Westinghouse operated at 1000°C, from 1 atm to 15 atm pressure. Source: [54].

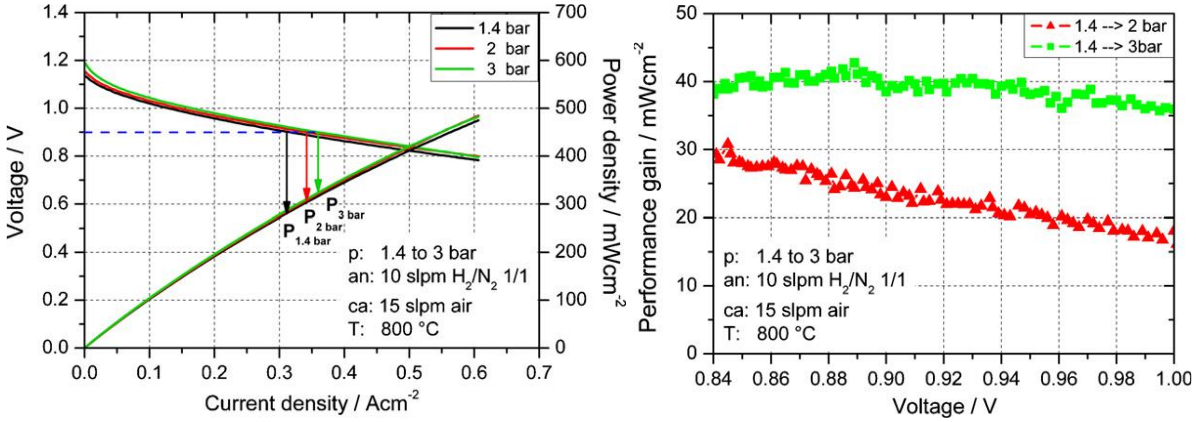

Figure 19 – Experimental performance of anode-supported SOFC as a function of pressure between 1.4-3 bar (left), and performance gain as a function of pressure increase (right), at 800°C operating temperature. Source: [50].

By analyzing the experimental data from the previous graphs, it is concluded that the general dependency of model parameters with pressure is adequately predicted for $b = 0.5$, i.e., as the square root of pressure. The parameter a is then calibrated individually for each fuel cell model operating parameter. With all the values of pressure in [Pa] and the units of each parameter as shown in Table 2, the following expressions are obtained as a result:

$$\Delta i_0(P) = 5 \cdot 10^{-4} \sqrt{(P - P_{ref})}$$

$$\Delta \alpha(P) = 0.0$$

$$\Delta ASR(P) = -8 \cdot 10^{-6} \sqrt{(P - P_{ref})}$$

$$\Delta c(P) = -6 \cdot 10^{-6} \sqrt{(P - P_{ref})}$$

$$i_{lim} \propto \frac{1}{P}$$

Using the previous equations, the impact of operating pressure on SOFC cell-level performance curve is shown in Figure 20.

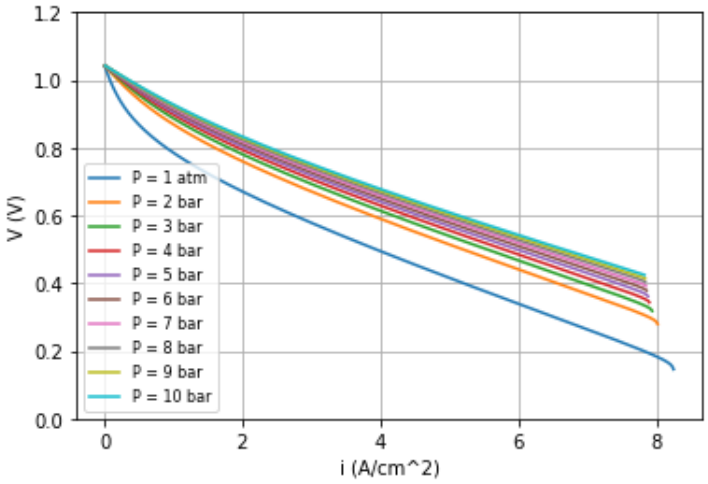

Figure 20 – Impact of operating pressure on SOFC cell-level performance curve.

5.1.3.3 EFFECT OF COMBINED TEMPERATURE AND PRESSURE VARIATIONS

The combined impact of pressure and temperature is modelled based on the work by Seidler et al. [50], in which an anode-supported 5-cell SOFC short stack with 84 cm^2 active area is characterized experimentally for operation between 1.4-3 bar and 750-800°C (Figure 21). The work by Zhou et al. [10], in which an anode-supported tubular SOFC single cell is characterized experimentally at pressures between 1-6 bar and temperatures between 650-800°C (Figure 22, Figure 23), is also considered for calibration.

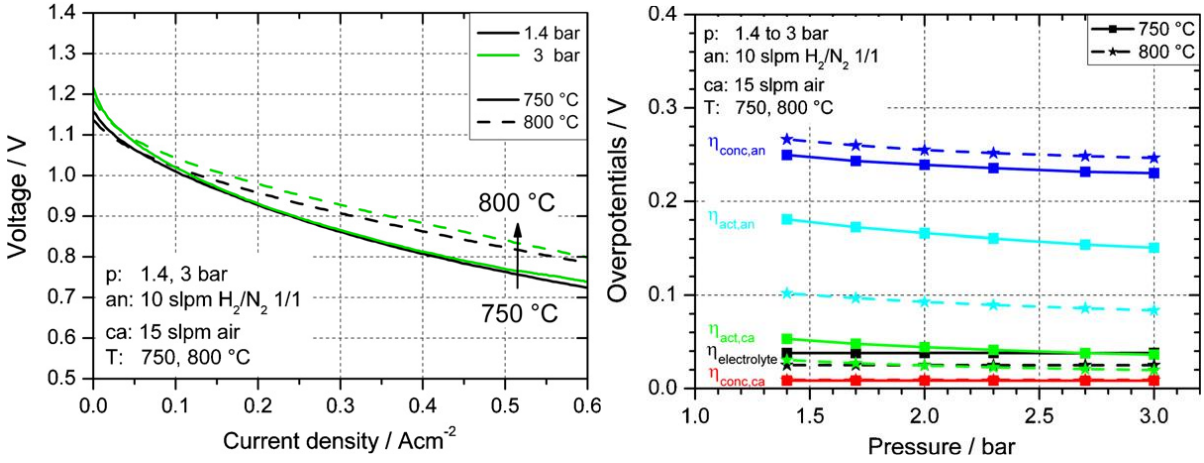

Figure 21 – Experimental data on the concurrent impact of temperature and pressure on anode-supported SOFC (left), and simulation data on the loss breakdown as a function of temperature and pressure (right). Source: [50].

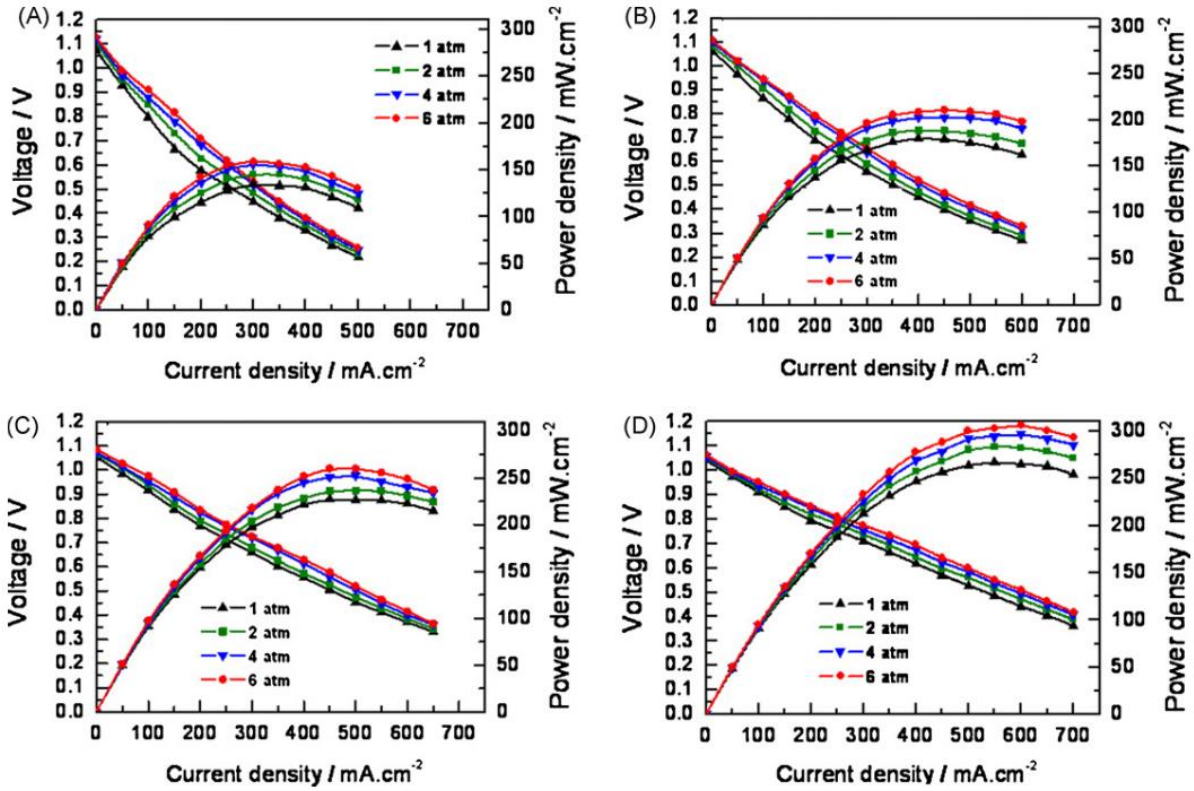

Figure 22 – Impact of pressure on performance of an anode-supported tubular SOFC single cell at (A) 650°C, (B) 700°C, (C) 750°C, (D) 800°C. Source: [10].

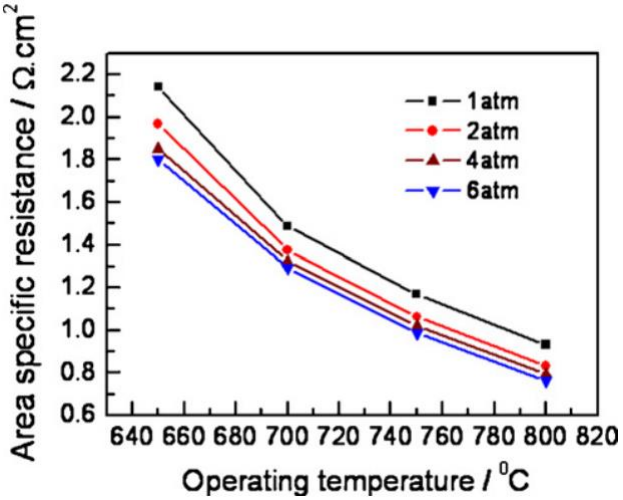

Figure 23 – Impact of operating temperature and pressure on ASR for an anode-supported tubular SOFC single cell. Source: [10].

The combined impact of temperature and pressure is modelled as follows, with P in [Pa] and T in [K]:

$$\Delta i_0(P,T) = 5 \cdot 10^{-12}\sqrt{PT}$$

$$\Delta\alpha(P,T) = 0.0$$

$$\Delta ASR(P,T) = 0.0$$

$$\Delta c(P,T) = 0.0$$

$$i_{lim} \propto 0.06\left(\frac{T}{71.7}\right)^{1.823}\frac{1}{P}$$

5.1.3.4 EFFECT OF AIR STOICHIOMETRY FACTOR

The impact of air stoichiometry factor λ_{air} on SOFC performance is now discussed. The results reported by O'Hayre [3] have been used to calibrate the SOFC model such that the impact of λ_{air} on performance is considered. O'Hayre [3] used a 1D SOFC performance model to characterize the impact of λ_{O_2} (assumed as equivalent to λ_{air} in this work) on SOFC performance. The results in terms of the i-v curve are shown in Figure 24. λ_{air} impacts cathodic activation and concentration losses, as this quantity determines oxygen concentration at the end of the cathode channel. Activation losses and concentration losses decrease with increasing λ_{air}.

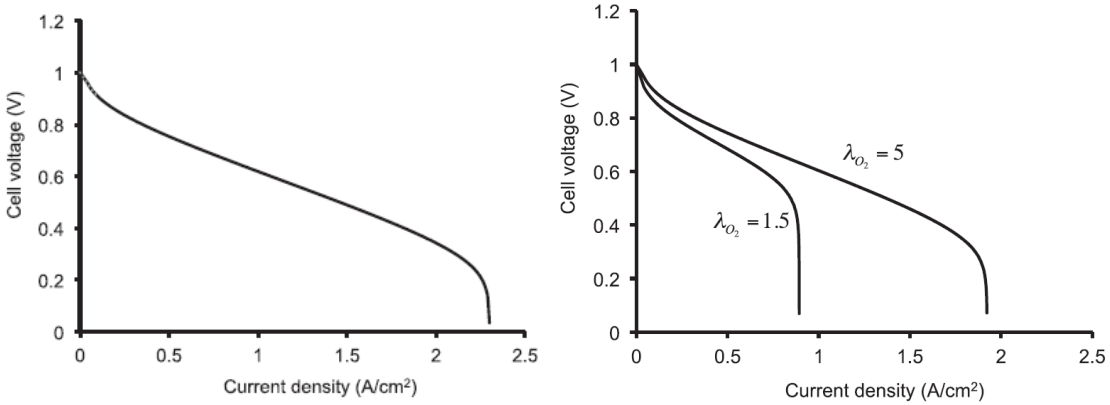

Figure 24 – Impact of oxygen stoichiometry on SOFC performance, using a 1D SOFC model. Source: [3].

Assuming a linear dependency of the performance parameters with λ_{air}, due to the lack of experimental data and the data shown in Figure 24, the following calibration with least-squares fitting is obtained:

$$\Delta i_0(\lambda_{air}) = 0.006(\lambda_{air} - \lambda_{air,ref})$$

$$\Delta\alpha(\lambda_{air}) = 0.0$$

$$\Delta ASR(\lambda_{air}) = 0.0$$

$$\Delta c(\lambda_{air}) = 0.01(\lambda_{air} - \lambda_{air,ref})$$

$$\Delta i_{\lim}(\lambda_{air}) = 1.0(\lambda - \lambda_{ref})$$

Based on the previous equations, the modelled sensitivity of SOFC cell-level performance to air stoichiometry factor is shown in Figure 25.

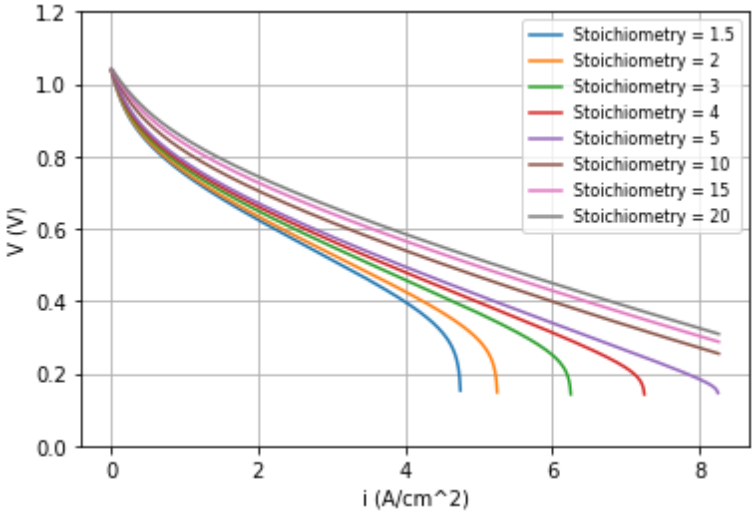

Figure 25 – Impact of air stoichiometry factor on SOFC cell-level performance curve.

5.1.3.5 EFFECT OF FUEL UTILIZATION

The work by Winkler [48] shows that fuel utilization impacts SOFC OCV, as the cell voltage is limited by the lowest local potential of the cell, which occurs close to the end of the fuel cell channels, where fuel depletion

leads to localized voltage reduction. Apart from this impact in the reversible loss terms of the fuel cell performance equation, fuel utilization affects activation losses and concentration losses. For low fuel utilization factors (<25%), concentration losses are negligible except in the case of very high current densities, as demonstrated by Udomsilp et al. [47]. The impact of fuel utilization on concentration losses is modelled by tuning the empirical parameter c, i_{lim}.

The impact of fuel utilization f_u on SOFC performance is calibrated using the experimental data from Zhou et al. [10] for an anode-supported tubular SOFC operating at 800°C and 4 atm. As noted by the authors, higher utilizations lead to steeper increase in concentration losses when increasing utilization. As seen in the left plot of Figure 26, from Singhal et al. [8], higher fuel utilization leads to lower OCV, as well as higher activation and concentration losses. Ohmic losses are negligibly affected by fuel utilization, as proven by the similar slope of the performance i-v curves for different f_u in the ohmic region in the right plot of Figure 26, from Zhou et al. [10]. The impact on activation losses is modelled based on the data from the right plot of Figure 26, considering the difference in overvoltage between the OCV (~0.05 V loss from $f_u = 0.5$ to $f_u = 0.9$) and the operation at 0.15 A/cm^2 (~0.1 V loss from $f_u = 0.5$ to $f_u = 0.9$). For $f_u > 0.5$, the impact on activation losses is quasi-linear with f_u. Therefore, the impact of fuel utilization on activation losses is modelled using the sole ΔV_{act} parameter. Leone et al. [55] determined that an increased fuel utilization leads to a significant reduction in the limiting current density. Due to the lack of available literature on the impact of fuel utilization on this quantity, a linear dependency of the limiting current density as a function of fuel utilization is assumed.

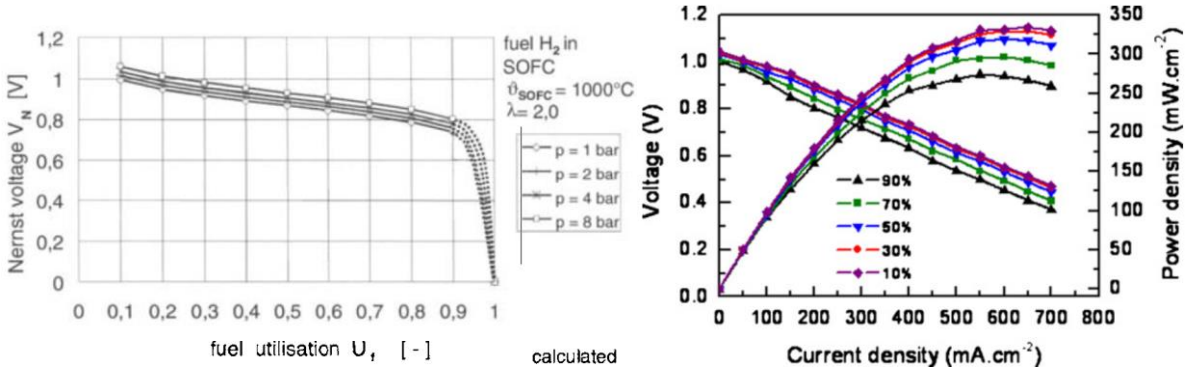

Figure 26 – Left: Impact of fuel utilization on open cell voltage for SOFCs, from [8]. Right: Impact of fuel utilization on performance for an anode-supported tubular SOFC single cell, from [10].

With the previous indications, the following expressions are derived to model the impact of fuel utilization on fuel cell performance:

$$\Delta i_0(f_u) = -0.02(f_u - f_{u,ref})$$

$$\Delta ASR(f_u) = 0.0$$

$$\Delta c(f_u) = 0.1(f_u - f_{u,ref})$$

$$\Delta i_{\lim}(f_u) = 7.8\left(1 - \left(f_u - f_{u_{ref}}\right)\right)$$

The modelled impact of fuel utilization on SOFC cell-level performance is shown in Figure 27.

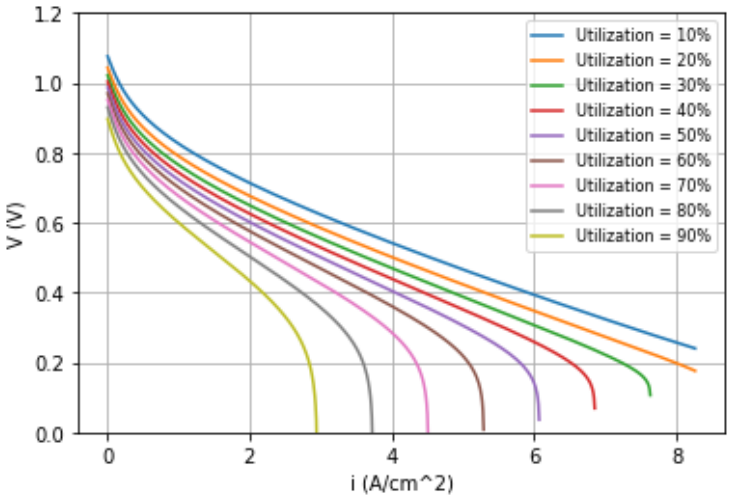

Figure 27 – Impact of fuel utilization on SOFC cell-level performance curve.

5.1.4 SOFC STACK PERFORMANCE MODEL

The methodology by Datta [5] for PEMFC stack performance computation is modified for SOFC applications.

The following steps are used to obtain the stack operating point and performance curve given the cell i-v curve, design efficiency, and electric power generation requirements:

- The stack nominal operating point on the cell i-v curve is selected based on the chosen design efficiency. This is equivalent to select the cell operating voltage v_{design} and current density i_{design}, namely

$$v_{design} = v(\eta_{design})$$

$$i_{design} = i(\eta_{design})$$

- Considering the net electric power $\dot{W}_{electric,useful}$ initially equal to $\dot{W}_{stack}$, and the nominal electric system operating voltage V_{stack}, the number of cells n_{cells} and the active area per cell A_{active} are computed:

$$n_{cells} = round\left(\frac{V_{stack}}{v_{design}}\right)$$

$$I_{stack} = \frac{\dot{W}_{stack}}{V_{stack}}$$

$$A_{active} = \frac{I_{stack}}{i_{design}}$$

- The mass flow rate of hydrogen ($\dot{m}_{H2,consumed}, \dot{m}_{H2,in}$), air ($\dot{m}_{air,required}$, $\dot{m}_{air,in}$, $\dot{m}_{air,out}$, $\dot{m}_{O2,consumed}$, $\dot{m}_{O2,in}$, $\dot{m}_{O2,out}$, $\dot{m}_{N2}$) and water vapor ($\dot{m}_{H2O,out}$) streams are computed using conservation equations considering the chemical reactions, the operating current, hydrogen utilization f_u and air stoichiometry factor λ_{air}.

$$\dot{m}_{H2,consumed} = \frac{M_{H2} I_{stack} n_{cells}}{2F}$$

$$\dot{m}_{anode,in} = \dot{m}_{H2,in} = \frac{\dot{m}_{H2,consumed}}{f_u}$$

$$\dot{m}_{H2,out} = \dot{m}_{H2,in} - \dot{m}_{H2,consumed}$$

$$\dot{m}_{air,required} = \frac{M_{air} I_{stack} n_{cells}}{4 \cdot 0.23 \cdot F}$$

$$\dot{m}_{cathode,in} = \dot{m}_{air,in} = \lambda_{air} \dot{m}_{air,required}$$

$$\dot{m}_{O2,consumed} = \frac{M_{O2} I_{stack} n_{cells}}{4F}$$

$$\dot{m}_{O2,in} = \lambda_{air} \dot{m}_{O2,consumed}$$

$$\dot{m}_{O2,out} = \dot{m}_{O2,in} - \dot{m}_{O2,consumed}$$

$$\dot{m}_{N2} = 0.77 \dot{m}_{air,in}$$

$$\dot{m}_{H2O,out} = \dot{m}_{O2,consumed} + \dot{m}_{H2,consumed}$$

$$\dot{m}_{cathode,out} = \dot{m}_{air,out} = \dot{m}_{air,in} - \dot{m}_{O2,consumed}$$

$$\dot{m}_{anode,out} = \dot{m}_{H2,out} + \dot{m}_{H2O,out}$$

- Based on the computed mass flow rates and heat generation, BoP power consumption is computed using the expressions reported in section *Balance of plant performance model*. Considering the expected BoP of the SOFC, the following expression applies:

$$\dot{W}_{BoP} = \dot{W}_{comp,SOFC}$$

- The power consumption from the BoP ($\dot{W}_{BoP}$) is summed to the useful electric power ($\dot{W}_{electric,useful}$) to obtain the electric power that the SOFC needs to produce ($\dot{W}_{stack}$):

$$\dot{W}_{stack} = \dot{W}_{electric,useful} + \dot{W}_{BoP}$$

- $\dot{W}_{stack}$ is fed back to step 2, updating the value of I_{stack} and A_{active}.
- The procedure is repeated until convergence.

5.1.5 BALANCE OF PLANT PERFORMANCE MODEL

Some BoP components consume electric power, that needs to be provided by the SOFC. To obtain a reliable estimation of this power requirement and its impact on SOFC system performance and sizing, the methodology for estimation of BoP power consumption proposed by Datta [5] for PEMFC system design for VTOL is here adapted for SOFC BoP applications.

The methodology by Datta [5] is based on a combination of physics-based and empirical expressions for power consumption estimation of each component of the BoP. The BoP components which require electric power in the SOFC system are:

- **SOFC air compressor**; typical PEMFC systems require an air compressor to raise the pressure from the atmospheric one to that at which the stack operates. In SOFC-GT hybrid electric powertrains, the GT compressor is used for this operation. Nevertheless, an air compressor is still required to enable the injection of the fuel cells byproducts into the GT combustor, to overcome the pressure drop between the air derivation to the SOFC and the combustion chamber. According to Datta [5], stack pressure drop in PEMFC is usually ~30 kPa. A detailed calculation of stack pressure drop is out of the scope of this work. Therefore, $\Delta P_{stack} = 30\ kPa$ is assumed to be representative of SOFC stack pressure losses. Further, a heat exchanger will be installed before the SOFC, to raise the air temperature up to the requires SOFC operating temperature. A value of $\Delta P_{HX} = 0.3\ kPa$ is assumed in the heat exchanger based on the work of Albanakis et al. [56]. A compressor is used to achieve the required pressure rise. Compressor power is computed using the following expression, with $\eta_{comp} = 0.75$ based on the indications by Datta [5]:

$$\dot{W}_{comp,SOFC} = \frac{c_{p,air}\ \dot{m}_{air} T_{t,in} \left(\left(\frac{P_{t,in} + \Delta P}{P_{t,in}} \right)^{\frac{\gamma-1}{\gamma}} - 1 \right)}{\eta_{comp}}$$

There are other elements of the powertrain which require power to be operated. In this work, it will be assumed that the power provided to these elements is included in the electric power to the payload in the power sizing methodology, defined by λ. For future work, information on modelling liquid hydrogen pumps is provided:

- **LH_2 tank boost pumps**: tank boost pumps raise the LH_2 pressure to a value that ensures its flow towards the engines, overcoming pressure losses in the distribution system. Brewer [41] indicates that

boost pump shall deliver fuel to the high-pressure pump inlet as a saturated liquid at >3.45 bar pressure. In this work, it is assumed that the boost pump increases the pressure of hydrogen up to the SOFC operating pressure, so that no additional pump or compressor is required for the SOFC fuel supply system. Therefore, the mass flow rate that the boost pump needs to provide is the sum of SOFC and GT fuel consumption ($\dot{m}_{LH2,SOFC+GT} = \dot{m}_{LH2,GT} + \dot{m}_{LH2,SOFC}$). Boost pump power consumption is computed using the following expression, assuming $\eta_{boost\ pump} = 0.7$:

$$\dot{W}_{boost\ pump} = \frac{\Delta P_{HP\ pump} \dot{m}_{LH2,SOFC+GT}}{\eta_{boost\ pump} \rho_{LH2}}$$

- **LH_2 high pressure pump**: the hydrogen high pressure pump is installed close to the engine, to pressurize the fuel at the required pressure at the injector inlet. Brewer indicates an efficiency of $\eta_{HP\ pump} = 0.6$ for a 2-stage pump design. The required pressure of fuel at the injector inlet is estimated as $P_{fuel,TO} = 5\ MPa$ during takeoff and climb, $P_{fuel,cruise} = 1.8\ MPa$ during cruise, and $P_{fuel,low\ power} = 0.5\ MPa$ during low-power operating conditions, based on the data provided by Brewer [41] for a liquid hydrogen turbofan engine. Hydrogen mass flow rate to this pump only includes fuel injected into the gas turbine, as the SOFC stream does not require such high pressure. The following expression is used to estimate high pressure pump power consumption:

$$\dot{W}_{HP\ pump} = \frac{\Delta P_{HP\ pump} \dot{m}_{LH2,GT}}{\eta_{HP\ pump} \rho_{LH2}}$$

5.2 SOFC-TURBOPROP PERFORMANCE MODEL

A SOFC-Turboprop design model is implemented in this work. The model is based on a combination of turboprop sizing equations and SOFC sizing equations as described in the following.

The equations used for engine component sizing are:

- Inlet:

$$T_{2t} = T_0 \left(1 + \frac{\gamma - 1}{2} M^2\right)$$

$$P_{2t} = P_0 \left(1 + \eta_{inlet} \frac{\gamma - 1}{2} M^2\right)^{\frac{\gamma}{\gamma - 1}}$$

- Compressor:

$$P_{3t} = P_{2t} \pi_c$$

$$T_{3t} = T_{2t} \left(1 + \frac{\left(\pi_c^{\frac{\gamma-1}{\gamma}} - 1\right)}{\eta_{compressor}}\right)$$

- Combustor:

$$P_{4t} = P_{3t} \pi_{comb}$$

$$T_{4t} = T_{3t} + \frac{\dot{m}_{fuel} LHV \eta_{comb}}{\dot{m}_3 c_p}$$

- Turbine:

$$T_{5t} = T_{4t} - \frac{\dot{m}_2 c_p (T_{3t} - T_{2t})}{\dot{m}_4 c_p \eta_{shaft}} = T_{4t} - \frac{\dot{W}_{shaft}}{\dot{m}_4 c_p \eta_{shaft}}$$

$$P_{5t} = P_{4t} \left(1 + \frac{\frac{T_{5t}}{T_{4t}} - 1}{\eta_{turbine}}\right)^{\frac{\gamma}{\gamma - 1}}$$

- Nozzle: assume adapted and choked nozzle at design point.

$$P_8 = P_0$$

$$M_8 = 1$$

$$T_8 = \frac{T_{5t}}{1 + \frac{\gamma - 1}{2}}$$

$$V_8 = M_8\sqrt{\gamma R T_8}$$

$$F = \dot{m}_8(V_8 - V_0)$$

- Gas turbine thermal efficiency:

$$\eta_{GT1} = \frac{\dot{m}_{GT} c_p \Delta T_{PT} + \frac{1}{2}\,\dot{m}_{GT}(V_8 - V_0)}{\dot{m}_{fuel,total} LHV}$$

Now, the SOFC performance model is integrated with the turboprop performance model. To this end, a stage 35 is defined as a mid-combustor stage at which the main fuel injection into the combustor has occurred, but the SOFC byproducts have not been injected yet. This stage is shown in the Process Flow Diagram in Figure 28.

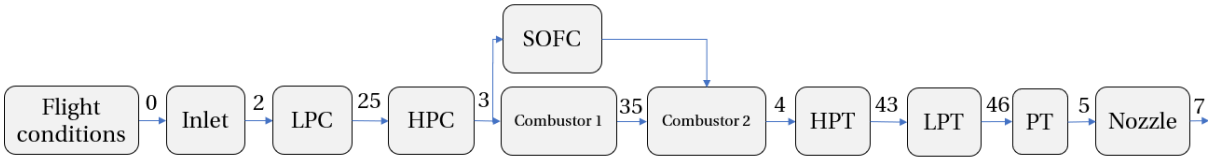

Figure 28 – Process Flow Diagram of the proposed powertrain.

The governing equations for the coupling read:

$$\dot{m}_3 = \dot{m}_2 - \frac{\lambda_{air} M_{air} I_{stack} n_{cells}}{2 \cdot 0.23 \cdot F}$$

$$P_{35t} = P_{3t}\pi_{comb,main}$$

$$T_{35t} = T_{3t} + \frac{\dot{m}_{fuel,GT} LHV \eta_{comb}}{\dot{m}_3 c_p}$$

$$\dot{m}_{35} = \dot{m}_3 + \dot{m}_{fuel,GT} = \dot{m}_2 - \frac{\lambda_{air} M_{air} I_{stack} n_{cells}}{2 \cdot 0.23 \cdot F}$$

The mass flow rate equations at the inlet and outlet of the SOFC are defined according to the interface between the SOFC and the gas turbine. In this respect, the air stream delivered to the SOFC comes from the engine HPC, while the streams leaving the SOFC are injected into the combustion chamber.

$$\dot{m}_{anode,in,H2} = \frac{M_{H2} I_{stack} n_{cells}}{2F f_u}$$

$$\dot{m}_{cathode,in,air} = \frac{\lambda_{air} M_{air} I_{stack} n_{cells}}{4 \cdot 0.23 \cdot F}$$

$$\dot{m}_{cathode,out,N2} = 0.77\,\frac{\lambda_{air} M_{air} I_{stack} n_{cells}}{4 \cdot 0.23 \cdot F}$$

$$\dot{m}_{cathode,out,O2} = \frac{(\lambda_{air} - 1) M_{air} I_{stack} n_{cells}}{4 \cdot 0.23 \cdot F}$$

$$\dot{m}_{anode,out,H2} = \frac{M_{H2} I_{stack} n_{cells}}{2F f_u}\left(\frac{1}{f_u} - 1\right)$$

$$\dot{m}_{anode,out,H2O} = \frac{M_{O2} I_{stack} n_{cells}}{4F} + \frac{M_{H2} I_{stack} n_{cells}}{2F}$$

$$\dot{m}_{exhaust,SOFC} = \dot{m}_{anode,out,H2O} + \dot{m}_{anode,out,H2} + \dot{m}_{cathode,out,O2} + \dot{m}_{cathode,out,N2}$$

Now, these mass flow rates are used to obtain the thermodynamic state and mass flow rate at the stages 35 and 4 of the engine. First, the change in total pressure is calculated. A total pressure loss parameter $\pi_{comb,SOFC\ byproducts}$ is defined to this end, accounting for the mixing losses resulting from SOFC byproducts injection and pressure losses from the combustion of the hydrogen in the SOFC exhausts:

$$P_{4t} = P_{35t}\pi_{comb,SOFC\ byproducts}$$

Then, the mass flow rate at the combustor exit is computed as a function of the mass flow rate coming from the intermediate combustor and the SOFC byproducts mass flow rates, previously computed using SOFC performance equations:

$$\dot{m}_4 = \dot{m}_{35} + \dot{m}_{exhaust,SOFC}$$

The relation for turbine inlet temperature (TIT or T_{4t}) is derived using an energy balance. In the design point calculations, T_{4t} is an input. It follows that the implementation of an iterative methodology to determine the fuel injection mass flow rate is required. This quantity depends on the enthalpy increase due to the combustion of the unutilized hydrogen from the SOFC, and the injection of SOFC byproducts. The equation for T_{4t} reads:

$$T_{4t} = \frac{\dot{m}_{35}\left(T_{35t} + \frac{\frac{M_{H2}I_{stack}n_{cells}}{2F}LHV\eta_{comb}}{\dot{m}_{35}c_p}\right) + \dot{m}_{exhaust,SOFC}T_{SOFC}}{\dot{m}_4}$$

The thermal efficiency seen by the SOFC byproducts injected into the gas turbine combustor, named η_{GT2}, is now defined. This parameter is required for powertrain power sizing, as explained in the chapter *Power sizing and energy sizing methodologies*. To this end, the useful enthalpy of the streams leaving the SOFC and entering the gas turbine is defined as follows:

$$\Delta\dot{H}_{SOFC\rightarrow GT} = \dot{Q}_{stack} + \dot{m}_{anode,out,H2}LHV$$

Where $\dot{Q}_{stack}$ is defined as follows:

$$\dot{Q}_{stack} = \dot{W}_{stack}\frac{(1-\eta_{cell})}{\eta_{cell}}$$

This enthalpy inflow is converted into useful power via its utilization in the power turbine. This is expressed as follows:

$$\dot{W}_{shaft,SOFC\rightarrow GT} = \dot{m}_{exhaust,SOFC}c_p\Delta T_{PT}$$

Therefore, η_{GT2} is defined as follows:

$$\eta_{GT2} = \frac{\dot{m}_{exhaust,SOFC}c_p\Delta T_{PT} + \frac{1}{2}\dot{m}_{exhaust,SOFC}\left(V_{8,eff}^2 - V_0^2\right)}{\dot{Q}_{stack} + \dot{m}_{anode,out,H2}LHV}$$

6 POWER SIZING AND ENERGY SIZING METHODOLOGIES

6.1 POWER SIZING METHODOLOGY

Aircraft performance capabilities are dependent on the power-to-weight ratio and the wing loading. Power-to-weight ($\frac{P_{SL,max}}{W}$) ratio is calculated as the standard sea level static maximum throttle power over the maximum takeoff weight. The relation between power-to-weight and thrust-to-weight is the following, with thrust and weight in Newton, and power in W:

$$\frac{T}{W} = \frac{\eta_P}{V}\frac{P}{W}$$

The wing loading ($\frac{W}{S}$) instead refers to the ratio between aircraft weight and wing area. At constant flight speed, lower lift coefficient requires higher wing area for the same performance. Further, wing loading is constrained by stall speed. Improved performance can be obtained either by higher wing area or by higher powerplant power at a given MTOW.

The performance constraint analysis is a standard design methodology for aircraft introduced by Loftin [57]. It is based on a physics-based mathematical representation of the performance requirements of the aircraft as a function of the power loading and wing loading. This methodology is outlined in reference aircraft design books such as Raymer [33], Torenbeek [34] and Sadraey [35]. The original formulation of the method only applies to conventional aircraft configurations, with turbofan or turboprop engines. When including hybrid propulsion configurations, additional degrees of freedom need to be considered. As explained in the *Hybrid electric aircraft design* section, de Vries [28] proposes a modification of the constraint analysis methodology for hybrid electric powertrains. In the modified methodology, component-oriented constraint diagrams are obtained, sizing each component of the propulsion and power system individually. This methodology has been adapted in this work to apply the constraint analysis to the SOFC-GT-Battery hybrid electric powertrains.

The baseline constraint analysis methodology, as presented by Sadraey [35], is based on the following steps:

- Derive a performance equation for each aircraft performance requirement, as a function of wing loading and power-to-weight ratio. This includes performance requirements defined by the aircraft designer, as well as those coming from certification needs. In this work, for regional aircraft sizing, the EASA CS25 requirements [44] are considered.
- Plot all the equations in one single chart, with $\frac{W}{S}$ on the horizontal axis and $\frac{P_{SL}}{W}$ on the vertical axis.
- Identify the acceptable region in the chart that meets all aircraft performance requirements.
- Determine the design point within the acceptable region which defines the aircraft wing loading and power-to-weight ratio.

6.1.1 AIRCRAFT PERFORMANCE EQUATIONS

The performance equations used in this work, based on reference aircraft design textbooks (Raymer [33], Torenbeek [34], Sadraey [35] [58]), are presented in Table 8.

A parameter ξ representing the throttle (system power production compared to the maximum power that the propulsion system can produce), defined as follows, is included in the expressions:

$$\xi = \frac{P_{throttle}}{P_{max}}$$

Table 8 – Equations for constraint analysis. Sources: [33] [34] [35] [44]

Performance requirement	Expression
Maximum cruise speed	$\left(\frac{P_{shaft,SL}}{W}\right)_{V_{max}} = \frac{1}{\xi_{cruise}}\left(\frac{\eta_{P,cruise} c_{D0} \rho_{SL} V_{max}^3}{2}\frac{1}{\frac{W}{S}} + \frac{2\eta_{P,cruise} k \rho_{SL}}{\rho_{cruise}^2 V_{max}}\frac{W}{S}\right)$

Stall speed	$$\left(\frac{W}{S}\right)_{V_s} = 0.5\rho_{SL}V_s^2 c_{L,max}$$
Takeoff distance	$$\left(\frac{P_{shaft,SL}}{W}\right)_{takeoff} = \frac{V_{TO}}{\xi_{TO}\eta_{P,TO}} \frac{\mu - \left(\mu + \frac{c_{Dg}}{c_{LR}}\right) e^{\frac{0.6\rho_{hTOmax} g c_{Dg} s_{TO}}{\frac{W}{S}}}}{1 - e^{\frac{0.6\rho_{hTOmax} g c_{Dg} s_{TO}}{\frac{W}{S}}}}$$
Landing distance	$$\left(\frac{W}{S}\right)_{landing} = \frac{c_{L,max}\rho \frac{s_{landing}}{0.5847}}{2\frac{W_{landing}}{W_{TO}}}$$
Maximum rate of climb	$$\left(\frac{P_{shaft,SL}}{W}\right)_{ROC_{max}} = \frac{1}{\xi_{TO}}\left(\frac{ROC_{max}}{\eta_{P,climb}} + \frac{1.155}{\eta_{P,climb}\left(\frac{L}{D}\right)_{max,SL}}\sqrt{\frac{2}{\rho_{SL}\sqrt{\frac{3c_{D0}}{k}}}\frac{W}{S}}\right)$$
Absolute ceiling	$$\left(\frac{P_{shaft,SL}}{W}\right)_{ceiling} = \frac{1.155}{\xi_{cruise}\eta_{P,cruise}\left(\frac{L}{D}\right)_{max,ceiling}\frac{\rho_{ceiling}}{\rho_{SL}}}\sqrt{\frac{2}{\rho_{ceiling}\sqrt{\frac{3c_{D0}}{k}}}\frac{W}{S}}$$
Maximum load factor	$$\left(\frac{P_{shaft,SL}}{W}\right)_{load\ factor} = \frac{1}{\xi_{cruise}}\left(\frac{\frac{1}{2}\rho V^3 c_{D0}}{\frac{W}{S}} + \frac{2kn_{max}^2}{\rho V}\frac{W}{S}\right)$$
EASA CS 25.111	$$\left(\frac{P_{shaft,SL}}{W}\right)_{CS25.111} = \frac{N(c_{gradient} + \frac{c_{D_{TO}}}{c_{L_{TO}}})\sqrt{\frac{2}{\rho_{SL}c_{L_{TO}}}\frac{W}{S}}}{\eta_{P_{max\ power}}(N-1)}$$
	If N=2: $$c_{gradient} = 0.012$$
	If N=3: $$c_{gradient} = 0.015$$
	If N=4: $$c_{gradient} = 0.017$$
EASA CS 25.119	$$\left(\frac{P_{shaft,SL}}{W}\right)_{CS25.119} = \frac{(c_{gradient} + \frac{c_{D_{landing}}}{c_{L_{landing}}})\sqrt{\frac{2}{\rho_{SL}c_{L_{landing}}}\frac{W}{S}}}{\eta_{P_{max\ power}}}$$ $$c_{gradient} = 0.032$$
EASA CS 25.121a	$$\left(\frac{P_{shaft,SL}}{W}\right)_{CS25.121a} = \frac{N(c_{gradient} + \frac{c_{D_g}}{c_{L_{TO}}})\sqrt{\frac{2}{\rho_{SL}c_{L_{TO}}}\frac{W}{S}}}{\eta_{P_{max\ power}}(N-1)}$$
	If N=2: $$c_{gradient} = 0.0$$
	If N=3: $$c_{gradient} = 0.003$$

If N=4:

$$c_{gradient} = 0.005$$

EASA CS 25.121b

$$\left(\frac{P_{shaft,SL}}{W}\right)_{CS25.121b} = \frac{N(c_{gradient} + \frac{c_{D_{TO}}}{c_{L_{TO}}})\sqrt{\frac{2}{\rho_{SL} c_{L_{TO}}}\frac{W}{S}}}{\eta_{P_{max\ power}}(N-1)}$$

If N=2:

$$c_{gradient} = 0.024$$

If N=3:

$$c_{gradient} = 0.027$$

If N=4:

$$c_{gradient} = 0.030$$

EASA CS 25.121c

$$\left(\frac{P_{shaft,SL}}{W}\right)_{CS25.121c} = \frac{N(c_{gradient} + \frac{c_{D_{cruise}}}{c_{L_{cruise}}})\sqrt{\frac{2}{\rho_{1500\,ft} c_{L_{cruise}}}\frac{W}{S}}}{\eta_{P_{max\ power}}(N-1)}$$

If N=2:

$$c_{gradient} = 0.012$$

If N=3:

$$c_{gradient} = 0.015$$

If N=4:

$$c_{gradient} = 0.017$$

EASA CS 25.121d

$$\left(\frac{P_{shaft,SL}}{W}\right)_{CS25.121d} = \frac{N(c_{gradient} + \frac{c_{D_{landing}}}{c_{L_{landing}}})\sqrt{\frac{2}{\rho_{SL} c_{L_{landing}}}\frac{W}{S}}}{\eta_{P_{max\ power}}(N-1)}$$

If N=2:

$$c_{gradient} = 0.021$$

If N=3:

$$c_{gradient} = 0.024$$

If N=4:

$$c_{gradient} = 0.027$$

6.1.2 COMPONENT-ORIENTED POWER-LOADING VS WING-LOADING DIAGRAMS

de Vries [28] proposes the use of component-oriented power-loading versus wing-loading diagrams for sizing the propulsion and power system, allowing for the sizing of each component of the powertrain based on a set of user-defined design parameters. To do this, a matrix including the fraction of total power from each component of the powertrain and its efficiency is developed. Each component is characterized by its design average power fraction and its estimated average operating efficiency for each flight phase.

The proposed methodology for SOFC-GT-Battery powertrain power sizing based on component-oriented $\frac{P}{W} - \frac{W}{S}$ diagrams is based on the following assumptions:

- Constant efficiency and fraction of power are assumed in each flight phase involved in the performance constraints.
- Steady state operation of all powertrain components.

- Operation of gas turbine and SOFC at constant equivalence ratio. Therefore, fuel and air flows are not independent variables.
- SOFC as adiabatic system, with no heat loss to the environment. All generated thermal energy within the SOFC is transported into the gas turbine combustion chamber.
- In case of failure of one gas turbine, the SOFC is powered by the other gas turbine, leading to production of half of the electric power. Based on this assumption, the system is considered as bi-engine ($N = 2$) for the EASA CS 25 performance requirements, as the critical failure condition (failure of a gas turbine engine) implies losing half of the propulsive power.
- If electric motor propulsive power was higher than 50% of total propulsive power (i.e., $P_{p2} > P_{p1}$), the critical failure mode would be the electric motor failure. In this situation, the climb gradient required as per EASA CS 25 would not be covered by current regulations, as this would mean that more than 50% of the power is lost. Therefore, maximum propulsive power provided by the electric motor is limited to 50% of total propulsive power
- Power management components are assumed to provide sufficient redundancy to be considered fail-safe, as proposed by de Vries [28].

The general system configuration for component-oriented constraint analysis, in a format inspired by the work of de Vries [28], is shown in Figure 29. In these figures, F refers to fuel system, GT to gas turbine, P to propulsor, V to distribution valve, SOFC to the solid oxide fuel cell, PM to power management, BAT to battery, EM to electric motor, and EP to electric payload. Regarding the power subscripts, f refers to fuel, b to byproducts, e to electric, s to shaft, and p to propulsive. The gas turbine power path is referred to as the primary power path, while the electric power path is referred to as the secondary one.

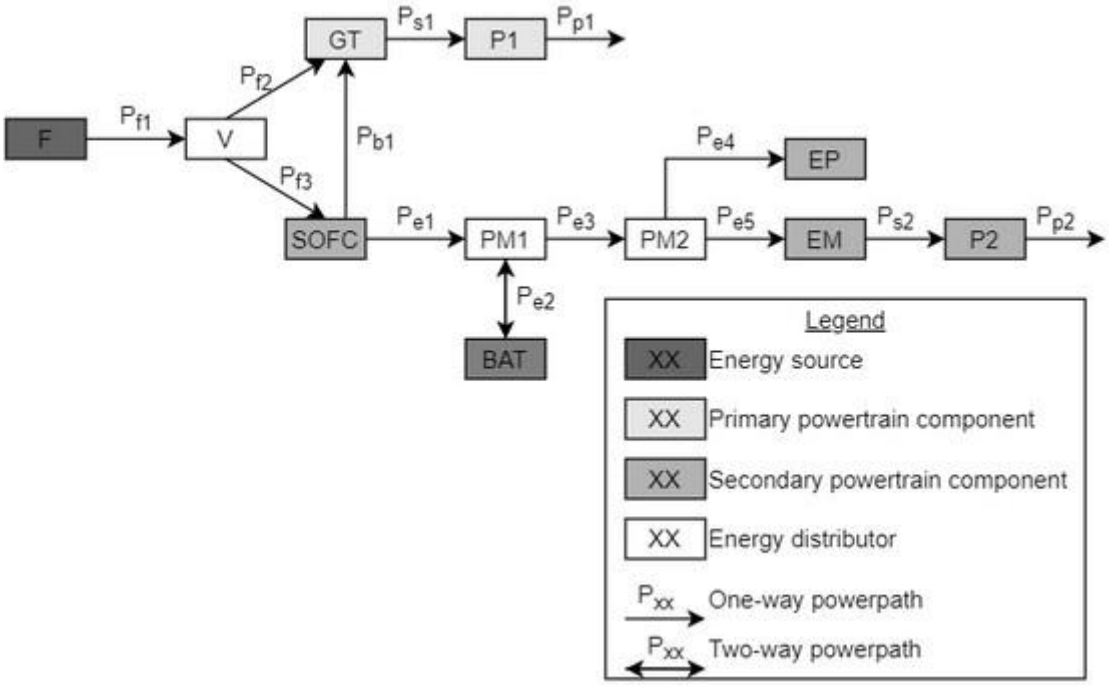

Figure 29 – SOFC-GT-Battery hybrid powertrain architecture for constraint analysis.

In Figure 29, the power transmission between different components of the powertrain is depicted. Using this scheme as a baseline, design power management variables shall be defined by the designer for each operating condition. These are:

- **Valve to distribute air and fuel flow between SOFC and GT (V)**: fraction of air and fuel flow that is injected to the gas turbine combustor compared to the total flows. The parameter Φ is used to characterize the amount of fuel and air that is injected to the SOFC and GT:

$$\Phi = \frac{P_{GT,fuel}}{P_{GT,fuel} + P_{SOFC,fuel}} = \frac{P_{f2}}{P_{f2} + P_{f3}}$$

- **Power split between SOFC and battery (PM1)**: fraction of electric power generated by SOFC and battery, to power the electric motor and the meet the demand of the electric payload. The parameter Ψ is used to define this power split. When this parameter is over 1, the battery is charging, while when its value is below 1, the battery is being discharged.

$$\Psi = \frac{P_{SOFC,el}}{P_{SOFC,el} + P_{battery}} = \frac{P_{e1}}{P_{e1} + P_{e2}}$$

- **Power split between electric motor and electric payload (PM2)**: fraction of electric power that is used to meet the demand of the electric payload of the aircraft (e.g., ECS, de-icing…). The parameter λ is used to describe this.

$$\lambda = \frac{P_{EP}}{P_{EP} + P_{EM}} = \frac{P_{e4}}{P_{e4} + P_{e5}}$$

- **Shaft power ratio**: auxiliary redundant parameter defining the ratio between shaft power of the gas turbine and electric motor. This parameter is redundant with Φ and Ψ. It is introduced for convenience when the fraction of shaft power achieved with each shaft needs to be characterized.

$$\Omega = \frac{P_{s1}}{P_{s1} + P_{s2}} = \frac{1}{1 + \frac{\eta_{PM1}\eta_{PM2}\eta_{EM}}{(1-\eta_{SOFC})\eta_{GT2} + \frac{\Phi}{1-\Phi}\eta_{GT1}}}$$

- **Propulsive power ratio**: auxiliary redundant parameter defining the ratio between the propulsive power of the gas turbine and electric motor. This parameter is redundant with Φ and Ψ. It is introduced for convenience when the fraction of propulsive power achieved by each propulsor needs to be characterized.

$$\beta = \frac{P_{p1}}{P_{p1} + P_{p2}} = \frac{1}{1 + \frac{\eta_{p2}}{\eta_{p1}}\left(\frac{1-\Omega}{\Omega}\right)}$$

Given the definition of the previous parameters, a system with the same number of equations as power unknowns (13) is defined. First, power balances between components are defined based on the following general equation:

$$\sum P_{out} = \eta \sum P_{in}$$

From the power balances, 9 equations are derived:

- Fuel distribution is represented by the following equation, where η_V refers to possible fuel losses during transmission from the fuel tank to the SOFC and/or GT. This parameter can be used to model venting losses from the liquid hydrogen tank when the pressure increase in the tank due to heat losses of the tank is higher than the rate of pressure decrease due to fuel consumption, and when venting pressure has been reached. This condition is expected to happen if insulation effectiveness is low during ground taxi, descent, and landing operations. $\eta_V = 1$ is assumed in this work, as a constant-pressure zero-venting operation of the liquid hydrogen tank is assumed to limit the scope of the work, as explained in section *Liquid hydrogen tank weight calculation*.

$$P_{f2} + P_{f3} = \eta_V P_{f1} \approx P_{f1}$$

- As the gas turbine engine has two main fuel inputs, its performance is described by two different efficiencies: η_{GT1} corresponds to the thermal and mechanical efficiency of the whole gas turbine, while η_{GT2} refers to the power production generated from the exhaust hydrogen-rich stream leaving the fuel cell. Further, a parameter δ is defined as the fraction of power from the SOFC that is injected into the combustion chamber of the gas turbine. Selecting $\delta = 0$, it is assumed that the heat and byproducts from the SOFC are not injected into the gas turbine. This is equivalent to assuming that the SOFC and gas turbine are operated in a parallel uncoupled way. Selecting $\delta = 1$, it is assumed that the SOFC system is adiabatic, and that all the byproducts, generated heat, and unburned hydrogen are injected into the gas turbine. In this work, $\delta = 1$ will be assumed for all calculations.

$$P_{s1} = \eta_{GT1} P_{f2} + \eta_{GT2} \delta P_{b1}$$

- The shaft power of the gas turbine is converted into propulsive power considering the propulsive efficiency of the propeller, fan and/or nozzle of the gas turbine engine.

$$P_{p1} = \eta_{P1} P_{s1}$$

- The total fuel power provided to the fuel cell P_{f3} results both into electric power generation P_{e1} as well as chemical and thermal power transported to the burner via the fuel cell exhausts P_{b1}, namely

$$P_{b1} + P_{e1} = P_{f3}$$

- The fraction of electric power that is generated by the SOFC is a function of the SOFC performance efficiency η_{SOFC} and the fuel utilization $\eta_{f,SOFC}$ as follows

$$P_{e1} = \eta_{SOFC} \eta_{f,SOFC} P_{f3}$$

- Total electric power available in the system is the sum of the SOFC electric power and battery power, considering the efficiency of the DC/DC converter and power electronics (represented as PM1).

$$P_{e3} = \eta_{PM1}(P_{e1} + P_{e2})$$

- Electric power is distributed to the electric motor and the electric payload via power electronics, with an efficiency η_{PM2}.

$$P_{e4} + P_{e5} = \eta_{PM2} P_{e3}$$

- Electric power is converted into shaft power by the electric motor, considering efficiency losses based on the operating point of the electric motor.

$$P_{s2} = \eta_{EM} P_{e5}$$

- Shaft power is converted into propulsive power by the propeller, with a propulsive efficiency defined based on the operating point of the propeller.

$$P_{p2} = \eta_{P2} P_{s2}$$

Moreover, three extra equations are derived for the power distribution parameters Φ, Ψ, λ, which represent additional degrees of freedom of the design and whose values must be set by the designer. These are:

- $(1 - \Phi)P_{f2} = \Phi P_{f3}$ for fuel split between SOFC and GT.
- $(1 - \Psi)P_{e1} = \Psi P_{e2}$ for the SOFC-Battery electric power split.
- $(1 - \lambda)P_{e4} = \lambda P_{e5}$ for the electric payload power consumption.

The final equation of the system is the overall required shaft power (powertrain sizing condition). First, propulsive power at each operating condition is determined using aircraft performance analysis. Then, considering the propulsive efficiency at each operating condition, the maximum required shaft power is computed. The overall propulsive power generated by the GT and electric propulsors is equal to the total propulsive power required by the aircraft as given by the component-oriented $\frac{P}{W} - \frac{W}{S}$ diagrams and the aircraft MTOW:

$$P_s = P_{s1} + P_{s2}$$

This system of equations can be expressed in matrix form as:

$$\begin{bmatrix} -\eta_V & 1 & 1 & 0 & 0 & 0 & 0 & 0 & 0 & 0 & 0 & 0 & 0 \\ 0 & -\eta_{GT1} & 0 & 1 & 0 & -\eta_{GT2}\delta & 0 & 0 & 0 & 0 & 0 & 0 & 0 \\ 0 & 0 & 0 & -\eta_{P1} & 1 & 0 & 0 & 0 & 0 & 0 & 0 & 0 & 0 \\ 0 & 0 & -1 & 0 & 0 & 1 & 1 & 0 & 0 & 0 & 0 & 0 & 0 \\ 0 & 0 & 0 & 0 & 0 & 0 & -\eta_{PM1} & -\eta_{PM1} & 1 & 0 & 0 & 0 & 0 \\ 0 & 0 & 0 & 0 & 0 & 0 & 0 & 0 & -\eta_{PM2} & 1 & 1 & 0 & 0 \\ 0 & 0 & 0 & 0 & 0 & 0 & 0 & 0 & 0 & 0 & -\eta_{EM} & 1 & 0 \\ 0 & 0 & 0 & 0 & 0 & 0 & 0 & 0 & 0 & 0 & 0 & -\eta_{P2} & 1 \\ 0 & (1-\Phi) & \Phi & 0 & 0 & 0 & 0 & 0 & 0 & 0 & 0 & 0 & 0 \\ 0 & 0 & 0 & 0 & 0 & 0 & (1-\Psi) & \Psi & 0 & 0 & 0 & 0 & 0 \\ 0 & 0 & 0 & 0 & 0 & 0 & 0 & 0 & 0 & (1-\lambda) & \lambda & 0 & 0 \\ 0 & 0 & -\eta_{SOFC} & 0 & 0 & 0 & 1 & 0 & 0 & 0 & 0 & 0 & 0 \\ 0 & 0 & 0 & 1 & 0 & 0 & 0 & 0 & 0 & 0 & 0 & 1 & 0 \end{bmatrix} \cdot \begin{bmatrix} P_{f1} \\ P_{f2} \\ P_{f3} \\ P_{s1} \\ P_{p1} \\ P_{b1} \\ P_{e1} \\ P_{e2} \\ P_{e3} \\ P_{e4} \\ P_{e5} \\ P_{s2} \\ P_{p2} \end{bmatrix} = \begin{bmatrix} 0 \\ 0 \\ 0 \\ 0 \\ 0 \\ 0 \\ 0 \\ 0 \\ 0 \\ 0 \\ 0 \\ 0 \\ P_s \end{bmatrix}$$

Each aircraft operating condition is characterized by different operating efficiency and power distribution amongst powertrain components. In this work, 3 different matrices with different values of efficiency and power management parameters are considered:

- **Takeoff, climb, and maximum power in emergency conditions**: applied to takeoff distance, maximum rate of climb, EASA CS 25.111, EASA CS 25.119, EASA CS 25.121a, EASA CS 25.121b, EASA CS 25.121c, and EASA CS 25.121d.
- **Cruise**: applied to maximum cruise speed, absolute ceiling, and maximum load factor.
- **Descent and landing**: not required for constraint definition but used for performance analysis.

These matrix systems are solved to determine the values of each component power P_i as a function of overall system required shaft power P_s.

6.1.3 POWERTRAIN FAILURE MODES

When considering the use of two gas turbine engines and one SOFC powering one electric powertrain, as proposed in this work, it is convenient to consider the system configuration as defined in Figure 30, for a better definition of failure modes.

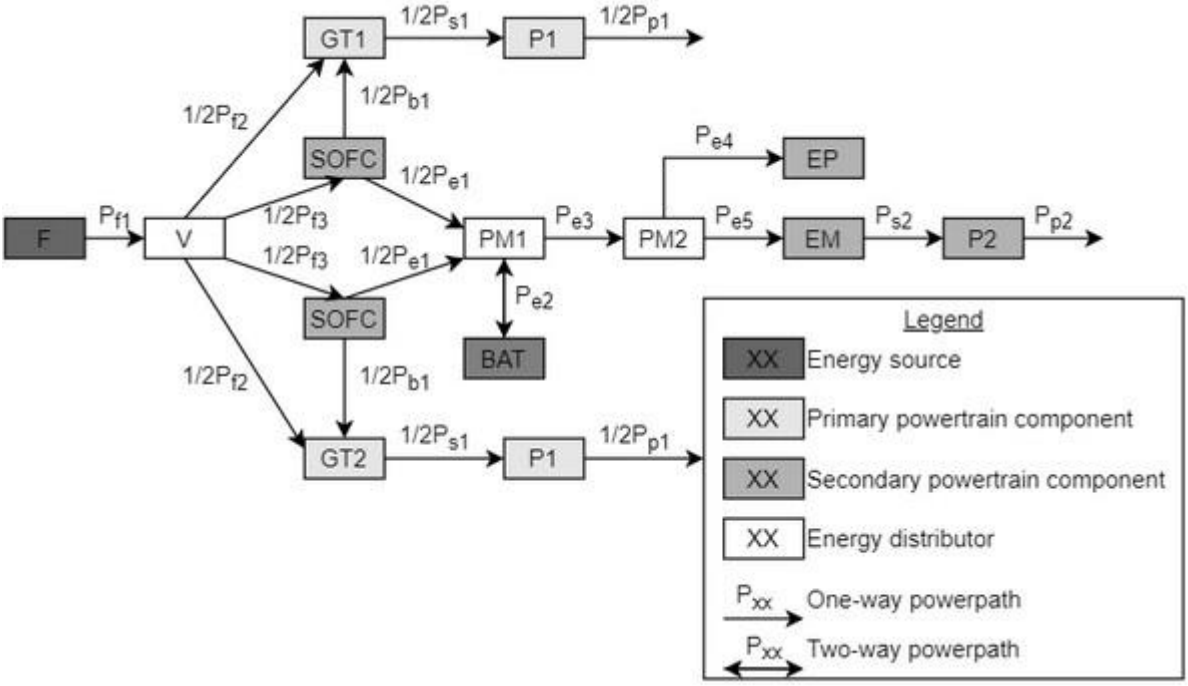

Figure 30 - SOFC-GT-Battery hybrid powertrain architecture for constraint analysis, considering 2 gas turbine engines and 1 electric powertrain.

The One-Engine-Inoperative (OEI) condition in EASA CS 25 corresponds to the failure of one propulsor in a conventional powertrain. When considering a tightly coupled SOFC-GT-Battery hybrid electric powertrain, a

detailed study on the failure modes of the system is required. The configuration shown in Figure 30 can be used for the definition of the failure conditions of the system, allowing to size the system considering EASA CS 25 regulations. The effect of single-component failure can be considered by oversizing the components of its branch by a factor $\frac{N}{N-N_f}$, where N is the total number of power production elements and N_f is the number of components that fail caused by a single component failure, as indicated by de Vries [28]. In total, five failure modes were identified for the configuration in Figure 30:

- **GT engine failure**: the consequences are no thrust from the GT engine and no air supplied to the connected SOFC. It results that approximately half of the propulsive power is unavailable in this situation. The battery is discharged to compensate for the engine that is off.
- **SOFC failure with charged battery**: the battery provides electric power to the electric motor and to the electric payload of the aircraft.
- **SOFC failure with depleted battery**: no electric power generated. The electric motor will be turned off in this condition. The APU will be required to meet the demand of the aircraft electric payload. A detailed analysis of this failure mode considering aircraft electric payload requirements and APU sizing is out of the scope of this work.
- **Battery failure**: the SOFC needs to provide all the electric power to the electric motor and electric payload. According to de Vries [28], accurate evaluation of impact of battery failure is complex, requiring detailed design and analysis of the electric system. Therefore, no detailed analysis is performed in this work.
- **Electric motor failure**: all the propulsive power from SOFC and battery cannot be used, with equivalent implications to the case of SOFC failure with discharged battery in terms of propulsive power. However, there is not impact on the production of electric power for the electric payload. As explained in the assumptions, the analysis is limited to maximum 50% power provided by the electric motor, to ensure fail-safe design of the powertrain.

Based on these failure modes and the modelling assumptions (one GT failure leads to the shutdown of the connected SOFC, electric motor cannot cover more than half the propulsive power, redundant power management with negligible failure probability), the critical failure mode is concluded to be equivalent to that of the GT engine failure for a twin-engine aircraft, which corresponds to standard EASA CS 25 OEI conditions with $N = 2$, as half of the propulsive power is lost in case of GT engine failure. More details on the failure analysis, including modifications to the power distribution matrices, are presented in *APPENDIX II – Failure mode analysis for power sizing with constraint analysis methodology*.

6.1.4 AIRCRAFT DESIGN POINT SELECTION

After the component-oriented $\frac{P}{W} - \frac{W}{S}$ diagrams are obtained for each component of the powertrain, the design point needs to be selected. Ideally, the selection of the design point would be performed via an aircraft-level optimization loop, running the entire aircraft design routine for different wing loadings and the corresponding component power sizing. The selected design would be based on minimum mission fuel energy consumption. Nevertheless, due to the complexity of this approach, a simplification is considered. The proposed methodology starts with the selection of the wing loading based on the stall speed constraint. When wing loading is selected, power loading of each component is fixed by the intersection between the vertical wing loading line in the diagram and the minimum power loading constraint.

6.1.5 SUMMARY OF POWER SIZING METHODOLOGY

Summarizing, the overall proposed methodology for power sizing and determining the wing loading is based on the following steps:

- First, the system of equations that defines the power balance between components of the powerplant, as well as the power management strategy decided by the designer for each mission segment, are set up and solved. This will lead to different values of $\frac{P_i}{P_{SL}}$, where i refers to each individual power element in the diagram.
- The previous step is repeated for each system of equations defined by each failure mode and operating condition. The maximum value of $\frac{P_i}{P_{SL}}$, considering normal operation and all failure modes, is selected for each component and each mission segment. In this case, as it is assumed that the critical failure mode is that related to the GT engine and that maximum propulsive power provided by the SOFC is

50%, only one failure mode needs to be considered. This is equivalent to OEI with $N = 2$ when two GT engines and one SOFC is used. Thus, this condition will be applied for the EASA CS 25.111, 25.119 and 25.121 performance constraints.

- The constraint analysis is performed solving the equations for $\frac{W}{P_{SL}}$ and $\frac{W}{S}$. A diagram for the overall propulsive power is obtained. This is, then, converted into component diagrams for each element of the powerplant, by multiplying the constraint equation by the corresponding $\frac{P_i}{P_{SL}}$ for the given component and mission segment.
- The design point of each component is determined by the intersection of the selected wing loading (vertical line in the component-oriented $\frac{P}{W} - \frac{W}{S}$ diagram) and the limiting power constraint.

6.2 ENERGY SIZING METHODOLOGY

In this work, the derivation by de Vries [28] for energy sizing of hybrid electric aircraft is adapted for liquid-hydrogen-fuelled SOFC-GT-Battery hybrid electric powertrains.

Total cruise block energy E_{tot} is the sum of consumed energy from fuel and battery:

$$E_{tot} = E_f + E_e$$

Fuel energy and battery electric energy can be directly related to fuel mass and battery mass via the fuel lower heating value LHV ($120\,\frac{MJ}{kg}$ for hydrogen) and the battery energy density e_{bat}, namely:

$$m_{fuel} = \frac{E_f}{LHV}$$

$$m_{bat} = \frac{E_e}{e_{bat}}$$

6.2.1 LIQUID HYDROGEN TANK WEIGHT CALCULATION

Liquid hydrogen tank mass is a function of the stored fuel content. Therefore, it is convenient to divide fuel-related aircraft mass $m_{fuel,tot}$ into two terms. The first term corresponds to the liquid hydrogen tank mass m_{tank}, which do not change over the mission, while the second is the liquid hydrogen mass m_{fuel}. Using this distinction, the following expression can be used:

$$m_{fuel,tot} = m_{fuel}(E_f) + m_{tank}(E_f)$$

A proper liquid hydrogen tank design is key for the feasibility of LH_2-fuelled aircraft. The initial studies by Lockheed California for supersonic and subsonic civil aircraft, outlined by Brewer [41], compared different shapes, structures, wall materials and insulation materials for liquid hydrogen tanks. Similar studies on tank design have been performed in the last 20 years by other authors (e.g., Mital et al. [59], Verstraete [60], Winnefeld et al. [61], Rompokos et al. [62]), as well as studies on tank integration into aircraft (e.g., Onorato [63], van Woensel [64]). These studies suggest that liquid hydrogen tank is expected to be a major contributor to hydrogen aircraft OEW. Therefore, reliable tank weight estimation is crucial for hydrogen aircraft design methodologies.

Liquid hydrogen tank design starts with conceptual design. Then, preliminary design is performed, including geometric design, structural design, and thermal design, as described by Verstraete [60] and Winnefeld et al. [61]. The preliminary design phase provides inputs for an initial estimation of the liquid hydrogen tank weight. In this work, a tank conceptual and preliminary design methodology is implemented for weight estimation. Constant operating pressure and no hydrogen venting during operation are assumed in this work for simplicity. For further information on pressure fluctuations and venting during operation, the interested reader is referred to works such as Verstraete et al. [65], Rompokos et al. [62] and Onorato [63].

The chosen conceptual design is defined as follows:

- The tank is cylindrical with spherical caps, to ensure simple manufacturing and appropriate integration into cylindrical fuselages.
- The tank features a double-walled constant-thickness structure, to achieve damage-tolerance characteristics and allow for high-performance vacuum MLI insulation.

- The external wall of the tank is the same structure as the fuselage, to reduce overall tank weight by exploiting the structural functions of the existing fuselage structure, as indicated by Brewer [41].
- The chosen wall material is Al 2219 due to its high TRL compared to composites and its higher strength-to-weight compared to stainless steel, as considered by Verstraete [60].
- The insulation material is the high-performance DAM/Dacron MLI with hard vacuum, to minimize tank heating over the mission.

A cylindrical tank barrel with spherical caps is considered. Integral double-wall architecture is selected, with the external wall diameter equal to the fuselage diameter. Inner shell diameter is determined by vacuum MLI insulation thickness, given by the maximum allowable thermal input. Tank length will be determined by the mission energy requirements as well as the required liquid hydrogen mass m_{LH2}. This quantity depends also on the chosen tank fill level $y_{fill} = \frac{V_{LH2}}{V_{tank,in}}$ and operating pressure P_{H2}. Tank internal and external volume are computed as follows:

$$V_{tank,in} = \frac{\pi D_{in}^3}{6} + \frac{\pi}{4} D_{in}^2 L_{barrel} = \frac{V_{LH2}}{y_{fill}} = \frac{m_{LH2}}{\rho_{H2} y_{fill}}$$

$$V_{tank,out} = \frac{\pi D_{fuselage}^3}{6} + \frac{\pi}{4} D_{fuselage}^2 L_{barrel}$$

A similar approach to that followed by Verstraete [60] and Rompokos [62] is used for structural design. The expressions in the ASME Boiler and Pressure Vessel Code (BPVC) Section VIII Division 1 [66] for design, manufacturing, and testing of pressure vessels with capacity higher than 250 liters, are used to size the inner shell thickness. In these expressions, MAWP is the Maximum Allowable Working Pressure, considered as the shell structural design pressure (maximum difference in pressure between inside and outside of a vessel) in MPa, r is the tank external radius in m, σ_a the maximum allowable stress in MPa, selected as $\sigma_{a,Al\ 2219} = 172.4\ MPa$ as indicated by Verstraete [60]; and e_w the weld efficiency, assumed as $e_w = 0.8$ as per the indications from Verstraete [60]. Different expressions apply for the cylindrical barrel and spherical caps; the most restrictive value will be selected, as the tank is designed as a constant-thickness structure. The equation used to determine the tank thickness is the following:

$$t_{inner\ shell} = \frac{MAWP\ r}{\sigma_a e_w - 0.6 MAWP}$$

Outer vessel design is based on elastic stability, due to compressive stresses generated by the vacuum that can lead to structural collapse. As the external shell of the cylindrical barrel is the same structure as a fuselage section, it is assumed that the fuselage structural sizing will account for the vacuum stresses. Given the more stringent mechanical requirements that apply to the fuselage, the impact of vacuum stresses on its design is assumed negligible. Therefore, only the hemispherical caps are sized for vacuum stress resistance.

The following expression is proposed by Barron [67] for thickness sizing of the hemispherical heads given the value of collapsing pressure:

$$t_{min,sph} = r_{out} \sqrt{\frac{P_{collapse}\sqrt{3(1-\nu^2)}}{E}}$$

A safety factor of 4 is selected based on the recommendations by ASME [66] ($P_{collapse} = 4P_{atm}$). Further, $r_{out} = \frac{1}{2} D_{fuselage}$ based on the assumptions made in the conceptual design.

For Al 2219, Poisson's ratio is $\nu_{Al2219} = 0.33$ and Young's modulus is $E_{Al2219} = 73100\ MPa$ [68].

As considered by Verstraete et al. [65], 10 layers of MLI with a density of 20 layers/cm is assumed for thermal insulation, leading to a 0.5 cm thick thermal insulation.

Once conceptual and preliminary design have been completed, the tank weight calculation is performed. Tank weight is the sum of the structural and insulation weight, as follows:

$$m_{tank} = m_{structural} + m_{thermal} = \rho_{Al\ 2219}(A_{inner\ wall} t_{inner\ wall} + A_{outer\ wall} t_{outer\ wall}) + \rho_{MLI} t_{MLI} A_{MLI}$$

The density of Al 2219 is taken equal to $2825\frac{kg}{m^3}$, as indicated by Verstraete [60] and Brewer [41]. The density of MLI is estimated equal to $60\frac{kg}{m^3}$ based on Mazzone et al. [69]. Areas are estimated using geometric relations.

Tank mass calculation is used to define liquid hydrogen storage density $\rho_{LH2\ storage}$ as:

$$\rho_{LH2\ storage} = \frac{m_{fuel}}{m_{tank}}$$

Considering the definition of fuel-related aircraft mass $m_{fuel,tot}$, the expression for this quantity to be used in the energy sizing methodology reads:

$$m_{fuel,tot} = m_{fuel} + m_{tank} = m_{fuel} + \frac{m_{fuel}}{\rho_{LH2\ storage}} = m_{fuel}\left(1 + \frac{1}{\rho_{LH2\ storage}}\right)$$

This expression will be used for the derivation of the range equation.

6.2.2 BATTERY WEIGHT CALCULATION

As per de Vries [28], battery mass can be determined by the chosen power or energy capacity. The calculation of battery weight given the energy capacity is based on the specific energy at pack level e_{bat} and the minimum state of charge. Battery weight calculation for power requirements is instead performed based on power-loading diagrams and power density values of state-of-the-art batteries. The final battery weight is the maximum among the values resulting from the application of the two sizing criteria.

Hepperle [36] presents a review on battery technology for electric aircraft applications in 2012, based on the work by Bruce et al. [70]. Li-Ion batteries provided 0.2 kWh/kg in 2012, with capabilities to increase this value to 0.25 kWh/kg by future developments. Lithium-Sulfur (LiS) and Lithium-Oxygen (LiO_2) batteries are highlighted as technologies with higher energy density on which extensive R&D work is performed, with LiS batteries at a higher TRL. LiS batteries are expected to achieve 0.5-1.25 kWh/kg in 2025, while LiO_2 batteries are expected to achieve 0.8-1.75 kWh/kg in 2025. The author recommends considering LiS battery technology for developments expected for the 2030s, due to the low TRL and development uncertainty of LiO_2 batteries.

Assuming the use of LiS battery technology, the data from Dorfler et al. [71] is used for the estimation of power density and energy density of a battery developed for EIS in 2035. It results that:

$$e_{bat} = 0.6\frac{kWh}{kg} = 2.16\frac{MJ}{kg}$$

$$\dot{w}_{bat} = 0.8\frac{kW}{kg}$$

Further, for long-term performance of batteries, they should not be discharged below a minimum state of charge (SOC_{min}). In this work, $SOC_{min} = 30\%$ is assumed. Based on this consideration, battery mass is computed as follows:

$$m_{bat} = \frac{E_{bat}}{e_{bat}(1 - SOC_{min})}$$

6.2.3 MODIFIED CRUISE RANGE EQUATION FOR LIQUID HYDROGEN SOFC-GT-BATTERY HYBRID ELECTRIC POWERTRAINS

The powertrain studied in this work is defined by 3 design power management parameters: Φ, Ψ and, λ. A novel range equation is derived, to describe the impact of these parameters and component efficiencies on aircraft range. A similar methodology to that presented by de Vries [40] is used for the derivation of the range equation.

First, fuel power ($P_f = P_{f1}$) and battery electric power ($P_e = P_{e2}$) are expressed in terms of fuel and battery energy (E_f, E_e), as per de Vries [40], namely:

$$P_f = -\frac{dE_f}{dt}$$

$$P_e = -\frac{dE_e}{dt}$$

The ratio between fuel energy/power and battery electric energy/power is now defined. To this end, the power balance equations are manipulated to obtain an expression that relates P_f to P_e as a function of Φ, Ψ, and component efficiencies. The following expression, representing the fraction of battery electric power with respect to fuel power, indicated with Ω, is obtained:

$$\Omega = \frac{P_e}{P_f} = \frac{(1-\Psi)(1-\Phi)\eta_{SOFC} f_u}{\Psi \eta_V}$$

It results that the total energy at the beginning of the mission is equal to

$$E_{tot} = E_e + E_f = (1+\Omega)E_f = \left(1 + \frac{1}{\Omega}\right) E_e$$

Several assumptions are now considered to derive the range equation for the SOFC-GT-Battery powerplant. These are:

- Propulsive power is computed assuming constant airspeed, and constant lift coefficient flight. This implies that flight altitude will be increased during flight. Nevertheless, constant altitude flight is assumed, as the flight path angle can be considered negligible. It results that:

$$P_p = TV = \frac{gmV}{\frac{L}{D}}$$

- Power required by the electric payload is assumed to be proportional to propulsive power. The variable λ can be then removed from the power management parameters. The proportionality parameter κ is set to $\kappa = 1.10$ based on the results of preliminary model runs and typical power requirements from aircraft subsystems (e.g., ECS, de-icing…). Considering the power terms as named in Figure 29, the following expression is used:

$$P_{required} = P_{p1} + P_{p2} + P_{e4} \cong \kappa P_p = \kappa(P_{p1} + P_{p2})$$

With these assumptions, the range equation is derived. No simplification of the powertrain architecture shown in Figure 29 is performed, as opposed to de Vries [28]. η_{PM} is considered as representative of η_{PM1} and η_{PM2} ($\eta_{PM} = \eta_{PM1}\eta_{PM2}$). Propulsive powers P_{p1} and P_{p2} can be expressed in terms of fuel and battery power as follows:

$$P_{p1} = P_f \Phi \eta_V \eta_{p1}(\eta_{GT1} + (1 - \eta_{SOFC} f_u)\eta_{GT2})$$

$$P_{p2} = P_e \eta_{PM}\eta_{EM}\eta_{p2} + P_f(1-\Phi)\eta_V \eta_{SOFC} f_u \eta_{PM}\eta_{EM}\eta_{p2}$$

The overall propulsive power equation then reads

$$P_p = P_{p1} + P_{p2} = P_f \Phi \eta_V \eta_{p1}(\eta_{GT1} + (1 - \eta_{SOFC} f_u)\eta_{GT2}) + P_e \eta_{PM}\eta_{EM}\eta_{p2} + P_f(1-\Phi)\eta_V \eta_{SOFC} f_u \eta_{PM}\eta_{EM}\eta_{p2}$$

$$P_p = P_f \cdot \left[\eta_V\left(\Phi \eta_{p1}\eta_{GT1} + (1-\Phi)\eta_{p1}(1 - \eta_{SOFC} f_u)\eta_{GT2} + (1-\Phi)\eta_{SOFC} f_u \eta_{PM}\eta_{EM}\eta_{p2}\right)\right] + P_e \cdot \left[\eta_{PM}\eta_{EM}\eta_{p2}\right]$$

To simplify the expressions, the parameters η_f and η_e are defined as:

$$\eta_f = \eta_V\left(\Phi \eta_{p1}\eta_{GT1} + (1-\Phi)\eta_{p1}(1 - \eta_{SOFC} f_u)\eta_{GT2} + (1-\Phi)\eta_{SOFC} f_u \eta_{PM}\eta_{EM}\eta_{p2}\right)$$

$$\eta_e = \eta_{PM}\eta_{EM}\eta_{p2}$$

A similar expression to that proposed by de Vries [28] is reached, namely:

$$P_p = \eta_f P_f + \eta_e P_e$$

Assuming constant speed at cruise, the mission range R is obtained as the integral of speed V over time t.

$$R = \int V dt$$

Cruise speed is obtained from the propulsive power equation as a function of powertrain power distribution parameters and efficiencies as

$$V = \frac{\eta_f P_f + \eta_e P_e}{\kappa g m} \frac{L}{D}$$

Substituting power values by energy values:

$$V = -\frac{\eta_f \frac{dE_f}{dt} + \eta_e \frac{dE_e}{dt}}{\kappa g m} \frac{L}{D}$$

Considering the ratio of battery-to-fuel power $\Omega = \frac{E_e}{E_f} = \frac{\frac{dE_e}{dt}}{\frac{dE_f}{dt}}$, it results that:

$$V = \frac{\eta_f + \eta_e \Omega}{\kappa g m} \frac{L}{D} \frac{dE_f}{dt}$$

This expression is then used to obtain the range equation, considering that weight is a function of time due to fuel consumption, namely:

$$R = \frac{\eta_f + \eta_e \Omega}{\kappa g} \frac{L}{D} \int_{t_1}^{t_2} \frac{1}{m(t)} \frac{dE_f}{dt} dt$$

$$m(t) = OEW + m_{PL} + m_{crew} + m_{bat} + m_{tank} + m_{fuel}(t)$$

Recalling the relation between mass and energy for fuel and battery, and substituting the equation for aircraft mass in the integral:

$$R = \frac{\eta_f + \eta_e \Omega}{\kappa g} \left(\frac{L}{D}\right)_{cruise} \int_{t_1}^{t_2} \frac{\frac{dE_f}{dt}}{OEW + m_{PL} + m_{crew} + \frac{E_e}{e_{bat}(1 - SOC_{min})} + \frac{E_f(t)}{LHV}\left(1 + \frac{1}{\rho_{LH2\ storage}(E_{f,max})}\right)} dt$$

This integral is analytically solved to obtain the general aircraft range between times t_1 and t_2, or to obtain the covered distance knowing the energy consumption for a discrete mission segment:

$$R = \frac{LHV(\eta_f + \eta_e \Omega)}{\kappa g} \left(\frac{L}{D}\right)_{cruise} \ln\left(\frac{OEW + m_{PL} + m_{crew} + \frac{E_e}{e_{bat}(1 - SOC_{min})} + \frac{E_f(t_2)}{LHV}\left(1 + \frac{1}{\rho_{LH2\ storage}(E_{f,max})}\right)}{OEW + m_{PL} + m_{crew} + \frac{E_e}{e_{bat}(1 - SOC_{min})} + \frac{E_f(t_1)}{LHV}\left(1 + \frac{1}{\rho_{LH2\ storage}(E_{f,max})}\right)}\right)$$

Now, the limits of this integral are modified to compute the total energy requirement for a given cruise range. To this end, the fuel and battery energy are expressed as $E_f(t_1) = E_{fuel} = m_{fuel,max} LHV$, $E_f(t_2) = 0$, $E_e(t_1) = E_{bat}$, $E_e(t_2) = 0$. In terms of battery and fuel mass, the final expression is:

$$R_{max} = \frac{LHV(\eta_f + \eta_e \Omega)}{\kappa g} \left(\frac{L}{D}\right)_{cruise} \ln\left(\frac{OEW + m_{PL} + m_{crew} + m_{bat} + m_{fuel}\left(1 + \frac{1}{\rho_{LH2\ storage}(m_{fuel})}\right)}{OEW + m_{PL} + m_{crew} + m_{bat} + \frac{m_{fuel}}{\rho_{LH2\ storage}(m_{fuel})}}\right)$$

In terms of total energy, the final expression is:

$$R_{max} = \frac{LHV(\eta_f + \eta_e \Omega)}{\kappa g} \left(\frac{L}{D}\right)_{cruise} \ln\left(\frac{OEW + m_{PL} + m_{crew} + E_{tot}\left(\frac{1}{e_{bat}\left(1 + \frac{1}{\Omega}\right)(1 - SOC_{min})} + \frac{1}{LHV(1 + \Omega)} + \frac{1}{\rho_{LH2\ storage}(E_f) LHV(1 + \Omega)}\right)}{OEW + m_{PL} + m_{crew} + E_{tot}\left(\frac{1}{e_{bat}\left(1 + \frac{1}{\Omega}\right)(1 - SOC_{min})} + \frac{1}{\rho_{LH2\ storage}(E_f) LHV(1 + \Omega)}\right)}\right)$$

This expression is used to determine aircraft cruise block energy consumption, as well as the energy capacity and the fuel mass m_{fuel}. However, to determine battery mass m_{bat}, the mass obtained via the energy sizing methodology needs to be compared to the mass obtained via the power sizing procedure and the maximum value shall be selected.

7 WEIGHTS CALCULATION AND SYSTEM INTEGRATION

7.1 OPERATIONAL EMPTY WEIGHT CALCULATION METHODOLOGY

Traditional OEW estimation methodologies for conceptual and preliminary design are mainly Class I, based on statistical information from previous aircraft and engines. This statistical data is not available for novel aircraft and powertrain concepts, such as the regional LH_2-fuelled SOFC-GT-Battery hybrid electric aircraft studied in this work. Therefore, modifications to traditional methodologies are required.

Based on the work by de Vries [28], a modified Class I method with detailed novel component weight estimation is developed, implemented, validated, and used for sensitivity studies in this work. The components for which novel weight estimation methodologies are required include the liquid hydrogen tank, hydrogen management system, the SOFC stack, the SOFC BoP, the battery, the electric power management components (DC/DC converter, inverter, cabling), the electric motor, and the ducted electric fan powered by the SOFC or batteries. Further, corrections on structural weight estimation will be required due to fundamental architecture modifications (no fuel stored in wings, higher $\frac{m_{landing}}{MTOW}$ for LH_2-powered aircraft than for conventional aircraft). The modified Class I OEW estimation method is based on the following expression:

$$OEW' = OEW_{ref} - m_{powerplant,ref} + m_{LH2\ tank} + m_{H2\ mgmt\ system} + m_{SOFC+BoP} + m_{bat} + m_{power\ mgmt} + m_{electric\ motor} + m_{ducted\ fan} + f_{wing} m_{wing,ref} + f_{LG} m_{LG,ref}$$

The OEW' includes all the components which mass is not increased or reduced during aircraft operation and cannot be considered as payload or crew. Nevertheless, there are two components from OEW', namely liquid hydrogen tank mass $m_{LH2\ tank}$ and m_{bat}, that are a function of their respective stored energy. Based on the methodology for weight calculation for hybrid electric aircraft proposed by de Vries [28], it is convenient to treat the components whose mass is a function of stored energy in the energy sizing methodology, and not in the OEW calculation. Therefore, OEW is defined in this work as:

$$OEW = OEW_{ref} - m_{powerplant,ref} + m_{H2\ mgmt\ system} + m_{SOFC+BoP} + m_{power\ mgmt} + m_{electric\ motor} + m_{ducted\ fan} + f_{wing} m_{wing,ref} + f_{LG} m_{LG,ref}$$

Furthermore, items included in OEW can be subdivided into two main classes, namely powertrain weight ($m_{powertrain}$) and extra structural weight ($m_{structural,extra}$), as shown by the following equations

$$m_{powertrain} = m_{H2\ mgmt\ system} + m_{SOFC+BoP} + m_{power\ mgmt} + m_{electric\ motor} + m_{ducted\ fan}$$

$$m_{structural} = f_{wing} m_{wing,ref} + f_{LG} m_{LG,ref}$$

Further, a new parameter is introduced in the OEW equation. This corresponds to the reference OEW minus the weight of the components that are the same of conventional aircraft and is called corrected reference OEW ($OEW_{ref,corrected}$), whose definition reads

$$OEW_{ref,corrected} = W_{ref} - m_{powerplant,ref} - m_{hydraulic+pneumatic}$$

Therefore, OEW estimation is performed using the following expression:

$$OEW = OEW_{ref,corrected} + m_{powertrain} + m_{structural,extra}$$

The methods to obtain the values of the terms in this equation are described in detail in the next section.

7.1.1 REFERENCE OEW CALCULATION

First, the OEW for a reference conventional kerosene-powered aircraft with similar configuration, mission, and development year as the target aircraft shall be estimated. In this work, the data presented by Hepperle [36] is used to estimate the OEW/MTOW of propeller aircraft with similar MTOW. From Figure 31, considering a weight structure reduction until the entry into service of the target aircraft, it is assumed that:

$$\frac{OEW}{MTOW} = 0.715 - 0.04 \log_{10}(MTOW)$$

$$OEW_{ref} = \frac{OEW}{MTOW} MTOW_{ref}$$

The OEW and MTOW data from similar aircraft, as presented in Table 20, are used for verification of this assumption.

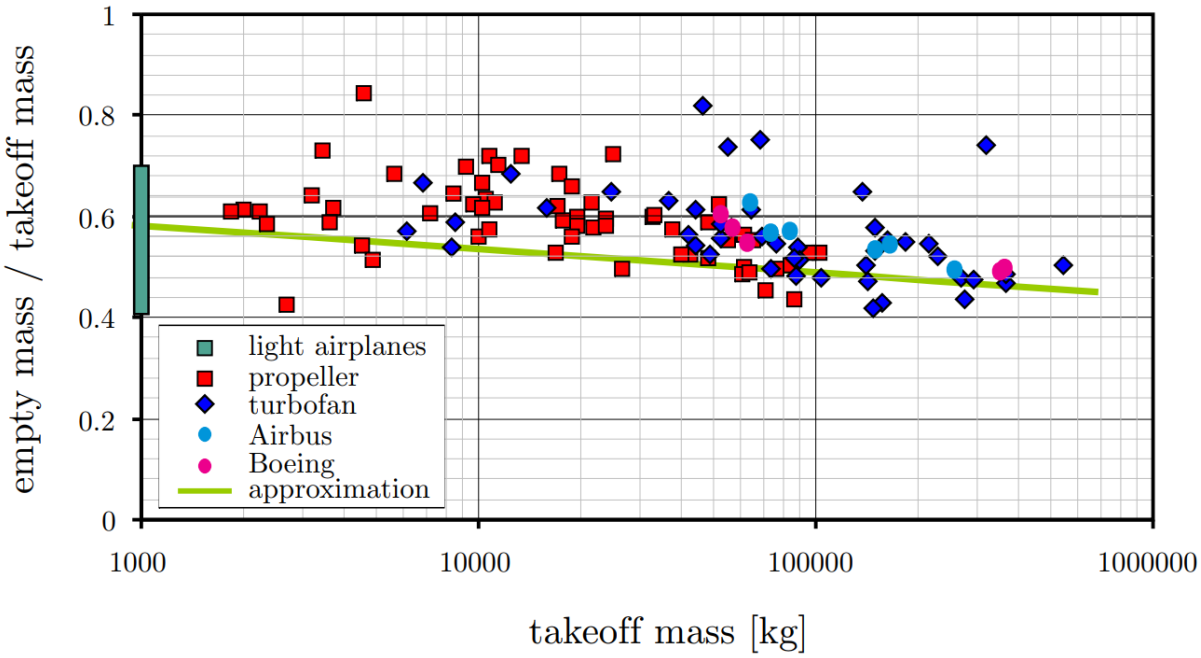

Figure 31 – OEW/MTOW for aircraft in the market with different MTOW. Source: [36].

7.1.2 TURBOPROP WEIGHT CALCULATION

The weight of the turboprop engine shall be estimated. The scope of this work does not involve high-fidelity estimation of turboprop engine weight. However, realistic values are required for the planned tradeoff studies. Therefore, a whole-engine-based methodology based on turboprop power density estimations considering statistical data from turboprop engines in the market is selected as a tradeoff solution between simplicity and accuracy. Based on the market data compiled by Marckwardt [72], power density of turboprop engines can be correlated to their power level using the following quadratic expression, with power density in $\frac{kW}{kg}$, and power in kW, valid for $\dot{W} \in (0, 5)\ MW$:

$$\left(\frac{\dot{W}}{m}\right)_{turboprop} = \frac{1}{0.324 - 5.32 \cdot 10^{-5}\ \dot{W} + 5.92 \cdot 10^{-9}\ \dot{W}^2} \left[\frac{kW}{kg}\right]$$

$$m_{turboprop} = \frac{\dot{W}_{turboprop}}{\left(\frac{\dot{W}}{m}\right)_{turboprop}}$$

7.1.3 SOFC STACK WEIGHT CALCULATION

Datta [5] developed a PEM fuel cell system model for preliminary design of hydrogen eVTOL aircraft. The methodology considers the design of the complete PEM fuel cell system, including cell, stack, and balance of plant (air management system, hydrogen storage and distribution system, cooling loops, water management system, electrical system). In this subsection, the proposed PEMFC stack weight estimation methodology is adapted for SOFCs.

The methodology proposed by Datta [5] starts with PEMFC system performance modelling. This step has already been covered in section *SOFC system performance modelling* of this report, which describes also balance of plant and stack performance modelling. Then, a part-by-part stack weight buildup methodology is proposed. Anode, cathode, electrolyte, seals, bipolar plates, current collectors, insulating plates, end plates, fastener, and other parts, are considered. Each component is characterized by its density ρ, thickness t, area A, and porosity factor Φ. Fastener weight and other parts' weight are modelled as a constant value, due to the wide

differences between systems (e.g., fastening via basic steel bolts and clamps, or via composite wraps). The general expression for the mass of each component, as proposed by Datta [5], is:

$$m_i = \rho_i t_i A_i \Phi_i$$

This methodology is adapted for the metal-supported SOFC presented by Udomsilp et al. [47]. Cell weight is the sum of the weight of the anode, cathode, electrolyte, GDLs, seals, and bipolar plates, according to the following equation

$$m_{cell} = m_{anode} + m_{cathode} + m_{electrolyte} + 2m_{GDL} + m_{seal} + m_{BP}$$

This weight is converted into stack weight via the number of cells and the current collectors, insulating layers, end plates, fastener, and other components if existing, namely:

$$m_{stack} = n_{cells} m_{cell} + 2 \cdot \left(m_{current\ collector} + m_{insulating\ layer} + m_{end\ plates}\right) + m_{fastener} + m_{other}$$

Table 9 includes the data used in this work for SOFC weight estimation, based on information regarding the microstructure of the metal-supported SOFC described by Udomsilp et al. [47], as seen in Figure 14 with the corresponding image scale. The data in Figure 14 is used to determine the materials and thicknesses for the weight estimation procedure, via measurements in Figure 14 using the available scale. Additional data on material densities, porosity and metal-supported SOFC manufacturing are obtained from Takino et al. [73] and Haydn et al. [74].

An estimation of bipolar plates porosity is obtained considering the design rules for planar SOFC interconnects and channels proposed by Tanner and Virkar [75]. In this journal article, analytical expressions for ASR as a function of interconnect geometry are developed for channel-based design and dimples-based design interconnect symmetries. The higher the interconnect contact spacing, the lower the interconnect weight due to the higher porosity, but the higher the interconnect contact resistance impact on ASR (see Figure 32). Based on these results, 1D channel geometry with 0.2 cm of interconnect contact spacing is selected for this work, to obtain cell-dominated resistance with negligible interconnect contact resistance (i.e., correction on cell ASR for contact resistance is not required in the performance model. Considering $x_0 = 10\ \mu m$ and thickness of the interconnect as $t_i = 1\ mm$ as per Tanner and Virkar, 40% porosity is considered (i.e., 40% of space covered by channels).

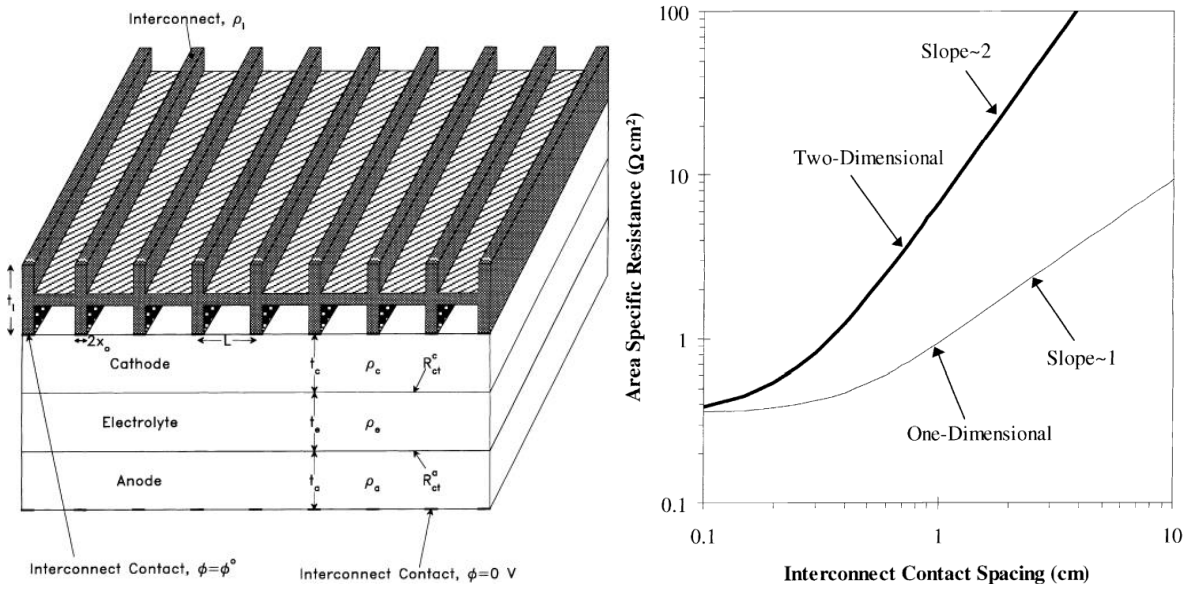

Figure 32 – Interconnect design with channels for anode-supported planar SOFC (left), and analytical data on the impact of interconnect contact spacing on SOFC ASR (right). Source: [75].

Concerning the components for which information cannot be directly retrieved from Udomsilp et al. [47], such as seals, current collectors, insulating layers, end plates, and fastener, their weight is estimated considering data on SOFC materials and design from several books (U.S. Department of Energy [9], Singhal [8], Larminie and Dicks [2], O'Hayre et al. [3]) and journal papers (Hodjati-Pugh et al. [76]). More in detail:

- Based on indications from [9], compressive hybrid glass-ceramic mica seals are considered. A typical value of seal thickness of 0.3 mm is assumed, as indicated by Rodriguez-Lopez et al. [77]. Seals are assumed to cover 5% of cell area, as per Datta [5].
- Hodjati-Pugh et al. [76] performed a 2021 review on the development of current collectors for microtubular SOFCs. The author indicates that most research done between 2015 and 2020 focuses on silver material, followed by nickel and platinum. The United States Department of Energy [9] refers to the use of silver as current collector material. Despite a planar SOFC is considered in this work, silver is assumed as current collector material. Regarding thickness, a value of 0.25 mm is set. This value represents a reasonable tradeoff between weight and electrical conductivity, based on the studies reviewed by Hodjati-Pugh et al. [76] and the value proposed by Takino et al. [73].
- SOFC insulating layers are described by Singhal [8] (referred to as side seals) as one of the major development gaps for SOFCs. In this work, it is assumed that insulating layers manufactured using hybrid mica. 10 times the thickness of interlayer seals is assumed for insulated layers.
- For end plates, the same material as for bipolar plates is assumed, based on the design by Bossel [78], assuming 1 cm thickness.

Information that cannot be retrieved from literature is estimated using the data for PEMFC design provided by Datta [5] and Zhang et al. [79].

Table 9 – Materials, density, thickness, and area of each component of the SOFC stack. Sources: [47] [5] [79] [74]

Component	Material	Density ($\frac{kg}{m^3}$)	Thickness (mm)	Area (fraction membrane area)	Porosity
Cathode	LSC ($La_{0.58}Sr_{0.4}CoO_{3-\delta}$)	6220	0.050	1	0.75
Electrolyte	YSZ (8%)	6100	0.002	1	0.9
Gas diffusion layer	GDC	7200	0.0008	1	0.6
Anode active layer	Ni/GDC 60/40	8220	0.022	1	0.6
Anode interlayer and base layer	Ni/YSZ 65/35	7920	0.050	1	0.6
Bipolar plates (metal supports)	Ferritic oxide dispersion-strengthened Fe-Cr alloy (Fe26Cr)	7800	0.3	1.1	0.7
Seal/Gasket	Hybrid mica	2700	0.3	0.05	1.0
Current collectors	Silver	10490	0.25	1.1	0.5
Insulating layers	Hybrid mica	2700	3.0	1.1	1.0
End plates	Ferritic oxide dispersion-strengthened Fe-Cr alloy (Fe26Cr)	7800	10.0	1.2	0.8

Fastener weight is estimated based on the work by Zhang et al. [79], considering fastening with clamping bolts in the endplates, as schematized in Figure 33. Ten bolts are used. Assuming ferritic oxide dispersion-strengthened Fe-Cr alloy bolts ($\rho_{bolts} = 7800 \frac{kg}{m^3}$), $D_{bolt} = 0.017\ m$ as per Zhang et al. [79], and that the bolts run through the entire stack, an expression for fastener weight estimation is derived:

$$m_{fastener} = 10\,\rho_{bolt}\frac{\pi}{4}D_{bolt}^2 t_{stack}$$

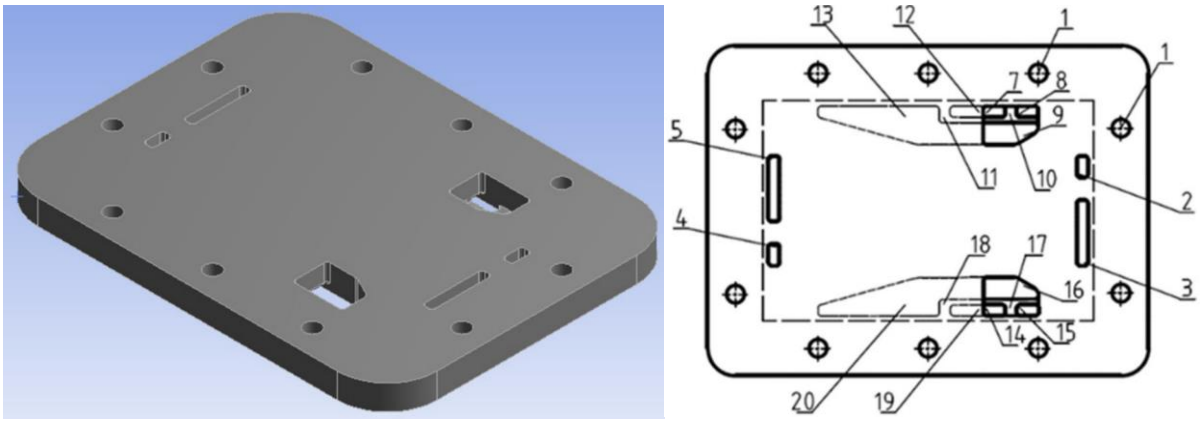

Figure 33 – Endplate design for PEMFC, with holes for clamping bolts (1). Source: [79].

7.1.4 SOFC BOP WEIGHT CALCULATION

As previously explained, the SOFC requires a compressor and a heat exchanger to supply air to the stack from HPC, and to ensure that injection of the fuel cell exhausts in the combustion chamber is possible. The methodology for weight estimation is based on the method of Datta [5] for compressors and heat exchangers, with $\dot{W}_{comp,SOFC}$ in W and $A_{radiator}$ in m^2.

$$m_{comp,SOFC} = 7 \cdot 10^{-4} \cdot \dot{W}_{comp,SOFC}\ [kg]$$

$$m_{HX,SOFC} = 3.54\ A_{HX}\ [kg]$$

Compressor power and heat transfer in the heat exchanger are calculated as follows, based on the work by Datta [5]:

$$\dot{W}_{comp,SOFC} = \frac{c_{p,air}\,\dot{m}_{air,in}T_{t,in}\left(\left(\frac{P_{t,in}+\Delta P}{P_{t,in}}\right)^{\frac{\gamma-1}{\gamma}}-1\right)}{\eta_{comp}}$$

$$\dot{Q}_{HX,SOFC} = \dot{m}_{air,in}c_{p,air}\Delta T_{air} = h_{radiator}A_{radiator}\Delta T_{air}$$

Further, as highlighted by Braun, Gummalla and Yamanis [16], the SOFC requires a pressure vessel to maintain the pressure of its surroundings equal to the operating pressure. The pressure vessel ensures that the SOFC structure is not subject to pressure differences that can lead to cracking and structural failure. Vessel design is performed considering the SOFC APU geometric model developed by Whyatt and Chick [14], shown in Figure 2. A cylindrical vessel design with flat caps is considered. Further, to determine the required size of the vessel, it is assumed that the stack houses all the subsystems of the SOFC system. A target volumetric power density of the SOFC system of 0.1 kW/l, is indicated by Udomsilp et al. [47]. Considering this indication, and assuming square cells, it is possible to obtain a_{SOFC} from t_{stack}.

For SOFC pressure vessel weight estimation, wall thickness is computed using the ASME BPVC equations [66], assuming $e_w = 0.8$, and assuming vessel diameter as 50% more than SOFC side dimension, to properly house the SOFC stack and potential peripherals:

$$t_{wall} = \frac{1.5\Delta P a_{SOFC}}{\sigma_a e_w - 0.6\,\Delta P}$$

Pressure vessel mass is determined as follows:

$$m_{inner\ shell,vessel,SOFC} = \rho_{wall}t_{wall}\frac{\pi}{4}(1.5a_{SOFC})^2 + \rho_{wall}L_{vessel}\frac{\pi}{4}((1.5a_{SOFC}+t_{wall})^2 - (1.5a_{SOFC})^{\,2})$$

Walls are assumed made of annealed Inconel 625, as recommended by Whyatt and Chick [14] to withstand the high operating temperature of the SOFC. Properties of annealed Inconel 625 at ambient temperature are

obtained from [80]. The main characteristics of this material are: $\rho_{Inconel\ 625} = 8440\,\frac{kg}{m^3}$, $\sigma_{Inconel\ 625} = 900\ MPa$, $E_{Inconel\ 625} = 207.5\ GPa$, $\nu_{Inconel\ 625} = 0.278$.

Further, the vessel shall be thermally insulated, to minimize the heat losses towards the environment. Whyatt and Chick [14] indicated a maximum acceptable heat loss of 0.5% of stack electric power output. Microtherm Super-G insulation is proposed by Whyatt and Chick [14] as the solution that leads to minimum vessel weight. In this work, a double-walled vacuum MLI insulation, as for the liquid hydrogen tank, is selected as solution, to have a redundant barrier for protection in case of system failure. Aluminum 2219 is considered as external wall material. DAM/Dacron MLI with 10 layers and 20 layers/cm layer density is selected as insulation. A description of the method for sizing double-walled vacuum MLI vessels is presented in section *Liquid hydrogen tank weight calculation*, and it is not repeated here for the sake of brevity. An equation for sizing the cylindrical vacuum barrel, the U.S. Experimental Model Basin formula [81] for short cylinders subject to external pressure, as proposed by Barron [67], is used. This expression correlates the collapse pressure of a vessel subject to vacuum loads to its size and thickness of its wall, as follows:

$$P_{collapse} = \frac{2.42E\left(\frac{t_{barrel,outer\ shell}}{2 \cdot 1.5 \cdot a_{SOFC}}\right)^{2.5}}{(1-\nu^2)^{0.75}\left(\frac{t_{stack}}{2 \cdot 1.5 \cdot a_{SOFC}} - 0.45\sqrt{\frac{t_{barrel,outer\ shell}}{2 \cdot 1.5 \cdot a_{SOFC}}}\right)}$$

This equation is solved numerically for a safety factor of 4 ($P_{collapse} = 4P_{atm}$).

Total mass of the pressure vessel is computed as follows:

$$m_{vessel,SOFC} = m_{inner\ shell} + m_{outer\ shell} + m_{insulation}$$

7.1.5 HYDROGEN MANAGEMENT SYSTEM WEIGHT ESTIMATION

Estimations on fuel system weight for aircraft are widely based on statistical data, and usually expressed as a fraction of OEW [35]. For hydrogen aircraft, due to the lack of historical information on existing LH_2-powered aircraft, this approach cannot be followed. The work from Brewer [41] for a subsonic civil aircraft fueled by liquid hydrogen (400 passengers, 5500 NM range, cruise Mach of 0.85) is the most detailed source on LH_2 fuel systems available, to the author's knowledge. The data presented by this author is used to estimate the weight of the hydrogen management system.

A simple approach to estimate LH2 fuel system weight, as proposed by Brewer [41], is to increase the weight of a comparable Jet A fuel system by 80% to account for insulation and vacuum tubing along fuel lines. In this work, to increase the fidelity of the results, the detailed weight breakdown proposed by Brewer [41] is adapted to the target aircraft, obtaining a component-based weight estimation for the liquid hydrogen fuel system. To this end, a sizing characteristic is defined for each component based on information provided by Brewer [41]. Then, the component weight is assumed to be proportional to the chosen sizing characteristic as in the methodology proposed by Datta [5] for PEMFC systems. More details about this methodology are provided in Table 10.

Table 10 – Definition of sizing characteristics for the hydrogen management system based on the component weight breakdown proposed by Brewer for liquid-hydrogen-fuelled commercial aircraft. Source: [41] + Own elaboration.

Component	Weight in Brewer (kg)	Comments	Sizing characteristic
LH_2 tank boost pump	17.7	0.03375 kg/s H_2 flow 3 per tank	3 x 524.4 kg/(kg/s H_2)
LH_2 tank high pressure pump	18.3	0.03375 kg/s H_2 flow	542.2 kg/(kg/s H_2)
Supply lines from tank to engine	292.5	~1.5 kg/m	1.5 kg/m
Exhaust HX per engine	77.1	0.166 kg/s H2	464.5 kg/(kg/s H_2) Per engine
Valves for engine	6.7	Per engine	6.7 kg/engine

supply system			
Refuel system per tank	82	Assume constant with tank size	82 kg
Vent and safety system per tank	66	Assume constant with tank size	66 kg

7.1.6 ELECTRIC POWER MANAGEMENT SYSTEM WEIGHT CALCULATION

The electric power management system includes:

- DC/DC converter and power electronics allowing for battery charge/discharge (PM1 connecting SOFC and battery in Figure 29).
- DC/DC converter and power electronics to supply the electric power to the electric motor and the electric payload.
- Electric motor inverter and controller unit.
- Electric cabling connecting all the components.

For the DC/DC converters, a power density value is obtained from the work by Zhou et al. [82].

$$\dot{w}_{DC/DC\ converter} = 2.5\frac{kW}{kg}$$

The electric motor controller and inverter weight is estimated using the data for a 250-kW system from Granger et al. [83]:

$$\dot{w}_{inverter} = 9.8\frac{kW}{kg}$$

For high-power electric cabling, the data from Aretskin-Hariton et al. [84] (calculation of cable mass per unit length based on the sum of the conductor, insulator and sheath weights) is used to define an empirical expression for cable weight per unit length and wire ampacity I, defined as the maximum current that will flow through the cabling, in Amperes:

$$\left(\frac{m}{L}\right)_{cable} = -0.033 + 0.00242\ I\ \left[\frac{kg}{m}\right]$$

7.1.7 ELECTRIC MOTOR AND PROPULSOR WEIGHT CALCULATION

Electric motor weight is a function of its rated power. Hepperle [36] presented in 2012 a review on electric motors available in the market for vehicles, concluding that 2-4 kW/kg power density could be achieved at that moment, with potential to increase the power density to 8 kW/kg by further developments of the technology, and up to 14 kW/kg for superconducting motors.

In this work, electric motor power density is estimated using publicly available data from Wright Electric [85] for a 2 MW electric motor for aeronautical applications:

$$\dot{w}_{electric\ motor} = 10\frac{kW}{kg}$$

As propulsor powered by the electric motor, a ducted fan is considered. Fan weight can be estimated as a function of takeoff thrust. First, the fan diameter is determined according to the correlation proposed by Svoboda [86] with D_{fan} in [in] and T_{TO} in [lb], which reads:

$$D_{fan} = 2 + 0.39\sqrt{T_{TO}}$$

Then, the expression by Sagerser, Lieblein and Krebs [87] is used to estimate fan weight in [lb] based on the and aspect ratio (i.e., ratio of blade height to blade chord, take 1.5 as reference value based on statistical data), namely:

$$m_{fan} = \frac{125 D_{fan}^{2.7}}{\sqrt{AR}}$$

Duct weight is estimated using an expression from Sagerser et al. [87] which reads:

$$m_{duct} = \pi D_{duct} L_{duct} t_{duct} \rho_{duct}$$

where $\rho_{duct} = 2770\ kg/m^3$ (aluminum density), $t_{duct} = 0.01\ m$. L_{duct} is instead assumed equal to 1 m. The diameter of the duct is obtained from Svoboda as:

$$D_{duct} = 5 + 0.39\sqrt{T_{TO}}$$

7.1.8 MODIFICATIONS TO THE STRUCTURAL WEIGHT ESTIMATION METHOD

Brewer [41] described other aircraft modifications required for LH_2 fuel system integration that lead to changes in weight. These are:

- An extension of strut length of the main landing gear is required to accommodate for an adequate tail-scrape angle needed for a longer aircraft body. In the case of a 234-passenger, 4200 NM range supersonic jet civil aircraft with $OEW = 111250\ kg$, this leads to increase in weight by 500 kg, according to Brewer [41]. Based on this information, it is assumed that the increase of landing gear weight is 0.45% OEW.
- Wing structural weight increases as no fuel is carried in the wings, leading to higher lift bending stresses at the wing root, requiring structural reinforcement. A 5% increase in wing weight is assumed to account for this effect.

Based on these indications by Brewer, in this work an increase of OEW by 1% to account for these 2 impacts is considered.

7.1.9 SUMMARY OF COMPONENT WEIGHT ESTIMATION METHODOLOGIES AND CORRELATIONS

The expressions and correlations used for component weight estimation are summarized in Table 11.

Table 11 – Summary of expressions and correlations used for weight estimation. Source: Own elaboration, based on sources indicated in right column.

System	Component	Expression/Correlation	Sources
Turboprop	**Turboprop**	$\frac{\dot{W}}{m} = \frac{1}{0.324 - 5.32 \cdot 10^{-5}\,\dot{W} + 5.92 \cdot 10^{-9}\,\dot{W}^2}\ \left[\frac{kW}{kg}\right]$	Marckwardt [72]
SOFC	**Stack**	$m_i = \rho_i t_i A_i \Phi_i$	Datta [5]
		$m_{cell} = m_{anode} + m_{cathode} + m_{electrolyte} + 2m_{GDL} + 2m_{seal} + 2m_{BP}$	Udomsilp et al. [47]
		$m_{stack} = n_{cells} m_{cell} + 2m_{current\ collector} + 2m_{insulating\ layer} + 2m_{end\ plates} + m_{fastener} + m_{other}$	Tanner and Virkar [75]
		$m_{fastener} = 10\ \rho_{bolt} \frac{\pi}{4} D_{bolt}^2 t_{stack}$	Zhang et al. [79]
		$m_{other} = 0.0\ kg$	Haydn et al. [74]
	Pressure vessel	$t_{wall} = \frac{1.5 \Delta P a_{SOFC}}{\sigma_a e_w - 0.6\,\Delta P}$	ASME BPVC [66]
		$P_{collapse} = \frac{2.42E \left(\frac{t_{barrel,outer\ shell}}{2 \cdot 1.5 \cdot a_{SOFC}}\right)^{2.5}}{(1-\nu^2)^{0.75}\left(\frac{t_{stack}}{2 \cdot 1.5 \cdot a_{SOFC}} - 0.45\sqrt{\frac{t_{barrel,outer\ shell}}{2 \cdot 1.5 \cdot a_{SOFC}}}\right)}$	Braun et al. [16]
		$m_{vessel,SOFC} = \rho_{wall} t_{wall} \frac{\pi}{4} (1.5 a_{SOFC})^2 + \rho_{wall} L_{vessel} \frac{\pi}{4} ((1.5 a_{SOFC} + t_{wall})^2 - (1.5 a_{SOFC})^2)$	
	Compressor	$m_{comp,SOFC} = 7 \cdot 10^{-4} \cdot \dot{W}_{comp,SOFC}[kg]$	Datta [5]

		$\dot{W}_{comp,SOFC} = \frac{c_{p,air}\,\dot{m}_{air,in}T_{t,in}\left(\left(\frac{P_{t,in}+\Delta P}{P_{t,in}}\right)^{\frac{\gamma-1}{\gamma}}-1\right)}{\eta_{comp}}$ $\dot{m}_{air,in} = \lambda_{air}\frac{M_{air}I_{stack}n_{cells}}{2\cdot 0.23\cdot F}$	
	Heat exchanger	$m_{HX,SOFC} = 3.54\,A_{HX}\,[kg]$ $\dot{Q}_{HX,SOFC} = \dot{m}_{air,in}c_{p,air}\Delta T_{air} = h_{HX}A_{HX}\Delta T_{air}$ $\dot{m}_{air,in} = \lambda_{air}\frac{M_{air}I_{stack}n_{cells}}{2\cdot 0.23\cdot F}$	Datta [5]
Liquid hydrogen	**Tank inner shell**	$t_{cyl,circumferential,min} = \frac{MAWP\,r}{\sigma_a e_w - 0.6MAWP}$ $t_{cyl,longitudinal,min} = \frac{MAWP\,r}{2\sigma_a e_w + 0.4MAWP}$	Verstraete [60] Rompokos [62] ASME BPVC [66]
	Tank outer shell	$t_{min,sph} = r_{out}\sqrt{\frac{P_{collapse}\sqrt{3(1-\nu^2)}}{E}}$	Barron [67]
	Overall tank weight estimation	$m_{tank} = \rho_{Al\ 2219}(A_{inner\ wall}t_{inner\ wall} + A_{outer\ wall}t_{outer\ wall}) + \rho_{MLI}t_{MLI}A_{MLI}$	
	LH_2 tank boost pump	$\left(\frac{m}{\dot{m}_{H2}}\right)_{boost\ pump} = 524.4\frac{kg}{\frac{kg}{s}H_2}$	Brewer [41]
	LH_2 tank high pressure pump	$\left(\frac{m}{\dot{m}_{H2}}\right)_{HP\ pump} = 542.2\frac{kg}{\frac{kg}{s}H_2}$	Brewer [41]
	Supply lines from tank to engine	$\left(\frac{m}{L}\right)_{H2\ supply} = 1.5\frac{kg}{m}$	Brewer [41]
	Exhaust HX per engine	$\left(\frac{m}{\dot{Q}}\right)_{exhaust\ HX} = 464.5\frac{kg}{\frac{kg}{s}H_2}$	Brewer [41]
	Valves for engine supply system per engine	$m_{valves} = 6.7\frac{kg}{engine}$	Brewer [41]
	Electrical system for pumps per LH_2 tank	$\left(\frac{m}{\dot{W}_{pump}}\right)_{electric\ system\ pump} = 1.7\frac{kg}{kW}$	Brewer [41]
	Refuel system per tank	$m_{refuel} = 82\frac{kg}{tank}$	Brewer [41]
	Vent and safety system	$\left(\frac{m}{\dot{m}_{H2}}\right)_{vent} = 66\frac{kg}{tank}$	Brewer [41]

	per tank		
Electric powertrain	**DC/DC converter**	$\dot{w}_{DC/DC\ converter} = 2.5\frac{kW}{kg}$	Zhou et al. [82]
	Electric motor controller and inverter	$\dot{w}_{inverter} = 9.8\frac{kW}{kg}$	Granger et al. [83]
	Cabling	$\left(\frac{m}{L}\right)_{cable} = -0.033 + 0.00242\ I\ \left[\frac{kg}{m}\right]$	Aretskin-Hariton et al. [84]
	Electric motor	$\dot{w}_{electric\ motor} = 10\frac{kW}{kg}$	Wright Electric [85]
	Ducted fan	$D_{fan} = 2 + 0.39\sqrt{T_{TO}}$	Svoboda [86]
		$m_{fan} = \frac{125 D_{fan}^{2.7}}{\sqrt{AR}}$	Sagerser, Lieblein and Krebs [87]
		$D_{duct} = 5 + 0.39\sqrt{T_{TO}}$	Sagerser et al. [87]
		$m_{duct} = \pi D_{duct} L_{duct} t_{duct} \rho_{duct}$	
Structures	**Landing gear**	$\Delta m_{LG} = 0.0045\ OEW$	Brewer [41]
	Wing	$m_{wing,LH2} = 1.05 m_{wing,Jet\ A}$	Brewer [41]

7.2 MAXIMUM TAKEOFF WEIGHT CALCULATION METHODOLOGY

MTOW is given by the sum of all the computed aircraft subsystem weights, namely:

$$MTOW = m_{payload} + m_{crew} + OEW + m_{bat} + m_{LH2\ tank} + m_{fuel}$$

The computed aircraft MTOW will likely differ from the initial estimated value, leading to an error in wing and powertrain mass estimation based on the power sizing diagrams. Therefore, the aircraft MTOW / OEW estimation and the power / energy sizing methodology have to be performed iteratively until convergence of the calculations, as shown in Figure 34 and in the overall schematic of the design methodology implemented in this work which is depicted in Figure 12.

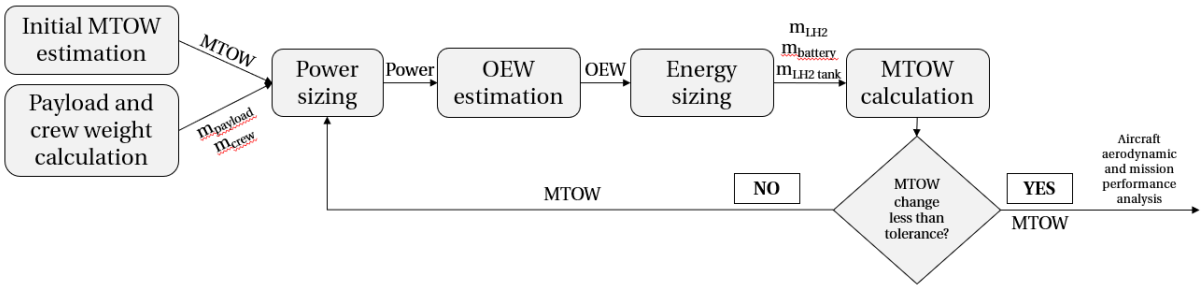

Figure 34 – Iterative loop to determine aircraft MTOW.

7.3 SYSTEM INTEGRATION

To assess the impact on aircraft design of the integration of the powertrain system into the fuselage, the geometry and volume of its components need to be estimated. Based on a qualitative analysis, it is expected that the liquid hydrogen tank, SOFC stack, and battery pack are the systems that require the largest volume, while the other subsystems have significantly smaller relevance in terms of footprint. Therefore, only the impact of these three systems on aircraft design has been then assessed. In the following subsections, methods to estimate their volume are proposed.

7.3.1 LIQUID HYDROGEN TANK GEOMETRY AND VOLUME CALCULATION

As explained in section *Liquid hydrogen tank weight calculation*, the selected tank geometry consists of a simple cylindrical barrel with spherical caps, whose outer diameter is equal to fuselage diameter. Tank volume is given by the following expression:

$$V_{tank} = \frac{\pi}{4} D_{fuselage}^2 L_{barrel} + \frac{\pi D_{fuselage}^3}{6}$$

where the barrel length is obtained as a function of LH_2 mass stored and fuselage diameter as follows:

$$L_{barrel} = \frac{4\, m_{LH2}}{\pi\, D_{fuselage}^2\, \rho_{LH2}} - \frac{2}{3}\, D_{fuselage}$$

Assuming that MLI thickness is low compared to fuselage diameter (layer density is selected as $N_t = 20 \frac{layers}{cm}$, MLI thickness is 0.5 cm for 10 layers), required increase of fuselage length as a function of liquid hydrogen mass can be estimated using the following equation, knowing that 2 hemispherical caps are used ($L_{caps} = D_{fuselage}$):

$$\Delta L_{fuselage,tank} = L_{barrel} + D_{fuselage} = \frac{4\, m_{LH2}}{\pi\, D_{fuselage}^2\, \rho_{LH2}} + \frac{1}{3} D_{fuselage}$$

7.3.2 SOFC SYSTEM GEOMETRY AND VOLUME CALCULATION

SOFC geometry is obtained from the SOFC sizing and weight estimation methodology presented in section *SOFC stack weight calculation*. Considering t_{stack} the overall height of the stack based on the estimated number of cells, as well as a stack-level volumetric power density of 1 kW/l and a system-level volumetric power density of 0.1 kW/l based on the indications from Udomsilp et al. [47], and assuming a square shape of the cells ($A_{stack} = a_{stack} \cdot b_{stack},\ a_{stack} = b_{stack} = \sqrt{A_{stack}}$), cell geometry is defined as a prism with dimensions a_{stack}, t_{stack}. Volume can be computed using the following expression:

$$V_{stack} = a_{stack}^2 t_{stack}$$

Based on the calculated volume of the stack the pressure vessel, which is a cylindrical barrel with flat caps, is sized. Assuming 5% extra length as a buffer space and for BoP integration, diameter D_{vessel}, length L_{vessel}, and volume V_{vessel} are given by the following expressions:

$$D_{vessel} = 1.5\, a_{stack}$$

$$L_{vessel} = 1.05\, t_{stack}$$

$$V_{vessel} = \frac{\pi}{4} D_{vessel}^2 L_{vessel}$$

Vessel volume is assumed to encompass the entire SOFC system (stack + BoP), and thus is used for SOFC system integration studies. Assuming that pressure vessel and fuselage are co-axial, required fuselage length increase due to SOFC integration is obtained as follows:

$$\Delta L_{fuselage,SOFC} = L_{vessel} = 1.05\, t_{stack}$$

7.3.3 BATTERY GEOMETRY AND VOLUME CALCULATION

Battery mass prediction, as presented in *Battery weight calculation*, is based simply on the assumed energy density and power density, which have been chosen based on current development trends of LiS batteries (see Dorfler et al. [71]). Therefore, as opposed to SOFC sizing, it is not necessary to estimate battery pack volume to calculate the mass of this component. The work by Liu et al. [88] indicates that volumetric energy density of LiS batteries lies between 325-580 Wh/l. In this work, considering future technology development, a value on the upper range is assumed:

$$e_{bat,vol} = 0.55 \frac{kWh}{l} \approx 2.0 \frac{MJ}{l}$$

Based on this value and assuming that the pack has a cubic form, battery volume and geometry are computed as follows:

$$V_{bat} = \frac{E_e}{e_{bat,vol}}$$

$$a_{bat} = b_{bat} = t_{bat} = \sqrt[3]{V_{bat}}$$

As for liquid hydrogen tanks and SOFCs, it is assumed that the battery is integrated within the fuselage. Therefore, an increase in fuselage length due to battery integration is assumed in the sizing methodology.

$$\Delta L_{fuselage,bat} = t_{bat}$$

7.3.4 INTEGRATION OF ADDITIONAL POWERTRAIN COMPONENTS INTO AIRCRAFT FUSELAGE

After the aircraft design methodologies have been updated to cope with the requirements of liquid hydrogen SOFC-GT-Battery powerplants, a methodology for system integration into the fuselage is developed. Additional fuselage length is required to integrate the novel systems, leading to modifications in the traditional fuselage sizing routine presented by reference aircraft design textbooks (e.g., Raymer [33], Torenbeek [34] and Sadraey [35]).

For liquid hydrogen SOFC-GT-Battery hybrid electric aircraft, traditional fuselage design methodologies shall be modified to include the extra fuselage length due to integration of the liquid hydrogen tank, SOFC and battery:

$$L_{fuselage} = L_{cabin} + L_{cockpit+nose} + L_{tail\ cone} + \Delta L_{fuselage,tank} + \Delta L_{fuselage,SOFC} + \Delta L_{SOFC,bat}$$

After integration of the novel components into the fuselage, the fuselage slenderness ($\lambda_{fuselage} = \frac{L_{fuselage}}{D_{fuselage}}$) needs to be reviewed to ensure that its value is within the allowable range. For 30-70 seat regional aircraft, as presented in Table 20, the typical range is between $\lambda_{fuselage} \in (8, 10)$.

8 IMPLEMENTATION, VERIFICATION AND VALIDATION OF THE METHODOLOGIES

8.1 POWER SIZING METHODOLOGY

First, the implemented constraint analysis methodology has been tested for a conventional turboprop powertrain. The results by de Vries [28] for the Dornier/RUAG Do228 twin-turboprop STOL utility aircraft have been used for the verification of the methodology. Though this is an EASA CS 23 aircraft, and the certification requirements in terms of performance are different, this test case has been selected due to the availability of the aerodynamic and performance data of the aircraft, as well as the choice by the author of the same independent variables chosen in this work to graphically represent the results of the constraint analysis, i.e., $\frac{P}{W}$ and $\frac{W}{S}$. As shown in Figure 35, the implemented constraint analysis tool predicts the design point as in the original work [28]. The discrepancy is only 1% for both the power loading and wing loading values. In addition, the following considerations can be made:

- The curve related to the takeoff constraint is similar to that shown in Figure 35 as calculated with Method A. In this work, the takeoff constraint is formulated through an empirical equation valid for EASA CS 25 aircraft. Therefore, differences are expected for a CS 23 aircraft. At the same time, these differences do not substantially impact the design point.
- The curves corresponding to the speed constraint differ slightly at low values of wing loading, because in this work the curve is defined based on the maximum aircraft speed, while in the work by de Vries based on the cruise speed. This difference does not substantially affect the results of the constraint analysis.
- The ROC and ROC with OEI constraints are correctly predicted by the implemented model. The small deviations are likely due to the slightly different values of the best climb speed.
- The stall speed constraint shows minimum differences, likely due to rounding errors.
- Landing distance and cruise ceiling are not included in the analysis by de Vries, but they do not affect the design point selection.

The methodology implementation is considered verified.

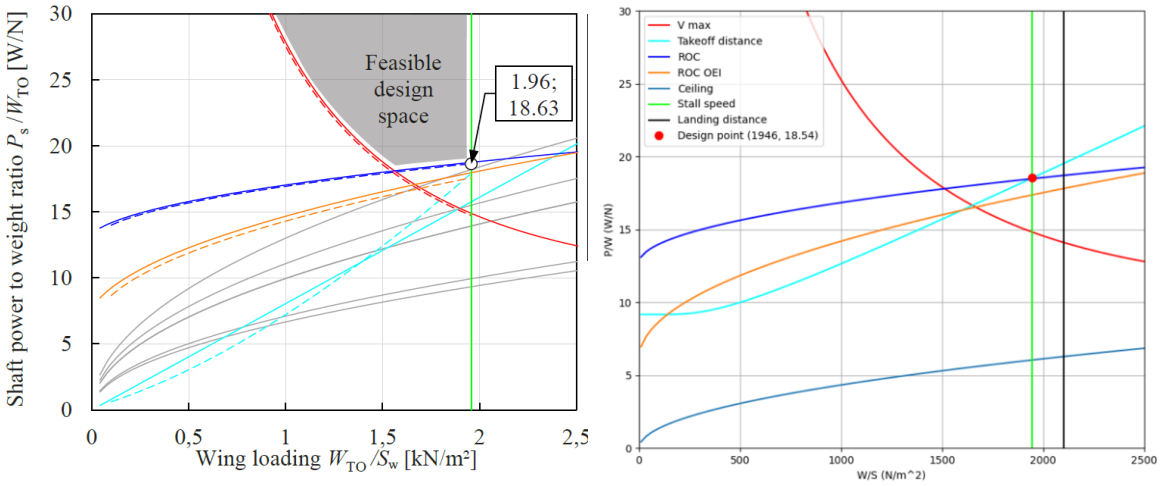

Figure 35 – Constraint analysis for the Dornier Do228. Color legend: Gray for EASA requirements, light blue for takeoff distance, red for cruise speed, green for stall speed, blue for ROC, orange for OEI ROC. Left: Result obtained by de Vries [28]. Right: Result obtained with own implementation.

The implementation of the component-oriented constraint analysis is now verified. The performance requirements and aerodynamic performance parameters are those of the target aircraft, while the considered design options are the following:

- **Case 1**: gas turbines and SOFC sized for cruise, while batteries sized to provide extra power during takeoff and climb.

- **Case 2**: no batteries, half of fuel flow injected into SOFC and half into a gas turbine engine over the entire operational envelope of the powertrain.
- **Case 3**: no batteries, SOFC only supplies required power to the electric payload, and all propulsive power from gas turbine engines.

The value of the design parameters for each case are presented in Table 12.

Table 12 – Design parameters for each case considered for the verification of the component-oriented constraint diagrams.

#	ξ_{TO}	Φ_{TO}	Ψ_{TO}	λ_{TO}	ξ_{climb}	Φ_{climb}	Ψ_{climb}	λ_{climb}	ξ_{cruise}	Φ_{cruise}	Ψ_{cruise}	λ_{cruise}	ξ_{app}	Φ_{app}	Ψ_{app}	λ_{app}
1	1.0	0.75	0.5	0.05	0.9	0.75	0.5	0.05	0.8	0.8	1.0	0.1	0.2	0.6	1.0	0.2
2	1.0	0.5	1.0	0.05	0.9	0.5	1.0	0.05	0.8	0.5	1.0	0.1	0.2	0.5	1.0	0.2
3	1.0	0.95	1.0	1.0	0.9	0.95	1.0	1.0	0.8	0.9	1.0	1.0	0.2	0.2	1.0	1.0

The efficiencies of the components are assumed to be the same in each study case, but dependent on the operating condition of the system. The assumed component efficiencies are presented in Table 13.

Table 13 – Assumed component efficiencies for the different operating conditions based on data for typical gas turbine engines in Mattingly [89], for the SOFC in Singhal [8], and for the electric motor in McDonald [90].

	η_V	η_{GT1}	η_{GT2}	η_{p1}	η_{SOFC}	$\eta_{u,SOFC}$	η_{PM1}	η_{PM2}	η_{EM}	η_{p2}
TO	1	0.42	0.50	0.70	0.55	0.75	0.99	0.99	0.92	0.70
Climb	1	0.42	0.50	0.70	0.55	0.75	0.99	0.99	0.92	0.70
Cruise	1	0.42	0.50	0.80	0.55	0.75	0.99	0.99	0.94	0.80
Approach	1	0.30	0.35	0.60	0.65	0.75	0.99	0.99	0.87	0.60

The constraint analysis for the baseline aircraft is shown in Figure 36, compared to the design points of similar aircraft, as reported in Table 23. With respect to similar aircraft currently in the market:

- The higher maximum cruise speed and nominal cruise speed compared to other similar aircraft lead to a restrictive constraint in terms of power loading.
- The stall speed requirement defines the maximum allowable wing loading, which is similar to that of the Dornier Do328 and the DeHavilland Dash 8 Q300.
- The takeoff distance requirement is not dominant in the target aircraft design.
- The ROC requirement is similar to that of the Dornier Do328.
- The ceiling requirement and the EASA CS 25 requirements do not impact the choice of the design point of the target aircraft.

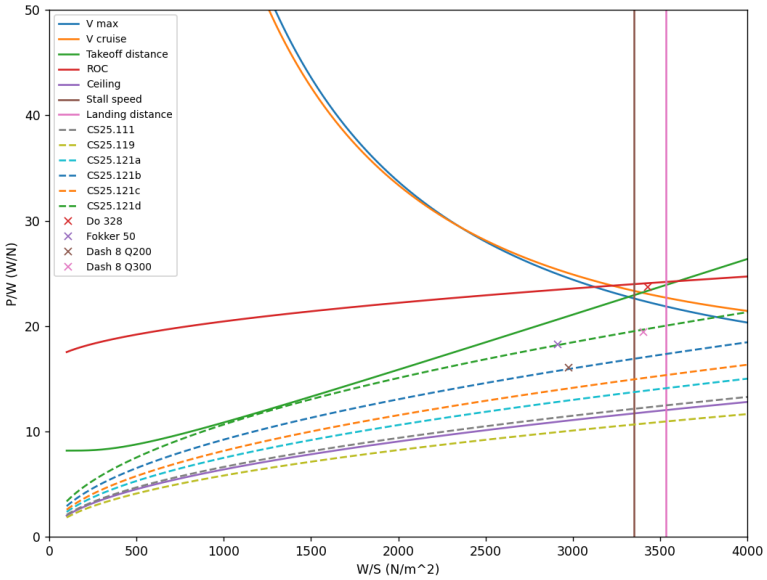

Figure 36 – Constraint analysis of the target aircraft with performance requirements compared to similar aircraft.

The component-oriented constraint diagrams obtained for each case are shown in the following figures.

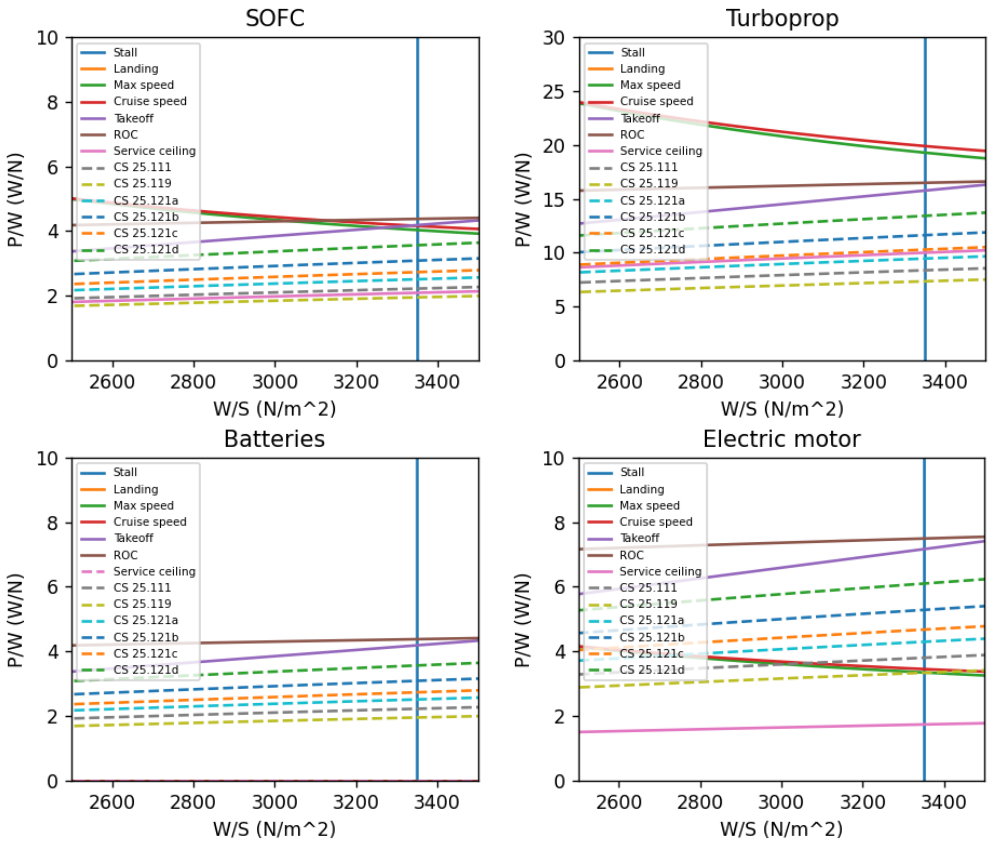

Figure 37 – Component-oriented constraint diagrams for Case 1.

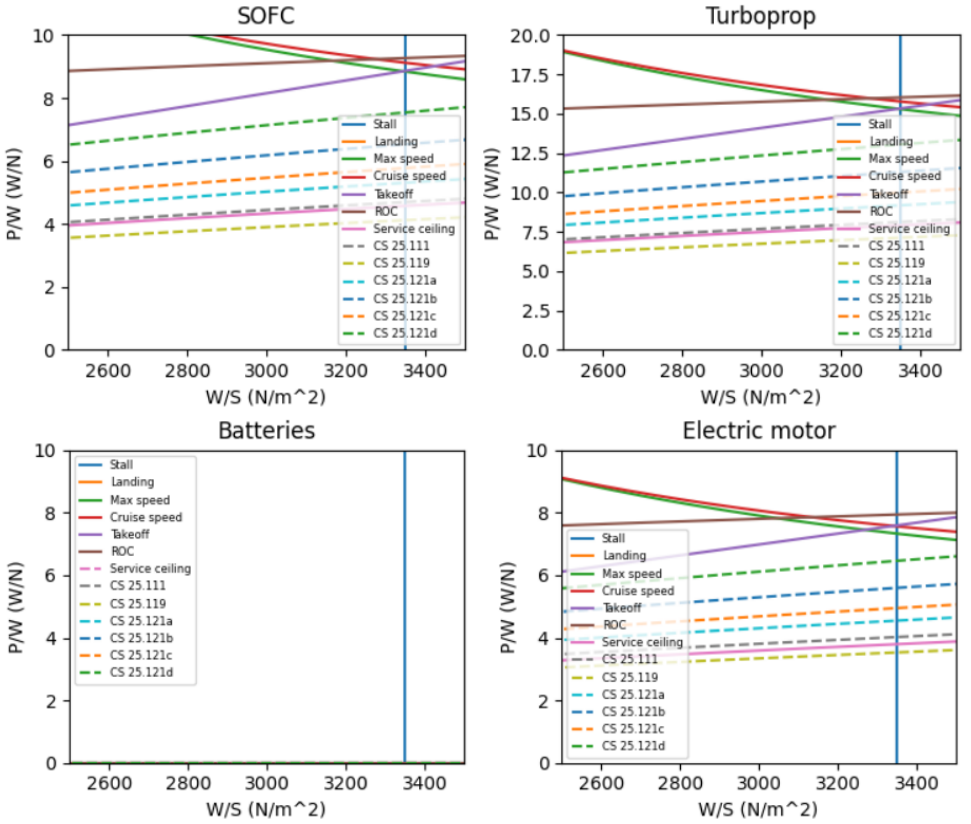

Figure 38 - Component-oriented constraint diagrams for Case 2.

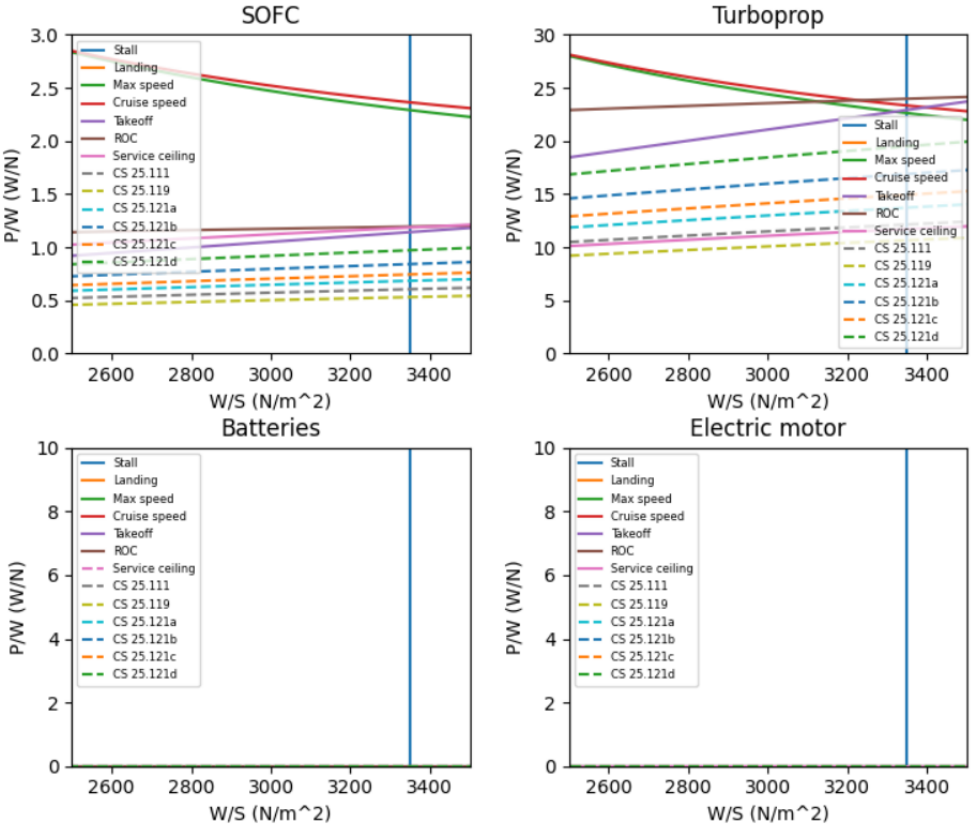

Figure 39 – Component-oriented constraint diagrams for Case 3.

From the figures, the following conclusions about the verification of the implemented model can be drawn:

- **Case 1**:
  - The optimal system design point is likely that featuring the maximum wing loading, which is determined by stall speed. Small benefits in terms of powertrain size reduction are seen in each component constraint diagram for lower values of the power loading.
  - The SOFC constraint diagram shows that the SOFC power is constrained by the cruise speed and takeoff distance.
  - The turboprop constraint diagram shows that, taking the wing loading corresponding to the stall speed requirement, the maximum power requirement is constrained by cruise speed. With respect to Figure 36, where the aircraft is only powered by 2 turboprop engines, the rate of climb and takeoff distance are not the limiting specifications anymore. The reason thereof is the use of battery and SOFC power during takeoff, which reduce the power requirement from the turboprop engine. This design could be further optimized by modifying the power split among the components during cruise. This would allow the downsizing of the turboprop engine.
  - The batteries are sized to contribute to power generation during takeoff and climb. For this reason, the cruise-related constraints do not appear in the graph, as expected. The battery size, considering maximum compliant wing loading, is constrained by the rate of climb, with the takeoff constraint being close to the design point. Such a battery size does not lead to a reduction in the size of the turboprop, as its power is constrained by cruise speed.
  - The electric motor power is constrained by the rate of climb, as during climb and takeoff it will be powered by the batteries and the SOFC (high power), while during cruise it will provide a power similar to that at cruise but being powered only by the SOFC. This result is expected given the selected power distribution.
- **Case 2**:
  - SOFC power requirement depends on cruise speed, rate of climb and stall speed. Although 50% of the fuel flow is injected into the SOFC, the electric power generated is much lower than that of the gas turbine engine, as only part of the chemical energy of the injected hydrogen into the fuel cell is converted into electric power ($f_u = 0.75$).
  - Turboprop power requirement is determined by cruise speed, rate of climb and stall speed.
  - As expected, the batteries constraint diagram does not show any constraint apart from the power-independent ones, as $\Psi = 1$ for all the operating conditions.
  - The power required to the electric motor for cruise operation is lower than that requested to the SOFC, due to the higher value of λ during cruise ($\lambda_{cruise} = 0.1$) compared to takeoff and climb ($\lambda_{TO} = \lambda_{climb} = 0.05$). This means that higher power consumption from the electric payload is observed at cruise with respect to other operating phases (e.g., for cabin pressurization using the ECS).
- **Case 3**:
  - SOFC minimum power is dictated by cruise operation. The reason for this is the higher electric payload power consumption with respect to other flight phases.
  - Turboprop power constraint is similar to that observed for the baseline aircraft (Figure 36), as it is the only propulsive element in the powertrain.
  - As expected, the batteries constraint diagram does not show any limitation regardless of the considered operating condition, as $\Psi = 1$ for all the operating conditions.
  - As expected, the electric motor constraint diagram does not show any constraint apart from the power-independent ones, as $\lambda = 1$ for all the operating conditions.

Based on the results obtained for the three case studies above, the model is deemed verified.

Validation of these diagrams using empirical data is not possible, as no real-life liquid-hydrogen-fueled SOFC-GT-Battery hybrid electric powertrains for aircraft exist currently. It remains as future work to perform the validation of these results when experimental data is available.

8.2 ENERGY SIZING METHODOLOGY

8.2.1 LIQUID HYDROGEN TANK WEIGHT CALCULATION METHODOLOGY

The implementation of the liquid hydrogen tank weight estimation method, based on the methodology explained in section *Liquid hydrogen tank weight calculation*, is now verified against data from literature. Due to the lack of experimental data about the weight of liquid hydrogen tanks for regional aircraft applications, the verification

is performed by comparing the results of the method with those of similar studies. In particular, the work by Verstraete et al. [65] has been used for this purpose. Verstraete et al. sized a LH_2 integral double-walled tank with Al 2219 walls and vacuum DAM/DSN MLI insulation for a 32-passenger regional aircraft (2100 km design range, cruise Mach of 0.65, cruise altitude of 9140 m). A 3 m diameter fuselage is considered, with a single LH_2 tank installed in the rear part of the fuselage. The venting pressure is set to 1.5 bar, while a layer density of 20 layers/cm is considered. The tank is filled by hydrogen up to 90% of the tank volume, leading to ~66.5 kg/m^3 liquid hydrogen storage density at 1.5 bar pressure. Gravimetric storage density ρ_{grav} is defined by the authors as follows:

$$\rho_{grav} = \frac{m_{LH2}}{m_{tank} + m_{LH2}}$$

With these inputs, Verstraete et al. [65] estimate a gravimetric storage density of 67.5%, a tank length of 3.74 m, and a weight of 555 kg with 0.5 cm insulation thickness (10 MLI layers). With the implemented model, tank length is correctly predicted as 3.74 m, while tank weight is predicted as 1045 kg, leading to 52.4% gravimetric storage density. The reason for the difference in weight estimation is the high weight of the two endcaps in the considered tank, as seen in the right chart of Figure 40. This is expected to be substantially heavier in comparison to the composite fairing and aluminum honeycomb proposed by Verstraete et al. [60] (left of Figure 40).

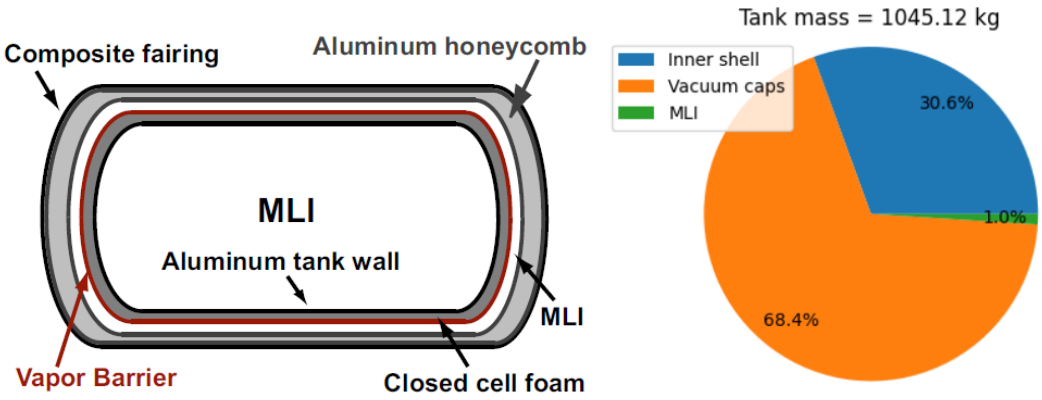

Figure 40 – Left: Tank configuration selected by Verstraete et al. Right: Weight breakdown of liquid hydrogen tank obtained with the implemented model. Source: [65] + Own elaboration.

8.3 OPERATIONAL EMPTY WEIGHT CALCULATION METHODOLOGY

8.3.1 SOFC SYSTEM WEIGHT CALCULATION METHODOLOGY

The SOFC system weight calculation methodology has been derived based on the methodology proposed by Datta [5] for PEMFC systems for VTOL applications. This methodology was implemented in Python and verified and validated against experimental data, as discussed in the following.

There is an important caveat which concerns the validation of the weight estimation results. The work by Udomsilp et al. [47] does not provide specific data about the weight of the metal-supported SOFC modelled in this work. Significant power density differences exist between different SOFC types, which may differ based on the interface between the reactants that can be tubular/planar, anode-supported/electrolyte-supported, etc.… (see section *Solid Oxide Fuel Cells* for more information). No clear indications on which technology is the most promising exist yet. As SOFC technology has been mainly considered for ground applications where system mass is not a design target, weight breakdown data of SOFC stack is not widely available in public literature. The development of SOFCs for aviation applications, in which high power density is nearly as important as high efficiency, has not been extensively pursued yet, as for example PEMFC development for aviation is. For this reason, component weight optimization has not been addressed yet for this technology, apart from a few cases (e.g., Udomsilp et al. [47] with metal-supported SOFC, Cable et al. [46] with bi-electrode supported SOFC). To further highlight the limitations preventing a thorough validation of SOFC weight estimation, it is worth underlining that there are no data available in the literature for aerospace graded SOFC concepts of the MW-power level (aircraft use). This means that the validation of the model considering >TRL4 scaled technologies is not possible, thus reducing the reliability of weight estimation results. Therefore, a one-to-one validation of the

weight estimation for the metal-supported SOFC modelled by Udomsilp et al. [47] and the implemented SOFC model in this work is not possible. Data from literature on other planar SOFC developments are instead used to compare weight breakdowns and trends, and then assess the reliability of the results.

The work by Steffen, Freeh, and Larosiliere [43] on SOFC-GT hybrid cycle technology for auxiliary aircraft power, which includes data about weight breakdown both at SOFC cell level and APU system-level, is used for verification and validation of the SOFC cell mass estimation methodology. To this end, a set of reference design values from the paper are selected. In this paper, a 440 kW Jet-A-fuelled SOFC-GT APU for a 300 passenger commercial transport aircraft with EIS in 2015 is studied, considering 2 different designs of planar, anode-supported stacks with metallic interconnects.

Steffen, Freeh, and Larosiliere [43] consider a 170-cell, 324-cm^2 stack producing 24 kW net electrical power. A cell-level weight breakdown is presented by the authors, for a cell operating at 0.747 V, 0.583 A/cm^2 current density, with 324-cm^2 surface area. The results are shown in Figure 41 (top figures). The top left case represents a planar anode-supported SOFC with metal interconnects, while the top right case represents a planar anode-supported SOFC with corrugated support anode (gas channels on the anode side instead of the interconnect) and metallic foil interconnect. The differences in cell weight distribution and final cell weight (right concept is almost half as heavy as left concept) highlight the difficulties in development of generalized weight estimation methods for SOFCs.

Cell-level weight calculations are performed with the model implemented in this work, representing the metal-supported SOFC by Udomsilp et al. [47], with inputs from Table 9, and for the same cell design point as Steffen, Freeh, and Larosiliere [43]. The results are compared in Figure 41. As apparent from the weight breakdown, for a metal-supported SOFC with metallic interconnect (top left chart and that at the bottom), the interconnect represents around 75-80% of the weight. Anode support weight is not accounted in the developed model, as a metal-supported SOFC is considered. Anode and cathode weights are thus of a similar order of magnitude, with slightly higher anode weight due to the use of high-density Ni/GDC as material. Cell weight is substantially lower in the metal-supported SOFC than in the anode-supported SOFC, as the metal-supported SOFC technology has been developed considering weight minimization as main goal. Overall, the weight breakdown predicted by the implemented model qualitatively and quantitatively reproduces the weight distribution at cell level of a planar metal-supported SOFC.

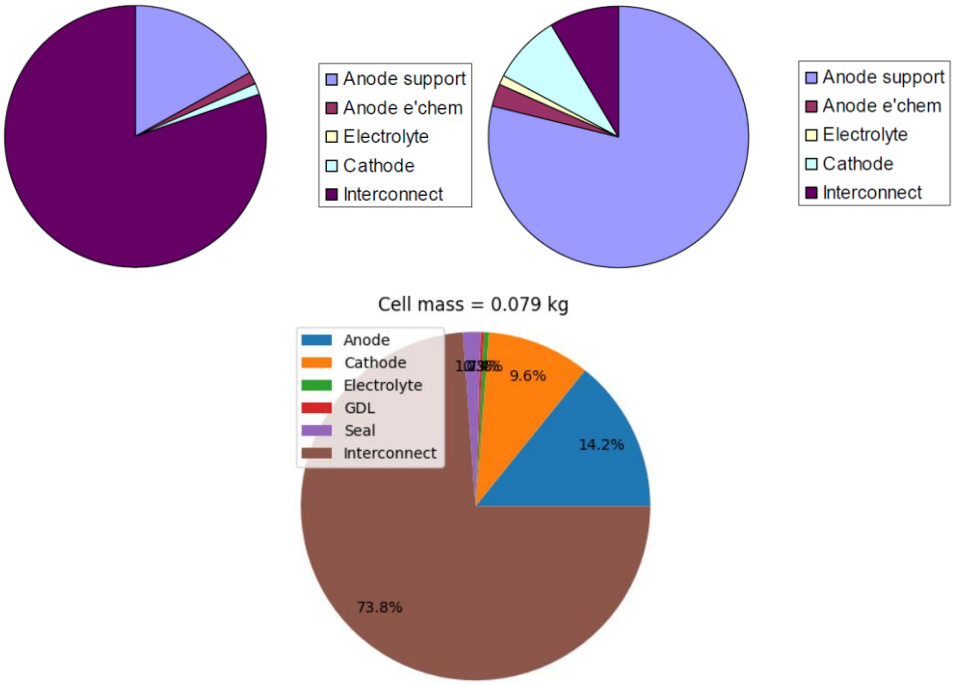

Figure 41 – SOFC cell weight breakdown for a planar metal-supported SOFC with metallic interconnect (top left, from Steffen, Freeh and Larosiliere [43], $m_{cell} = 0.502\ kg$), planar anode-supported SOFC with corrugated support anode (top right, from Steffen, Freeh and Larosiliere [43], $m_{cell} = 0.269\ kg$), and planar metal-supported SOFC from Udomsilp et al. [47] (bottom, modelled in this work, $m_{cell} = 0.079\ kg$).

At SOFC stack level, in the work by Steffen, Freeh, and Larosiliere [43], twelve stacks are considered, leading to 240 kW of total power. The SOFC operates at 700°C, 2.08 bar, 85% fuel (Jet-A) utilization, 127 V at stack level, and 189 A system current. At this operating condition, 62% system efficiency and 0.266 kW/kg specific power at SOFC stack level are obtained ($m_{stack} = 75.2\ kg$). This information is compared with the prediction obtained for the same inputs using the developed methodology. The following results are obtained for the stack mass and power density, while the corresponding weight breakdown is shown in Figure 42:

$$m_{stack} = 21.6\ kg$$

$$\dot{w}_{stack} = 1.11\,\frac{kW}{kg}$$

As expected, stack power density is substantially higher for the metal-supported SOFC by Udomsilp et al. [47], as this solution was designed to achieve weight minimization. At the same time, a 15-year technology gap exists between both the work of Udomsilp et al. and that of Steffen, Freeh, and Larosiliere.

Regarding the weight breakdown shown in the left of Figure 42, only one similar study has been found that provides stack-level SOFC weight breakdown. Further, weight breakdown depends on the number of cells per stack, as the higher the number of cells, the higher the fraction of weight of the cells in the stack. For these reasons, data from SOFC stack mass breakdown from Collins and McLarty [21] (including vessel and insulation weight in this case), and data from PEMFC stack mass breakdown from Sharma and Pandey [91] are used for comparison, assuming a certain degree of similarity for a qualitative comparison. As seen in the right of Figure 42, bipolar plates dominate PEMFC weight. The same applies to the metal-supported 170-cell SOFC stack, where 46% of total weight corresponds to the bipolar plates. Anodes and cathodes are heavier, due to their ceramic substrate. End plates are substantially heavier, due to the requirement to withstand high operating temperatures. Regarding SOFC weight breakdown, when subtracting insulation and vessel weight from the results by Collins and McLarty [21], interconnect weight is 68% of stack weight, while cell and seal weight are 28.7% and 2.9%, respectively. Collins and McLarty [21] do not consider current collectors, insulating layers, end plates and fasteners in their estimation, making a direct quantitative comparison not possible. Nevertheless, the data of Collins and McLarty are qualitatively in line with the obtained results, where 46% of the weight belongs to the interconnects, 15.2% to the cell, and 1% to the seals. Overall, the stack weight breakdown estimated by the implemented model matches the expected trends based on the information available in the literature.

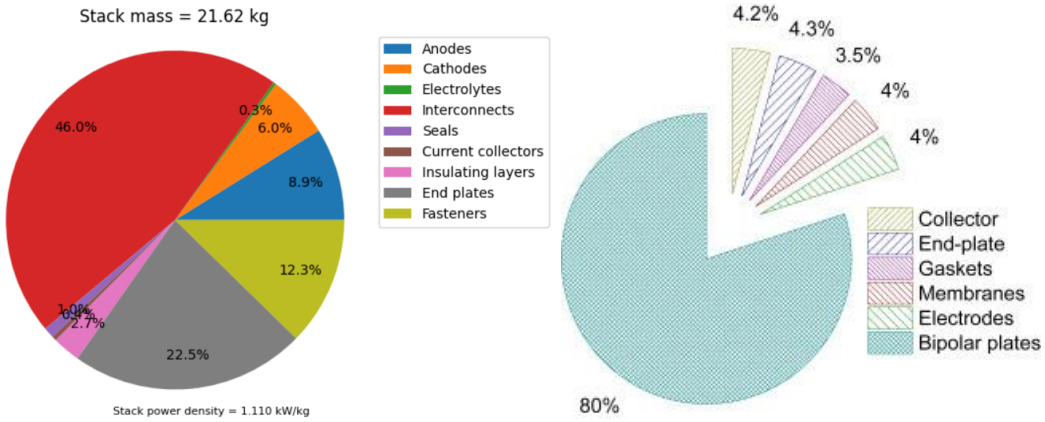

Component	Volume (cm^3)	Density ($kg \cdot m^{-3}$)	Mass (g)	Mass (%)
Interconnect	2.82	7700	21.7	52.1
Seal (×2)	0.38	1200	0.91	2.2
SOFC	1.50	6000	9.1	21.9
Insulation	16.87	64	1.1	2.6
Vessel	4.9	1800	8.8	21.2
Total			41.6	

Figure 42 – Top left: Metal-supported SOFC stack weight breakdown estimated based on data from Steffen, Freeh, and Larosiliere [43]. Top right: Typical weight breakdown of PEMFC, from Sharma and Pandey [91]. Bottom: SOFC stack component mass fractions, from Collins and McLarty [21].

The system weight estimation method is validated based on the results from Braun et al. [16] for a 300-kW Jet-A-fueled metal-supported SOFC APU system, shown in Figure 3. The BoP presented by Braun et al. [16] consists of a fuel processing subsystem (fuel pump, desulphurizer, autothermal reformer, air blower, fuel HX), turbomachinery, a pressure vessel, and a power conditioning system (PCS, consisting of a DC/DC converter). The BoP requirements of LH_2-fuelled SOFC-GT-Battery hybrid systems are substantially different to that of Jet-A-fueled SOFC systems, as the air compression is mainly performed by the gas turbine, and thermal management is simplified by injecting the exhausts into the combustion chamber of the gas turbine. This effectively leads to a significant reduction in SOFC BoP weight, power requirements, and complexity. Therefore, a one-to-one comparison with the data of Braun et al. is not possible. Nevertheless, this data can be used for a comparative validation based on the share of each component in SOFC system weight, and to assess where major BoP weight savings are enabled by the integration with the gas turbine.

The comparison of the results from the implemented model and data from Braun et al. [16] is shown in Figure 43, considering the sizing of the SOFC stack for a 125 kW ground power application using 20 x 30 cm^2 thin cells. Total SOFC system mass from the calculations of Braun et al. is ~605 kg. The SOFC operates at 3 atm, 615°C, and 80% fuel utilization. The air stoichiometry factor is not explicitly indicated. The authors only mention that "a substantial amount of excess air is supplied to the SOFC to maintain the stack operating temperature" [16]. Based on this indication and typical operating conditions of SOFC, an air stoichiometry factor of 5 is assumed. 45% system-level efficiency is achieved at ground conditions (250 kW power from two stacks), and 64% at cruise conditions (operation at part load). Operation of each cell at 0.6 V is assumed. Considering that the design condition leads to a power density of 0.25 W/cm^2, this implies that current density is 0.417 A/cm^2, leading to an operating current of 250 A. This implies that, for 125 kW, operating voltage is 500 V, implying that 834 cells per stack are used.

The weight breakdown of the SOFC system, sized based on the assumptions above, is shown on the left of Figure 43. On the right, the weight breakdown by Braun et al. [16] is presented. Several conclusions can be drawn:

- As expected, stack mass is the major element contributing to SOFC system weight. Stack weight is 169.4 kg in the work by Braun et al. [16], while the estimated value in this work is 143.9 kg (0.87 kW/kg). The results are similar, as expected because metal-supported SOFC stacks are considered in both works. The 15% weight reduction estimated in the present work can be explained from the improvement in SOFC structure introduced by Udomsilp et al. [47].
- The weight fraction of the DC/DC converter (power conditioning system, PCS, in Braun et al. [16]) is higher in the SOFC system proposed in this work, as expected based on the overall lower SOFC system weight. Its mass is 60.5 kg for Braun et al. [16] (2.07 kW/kg) while 50 kg in the present work (2.5 kW/kg). This higher power density is deemed reasonable based on the technological development arguably occurred from 2009.
- Turbomachinery weight is substantially different in the two works (115 kg for Braun et al. [16], 13.5 kg for the present work), as Braun et al. considered a turbocharger architecture in which all required pressurization is performed by a standalone centrifugal compressor, while the SOFC compressor in this work is used only to overcome the SOFC system pressure losses.
- No fuel processing system or piping is considered in the present work.
- No heat exchanger was considered in the work by Braun et al. [16]. In this work, assuming that the air is preheated by 100°C, the heat exchanger accounts for 2.7% of the system weight.
- Regarding pressure vessel weight estimation, mass estimation is lower due to the larger size of the pressure vessel in the work by Braun et al. [16].

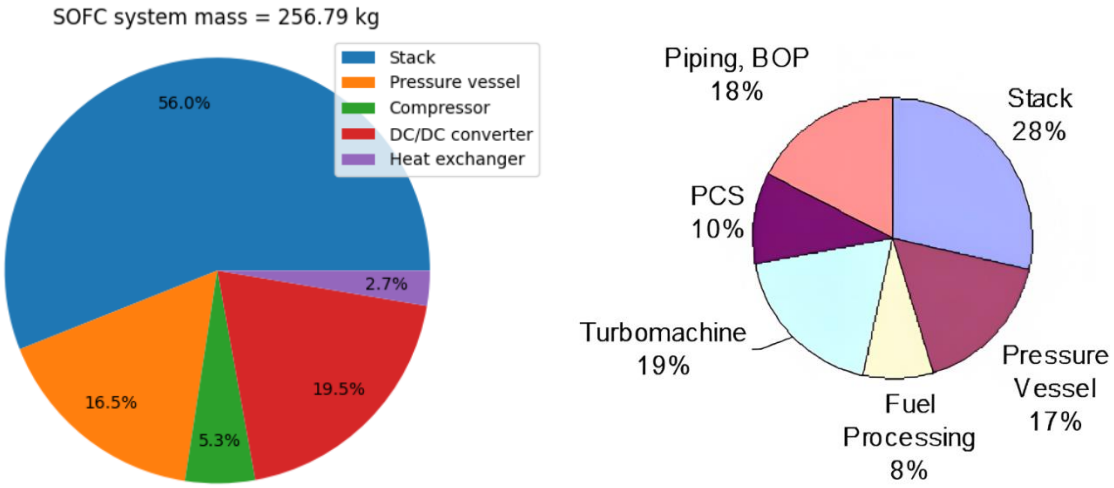

Figure 43 – Left: SOFC system weight estimation with the implemented model ($m_{system} \approx 256.8\ kg$, 0.49 kW/kg power density). Right: Weight distribution of 300 kW (2 x 150 kW) lightweight metal-supported SOFC system for APU applications, considering 2015 technology level, from Braun, Gummalla and Yamanis [16] ($m_{system} \approx 605\ kg$, 0.21 kW</kg power density).

The study on SOFC-GT APU for aircraft by Tornabene et al. [42], as a continuation of the work by Steffen, Freeh, and Larosiliere [43], refers to a system-level power density of 0.315 kW/kg. The study on SOFC APU by Whyatt and Chick [14] considers the Delphi Gen4 100-cell planar SOFC stack, with 1.75 times the power density of 2012-state-of-the-art SOFCs, leading to 0.292 kW/kg system-level power density for a 972-kW system. In both cases, system-level power density is around 0.3 kW/kg (0.42 kW/kg is obtained in the present work), and SOFC stack weight contributes to around 75% of system mass (48% in the present work). Further studies considering the SOFC-GT system as main powertrain were developed by Bradley and Droney [92], indicating 0.356 kW/kg SOFC-system-level power density.

8.3.2 CORRECTED REFERENCE OEW AND ENGINE DRY MASS CALCULATION METHODOLOGY

The methodology described in section *Operational Empty Weight calculation methodology* for computation of $OEW_{ref,corrected}$ is validated against the data collected for the aircraft presented in the market study described in *APPENDIX I – Tables of market study of regional aircraft*. The results of the validation study are presented in Table 14. General agreement in the prediction of engine mass is observed. The error is less than 10% in most cases. Further, the most similar aircraft to the one considered in this work, the deHavilland Dash 8 Q300, shows mass estimation error below 2%.

Table 14 – Validation study for $OEW_{ref,corrected}$ and engine mass estimations. Aircraft data from Table 20.

Aircraft	MTOW (kg)	OEW (kg)	OEW fraction	Engine power (MW)	Engine dry mass (kg)	Estimated engine mass (kg)	% Error engine mass
EMB120	11500	7070	0.61	1.34	390.5	352.9	-9.6
EMB120ER	11990	7580	0.63	1.34	390.5	352.9	-9.6
Fokker 50	20820	12750	0.61	1.87	480.8	458.6	-4.6
Do228	6575	3900	0.59	0.29	170.1	89.6	-47.3
Do328	15660	9420	0.60	1.63	411.4	412.4	+0.2
Dash 8 Q100	15600	10477	0.67	1.6	450.0	406.5	-9.7
Dash 8 Q200	16466	10477	0.64	1.3	417.3	344.3	-17.5
Dash 8	19505	11793	0.60	1.86	450.0	456.7	+1.5

Q300							
Dash 8 Q400	30481	17819	0.58	3.78	716.9	784.3	+9.4

8.3.3 SOFC-GT-BATTERY POWERTRAIN WEIGHT CALCULATION METHODOLOGY

Collins and McLarty [21] assessed the powertrain weight of a LH_2-fuelled all-electric SOFC-GT-Battery powerplant for a retrofitted Boeing 787-8. The authors study assumed fixed in their analysis the aerodynamic parameters and MTOW of the aircraft, which were taken according to the information available for the Boeing 787-8. Information on the thrust, altitude and speed profiles were obtained from Piano-X. The thrust profile was converted into an equivalent electric motor shaft power using propeller efficiency and thrust coefficient. A verification and validation study on powerplant mass estimation using these data is now performed. The simulation is performed considering the following inputs:

- The Boeing 787-8 aircraft is originally equipped with two Rolls Royce Trent 1000 turbofan engines (6033 kg engine dry weight, 280 kN rated standard SL thrust) as powerplant.
- The weight of the Boeing 787-8 reference aircraft is $MTOW = 219539\,kg$, $m_{PL} = 23052\,kg$, $m_{fuel} = 82935\,kg$, $OEW = 119950\,kg$.
- The maximum takeoff shaft power is 43.1 MW, while that at cruise is 28.7 MW. It is assumed that the required power during takeoff is provided by the gas turbine for 4.7 MW, the SOFC for 25.9 MW, and the battery for 12.5 MW.
- The SOFC stack modeled by Collins and McLarty operates at 750°C and $ASR = 0.25\,\Omega cm^2$. The turbocompressor has a pressure ratio of 15, leading to 15 bar operating pressure at sea level, and its efficiency is assumed equal to 80%. Each cell features an active area of 81 cm^2 and is designed for operation at 0.785 V (63.3% operating efficiency) at a current density of 0.6711 A/cm^2. It follows that the cell current is 54.4 A.
- The pressure vessel is 23.8% of the fuel cell stack mass in the work by Collins and McLarty. The same assumption is considered in this simulation.
- Collins and McLarty assumed 0.35 kWh/kg battery energy density. In this work, 0.6 kWh/kg and 0.8 kW/kg are instead considered.
- High-power-density (24 kW/kg), high-efficiency (98.6%) superconducting electric motors are considered by Collins and McLarty. This high efficiency is obtained via cryogenic cooling using liquid hydrogen, adding to the heat exchanger weight. This technical solution is not considered in the present work, due to the low TRL of superconducting technology for aviation. For this reason, 10 kW/kg power density and 96% efficiency are assumed for the electric motors.

The comparison of the model results and those by Collins and McLarty [21] is shown in Figure 44. In both models, the SOFC mass fraction is similar. However, the estimated SOFC weight is higher than that reported by the two authors, namely 29.7 ton vs 26.6 ton. This can be partially explained by the fact current collectors, insulating layers, end plates, and fasteners are accounted while estimating the stack weight, as opposed to Collins and McLarty [21]. The gas turbine mass fraction computed by the authors is similar to that estimated in the present work for the turboprop. Regarding the other components, the heat exchanger mass estimated by the model is substantially different, due to the different heat management concept required by the SOFC in the present model with respect to that in [21]. The propulsor weight is also slightly lower, due to the turboprop producing part of the powertrain thrust. Collins and McLarty do not consider the impact of DC/DC converter and inverter on system mass, which account for 22.8% of total system mass (i.e., 19275 kg). If we neglect the weight of these components, a powertrain mass of 55.2 ton is obtained, which is 3.5% below the value calculated by Collins and McLarty. Considering the substantial differences in the characteristics of the powertrains modelled in the two works, and the similar results obtained for the weight breakdown, the powertrain weight estimation methodology is considered as correctly implemented.

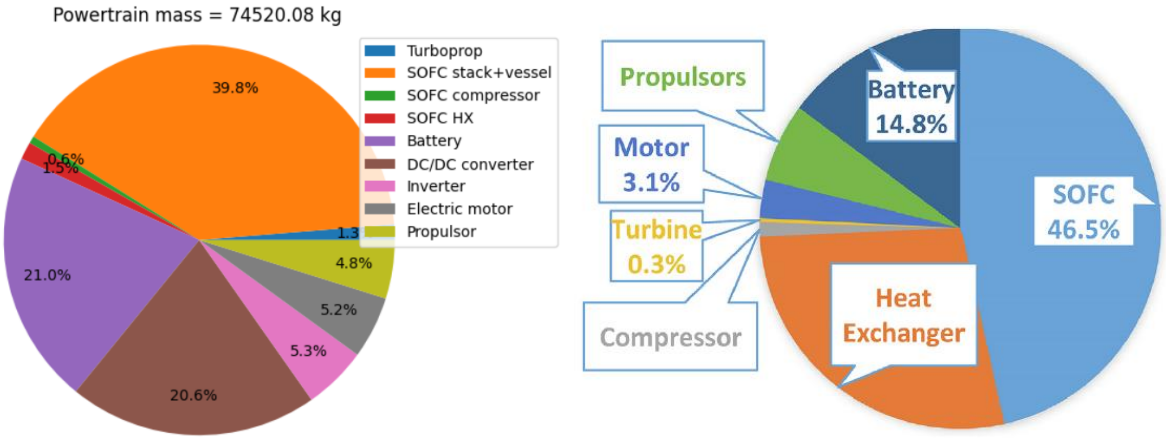

Figure 44 – Left: Estimated powertrain weight breakdown of a SOFC-GT-Battery powertrain for a Boeing 787-8 ($m_{powertrain} = 74520\ kg$, 0.58 kW/kg). Right: Results from Collins and McLarty [21] on the mass contribution estimations of powertrain components for a LH_2-fuelled all-electric SOFC-GT-Battery hybrid powertrain sized for a Boeing 787-8 ($m_{powertrain} = 57209\ kg$).

Once these data about the powertrain are available, it is possible to perform the calculation of the OEW for the B787-8 aircraft using the proposed modified Class I method. The following estimates are obtained:

$$OEW_{ref,corrected} = OEW_{ref} - m_{powertrain,ref} = 119950 - 12066 = 107884\ kg$$

$$m_{powertrain} = 74520\ kg$$

$$m_{structural,extra} \approx 0.01 OEW$$

$$OEW = 183955\ kg$$

The calculated OEW represents a 53% increase compared to the reference OEW of the B787-8 aircraft. This highlights the need of improving the power density of SOFC-GT-Battery powertrains.

9 RESULTS AND DISCUSSION

9.1 SOFC-TURBOPROP PERFORMANCE STUDIES

The performance model of the SOFC-Turboprop system has been implemented in Python. This model is used to perform sensitivity studies on powertrain efficiencies as a function of powertrain design parameters. The reference inputs for the sensitivity analyses are presented in Table 15.

Table 15 – Reference inputs for sensitivity studies on performance of SOFC-Turboprop powertrain.

Parameter	Units	Reference value
Design altitude	m	7620
Design Mach number	-	0.60
$\boldsymbol{\Phi_{design} = \frac{\dot{m}_{H2,GT}}{\dot{m}_{H2,total}}}$	-	0.90
Turboprop shaft power	kW	100
$\boldsymbol{\dot{m}_{air,GT}}$	kg/s	0.5
TIT	K	1400
OPR	-	16
LPC efficiency	-	0.90
HPC efficiency	-	0.88
HPT efficiency	-	0.92
LPT efficiency	-	0.90
Power turbine efficiency	-	0.88
Combustor pressure loss	-	0.98
Combustion efficiency	-	0.995
Nozzle efficiency	-	0.98
Shaft efficiency	-	0.99
SOFC operating temperature	K	923
SOFC fuel utilization	-	0.8
SOFC air stoichiometry factor	-	3.0
SOFC active area	m^2	0.3
SOFC number of cells	-	10

The impact of SOFC operating temperature on powertrain efficiencies is shown in the left plot of Figure 45. As seen in the plot, the higher the SOFC operating temperature, the higher the SOFC efficiency, as well as the equivalent gas turbine efficiency (indicated as GT2 in Figure 45) associated with the SOFC exhausts injected into the gas turbine, due to their higher enthalpy. On the contrary, turboprop thermal efficiency (indicated as GT1 in Figure 45) is not a function of SOFC operating temperature.

The impact of engine OPR on powertrain efficiencies is shown in the right of Figure 45. Higher OPR leads to increase in SOFC efficiency and turboprop thermal efficiency, as expected from thermodynamic cycle analysis. The GT2 efficiency value is around 42% for different values of OPR. The value fluctuation does not represent any existing physical phenomenon within the system. The reason for this fluctuation is numerical limitations of the implementation.

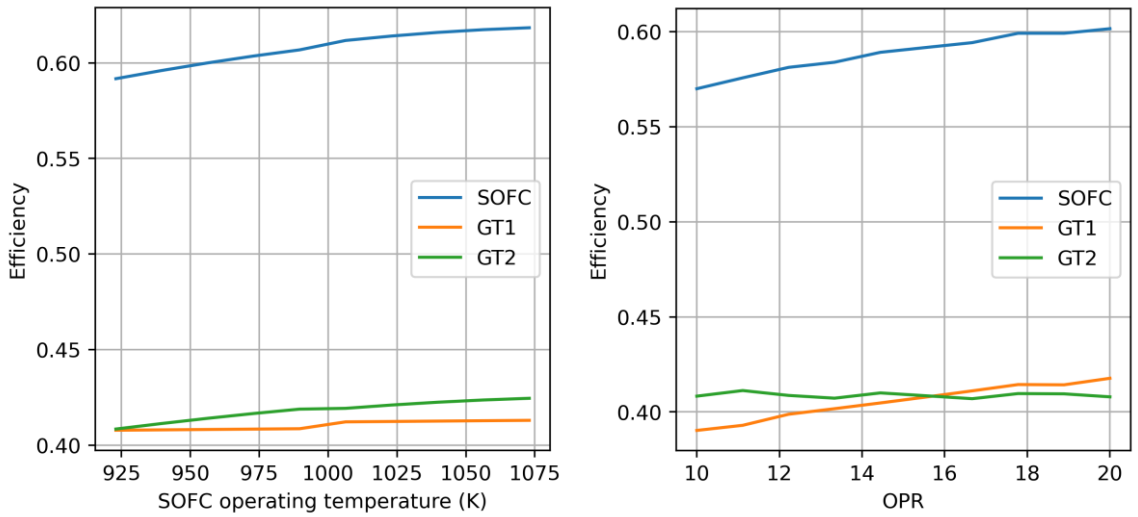

Figure 45 – Left: Impact of SOFC operating temperature on powertrain efficiencies. Right: Impact of gas turbine OPR on powertrain efficiencies.

The impact of SOFC fuel utilization on powertrain efficiencies is shown in the left chart of Figure 46. As expected from the trends in Figure 27, higher fuel utilization leads to a decline in SOFC efficiency. Nevertheless, higher fuel utilization enhances the conversion efficiency associated with SOFC exhaust, leading to an increase in η_{GT2}. For fuel utilization below 0.6, the predicted SOFC efficiency is excessively high, due to limitations of the model calibration.

The impact of SOFC air stoichiometry factor on powertrain efficiencies is shown in the right chart of Figure 46. As illustrated in Figure 25, higher air stoichiometry factor leads to an increase in SOFC efficiency. Furthermore, it also leads to a slight increase in turboprop efficiency, as well as an increase in the so-called η_{GT2}.

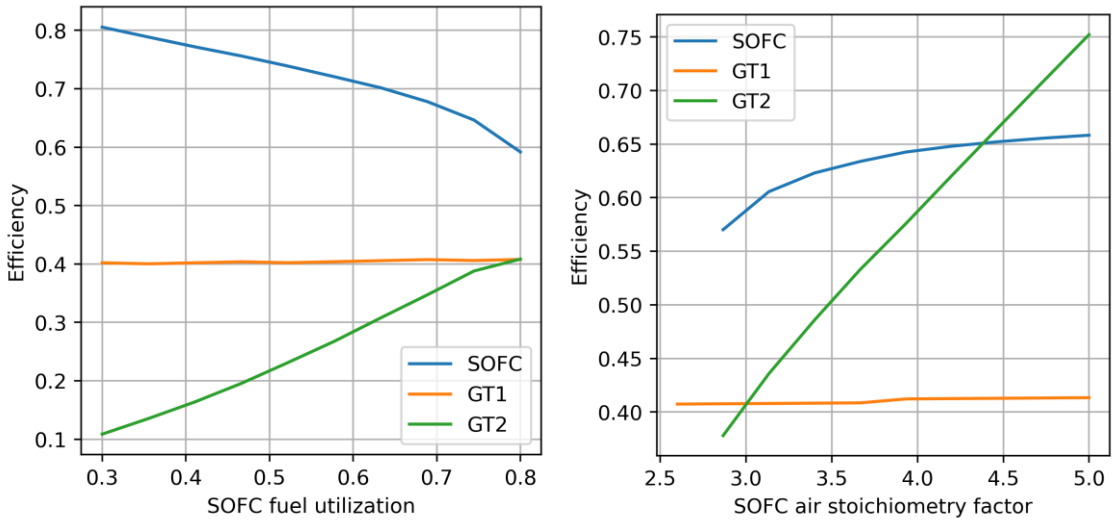

Figure 46 – Left: Powertrain efficiencies as function of SOFC fuel utilization. Right: Powertrain efficiencies as a function of SOFC air stoichiometric factor.

The impact of a variation in SOFC cell number on powertrain efficiencies is shown in the left chart of Figure 47. In the right chart of the same figure, the effect of SOFC active area variation on powertrain efficiencies is shown. Both quantities have a similar impact on powertrain performance: increase in SOFC and GT2 efficiencies with constant turboprop efficiency. This is because both parameters have similar effects on SOFC sizing and mass flow rates.

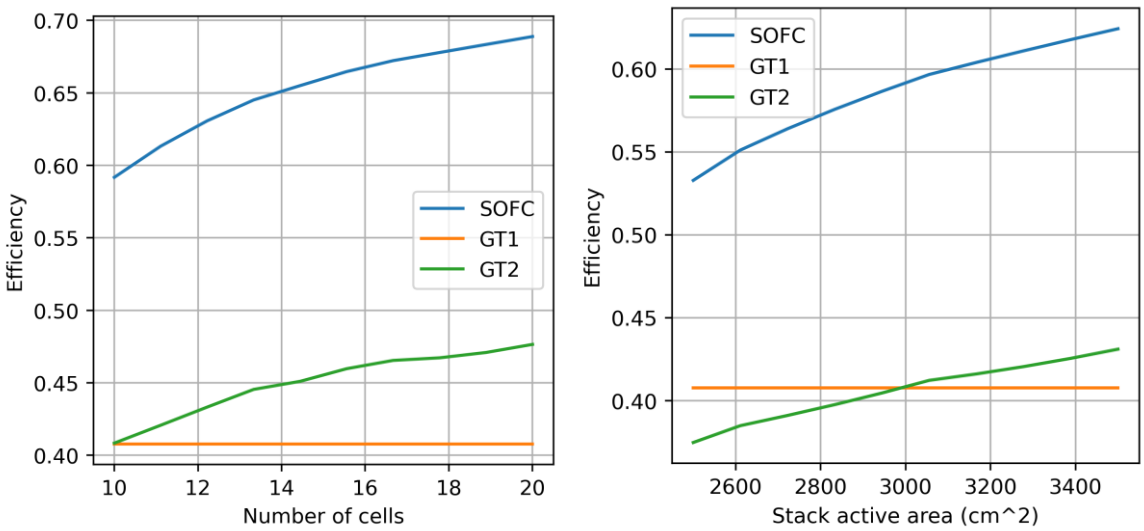

Figure 47 – Left: Powertrain efficiencies as function of SOFC cell number. Right: Powertrain efficiencies as function of SOFC stack active area.

9.2 POWER SIZING METHODOLOGY: SENSITIVITY STUDIES

To gain a better understanding about the design flexibility that the proposed hybrid-electric powertrain brings, as well as the optimal design choices in terms of power distribution (i.e., selection of Φ, Ψ, λ for minimum weight or maximum efficiency), a sensitivity study on the powertrain weight and cruise efficiency as a function of power distribution is performed.

The overall system cruise efficiency is defined as the system output power (propulsive power plus electric payload power) divided by the fuel and battery power inputs:

$$\eta_{cruise,overall} = \frac{P_{useful,out}}{P_{in}} = \left(\frac{P_{p1} + P_{p2} + P_{e4}}{P_{f1} + P_{e2}}\right)_{cruise}$$

A routine has been implemented in Python for the calculation of this quantity as a function of the power distribution parameters. As λ is fixed by the electric payload requirements of the aircraft, assumed as 3% of fuel power P_{f1}, the following expression for λ can be written:

$$\lambda = 0.03 \frac{\Psi}{\eta_V \eta_{SOFC} \eta_{util,SOFC} \eta_{PM1} \eta_{PM2} (1 - \Phi)}$$

With the value of λ fixed as a function of component efficiencies and Φ, Ψ, the sensitivity study is performed as a function of Φ and Ψ. The results are shown in Figure 48. The obtained results are in line with those reported in the literature (e.g., results presented by Hepperle [36]), showing 70-75% overall efficiency for battery-only aircraft, 40-45% overall efficiency for SOFC-only aircraft, and 35-40% for turboprop-only aircraft.

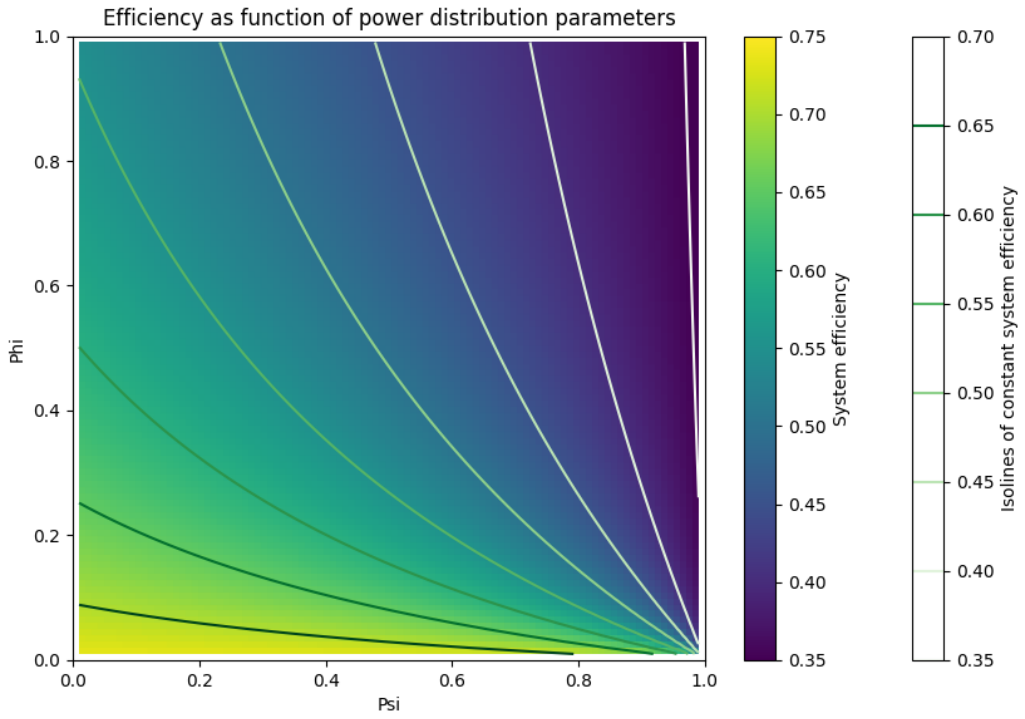

Figure 48 – Overall powertrain cruise efficiency as a function of powertrain sizing parameters.

Several conclusions can be drawn from Figure 48:

- Lower values of Φ (higher SOFC/electric powertrain power fraction) and Ψ (higher battery power fraction) lead to higher system efficiency.
    - The effect of Φ is due to the higher efficiency of the SOFC compared to the gas turbine, as well as the fact that the waste heat, unused hydrogen and byproducts from the SOFC are injected back into the gas turbine engine, leading to higher overall efficiency.
    - The effect of Ψ is due to the 100% efficiency of the electric power provided by the battery, as opposed to the fuel power that needs to be converted thermally (gas turbine) or electrochemically (SOFC) into useful power, with the subsequent significant thermodynamic losses.
- While design points close to $\Phi = 0$ lead to overall system efficiency over 70% for $\Psi < 0.8$, design points close to $\Psi = 0$ result in powertrains with a steeper decrease in efficiency with increasing Φ.
- For $\Phi > 0.6$, the sensitivity of system efficiency to Ψ increases compared to low values of Φ.
- Although highest efficiencies are estimated for low Φ, Ψ, this design decision implies increasing the size of the SOFC and battery with respect to the gas turbine. Due to their substantially lower power density and energy density compared to gas turbine engines, a study at aircraft level is required to determine the optimal design point allowing for the minimization of mission energy consumption. Special caution should be kept with the results for $\Psi_{\text{cruise}} < 1$, as the battery will be sized to supply energy also during cruise, likely leading to decreased payload/range and/or excessive powertrain weight due to the low energy density of state-of-the-art batteries.

High-power gas turbine engines are generally more efficient than low-power gas turbine engines. This impact is not considered in the model. If considered, the system overall efficiency at high Φ and Ψ would be higher than shown in the graph.

Due to the strong impact of choosing $\Psi_{cruise} < 1$ on powertrain weight (sizing of batteries for energy supply during cruise is expected to lead to excessive OEW), the analysis is repeated for varying Φ_{cruise} with $\Psi_{cruise} = 1$, and varying the gas turbine thermal efficiency, SOFC efficiency and SOFC fuel utilization. These results are shown in Figure 49. As expected, lower values of Φ (higher hydrogen flow into the SOFC) lead to higher overall cruise system efficiencies, due to the higher thermal efficiency of the SOFC and the injection of the exhausts, and unused hydrogen into the combustion chamber, further generating power. However, due to the lower power density of the SOFC compared to gas turbine engines, studies at aircraft-level are required to

determine the optimal Φ_{cruise} that minimizes reference mission energy consumption. At the same time, higher SOFC efficiencies and fuel utilization lead to higher $\eta_{cruise,overall}$ at low Φ_{cruise}, while higher GT efficiencies lead to higher $\eta_{cruise,overall}$ at high Φ_{cruise}. The penalty of reduced gas turbine efficiencies on overall system efficiency is higher than that observed for SOFC efficiency. This is because of the fuel cell exhausts and unused hydrogen are injected into the GT combustion chamber, thus generating extra power.

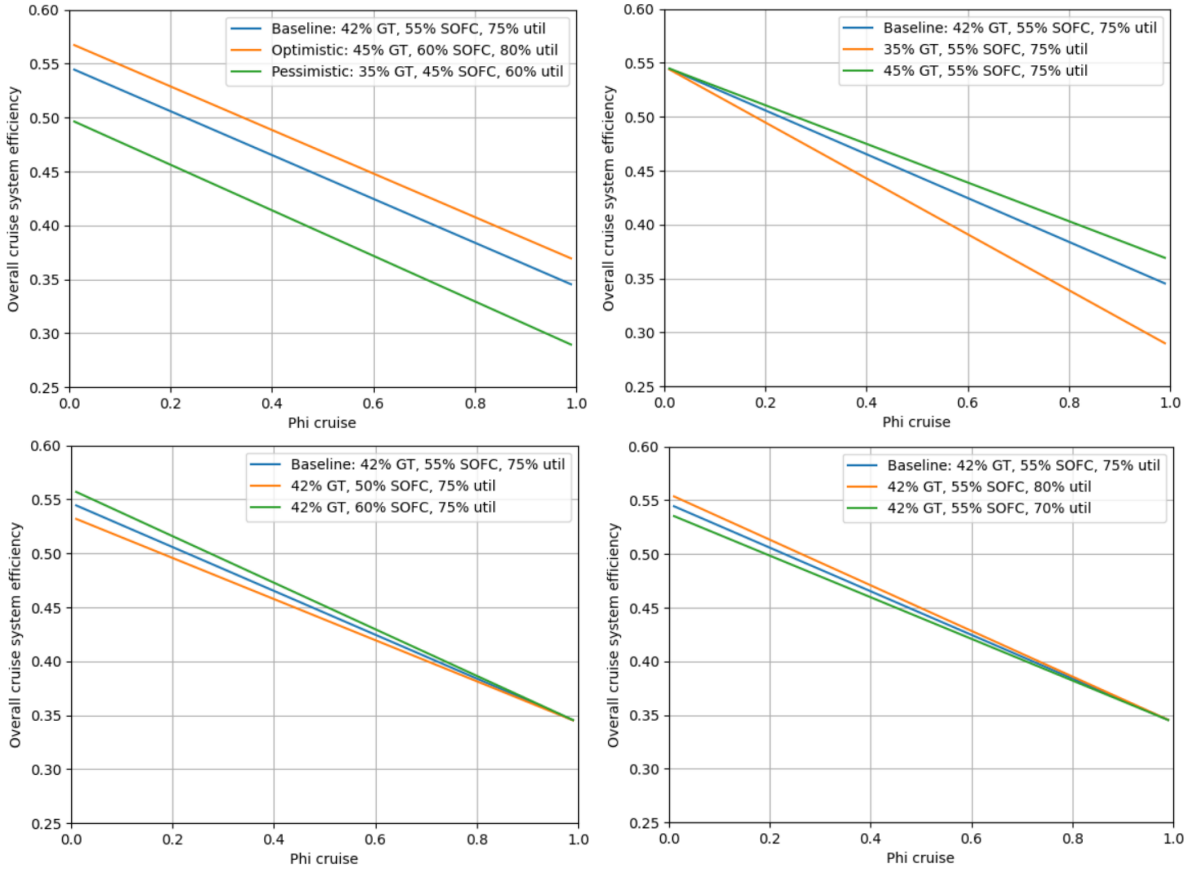

Figure 49 – Overall system cruise efficiency as a function of Φ_{cruise}, GT efficiency, SOFC efficiency and SOFC fuel utilization.

After studying the impact of selection of the power management variables on powertrain efficiency, the impact in terms of powertrain weight is studied. The weight of the powertrain is determined using reference state-of-the-art power density values (w_i) for each component and considering its characteristic power:

$$m_{powertrain} = w_{SOFC}P_{e1} + w_{turboprop(GT+Prop)}P_{s1} + w_{BAT}P_{e2} + w_{PM1}P_{e3} + w_{PM2}P_{e3} + w_{EM+P2}P_{s2}$$

This weight estimation is preliminary, as a more accurate weight estimation methodology will be applied later for aircraft OEW assessment. The following values of component power density are assumed:

$$w_{SOFC} = 0.4\,\frac{kg}{kW}$$ [2]

$$w_{turboprop(GT+Prop)} = 0.231\,\frac{kg}{kW}$$ [3]

$$w_{PM1} = w_{PM2} = 0.02\,\frac{kg}{kW}$$

$$w_{EM+P2} = 0.1\,\frac{kg}{kW}$$ [4]

[2] NASA high power density solid oxide fuel cell [99]
[3] Based on the data by Gudmunsson [98]
[4] Wright Electric

To size each component in terms of power, the component-oriented constraint diagrams are used. Due to the preliminary character of this analysis, and based on the constraint diagram shown in Figure 36 for the baseline aircraft, the design point for each component is selected by considering the wing loading corresponding to stall speed, and by selecting the minimum power of each component that fulfils the power loading requirement for the given wing loading.

With this approach, the design point of each component is determined for each combination of power distribution parameters Φ and Ψ for each operating condition, with λ fixed as for efficiency calculation.

As seen in Figure 36, the minimum power of the turboprop engine is closely limited by cruise speed, rate of climb, and takeoff distance. Therefore, the tuning of Φ and/or Ψ only for a single operating condition (cruise, climb, takeoff) is not expected to enable the downsizing of the turboprop engine. Further, when considering $\Psi_{cruise} < 1$, the battery is consuming energy during the cruise portion of the flight. In that case, the battery weight will be determined by its energy density, and not by its power density. The same condition is likely to apply to the climb phase. If battery power is not used for climb or cruise, based on the results in Figure 36 and Figure 37, it is unlikely that including a battery for assisting takeoff will lead to SOFC and turboprop downsizing. As constraint analysis is a tool for power sizing, information on aircraft mission energy consumption is not yet available. Thus, it is not possible to accurately estimate required battery weight for $\Psi_{climb} < 1$ and $\Psi_{cruise} < 1$. Therefore, the analysis is performed considering $\Psi_{cruise} = \Psi_{climb} = \Psi_{takeoff} = 1$.

Considering that Ψ and λ are fixed in the problem, to reduce further the degrees of freedom of the analysis, Φ_{climb} is taken equal to $\Phi_{takeoff}$. In this way, the impact of SOFC integration on the overall powertrain power density is assessed for different power management strategies. $MTOW = 15\ ton = 147\ kN$ is selected as reference weight.

The variation of the minimum $\frac{P}{W}$ ratio of the SOFC and turboprop for the $\left(\frac{W}{S}\right)_{stall}$ wing loading as a function of Φ_{cruise} and $\Phi_{TO} = \Phi_{climb}$ is shown in Figure 50. As expected, higher values of Φ lead to higher turboprop power requirements, while lower values lead to higher SOFC power requirements. When $\Phi_{cruise} \approx \Phi_{TO,climb}$, the power loading of each component tends to be lower.

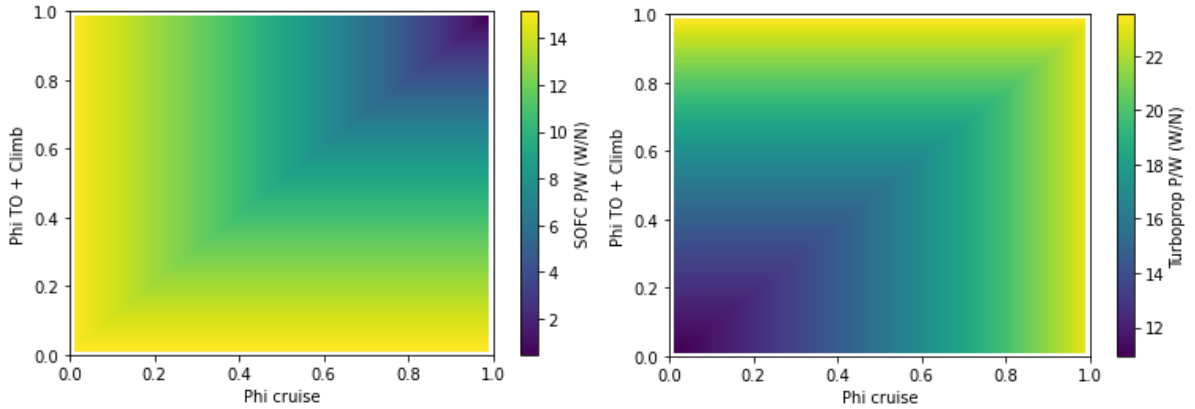

Figure 50 – Power loading of SOFC and turboprop as function of SOFC input power fraction during takeoff, climb and cruise. Design condition with no batteries ($\Psi = 1$) and λ fixed by design conditions. Input parameters summarized in Table 4, Table 5.

The powertrain weight variation as a function of Φ_{cruise} and $\Phi_{TO} = \Phi_{climb}$ is shown in Figure 51. The following considerations can be made:

- As expected, due to the higher power density of GTs, minimum powertrain weight is obtained for high values of Φ for takeoff, climb and landing.
- This analysis is based on the gas-turbine-only constraint diagram shown in Figure 36, where the cruise, takeoff and climb constraints are all very close to be the limiting constraint, thus requiring SOFC power in all conditions to achieve gas turbine downsizing. For this reason, there is a region of the design space where the powertrain weight is lower also when around 50% of power is supplied by the SOFC, as SOFC helps reducing the power required to the GT in takeoff, climb and cruise.

Furthermore, as the SOFC is sized based on the power required during takeoff, it is also convenient to use it to provide power during cruise.

- When relaxing the takeoff distance and ROC requirements (e.g., from 1300 m to 1500 m, and from 2000 ft/min to 1500 ft/min), the impact of $\Phi_{TO,climb}$ on powertrain weight decreases, leading to the line of optimal powertrain design (in terms of minimum weight) to be displaced towards higher values of Φ_{cruise} for the same $\Phi_{TO,climb}$. This is seen by comparing subplots in Figure 51 at the center and the left-hand side of the figure. As performance requirements are relaxed, the required propulsive power is reduced, thus leading to lower system weight, see the wider blue area in the subplot at the center compared to that in the chart on the left.
- When relaxing the maximum speed and cruise speed requirements (e.g., maximum speed from M=0.6 to M=0.55, cruise speed from M=0.55 to M=0.50), the impact of Φ_{cruise} on powertrain weight decreases, as the SOFC addition does not allow for GT downsizing, as its power is constrained by takeoff distance and ROC. This is shown by comparing the chart on the left with that on the right of Figure 51. As performance requirements are relaxed, the required propulsive power is reduced, thus leading to lower system weight, see the wider blue area in the right chart compared to that in the left graph.

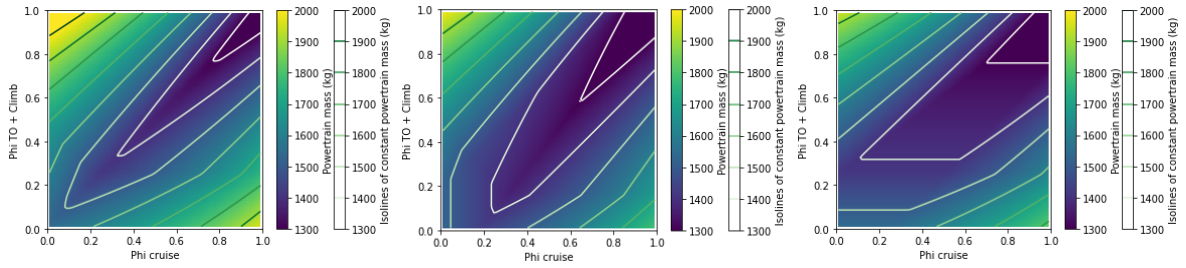

Figure 51 – Powertrain mass as function of Φ during takeoff, climb and cruise. Design condition with no batteries ($\Psi = 1$) and λ fixed by design conditions. Input parameters summarized in Table 4, Table 5. Left: Baseline performance. Center: Relaxed takeoff distance (1500 m) and ROC (1500 ft/min). Right: Relaxed maximum cruise speed (M=0.5) and normal cruise speed (M=0.45).

The variation of the weight of each individual component of the powertrain as a function of Φ_{cruise} and $\Phi_{TO} = \Phi_{climb}$ is shown in Figure 52.

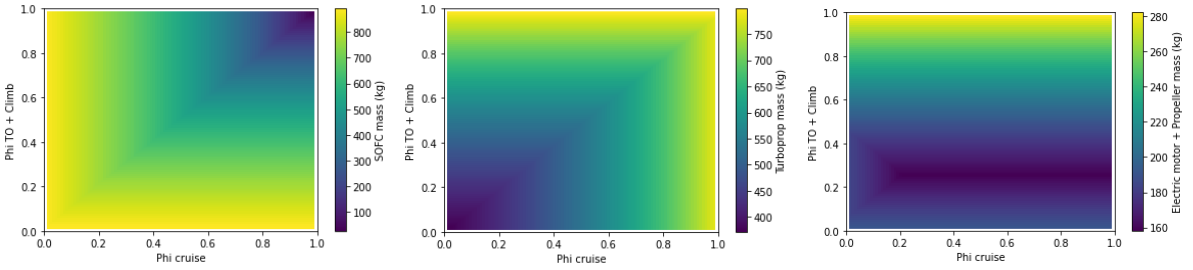

Figure 52 – Weight of the main components of the powertrain as function of Φ during takeoff, climb and cruise. Design condition with no batteries ($\Psi = 1$) and λ fixed by design conditions. Input parameters summarized in Table 4, Table 5.

From Figure 51, it can be concluded that the optimal design of the system strongly depends on the high-level performance requirements of the aircraft. Considering the current state of the art, the SOFC should be operated at constant power as much as possible, due to its poor transient performance and its susceptibility to thermal cycling. This condition would imply that Φ_{cruise} and $\Phi_{TO,climb}$ are not independent variables. Thus, the design space reduces to a single line in the Φ_{cruise} vs $\Phi_{TO,climb}$ plane.

Considering a pessimistic estimation of SOFC power density ($w_{SOFC,pessimistic} = 5\frac{kg}{kW}$), the overall powertrain weight increases substantially for $\Phi_i < 1$, see Figure 53. With this assumption, the powertrain weight becomes unacceptably high for values of $\Phi_i < 1$. Therefore, high SOFC power density is a requirement for the technical and economic feasibility of SOFC-GT-Battery hybrid electric powertrains for aircraft.

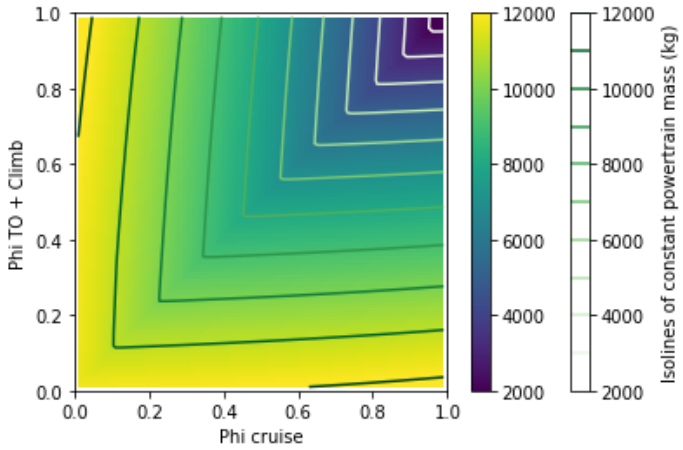

Figure 53 – Powertrain mass as function of SOFC input power fraction during takeoff, climb and cruise, for pessimistic SOFC power density estimation. Design condition with no batteries ($\Psi = 1$) and λ fixed by design conditions. Input parameters summarized in Table 4, Table 5.

Future work should include a more thorough sensitivity study considering the independent variations of the 9 power management variables for the 3 operating conditions (Φ_{cruise}, Φ_{climb}, $\Phi_{takeoff}$, Ψ_{cruise}, Ψ_{climb}, $\Psi_{takeoff}$, λ_{cruise}, λ_{climb}, $\lambda_{takeoff}$).

9.3 COMBINATION OF EFFICIENCY AND WEIGHT SENSITIVITY ANALYSES: PARETO FRONT OF SYSTEM CRUISE EFFICIENCY AND WEIGHT

The results from the previous section for $\Psi = 1$ and fixed λ can be combined to understand the impact of Φ_{cruise} on system efficiency and weight. As seen in Figure 51, selecting $\Phi_{cruise} = \Phi_{TO,climb}$ for the performance design specifications in Table 22 leads to solutions with minimum powertrain weight. Therefore, this design choice is used hereafter. The values of $\eta_{cruise,overall}$ and $m_{powertrain}$ are obtained for each value of Φ, and they are plotted together in Figure 54. As expected, higher powertrain mass (higher SOFC contribution) corresponds to higher overall efficiency. The change in slope observed in the curve around 1415 kg can be explained by the fact that the active set of design constraint changes for the value of Φ that leads to this powertrain mass.

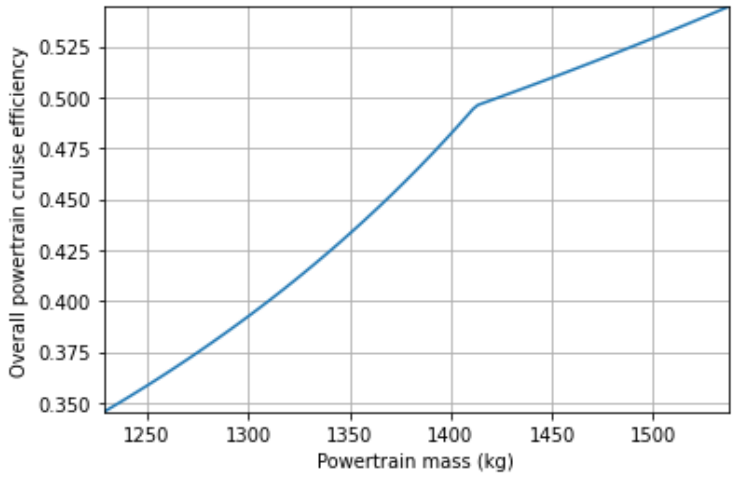

Figure 54 – Cruise overall efficiency and powertrain weight for different values of Φ. Input parameters summarized in Table 4, Table 5.

The trends shown in Figure 52 and Figure 54 are compared with the weight and efficiency trends obtained by Seitz et al. [6], shown in Figure 55. As seen in the figure below, the higher the power fraction produced by the fuel cell, the higher the powertrain mass, and the higher the propulsion system efficiency. This trend is correctly predicted by the implemented model.

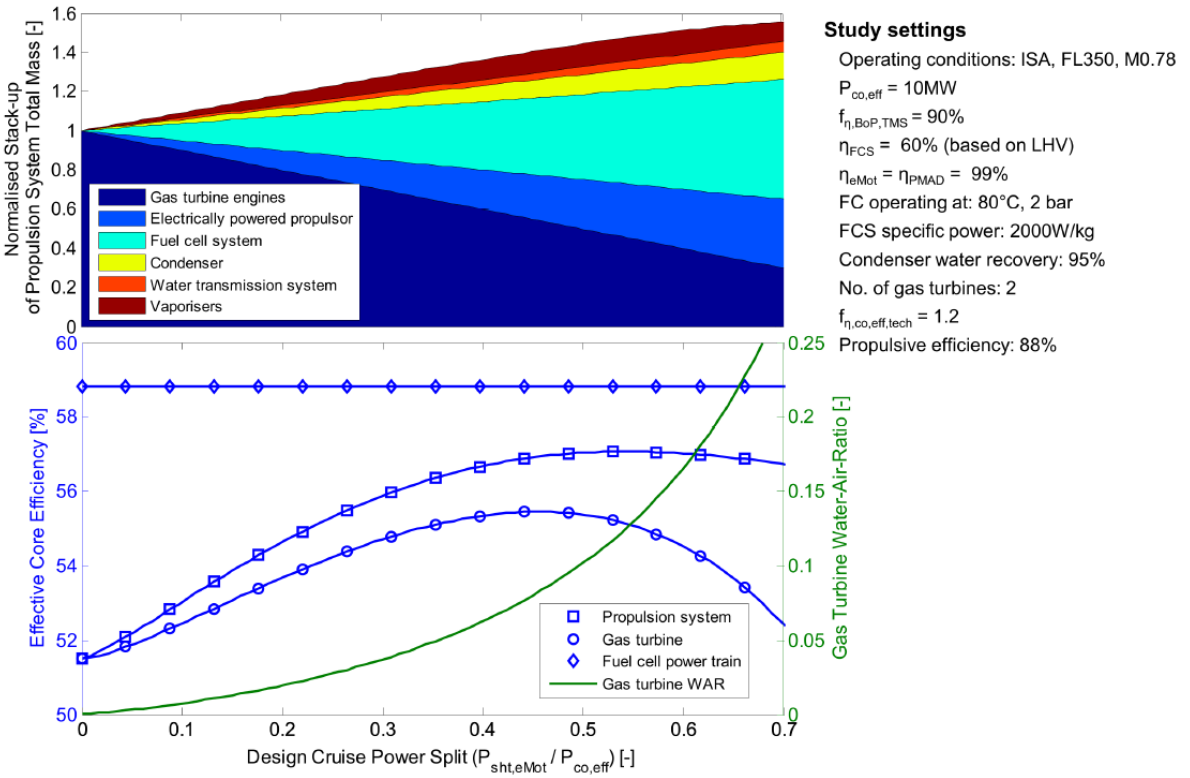

Figure 55 – Propulsion system mass breakdown (top) and propulsion system efficiency (bottom) as a function of design cruise power split $\left(\frac{P_{electric\ motor}}{P_{total}}\right)$ *for the fuel cell-GT hybrid powertrain studied by Seitz et al., see the system architecture in Figure 7, and the design and operating conditions shown in the top right of the figure. Source: [6]*

9.4 SENSITIVITY STUDIES ON LIQUID HYDROGEN TANK STORAGE DENSITY

An integral vacuum-MLI-insulated liquid hydrogen tank is integrated into the aircraft. The value of $\rho_{LH2\ storage}$ as a function of fuselage diameter and liquid hydrogen mass requirement is simulated and presented in Figure 56. Maximum fill level of 90%, design pressure of 3 bar, and 10 layers MLI at 20 layers/cm MLI layer density are considered. The value corresponding to the design fuselage diameter and the required liquid hydrogen mass for a given range will be provided as an input to the range equation.

Due to the assumed integration concept, the external tank diameter is equal to fuselage diameter. Thus, an increase in tank volume will be reflected as an increase in tank length, leading to increase in the hydrogen storage density $\rho_{LH2\ storage} = \frac{m_{LH2}}{m_{tank}}$. A linear increase of inner wall mass is observed in the graph at the bottom left of Figure 40. From this graph, it is concluded that tank mass is directly proportional to tank length. Further, a higher diameter implies a higher mass of the semi-spherical end caps of the tank, while increase of liquid hydrogen mass does not impact caps weight, as seen in the bottom center sub-plot of Figure 56. Vacuum shells dominate tank weight according to the weight breakdown in Figure 40, leading to lower $\rho_{LH2\ storage}$ as fuselage diameter increases, thus heavier tanks for equal liquid hydrogen mass with increasing fuselage diameter.

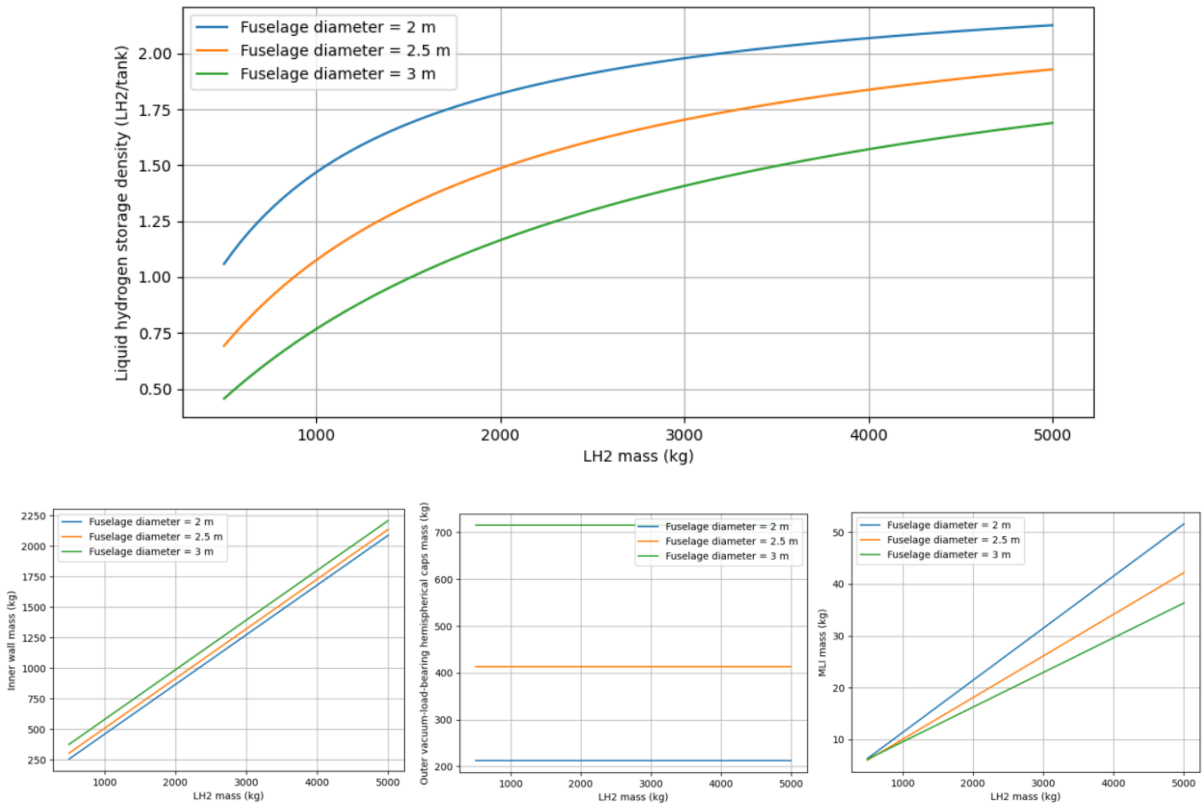

Figure 56 – Liquid hydrogen storage density $\rho_{LH2\ storage}$ as a function of fuselage diameter and liquid hydrogen mass (top), together with LH_2 tank mass breakdown as function liquid hydrogen mass and fuselage diameter (bottom).

9.5 MTOW CALCULATION: CASE STUDY AND SENSITIVITY ANALYSES

The aircraft considered in the first case study for application of the MTOW estimation methodology is the deHavilland Dash 8 Q300, whose data are listed in the tables in *APPENDIX I – Tables of market study of regional aircraft*. The powertrain is sized by selecting $\Phi = 0.5$, $\Psi = 0.9$ and $\lambda = 0.1$ in all the operating conditions. The original aircraft MTOW and weight breakdown is compared to that of the LH_2-fuelled retrofitted aircraft with a SOFC-GT-Battery hybrid electric powertrain, see Figure 57. As expected, aircraft MTOW increases in the retrofitted aircraft, due to the heavy powertrain. Fuel weight is reduced due to the higher propulsion system efficiency, the use of batteries, and the higher LHV of liquid hydrogen compared to Jet A.

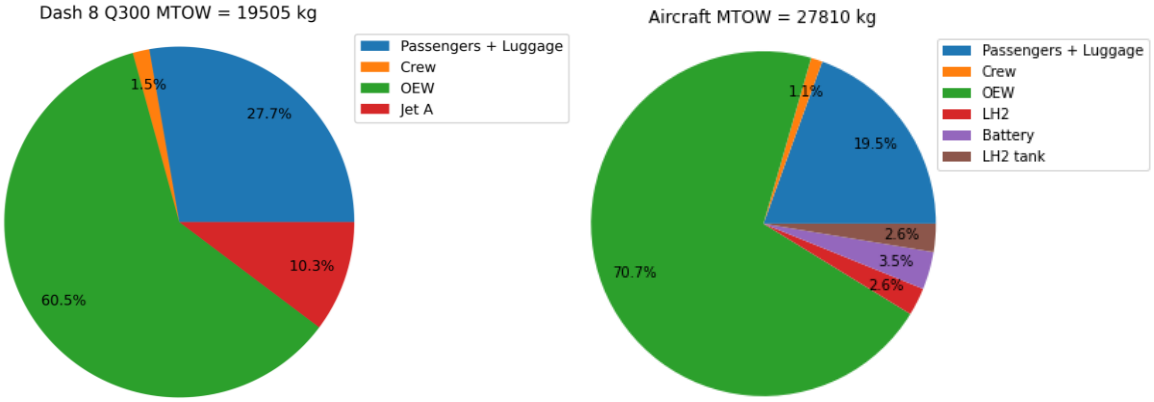

Figure 57 – Comparison between MTOW and weight breakdown from original Dash 8 Q300 aircraft (left) and modified Dash 8 Q300 aircraft with LH_2 fuel and SOFC-GT-Battery hybrid electric powertrain (right).

A sensitivity analysis aimed at assessing the variation of aircraft MTOW as a function of power management parameters Φ and Ψ, when the parameters have the same value during all the flights phases, as well as when the value of Φ_{cruise} and Φ_{TO} are varied independently, is now performed.

The variation of MTOW as a function of Φ and Ψ is shown in Figure 58. Despite the increase in powertrain efficiency for lower Φ and Ψ, as also demonstrated by Figure 48, the weight reduction due to the lower fuel consumption does not offset the increase in MTOW due to the lower power density of the SOFC with respect to the turboprop, and the lower energy density of the battery with respect to liquid hydrogen fuel.

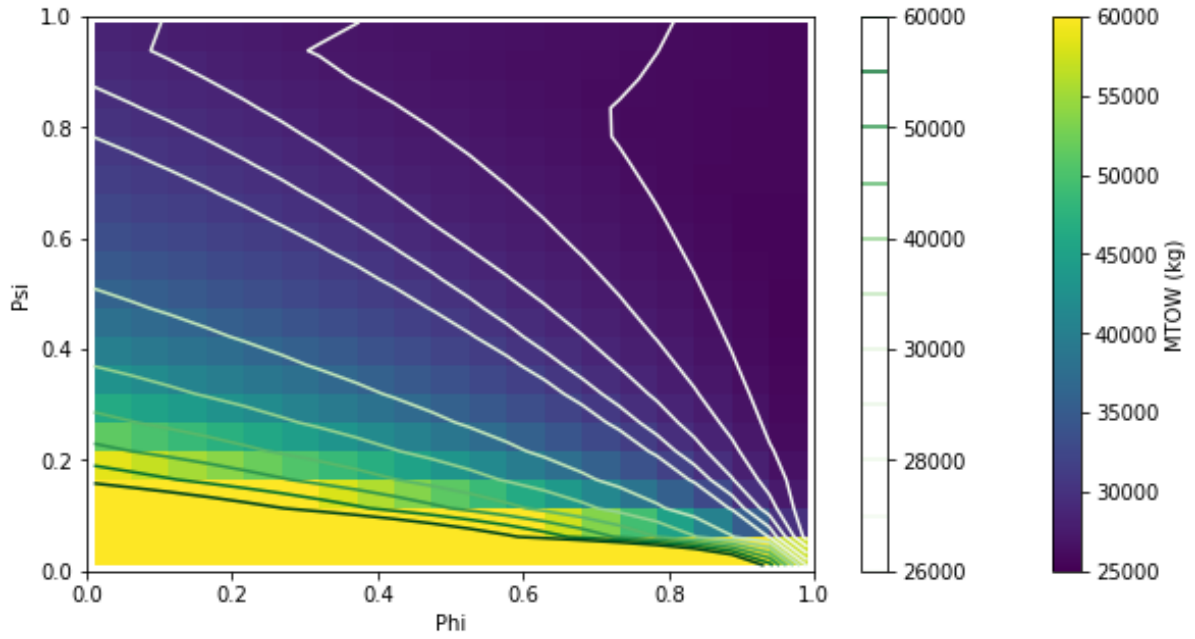

Figure 58 – Aircraft MTOW as function of Φ and Ψ, for a modified deHavilland Dash 8 Q300 with a LH_2-fuelled SOFC-GT-Battery hybrid electric powertrain.

The MTOW change when Φ_{cruise} and $\Phi_{TO} = \Phi_{climb}$ are varied, for the case of no batteries onboard ($\Psi = 1$) is shown in Figure 59. The minimum aircraft MTOW is obtained for the case of no SOFC use ($\Phi_{cruise} = \Phi_{TO} = \Phi_{climb} = 1.0$). This result is strongly dependent on SOFC power density. If the same simulation is repeated considering a double current density of the SOFC, namely $i_{SOFC} = 4\frac{A}{cm^2}$ instead of $i_{SOFC} = 2\frac{A}{cm^2}$, the MTOW varies as shown in Figure 60. As expected, an increase in current density leads to a less steep increase of MTOW as Φ_i decreases. The reason for this is the higher power density of the SOFC, that leads to a lighter powertrain.

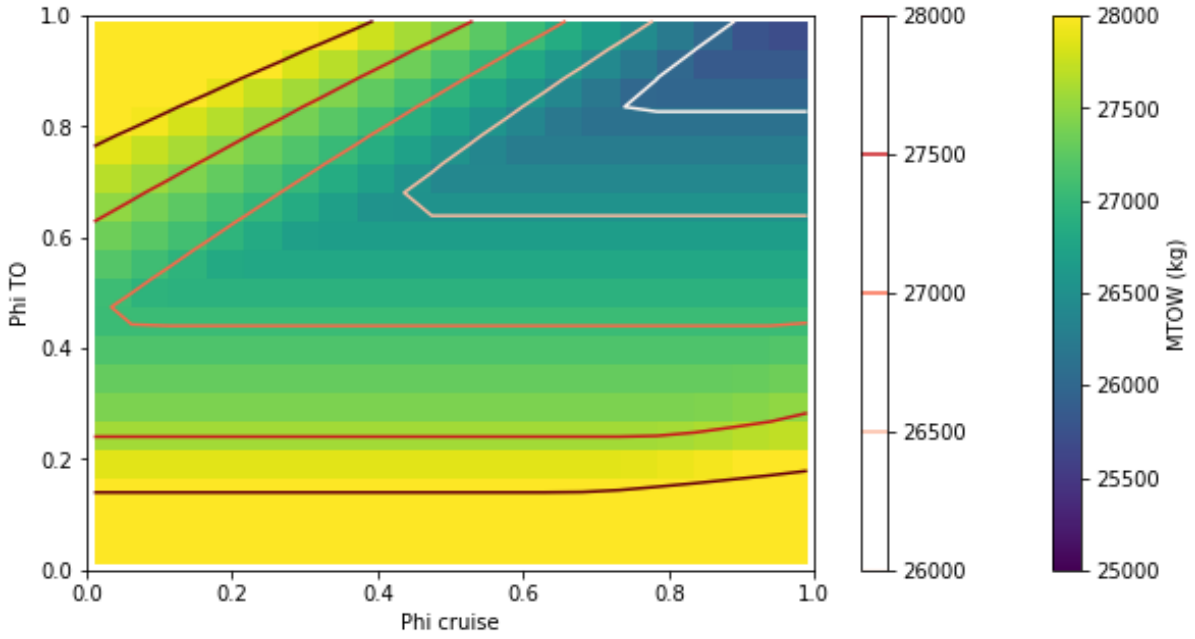

Figure 59 – Aircraft MTOW as function of Φ_{cruise} and $\Phi_{TO} = \Phi_{climb}$, for a modified deHavilland Dash 8 Q300 with a LH_2-fuelled SOFC-GT-Battery hybrid electric powertrain, considering no batteries ($\Psi_i = 0$). SOFC operating current density of 2.0 A/cm^2 at a voltage of 0.8 V and 80% fuel utilization.

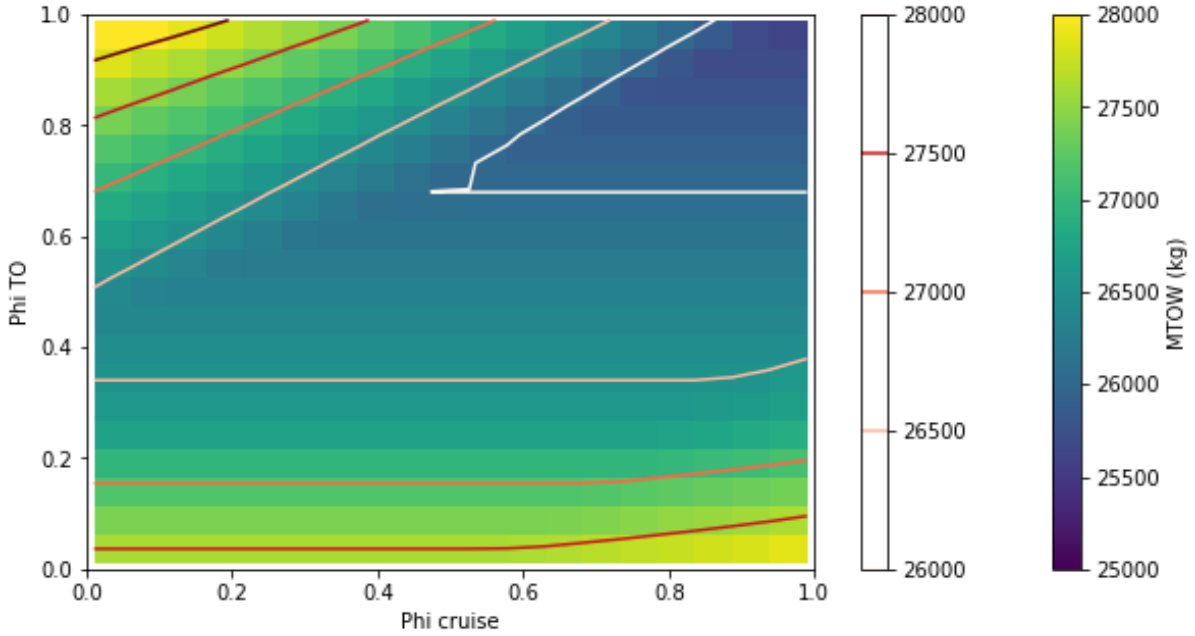

Figure 60 – Aircraft MTOW as function of Φ_{cruise} and $\Phi_{TO} = \Phi_{climb}$, for a modified deHavilland Dash 8 Q300 with a LH_2-fuelled SOFC-GT-Battery hybrid electric powertrain, considering no batteries ($\Psi_i = 0$). SOFC operating current density of 4.0 A/cm^2 at a voltage of 0.8 V and 80% fuel utilization.

9.6 TARGET AIRCRAFT DESIGN

The implemented overall methodology, as schematized in Figure 12, is now applied to the target aircraft. This aircraft is a 50-seater fueled by liquid hydrogen with design inputs as presented in section *Target aircraft definition*. 3 studies with different powertrain definition are performed:

- **Case 1**: Turboprop-powered aircraft.
- **Case 2**: SOFC-Turboprop powered aircraft with no batteries and a SOFC to power only the electric payload.

- **Case 3**: SOFC-Turboprop-Battery powertrain, with an electric motor and fan providing a fraction of the propulsive power.

A reference MTOW of 18 ton is assumed. The design values of the power management variables for each sizing case are summarized in Table 16.

Table 16 – Design power management variables for the three test cases.

Case	Φ_{TO}	Ψ_{TO}	λ_{TO}	Φ_{cruise}	Ψ_{cruise}	λ_{cruise}
1	1	0	1	1	0	1
2	0.9	1	1	0.9	1	1
3	0.5	0.9	0.1	0.5	0.9	0.1

Initially, the study cases are assessed assuming constant efficiencies for the constraint analysis, with values indicated in Table 17.

Table 17 – Assumed component efficiencies for constraint analysis.

	η_V	η_{GT1}	η_{GT2}	η_{p1}	η_{SOFC}	$\eta_{u,SOFC}$	η_{PM1}	η_{PM2}	η_{EM}	η_{p2}
TO	1	0.42	0.50	0.70	0.55	0.75	0.99	0.99	0.92	0.70
Climb	1	0.42	0.50	0.70	0.55	0.75	0.99	0.99	0.92	0.70
Cruise	1	0.42	0.50	0.80	0.55	0.75	0.99	0.99	0.94	0.80
Approach	1	0.30	0.35	0.60	0.65	0.75	0.99	0.99	0.87	0.60

These initial studies are performed assuming operation of the SOFC at 0.8 V, 2 A/cm^2, 800°C operating temperature, 16 bar operating pressure, 80% fuel utilization, air stoichiometry factor equal to 5, with a cell area of 200 cm^2.

The constraint analysis results are shown in Figure 61, Figure 62, and Figure 63.

- In Case 1, the design point is close to that of similar aircraft, such as the Dash 8 Q300, as expected. The design is mainly determined by the constrain on stall speed and takeoff distance.
- In Case 2, both turboprop and SOFC are sized based on the requirements resulting from takeoff operation. SOFC power is 10% of that of turboprop given the assumed design parameters in Table 16.
- In Case 3, both batteries and SOFC generate electric power, that is supplied to both the electric fan and the electric payload. The turboprop is main propulsor of the aircraft.

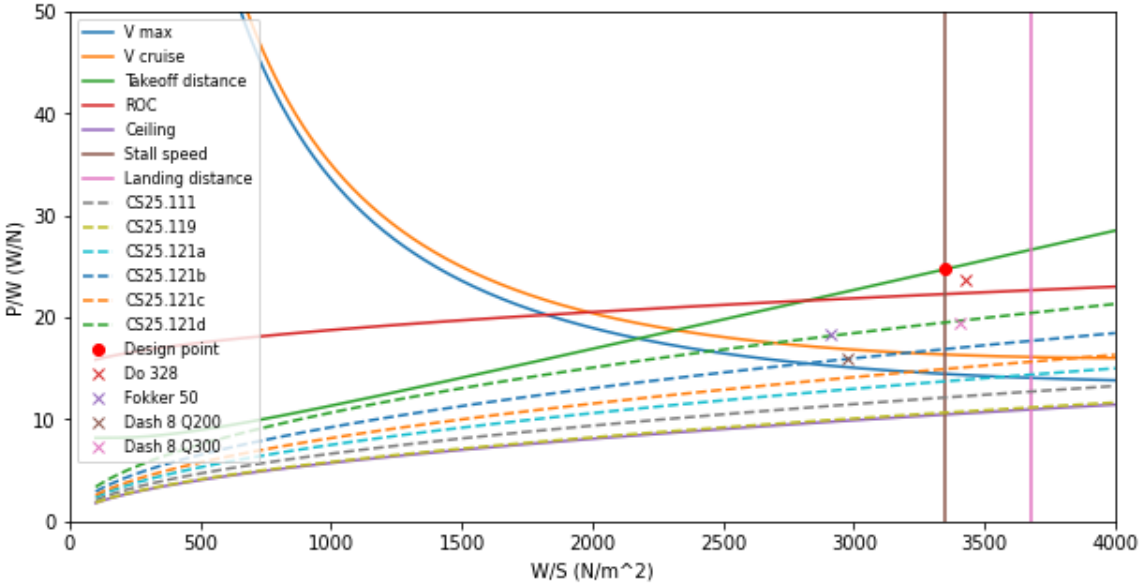

Figure 61 – Constraint analysis graph for Case 1.

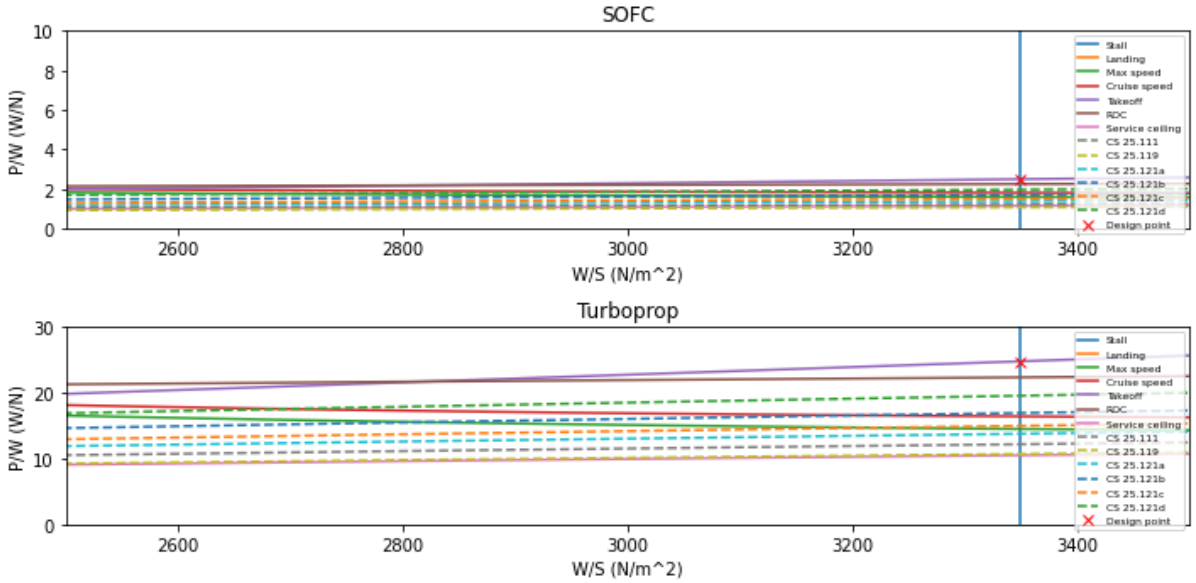

Figure 62 – Constraint analysis graph for Case 2.

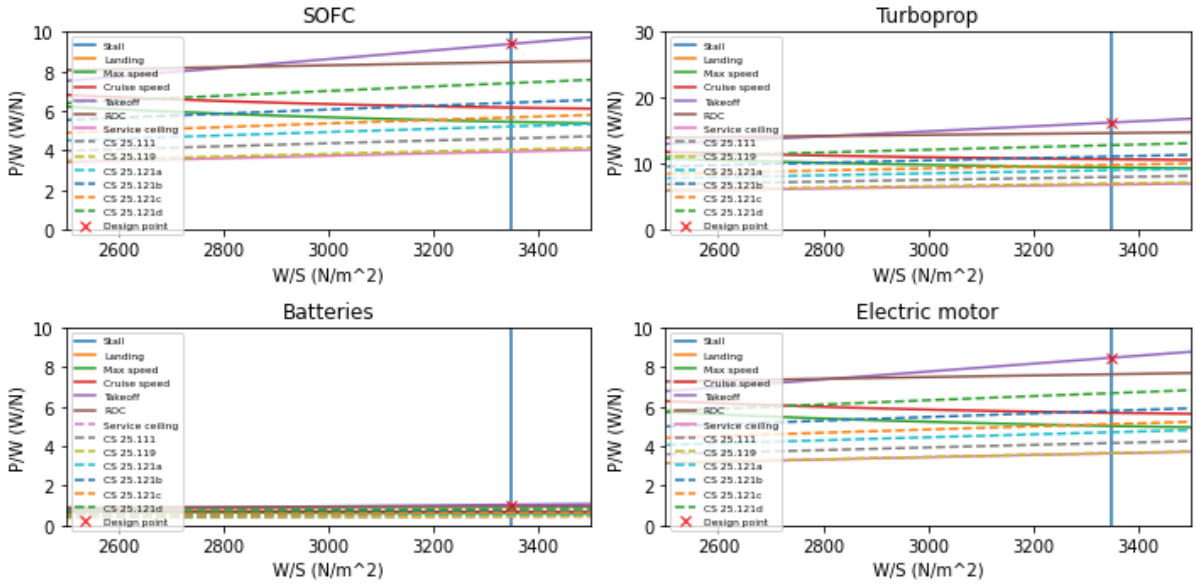

Figure 63 – Constraint analysis graph for Case 3.

The MTOW and weight breakdown results are compared in Figure 64. As seen in the figure, the use of a SOFC hybridization of the gas turbine leads to increase in the aircraft MTOW by 2182 kg from Case 1 to Case 2, thus increasing design mission block energy consumption. The adoption of batteries in the powertrain and the use of the SOFC stack to contribute to propulsive power generation, as simulated in Case 3, leads to a substantial MTOW increase, by 11.6 ton compared to Case 1. From these results, it is concluded that further improvements in power density and efficiency of state-of-the-art SOFC and battery packs are required to achieve a reduction of MTOW, and potentially block energy consumption, compared to gas turbine powertrains.

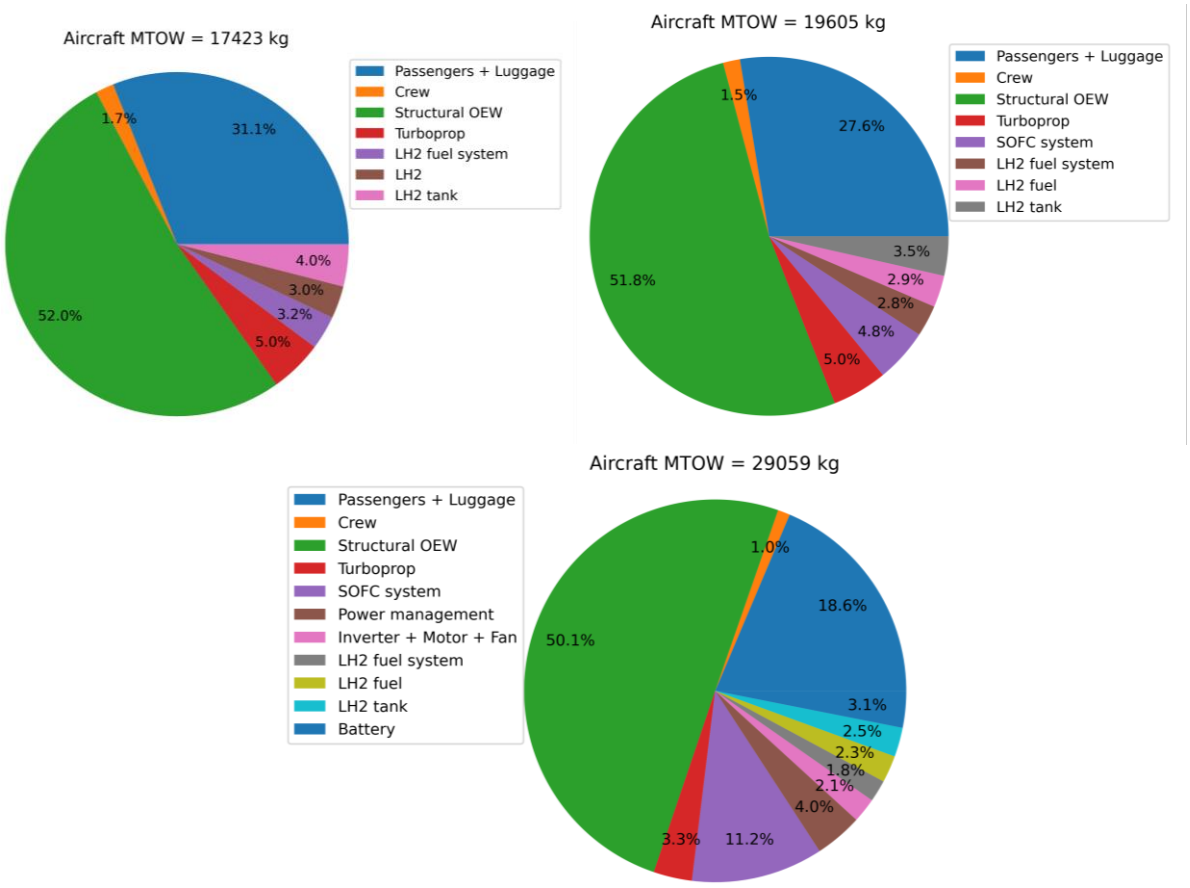

Figure 64 – Comparison of MTOW and weight breakdown between Case 1 (top left), Case 2 (top right), and Case 3 (bottom).

The power of each powertrain component for each study case is presented in Table 18. While the first case study requires around 4.2 MW of installed power, case study 3 requires around 7.5 MW. The higher installed power arises from the selection of the design power management variables, as well as from the higher MTOW. The SOFC system power density is estimated as 0.51 kW/kg for Case 2 and 0.82 kW/kg for Case 3. The reason behind this difference in power density is the sizing of the SOFC pressure vessel.

Table 18 – Power of each powertrain component for each study case of the target aircraft.

Case study	Turboprop power (kW)	SOFC power (kW)	Battery power (kW)
1	4226	0	0
2	4754	481	0
3	4633	2677	246

Integration considerations are included in the design via the methodology to compute increase in fuselage length. A fuselage diameter of 2.7 m has been assumed. Results on the 3 case studies have been obtained. These results are summarized in Table 19. The computed fuselage length increase is 2.4 m for Case 1, 3.5 m for Case 2, and 9.0 m for Case 3. Considering that cabin length is 12.6 m for the deHavilland Dash 8 Q300 aircraft, and fuselage length is 25.7 m (9.5 baseline slenderness), the fuselage length increase of Case 3 is considered excessive to achieve a feasible aircraft design. For Case 1 and Case 2, considering bigger fuselage diameter is recommended.

Table 19 – Size of novel components for integration into the aircraft fuselage, for the 3 study cases.

Case study	LH_2 tank length (m)	SOFC length (m)	Battery length (m)	Resulting slenderness with 25.7 m baseline fuselage length
1	2.4	0	0	10.4
2	2.5	1.0	0	10.8
3	2.6	5.4	1.0	12.9

Considering a more conservative stack volumetric power density of 1 kW/l, based on the indications by Udomsilp et al. [47], the sizing simulations are performed again. The results for Case 2 are presented in Figure 65. The results for Case 3 are not obtained, as the model does not converge to a MTOW value. For Case 2, a SOFC system-level power density of 0.129 kW/kg is obtained (827 kW produced by a system that weighs 6415 kg). This value is within the expected range of system-level power density indicated by Udomsilp et al. [47] (0.12-0.14 kW/kg) for SOFC systems with 1-1.2 kW/l volumetric power density. This result provides further confidence on the validity of SOFC weight calculation methods implemented in this work.

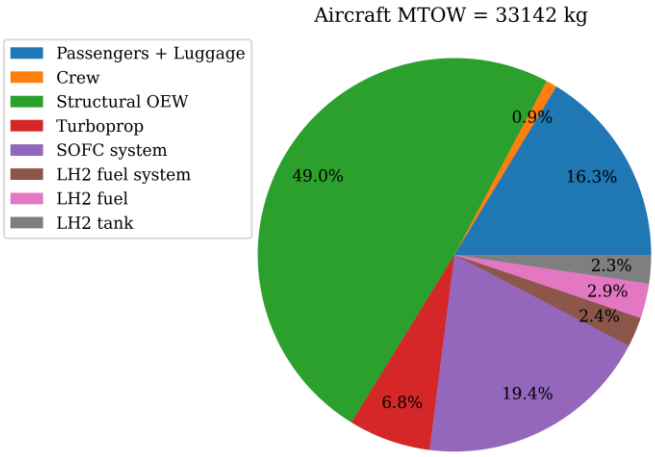

Figure 65 – Aircraft MTOW for Case 2 for conservative stack volumetric power density estimation.

Considering the excessively high MTOW obtained with conservative volumetric power density values of the SOFC system, a sensitivity study on aircraft MTOW as a function of SOFC system power density is performed in the following section.

9.6.1 SENSITIVITY STUDY OF MTOW AS A FUNCTION OF SOFC SYSTEM POWER DENSITY

A study on the sensitivity of MTOW of the target aircraft to SOFC system power density is performed. This study serves to define technological requirements of SOFC systems for aviation applications. Different values of Φ, assuming $\Phi_{cruise} = \Phi_{TO}$, are considered to perform the sensitivity study, as well as $\Psi = 1$ (no battery) and $\lambda = 0.1$ (electric payload consumes 10% of energy generated by SOFC). The results are shown in Figure 66. As seen in the figure, the lower the SOFC system power density, the higher the impact on MTOW. For most combinations of Φ and SOFC system power density, the aircraft is excessively heavy for its application as 50-seat regional aircraft. It is concluded that advancements in SOFC system power density to values above 1 kW/kg (19 ton for $\Phi = 0.9$) are required for their use onboard aircraft.

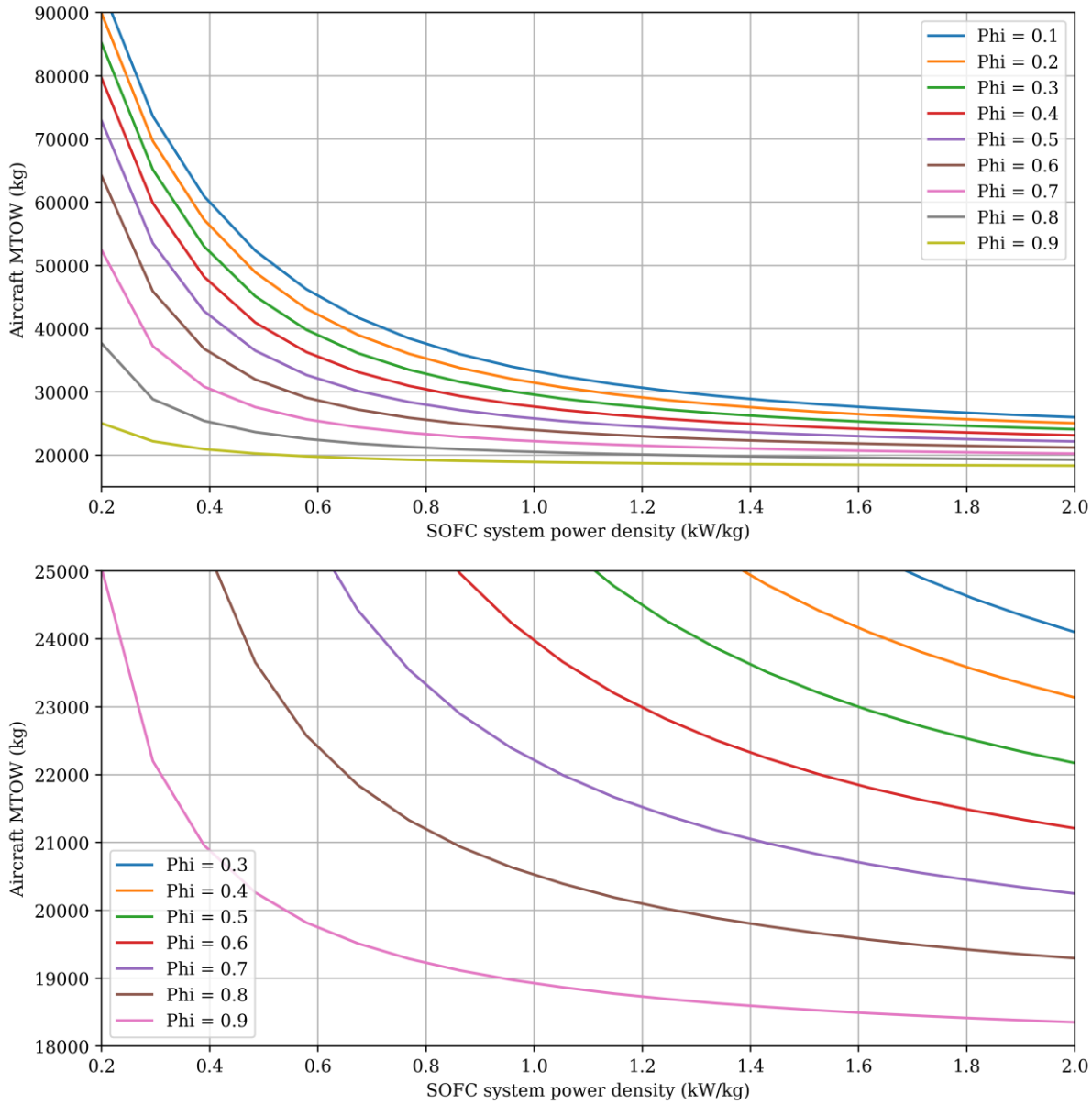

Figure 66 – Target aircraft MTOW as a function of SOFC system power density and design power management parameter Φ. Top: Full range. Bottom: Typical MTOW range for 50-seat regional aircraft.

9.7 DISCUSSION

Based on the results presented in the previous sections, it is possible to answer the research questions set at the beginning of the project.

1. **What modifications are required to the traditional design methodologies of tube-and-wing aircraft for regional missions if a LH2-fuelled SOFC-GT-Battery hybrid electric system is adopted for propulsion and power generation?**

The aircraft design methodologies that have been adapted for their application for design of aircraft with LH_2-fuelled SOFC-GT-Battery hybrid electric powertrains include:

- **Powertrain performance modelling**: a 0D SOFC cell-level performance model has been developed in this work. This model includes the impact of operating temperature, pressure, fuel utilization, and air stoichiometry factor on cell performance. The cell-level model has been integrated into a stack-level model of the SOFC for stack sizing. Further, the stack model has been implemented into a SOFC system model, including BoP performance modelling, for SOFC system sizing. Then, the SOFC system performance model has been integrated into a turboprop performance model, considering the extraction

of air from the HPC exhaust for its use in the SOFC cathode, and the injection of the SOFC exhaust byproducts into the combustion chamber. This novel performance model of SOFC-GT powertrains can be implemented into existing aircraft design tools.

- **Power sizing**: a methodology to determine the power capacity of each powertrain component based on aircraft performance requirements has been developed in this work, based on the work by de Vries [28].
- **Energy sizing**: a novel range equation for aircraft with liquid-hydrogen-fueled SOFC-GT-Battery powertrains is derived in this work, based on the system parameterization defined in the power sizing methodology.
- **OEW calculation**: a modified Class I method for weight estimation has been developed and validated in this work. This methodology is based on estimating the OEW of aircraft with similar MTOW, range and number of passengers based on statistical data; estimating the weight of components that are not installed in the target aircraft with the novel powertrain, and subtracting it from the estimated OEW, obtaining the corrected OEW; and calculating the weight of the novel components for which statistical data for aviation applications is not available, and summing it to the corrected OEW. In this work, a set of physics-based and empirical expressions have been derived or obtained from literature for calculation of the weight of the novel components.
- **MTOW calculation**: the methodologies for MTOW calculation results from the integration of all the methodologies listed above.
- **System integration**: the integration of the hydrogen tank, SOFC and battery into the fuselage leads to a length increase of the aircraft fuselage. In this work, models for the fuselage length increase based on novel component sizing have been derived and implemented.

These novel methodologies can be integrated into traditional tube-and-wing aircraft design tools to obtain aircraft sizing and weight estimation.

2. **What is the effect on powertrain sizing and performance of varying the relative power capacity of the various components of a LH2-fuelled SOFC-GT-Battery hybrid electric system?**

The quantitative impact of the design parameters of the components on powertrain size and performance has been widely characterized in the Results chapter. The main results are highlighted here:

- Increase of the overall system cruise efficiency from 35% to 75% is possible by adopting a fully electrical powertrain (Φ, Ψ equal to 0).
- Given the performance requirements of the target aircraft, minimum powertrain size is achieved for $\Phi_{TO} = \Phi_{climb} = \Phi_{cruise}$. Changing the performance requirements leads to a different optimum.
- Bigger liquid hydrogen tank size and lower tank diameter leads to higher liquid hydrogen storage density.
- Lower values of Φ and Ψ lead to substantially higher MTOW, from less than 25 ton for values of Φ and Ψ over 0.6 to more than 60 ton for values below 0.2.

These results highlight the need to develop SOFC systems with higher power density. System optimization at powertrain level will be required for aircraft design, due to the complexity and interrelations between the powertrain design parameters.

3. **What is the effect of the use of LH2-fuelled SOFC-GT-Battery hybrid electric systems on regional aircraft weight and system integration?**

For the 50-seater target regional aircraft, MTOW increases substantially with the increase of battery and SOFC contributions, increasing from 17.4 ton at $\Phi = 1, \Psi = 0,\ \lambda = 1$ to 29.1 ton at $\Phi = 0.5, \Psi = 0.9, \lambda = 0.1$. In terms of system integration, fuselage length increase due to the integration of LH2 equipment rises from 2.4 meter to 9.0 meter for constant fuselage diameter. Considering the sensitivity of aircraft MTOW to SOFC system power density, to achieve a MTOW below 21 ton for the target aircraft, power density above 0.4 kW/kg is required for $\Phi = 0.9$, above 0.85 kW/kg for $\Phi = 0.8$, and above 1.4 kW/kg for $\Phi = 0.7$.

10 CONCLUSIONS, RECOMMENDATIONS, AND NEXT STEPS

10.1 CONCLUSIONS

In this work, novel design methodologies for regional aircraft with liquid hydrogen fuel and SOFC-GT-Battery powertrains were developed, implemented, validated, and used for sensitivity analyses and to assess several case studies. Several conclusions can be drawn from the results of this work:

- SOFC performance is affected by operating temperature, pressure, fuel utilization and air stoichiometry factor. In general, SOFC stack operating efficiency is increased by increasing temperature, increasing pressure, decreasing fuel utilization, and increasing air stoichiometry factor. The modelling of these effects has been performed using empirical expressions calibrated with experimental data, as recommended by Datta [5] for PEMFCs. However, due to the use of different data sources, the impact of operating conditions on SOFC performance does not necessarily represent the performance of an actual state-of-the-art SOFC. Nevertheless, the general trends of SOFC performance as a function of operating conditions are correctly represented, enabling sensitivity analyses on the impact of design operating conditions on the fuel cell performance and sizing.
- The on-design performance of SOFC-GT powertrains has been modelled. This information has been used to perform sensitivity studies. Higher SOFC operating temperatures, higher gas turbine OPR, lower fuel utilization and higher SOFC air stoichiometry factor lead to higher SOFC operating efficiency. Gas turbine operating efficiency is mainly a function of OPR, while it is weakly dependent on the rest of design parameters. Gas turbine thermal efficiency associated with the SOFC exhausts increases with increasing SOFC operating temperature, fuel utilization, and air stoichiometry factor. These trends are considered in the selection of the optimal SOFC-GT hybrid system design variables.
- The component-oriented power sizing methodology based on performance constraint diagrams has been successfully verified and validated. The performed sensitivity analyses show that lower values of Φ and Ψ lead to higher system efficiency, due to the higher fraction of power obtained from the SOFC and from the battery. Nevertheless, at system level, this efficiency increase is offset by the significant increase in system weight. Gas turbine thermal efficiency is more relevant for overall system cruise efficiency than SOFC efficiency, due to the injection of SOFC exhausts into the gas turbine. An optimal selection of Φ for cruise, takeoff and climb would allow for powertrain size minimization, thanks to the downsizing of certain components of the powertrain. This optimal solution depends strongly on the performance requirements (takeoff distance, maximum ROC, cruise speed…), and should be identified via system optimization.
- The novel energy sizing equation for regional aircraft with liquid hydrogen fuel and SOFC-GT-Battery powertrains, which includes a validated liquid hydrogen tank weight estimation method, has been implemented and used for range calculation of the target aircraft.
- A modified Class I method for OEW calculation of regional aircraft with liquid hydrogen fuel and SOFC-GT-Battery powertrains is proposed in this work. This method is based on a modification of the traditional OEW estimation methods by including the new components of the powertrain, as well as structural modifications required due to the specificities of the design. Novel physics-based and empirical relations for aircraft OEW have been derived. The implemented SOFC system weight estimation methodology has been validated at cell-level, stack-level, and system-level. The overall powertrain weight estimation methodology has been implemented and validated. The implemented methodology achieves reasonably accurate estimations of OEW, considering the typical limitations in accuracy of Class I methodologies.
- A modified MTOW estimation methodology combining all the previous novel methodologies has been implemented and tested on several case studies. The results of the case study of the deHavilland Dash 8 Q300 aircraft show an increase in aircraft MTOW from 19505 kg to 27810 kg when selecting $\Phi = 0.5$, $\Psi = 0.9$ and $\lambda = 0.1$. This highlights the need for R&D efforts to make SOFC technology lightweight, as the overall efficiency increase that SOFC-GT-Battery powertrains enable is currently offset by the extra energy consumption due to higher MTOW.
- The previous methodologies have been implemented into an iterative aircraft sizing framework and used to perform studies on 50-seat regional aircraft with different powertrain definitions. Results show that aircraft MTOW increases as the share of power provided by SOFC and/or batteries increases,

leading to higher block energy consumption. As mentioned in the previous point, an increase in power density of SOFC systems, and in energy density and power density of batteries, is crucial for the feasibility of this novel powertrain concept.

- The integration studies show that fuselage length needs to be increased by 9.0 m in the worst simulated case. This will lead to further modifications in aircraft aerodynamic performance and structural design, that should be accounted in the preliminary design methodology. This can be achieved by integrating the developed models into available aircraft design tools.

10.2 RECOMMENDATIONS

Several recommendations are proposed by the author to further strengthen the preliminary results obtained in this thesis:

- As highlighted throughout this work, the impact of operating conditions on SOFC performance is highly configuration-dependent, design-dependent, and size-dependent. Therefore, to properly optimize the operation and design of the powertrain, the SOFC model should be calibrated with experimental data of a SOFC stack with a power capacity suitable for the target aircraft. At the moment, these data are not available.
- Develop an off-design model of the SOFC-Turboprop powertrain, to better define the operating efficiency at each flight condition.
- Assess the power density potentially achievable by the components of the powertrain, as many of these have never been developed for aircraft applications, in which lightweight design is crucial.
- Include a more accurate estimation of energy consumption during takeoff, climb, descent and landing in the energy sizing equations, based on a detailed aircraft and powertrain performance analysis.
- For future application of the methodologies proposed in this work, the author recommends reviewing and adapting the technological assumptions as more information is available, to ensure that the obtained results are in line with what is achievable in the moment of the simulation or projected in the near future.

10.3 NEXT STEPS

In future steps of this work, the developed sizing methodology can be converted into a tool coupled with SUAVE, considering the design framework shown in Figure 67:

- Engine performance analysis is implemented into pyCycle [93] and a powertrain surrogate model for SUAVE is generated.
- The aerodynamic characteristics of the aircraft are determined using the Athena Vortex Lattice (AVL) software.
- Aircraft performance analysis is performed using SUAVE.
- Detailed powertrain thermal modelling using the OpenConcept Python library [30].
- A detailed integration concept is proposed for OpenVSP [94].

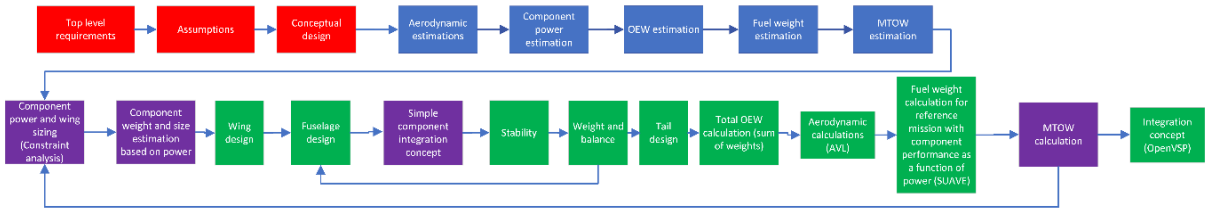

Figure 67 – Proposed aircraft design framework for future developments, implemented in SUAVE.

The following next research steps are envisaged:

- Implementation of a SOFC-GT model in pyCycle, to increase the fidelity of efficiency estimations, and to compute accurately the off-design performance of the powertrain in all operating conditions.
- Implementation of the novel sizing methodologies in aircraft design, sizing and performance study tools, such as SUAVE [95] or the Aircraft Design Initiator.
- Inclusion of aerodynamic analysis in the aircraft design loop, to increase the fidelity of the aerodynamic parameter estimations considered in the constraint analysis.

- Improvement of the fidelity of the OEW estimation methodology by considering the effect of variations in aircraft component size (wing, fuselage, tail) resulting from the design point identified through the constraint analysis and the requirements due to powertrain integration.
- Implementation of the system integration methodology into an automatic tool, such as OpenVSP.
- Implementation of the novel methodologies into an aircraft design optimization tool. It is proposed to run the optimization problem considering minimization of reference mission block energy consumption, to understand the optimal powertrain design parameters that would lead to minimal energy consumption.

11 REFERENCES

[1] FCHJU, "Hydrogen-powered aviation A fact-based study of hydrogen technology, economics and climate impact by 2050," Clean Sky 2, Belgium, 2020.

[2] J. Larminie, A. Dicks and M. S. McDonald, Fuel cell systems explained, Chichester, UK: J. Wiley, 2003.

[3] R. O'Hayre, S. Cha, W. Colella and F. Prinz, Fuel cell fundamentals, Hoboken: John Wiley & Sons, Inc., 2016.

[4] D. Juschus, "Preliminary propulsion system sizing methods for PEM fuel cell aircraft," TU Delft, Delft, 2021.

[5] A. Datta, "PEM fuel cell model for conceptual design of hydrogen eVTOL aircraft," NASA, Maryland, 2021.

[6] A. Seitz, M. Nickl, F. Troeltsch and K. Ebner, "Initial assessment of a fuel cell-gas turbine hybrid propulsion concept," *Aerospace*, vol. 9, no. 68, 2022.

[7] C. Colpan, I. Dincer and F. Hamdullahpur, "A review on macro-level modeling of planar solid oxide fuel cells," *International Journal of Energy Research*, vol. 32, pp. 336-355, 2008.

[8] S. Singhal and K. Kendall, High temperature solid oxide fuel cells: Fundamentals, design and applications, Bodmin: Elsevier, 2003.

[9] EG&G Technical Services, Inc., Fuel Cell Handbook 7th Ed., Morgantown: U.S. Department of Energy, 2004.

[10] L. Zhou, M. Cheng, B. Yi, Y. Dong, Y. Cong and W. Yang, "Performance of an anode-supported tubular solid oxide fuel cell (SOFC) under pressurized conditions," *Electrochimica Acta*, vol. 53, pp. 5195-5198, 2008.

[11] K. Wang, D. Hissel, M. Pera, N. M. D. Steiner, M. Sorrentino, C. Pianese, M. Monteverde, P. Cardone and J. Saarinen, "A review on solid oxide fuel cell models," *International Journal of Hydrogen Energy*, vol. 36, pp. 7212-7228, 2011.

[12] A. Salogni and P. Colonna, "Modeling of solid oxide fuel cells for dynamic simulations of integrated systems," *Applied Thermal Engineering*, vol. 30, pp. 464-477, 2010.

[13] M. Fernandes, S. Andrade, V. Bistrizki, R. Fonseca, L. Zacarias, H. Goncalves, A. de Castro, R. Domingues and T. Matencio, "SOFC-APU systems for aircraft: A review," *International Journal of Hydrogen Energy*, vol. 43, pp. 16311-16333, 2018.

[14] G. Whyatt and L. Chick, "Electrical generation for more-electric aircraft using solid oxide fuel cells (Report PNNL-21382)," US Departmento of Energy under Contract DE-AC05-76RL01830, Alexandria, 2012.

[15] Delphi, "Delphi Solid Oxide Fuel Cell Stack," [Online]. Available: https://studylib.net/doc/18801859/delphi-solid-oxide-fuel-cell-stack. [Accessed July 2022].

[16] R. Braun, M. Gummalla and J. Yamanis, "System architectures for solid oxide fuel cell-based auxiliary power units in future commercial aircraft applications," *Journal of Fuel Cell Science and Technology*, vol. 6, 2009.

[17] Z. Ji, J. Qin, K. Cheng, H. Liu, S. Zhang and P. Dong, "Performance evaluation of a turbojet engine integrated with interstage turbine burner and solid oxide fuel cell," *Energy*, vol. 168, pp. 702-711, 2019.

[18] Z. Ji, J. Qin, K. Cheng, F. Guo, S. Zhang and P. Dong, "Performance characteristics of a solid oxide fuel

cell hybrid jet engine under different operating modes," *Aerospace Science and Technology,* vol. 105, 2020.

[19] M. Bahari, M. Rostami, A. Entezari, S. Ghahremani and M. Etminan, "A comparative analysis and optimization of two supersonic hybrid SOFC and turbine-less jet engine propulsion system for UAV," *Fuel,* vol. 319, 2022.

[20] S. Seyam, I. Dincer and M. Agelin-Chaab, "Investigation of two hybrid aircraft propulsion and powering systems using alternative fuels," *Energy,* vol. 232, no. 121037, 2021.

[21] J. Collins and D. McLarty, "All-electric commercial aviation with solid oxide fuel cell-gas turbine-battery hybrids," *Applied Energy,* vol. 265, 2020.

[22] D. Waters, "Modeling of gas turbine-solid oxide fuel cell systems for combined propulsion and power on aircraft (PhD thesis)," University of Maryland, Washington, 2015.

[23] D. Waters and C. Cadou, "Engine-integrated solid oxide fuel cells for efficient electrical power generation on aircraft," *Journal of Power Sources,* vol. 284, pp. 588-605, 2015.

[24] L. Pratt, "Gas turbine/Solid Oxide Fuel Cell hybrids: Investigation of aerodynamic challenges and progress towards a bench-scale demonstrator," University of Maryland, 2019.

[25] D. Waters, L. Pratt and C. Cadou, "Gas turbine/Solid Oxide Fuel Cell hybrids for aircraft propulsion and power," *Journal of Propulsion and Power,* vol. 37, no. 3, pp. 349-362, 2021.

[26] J. Freeh, J. Pratt and J. Brouwer, "Development of a solid-oxide fuel cell/gas turbine hybrid system model for aerospace applications (NASA/TM—2004-213054)," in *Proceedings of ASME Turbo Expo 2004*, Vienna, 2004.

[27] V. Chakravarthula, "Transient analysis of a solid oxide fuel cell/gas turbine hybrid system for distributed electric propulsion," Wright State University, 2016.

[28] R. de Vries, "Hybrid-Electric Aircraft with Over-the-Wing Distributed Propulsion: Aerodynamic Performance and Conceptual Design," TU Delft, Delft, 2022.

[29] A. Isikveren, S. Kaiser, C. Pornet and P. Vratny, "Pre-design strategies and sizing techniques for dual-energy aircraft," *Aircraft Engineering and Aerospace Technology,* vol. 26, no. 6, pp. 525-542, 2014.

[30] B. Brelje and J. Martins, "Development of a conceptual design model for aircraft electric propulsion with efficient gradients," in *Electric Aircraft Technologies Symposium*, Cincinatti, 2018.

[31] D. Finger, "Methodology for Multidisciplinary Aircraft Design under Consideration of Hybrid-Electric Propulsion Technology," RMIT University, Aachen, 2020.

[32] B. Brelje, "Multidisciplinary Design Optimization of Electric Aircraft Considering Systems Modeling and Packaging," University of Michigan, Michigan, 2021.

[33] D. Raymer, Aircraft Design: A Conceptual Approach, American Institute of Aeronautics and Astronautics, Inc., 2012.

[34] E. Torenbeek, Synthesis of subsonic airplane design: an introduction to the preliminary design of subsonic general aviation and transport aircraft, with emphasis on layout, aerodynamic design, propulsion and performance, Springer Science & Business Media, 2013.

[35] M. Sadraey, Aircraft design: A systems engineering approach, John Wiley & Sons, 2012.

[36] M. Hepperle, "Electric flight - Potential and limitations," DLR, 2012.

[37] M. Marwa, S. M. Martin, B. C. Martos and R. P. Anderson, "Analytic and Numeric Forms for the Performance of Propeller-Powered Electric and Hybrid Aircraft," in *55th AIAA Aerospace Sciences*

Meeting, Grapevine, 2017.

[38] R. Ravishankar and S. Chakravarthy, "Range equation for a series hybrid electric aircraft," in *2018 Aviation Technology, Integration, and Operations Conference*, Atlanta, Georgia, 2018.

[39] S. Elmousadik, V. Ridard, N. Secrieru, A. Joksimovic and C. Maury, "New Preliminary Sizing Methodology for a Commuter Airplane with Hybrid-Electric Distributed Propulsion," in *Advanced Aircraft Efficiency in a Global Air Transport System (AEGATS 18)*, Toulouse, 2018.

[40] R. de Vries, M. Hoogreef and R. Vos, "Range equation for hybrid-electric aircraft with constant power split," *Journal of Aircraft*, vol. 57, no. 3, pp. 1-6, 2020.

[41] D. C. Brewer, Hydrogen Aircraft Technology, Boca Raton: CRC Press Inc., 1991.

[42] R. Tornabene, X. Wang, C. Steffen and J. Freeh, "Development of parametric mass and volume models for an aerospace SOFC/Gas turbine hybrid system," in *ASME Turbo Expo 2005*, Reno, 2005.

[43] C. Steffen, J. Freeh and L. Larosiliere, "Solid Oxide Fuel Cell/Gas Turbine Hybrid Cycle Technology for Auxiliary Aerospace Power (NASA/TM—2005-213586 GT2005–68619)," in *Turbo Expo 2005*, Reno, 2005.

[44] EASA, *Certification Specifications and Acceptable Means of Compliance for Large Aeroplanes (CS-25) Amendment 27*, EASA, 2021.

[45] R. Schaufele, The elements of aircraft preliminary design, Santa Ana: Aries Publications, 2000.

[46] T. L. Cable and S. W. Sofie, "Symmetrical, bi-electrode supported solid oxide fuel cell (https://patents.google.com/patent/US7534519B2/en)". USA Patent US7534519B2, 19 May 2009.

[47] D. Udomsilp, J. Rechberger, A. Opitz, O. Guillon and M. Bram, "Metal-Supported Solid Oxide Fuel Cells with Exceptionally High Power Density for Range Extender Systems," *Cell Reports Phsical Science*, vol. 1, 2020.

[48] W. Winkler, "Thermodynamics," in *High Temperature Solid Oxide Fuel Cells: Fundamentals, Design and Applications*, Amsterdam, Elsevier Limited, 2003, pp. 53-75.

[49] S. Song, X. Xiong, X. Wu and Z. Xue, "Modeling the SOFC by BP neural network algorithm," *International Journal of Hydrogen Energy*, vol. 46, pp. 20065-20077, 2021.

[50] S. Seidler, M. Henke, J. Kallo, W. Bessler, U. Maier and K. Friedrich, "Pressurized solid oxide fuel cells: Experimental studies and modeling," *Journal of Power Sources*, vol. 196, pp. 7195-7202, 2011.

[51] L. Duan, X. Zhang and Y. Yang, "Exergy analysis of a novel SOFC hybrid system with zero CO2 emission," North China Electric Power University, 2014.

[52] C. Willich, C. Westner, S. Seidler, F. Leucht, M. Henke, J. Kallo, U. Maier and K. Friedrich, "Pressurized Solid Oxide Fuel Cells: Operational Behaviour," DLR, 2011.

[53] A. Momma, K. Takano, Y. Tanaka and T. Y. A. Kato, "Experimental Investigation of the Effect of Operating Pressure on the Performance of SOFC and SOEC," *ECS Transactions*, vol. 57, no. 1, pp. 699-708, 2013.

[54] A. Virkar, K. Fung and S. Singhal, "The effect of pressure on solid oxide fuel cell performance," OSTI, Salt Lake City, 1997.

[55] P. Leone, T. Matencio, M. Garcia, Z. Domigues, A. Lanzini and M. Santarelli, "Limiting factors for a planar solid oxide fuel cell under different flow and temperature conditions," *Fuel Cells*, 2013.

[56] C. Albanakis, K. Yakinthos, K. Kritikos, D. Missirlis, A. Goulas and P. Storm, "The effect of heat transfer on the pressure drop through a heat exchanger for aero engine applications," *Applied Thermal Engineering*,

vol. 29, no. 4, pp. 634-674, 2008.

[57] L. Loftin, "NASA Reference publication 1060 - Subsonic aircraft: Evolution and the matching of size to performance," NASA , 1980.

[58] M. H. Sadraey, Aircraft performance: an engineering approach, CRC Press, 2017.

[59] S. Mital, J. Gyekenyesi, S. Arnold, R. Sullivan, J. Manderscheid and P. Murthy, "Review of current state of the art and key design issues with potential solutions for liquid hydrogen cryogenic storage tank structures for aircraft applications," NASA, Ohio, 2006.

[60] D. Verstraete, "The potential of liquid hydrogen for long range aircraft propulsion," Cranfield University, Cranfield, 2009.

[61] C. Winnefeld, T. Kadyk, B. Bensmann, U. Krewer and R. Hanke-Rauschenback, "Modelling and Designing Cryogenic Hydrogen Tanks for Future Aircraft Applications," *Energies,* pp. 105-128, 2018.

[62] P. Rompokos, A. Rolt, D. Nalianda, T. Sibili and C. Benson, "Cryogenic fuel storage modelling and optimization for aircraft applications," *Turbo Expo: Power for land, sea and air,* vol. 84997, no. ASME, p. V006T03A001, 2021.

[63] G. Onorato, "Fuel tank integration for hydrogen airliners," TU Delft, Delft, 2021.

[64] C. van Woensel, "Integration of a Liquid Hydrogen Fuel Tank into the Concept of the Flying-V," TU Delft, Delft, 2021.

[65] D. Verstraete, P. Hendrick, P. Pilidis and K. Ramsden, "Hydrogen fuel tanks for subsonic transport aircraft," *International Journal of Hydrogen Energy,* vol. 35, pp. 11085-11098, 2010.

[66] ASME, Boiler and Pressure Vessel Code, ASME, 2019.

[67] R. Barron, Cryogenic Systems, Second Edition, Louisiana: Louisiana Tech University, 1985.

[68] Aerospace Specification Metals Inc., "Aluminum 2219 T-62," Aerospace Specification Metals Inc., 2022. [Online]. Available: https://asm.matweb.com/search/SpecificMaterial.asp?bassnum=ma2219t62. [Accessed July 2022].

[69] L. Mazzone, G. Ratcliffe, J. Rieubland and G. Vandoni, "Measurements of multi-layer insulation at high boundary temperature using a simple non-calorimetric method," in *19th International Cryogenic Engineering Conference (ICEC 19)*, Grenoble, France, 2002.

[70] P. Bruce, S. Freunberger, J. Hardwick and J. Tarascon, "Li-O2 and Li-S batteries with high energy storage," *Nature Materials,* vol. 11, 2012.

[71] S. Dorfler, S. Walus, J. Locke, A. Fotouhi, D. Auger, N. Shateri, T. Abendroth, P. Hartel, H. Althues and S. Kaskel, "Recent progress and emerging application areas for lithium-sulfur battery technology," *Energy Technology,* vol. 9, no. 2000964, 2021.

[72] K. Marckwardt, Unterlagen zur Vorlesung Flugzeugentwurf, Hamburg: Fachhochschule Hamburg, Fachbereich Fahrzeugtechnik, 1998.

[73] K. Takino, Y. Tachikawa, K. Mori, S. Lyth, Y. Shiratori, S. Taniguchi and K. Sasaki, "Simulation of SOFC performance using a modified exchange current density for pre-reformed methane-based fuels," *International Journal of Hydrogen Energy,* vol. 45, no. 11, pp. 6912-6925, 2020.

[74] M. e. a. Haydn, "Multi-layer thin-film electrolytes for metal supported solid oxide fuel cells," *Journal of Power Sources,* vol. 256, pp. 52-60, 2014.

[75] C. Tanner and A. Virkar, "A simple model for interconnect design of planar solid oxide fuel cells," *Journal of Power Sources,* vol. 113, no. 1, pp. 44-56, 2003.

[76] O. Hojdati-Pugh, A. Dhir and R. Steinberger-Wilckens, "The development of current collection in micro-tubular solid oxide fuel cells - A review," *Applied Sciences,* vol. 11, no. 1077, 2021.

[77] S. Rodriguez-Lopez, J. Malzbender, V. Justo, F. Serbena, S. Gross and M. Pascual, "Thermo-Mechanical Stability and Gas-Tightness of Glass-Ceramics Joints for SOFC in the System MgO-BaO/SrO-B2O3-SiO2," *Frontiers in Materials,* vol. 7, 2020.

[78] U. Bossel, "Rapid startup SOFC modules," *Energy Procedia,* vol. 28, pp. 48-56, 2012.

[79] Z. Zhang, J. Zhang and T. Zhang, "Endplate Design and Topology Optimization of Fuel Cell Stack Clamped with Bolts," *Sustainability,* vol. 14, no. 4730, 2022.

[80] Special Metals, "INCONEL Alloy 625," 2013. [Online]. Available: https://www.specialmetals.com/documents/technical-bulletins/inconel/inconel-alloy-625.pdf. [Accessed July 2022].

[81] D. F. Windenburg and T. C., "Collapse by instability of thin cylindrical shells under external pressure," *Transportation ASME,* vol. 11, pp. 819-825, 1934.

[82] X. Zhou, B. Sheng, W. Liu, Y. Chen, A. Yurek, Y. Liu, P. Sen and K. Iyer, "A high efficiency high power-density LLC DC-DC converter for electric vehicles (EVs) on-board low voltage DC-DC converter (LDC) application," *IEEE,* pp. 1339-1346, 2020.

[83] M. Granger, D. Avanesian, R. Jansen, S. Kowalewski, A. Leary, R. Bowman, A. Dimston and E. Stalcup, "Design of a High Power Density, High Efficiency, Low THD 250kW Converter for Electric Aircraft," in *2021 Electric Aircraft Technologies Symposium (EATS)*, 2021.

[84] E. Aretskin-Hariton, M. Bell, S. Schnulo and J. Gray, "Power cable mass estimation for electric aircraft propulsion," in *AIAA AVIATION 2021 FORUM*, 2021.

[85] Wright Electric, "The Wright Motor," Wright Electric, 2022. [Online]. Available: https://www.weflywright.com/technology. [Accessed July 2022].

[86] C. Svoboda, "Turbofan engine database as a preliminary design tool," University of Kansas, Lawrence, 2004.

[87] D. Sagerser, S. Lieblein and R. Krebs, "Empirical expressions for estimating length and weight of axial flow components of VTOL powerplants," NASA, Washington D.C., 1971.

[88] Y. Liu, S. Liu, G. Li, T. Yan and X. Gao, "High volumetric energy density sulfur cathode with heavy and catalytic metal oxide host for lithium-sulfur battery," *Advanced Science,* vol. 7, no. 12, 202.

[89] J. Mattingly, W. Heiser and D. Pratt, Aircraft Engine Design 2nd Edition, Reston, Virginia: AIAA, 2002.

[90] R. McDonald, "Electric propulsion modeling for conceptual aircraft design," in *52nd Aerospace Sciences Meeting*, National Harbor, Maryland, 2014.

[91] P. Sharma and O. Pandey, "Chapter 1 - Proton exchange membrane fuel cells: fundamentals, advanced technologies, and practical applications," in *PEM Fuel Cells Fundamentals, Advanced Technologies, and Practical Application*, Elsevier, 2022, pp. 1-24.

[92] M. Bradley and C. Droney, "Subsonic Ultra Green Aircraft Research Phase II: Advanced concept development," NASA, Huntington Beach, 2012.

[93] E. Hendricks and J. Gray, "pyCycle: A tool for efficient optimization of gas turbine engine cycles," *Aerospace,* vol. 6, no. 87, 2019.

[94] R. McDonald and J. Gloudemans, "Open Vehicle Sketch Pad: An open source parameteric geometry and analysis tool for conceptual aircraft design," in *AIAA SciTech Forum*, San Diego, 2022.

[95] T. W. W. A. D. C. M. E. T. D. A. J. J. O. T. H. &. I. C. Lukaczyk, "SUAVE: An open-source environment for multi-fidelity conceptual vehicle design," in *16th AIAA/ISSMO Multidisciplinary Analysis and Optimization Conference*, 2015.

[96] J. Hunter, Jane's All the World's Aircraft, 2018.

[97] Federal Aviation Administration, "Aircraft characteristics database," FAA, 30 November 2022. [Online]. Available: https://www.faa.gov/airports/engineering/aircraft_char_database.

[98] S. Gudmundsson, General aviation aircraft design: Applied methods and procedures, Oxford: Elsevier, 2014.

[99] NASA, "Symmetrical, bi-electrode supported solid oxide fuel cell". United States Patent 7,534,519, 16 September 2005.

APPENDIX I – TABLES OF MARKET STUDY OF REGIONAL AIRCRAFT

Table 20 – General characteristics of reference aircraft between 30-90 seats. Gray cells refer to jet aircraft, yellow cells refer to turboprop aircraft. Assumptions/estimations are indicated in italics. Sources: [96] [97]

OEM	Aircraft	EIS	# Seats	Range (km)	Cruise altitude (m)	Cruise Mach
Embraer	ERJ135LR	1999	37	3240	11000	0.78
	ERJ140LR	1999	44	3060	11000	0.78
	ERJ145XR	1997	50	3700	11000	0.78
	EMB120	1985	30	1020	6100	0.485
	EMB120ER	1993	30	1560	6100	0.53
Bombardier	CRJ100	1991	50	3050	11000	0.74
	CRJ200	1991	50	3150	11000	0.74
	CRJ700	1997	78	2550	11000	0.78
	CRJ900	2003	90	2880	11000	0.78
	CRJ1000	2010	104	3000	11000	0.78
Fokker	50	1987	56	1700	-	0.45
Dornier	228	1981	19	396	3000	0.35
	328	1993	30-33	1850	7620	-
	328JET	1998	30-33	2740	-	-
DeHavilland	Dash 8 Q100	1984	40	1890	7620	0.45
	Dash 8 Q200	1984	40	2080	7620	0.48
	Dash 8 Q300	1984	50-56	1710	7620	0.48
	Dash 8 Q400	1984	90	2040	8230	0.60
-	Target aircraft	2035	50	1300	7620	0.60

Table 21 – Weights and powerplant of reference aircraft with 30-90 seats. Assumptions/estimations are indicated in italics. Sources: [96] [97]

Aircraft	MTOW (kg)	MLW (kg)	Max payload (kg)	Max fuel (kg)	OEW (kg)	Powerplant	TO thrust or power
ERJ135LR	20000	18500	4499	5136	11500	RR AE3007-A1/3 Turbofan (2x)	67.4 kN
ERJ140LR	21100	18700	5292	5136	11816	RR AE3007-A1/3 Turbofan (2x)	67.4 kN
ERJ145LR	22000	19300	5786	5136	12114	RR AE3007-A1E Turbofan (2x)	79.4 kN
EMB120	11500	11250	2930	-	7070	P&W PW118 Turboprop (2x)	2.68 MW
EMB120ER	11990	11700	3320	2656	7580	P&W PW118 Turboprop (2x)	2.68 MW
CRJ100	24040	21319	6124	6489	13835	GE CF34-3A1 Turbofan (2x)	77.6 kN
CRJ200	24040	21319	6124	6489	13835	GE CF34-3B1 Turbofan (2x)	77.6 kN

CRJ700	34019	30390	8190	8888	20069	GE CF34-8C5B1 Turbofan (2x)	122.6 kN
CRJ900	38330	33345	10247	8888	21845	GE CF34-8C5 Turbofan (2x)	129.0 kN
CRJ1000	41640	36968	11966	8822	23188	GE CF34-8C5A1 Turbofan (2x)	129.0 kN
Fokker 50	20820	20030	5500	4120	12750	P&W Canada PW125B (2x turboprop)	3.73 MW
Do228	6575	6575	1724	1885	3900	Honeywell TPE331 Turboprop (2x)	0.58 MW
Do328	15660	14390	6240	3634	9420	P&W PW119B Turboprop (2x)	3.25 MW
Do328JET	15660	14390	6240	3634	9420	P&W PW306B Turbofan (2x)	107.6 kN
Dash 8 Q100	15600	15600	4647	2540	10477	P&W PW123C/D Turboprop (2x)	3.2 MW
Dash 8 Q200	16466	16400	4647	2540	10477	P&W PW120 Turboprop (2x)	2.6 MW
Dash 8 Q300	19505	19050	6124	2540	11793	P&W PW123B/E Turboprop (2x)	3.72 MW
Dash 8 Q400	30481	28000	8489	5247	17819	P&W PW150 Turboprop (2x)	7.56 MW

Table 22 – Performance characteristics of reference aircraft with 30-90 seats. Assumptions/estimations are indicated in italics. Sources: [96] [97]

Aircraft	Pax	Type (Jet, Prop)	Max cruise Mach	Cruise ceiling (m)	ROC (ft/min)	Takeoff distance (m)	Landing distance (m)	Stall speed (m/s)
Do 328JET	33	Jet	0.66	11000	3690	1370	1310	-
ERJ135LR	37	Jet	0.78	11278	2350	1760	1360	-
ERJ140LR	44	Jet	0.78	11278	2200	1850	1380	-
ERJ145XR	50	Jet	0.8	11278	1950	2270	1400	45
CRJ100	50	Jet	0.81	12496	3000	1920	1480	-
CRJ200	50	Jet	0.81	12496	3000	1920	1480	-
CRJ700	78	Jet	0.825	12496	3000	1605	1540	-
CRJ900	90	Jet	0.82	12496	3000	1940	1630	-
CRJ1000	104	Jet	0.82	12496	3000	2120	1750	-
Do228NG	19	Prop	0.35	3000	1575	793	451	34.5
EMB120	30	Prop	0.535	9750	2120	1420	-	45
EMB120ER	30	Prop	0.535	9750	2500	1560	1380	-
Do 328	33	Prop	0.55	9500	2060	1100	1075	-
Dash 8 Q100	40	Prop	0.45	7620	1475	1000	780	-
Dash 8 Q200	40	Prop	0.48	7620	1800	1000	780	-

Fokker 50	50	Prop	0.51	7620	2800	1350	1130	-
Dash 8 Q300	50	Prop	0.48	7620	1800	1180	1040	-
Dash 8 Q400	90	Prop	0.60	8230	2200	1425	1290	-
Target aircraft	50	P+SOFC	0.60	9500	2000	1300	1000	45

Table 23 – Estimation of aerodynamic and performance characteristics of the target aircraft and their comparison with similar aircraft currently on the market. Estimated values are indicated in italics. Sources: [96] [97]

Parameter	**Units**	**Do 228**	**Do 328**	**Fokker 50**	**Dash 8 Q200**	**Dash 8 Q300**	**ERJ145**	**Target aircraft**
Wing area	m^2	32	40	70	54.4	56.2	51.2	Unknown
Wing span	m	17	21	29	25.9	27.4	20	Unknown
Aspect ratio	-	9	11	12	12.3	13.4	7.9	*12.0*
Oswald efficiency factor	-	0.63	-	-	-	*12.0*	-	*0.8*
K polar	-	0.056	-	-	-	*0.8*	-	*0.0332*
Zero-lift drag coefficient	-	0.029	-	-	-	*0.0332*	-	*0.02*
$c_{L,cruise}$	-					*0.02*		*0.9*
Propeller propulsive efficiency at cruise	-	0.8	-	-	-	*0.9*	-	*0.8*
Propeller propulsive efficiency at takeoff and climb	-	0.7	-	-	-	*0.8*	-	*0.7*
μ	-	0.04	-	-	-	*0.7*	-	*0.03*
c_{D0LG}	-	0.015	-	-	-	*0.03*	-	*0.010*
$c_{D0HLD,TO}$	-	0.010	-	-	-	*0.010*	-	*0.008*
$c_{D0HLD,landing}$	-	0.045				*0.008*		*0.035*
$\Delta c_{L,HLD,TO}$	-	0.73	-	-	-	*0.035*	-	*0.8*
$\Delta c_{L,HLD,landing}$		0.97				*0.8*		*1.0*
Maximum c_L without flaps	-	1.7				*1.0*		*1.7*
Maximum c_L with TO flaps	-	2.43	-	-	-	*1.7*	-	*2.5*
Maximum c_L with landing flaps	-	2.67				*2.5*		*2.7*
L/D max SL	-	16.0	-	-	-	*2.7*	-	*15*
$\frac{W_{landing}}{W_{TO}}$	-	0.6				*15*		*0.8*

Wing loading	N/m^2	1962	3430	2915	2975	3405	4620	Unknown
Power loading	W/N	18.4	23.7	18.3	16.05	19.45	-	Unknown

APPENDIX II – FAILURE MODE ANALYSIS FOR POWER SIZING WITH CONSTRAINT ANALYSIS METHODOLOGY

The power distribution matrix obtained from Figure 30 is the following:

$$\begin{bmatrix}
-\eta_V & 1 & 1 & 1 & 0 & 0 & 0 & 0 & 0 & 0 & 0 & 0 & 0 & 0 & 0 & 0 & 0 & 0 & 0 \\
0 & 1 & -1 & 0 & 0 & 0 & 0 & 0 & 0 & 0 & 0 & 0 & 0 & 0 & 0 & 0 & 0 & 0 & 0 \\
0 & -\eta_{GT1} & 0 & 0 & 1 & 0 & 1 & 0 & -\eta_{GT2} & 0 & 0 & 0 & 0 & 0 & 0 & 0 & 0 & 0 & 0 \\
0 & 0 & -\eta_{GT1} & 0 & 0 & 1 & 0 & 1 & 0 & -\eta_{GT2} & 0 & 0 & 0 & 0 & 0 & 0 & 0 & 0 & 0 \\
0 & 0 & 0 & 0 & 0 & 0 & -\eta_{p1} & 0 & 1 & 0 & 0 & 0 & 0 & 0 & 0 & 0 & 0 & 0 & 0 \\
0 & 0 & 0 & 0 & 0 & 0 & 0 & 0 & 0 & -\eta_{p1} & 0 & 1 & 0 & 0 & 0 & 0 & 0 & 0 & 0 \\
0 & 0 & 0 & -1 & 0 & 0 & 0 & 0 & 1 & 1 & 1 & 0 & 0 & 0 & 0 & 0 & 0 & 0 & 0 \\
0 & 0 & 0 & 0 & 0 & 0 & 0 & 0 & -1 & 1 & 0 & 0 & 0 & 0 & 0 & 0 & 0 & 0 & 0 \\
0 & 0 & 0 & 0 & 0 & 0 & 0 & 0 & 0 & 0 & -\eta_{PM1} & -\eta_{PM1} & 1 & 0 & 0 & 0 & 0 & 0 & 0 \\
0 & 0 & 0 & 0 & 0 & 0 & 0 & 0 & 0 & 0 & 0 & 0 & -\eta_{PM2} & 1 & 1 & 0 & 0 & 0 & 0 \\
0 & 0 & 0 & 0 & 0 & 0 & 0 & 0 & 0 & 0 & 0 & 0 & 0 & -\eta_{EM} & 1 & 0 & 0 & 0 & 0 \\
0 & 0 & 0 & 0 & 0 & 0 & 0 & 0 & 0 & 0 & 0 & 0 & 0 & 0 & -\eta_{P2} & 1 & 0 & 0 & 0 \\
0 & (1-\Phi) & (1-\Phi) & \Phi & 0 & 0 & 0 & 0 & 0 & 0 & 0 & 0 & 0 & 0 & 0 & 0 & 0 & 0 & 0 \\
0 & 0 & 0 & 0 & 0 & 0 & 0 & 0 & 0 & 0 & (1-\Psi) & \Psi & 0 & 0 & 0 & 0 & 0 & 0 & 0 \\
0 & 0 & 0 & 0 & 0 & 0 & 0 & 0 & 0 & 0 & 0 & 0 & (1-\lambda) & \lambda & 0 & 0 & 0 & 0 & 0 \\
0 & 0 & 0 & -\eta_{SOFC} & 0 & 0 & 0 & 0 & 0 & 0 & 1 & 0 & 0 & 0 & 0 & 0 & 0 & 0 & 0 \\
0 & 0 & 0 & 1 & 0 & 0 & 0 & 0 & 0 & 0 & 0 & 0 & 0 & 0 & 0 & 0 & -1 & 0 & P_p \\
0 & 0 & 0 & 0 & 0 & 0 & 0 & 0 & 0 & 0 & 1 & 0 & 0 & 0 & 0 & 0 & 0 & -1 & 0 \\
0 & 0 & 0 & 0 & 0 & 0 & 1 & 1 & 0 & 0 & 0 & 0 & 0 & 0 & 0 & 0 & 1 & 0 & 0
\end{bmatrix}
\cdot
\begin{bmatrix} P_{f1} \\ 1/2P_{f2} \\ 1/2P_{f2} \\ 1/2P_{f3} \\ 1/2P_{s1} \\ 1/2P_{s1} \\ 1/2P_{p1} \\ 1/2P_{p1} \\ 1/2P_{b1} \\ 1/2P_{b1} \\ 1/2P_{e1} \\ P_{e2} \\ P_{e3} \\ P_{e4} \\ P_{e5} \\ P_{s2} \\ P_{p2} \\ 1/2P_{f3} \\ 1/2P_{e1} \end{bmatrix}
=
\begin{bmatrix} 0 \\ 0 \\ 0 \\ 0 \\ 0 \\ 0 \\ 0 \\ 0 \\ 0 \\ 0 \\ 0 \\ 0 \\ 0 \\ 0 \\ 0 \\ 0 \\ P_p \\ 0 \\ 0 \end{bmatrix}$$

This power distribution matrix modified for each failure mode, considering that several power values are zero in case of failure:

- **Turbofan engine failure**: $\frac{1}{2}P_{f2}$, $\frac{1}{2}P_{f3}$, $\frac{1}{2}P_{s1}$, $\frac{1}{2}P_{p1}$, $\frac{1}{2}P_{e1}$ are equal to zero.

$$\begin{bmatrix}
-\eta_V & 1 & 1 & 1 & 0 & 0 & 0 & 0 & 0 & 0 & 0 & 0 & 0 & 0 & 0 & 0 & 0 & 0 & 0 \\
0 & 1 & -1 & 0 & 0 & 0 & 0 & 0 & 0 & 0 & 0 & 0 & 0 & 0 & 0 & 0 & 0 & 0 & 0 \\
0 & -\eta_{GT1} & 0 & 0 & 1 & 0 & 1 & 0 & -\eta_{GT2} & 0 & 0 & 0 & 0 & 0 & 0 & 0 & 0 & 0 & 0 \\
0 & 0 & -\eta_{GT1} & 0 & 0 & 1 & 0 & 1 & 0 & -\eta_{GT2} & 0 & 0 & 0 & 0 & 0 & 0 & 0 & 0 & 0 \\
0 & 0 & 0 & 0 & 0 & 0 & -\eta_{p1} & 0 & 1 & 0 & 0 & 0 & 0 & 0 & 0 & 0 & 0 & 0 & 0 \\
0 & 0 & 0 & 0 & 0 & 0 & 0 & 0 & 0 & -\eta_{p1} & 0 & 1 & 0 & 0 & 0 & 0 & 0 & 0 & 0 \\
0 & 0 & 0 & -1 & 0 & 0 & 0 & 0 & 1 & 1 & 1 & 0 & 0 & 0 & 0 & 0 & 0 & 0 & 0 \\
0 & 0 & 0 & 0 & 0 & 0 & 0 & 0 & -1 & 1 & 0 & 0 & 0 & 0 & 0 & 0 & 0 & 0 & 0 \\
0 & 0 & 0 & 0 & 0 & 0 & 0 & 0 & 0 & 0 & -\eta_{PM1} & -\eta_{PM1} & 1 & 0 & 0 & 0 & 0 & 0 & 0 \\
0 & 0 & 0 & 0 & 0 & 0 & 0 & 0 & 0 & 0 & 0 & 0 & -\eta_{PM2} & 1 & 1 & 0 & 0 & 0 & 0 \\
0 & 0 & 0 & 0 & 0 & 0 & 0 & 0 & 0 & 0 & 0 & 0 & 0 & -\eta_{EM} & 1 & 0 & 0 & 0 & 0 \\
0 & 0 & 0 & 0 & 0 & 0 & 0 & 0 & 0 & 0 & 0 & 0 & 0 & 0 & -\eta_{P2} & 1 & 0 & 0 & 0 \\
0 & (1-\Phi) & (1-\Phi) & \Phi & 0 & 0 & 0 & 0 & 0 & 0 & 0 & 0 & 0 & 0 & 0 & 0 & 0 & 0 & 0 \\
0 & 0 & 0 & 0 & 0 & 0 & 0 & 0 & 0 & 0 & (1-\Psi) & \Psi & 0 & 0 & 0 & 0 & 0 & 0 & 0 \\
0 & 0 & 0 & 0 & 0 & 0 & 0 & 0 & 0 & 0 & 0 & 0 & (1-\lambda) & \lambda & 0 & 0 & 0 & 0 & 0 \\
0 & 0 & 0 & -\eta_{SOFC} & 0 & 0 & 0 & 0 & 0 & 0 & 1 & 0 & 0 & 0 & 0 & 0 & 0 & 0 & 0 \\
0 & 0 & 0 & 1 & 0 & 0 & 0 & 0 & 0 & 0 & 0 & 0 & 0 & 0 & 0 & 0 & -1 & 0 & P_p \\
0 & 0 & 0 & 0 & 0 & 0 & 0 & 0 & 0 & 0 & 1 & 0 & 0 & 0 & 0 & 0 & 0 & -1 & 0 \\
0 & 0 & 0 & 0 & 0 & 0 & 1 & 1 & 0 & 0 & 0 & 0 & 0 & 0 & 0 & 0 & 1 & 0 & 0
\end{bmatrix}
\cdot
\begin{bmatrix} P_{f1} \\ 0 \\ 1/2P_{f2} \\ 1/2P_{f3} \\ 0 \\ 1/2P_{s1} \\ 0 \\ 1/2P_{p1} \\ 1/2P_{b1} \\ 0 \\ 1/2P_{e1} \\ P_{e2} \\ P_{e3} \\ P_{e4} \\ P_{e5} \\ P_{s2} \\ P_{p2} \\ 0 \\ 0 \end{bmatrix}
=
\begin{bmatrix} 0 \\ 0 \\ 0 \\ 0 \\ 0 \\ 0 \\ 0 \\ 0 \\ 0 \\ 0 \\ 0 \\ 0 \\ 0 \\ 0 \\ 0 \\ 0 \\ P_p \\ 0 \\ 0 \end{bmatrix}$$

- **SOFC failure with charged battery**: 2 times $\frac{1}{2}P_{f3}$, 2 times $\frac{1}{2}P_{e1}$, 2 times $\frac{1}{2}P_{b1}$ are equal to zero.

$$\begin{bmatrix}
-\eta_V & 1 & 1 & 1 & 0 & 0 & 0 & 0 & 0 & 0 & 0 & 0 & 0 & 0 & 0 & 0 & 0 & 0 & 0 \\
0 & 1 & -1 & 0 & 0 & 0 & 0 & 0 & 0 & 0 & 0 & 0 & 0 & 0 & 0 & 0 & 0 & 0 & 0 \\
0 & -\eta_{GT1} & 0 & 0 & 1 & 0 & 1 & 0 & -\eta_{GT2} & 0 & 0 & 0 & 0 & 0 & 0 & 0 & 0 & 0 & 0 \\
0 & 0 & -\eta_{GT1} & 0 & 0 & 1 & 0 & 1 & 0 & -\eta_{GT2} & 0 & 0 & 0 & 0 & 0 & 0 & 0 & 0 & 0 \\
0 & 0 & 0 & 0 & 0 & 0 & -\eta_{p1} & 0 & 1 & 0 & 0 & 0 & 0 & 0 & 0 & 0 & 0 & 0 & 0 \\
0 & 0 & 0 & 0 & 0 & 0 & 0 & 0 & 0 & -\eta_{p1} & 0 & 1 & 0 & 0 & 0 & 0 & 0 & 0 & 0 \\
0 & 0 & 0 & -1 & 0 & 0 & 0 & 0 & 1 & 1 & 1 & 0 & 0 & 0 & 0 & 0 & 0 & 0 & 0 \\
0 & 0 & 0 & 0 & 0 & 0 & 0 & 0 & -1 & 1 & 0 & 0 & 0 & 0 & 0 & 0 & 0 & 0 & 0 \\
0 & 0 & 0 & 0 & 0 & 0 & 0 & 0 & 0 & 0 & -\eta_{PM1} & -\eta_{PM1} & 1 & 0 & 0 & 0 & 0 & 0 & 0 \\
0 & 0 & 0 & 0 & 0 & 0 & 0 & 0 & 0 & 0 & 0 & -\eta_{PM2} & 1 & 1 & 0 & 0 & 0 & 0 & 0 \\
0 & 0 & 0 & 0 & 0 & 0 & 0 & 0 & 0 & 0 & 0 & 0 & -\eta_{EM} & 1 & 0 & 0 & 0 & 0 & 0 \\
0 & 0 & 0 & 0 & 0 & 0 & 0 & 0 & 0 & 0 & 0 & 0 & 0 & -\eta_{P2} & 1 & 0 & 0 & 0 & 0 \\
0 & (1-\Phi) & (1-\Phi) & \Phi & 0 & 0 & 0 & 0 & 0 & 0 & 0 & 0 & 0 & 0 & 0 & 0 & 0 & 0 & 0 \\
0 & 0 & 0 & 0 & 0 & 0 & 0 & 0 & 0 & (1-\Psi) & \Psi & 0 & 0 & 0 & 0 & 0 & 0 & 0 & 0 \\
0 & 0 & 0 & 0 & 0 & 0 & 0 & 0 & 0 & 0 & 0 & 0 & (1-\lambda) & \lambda & 0 & 0 & 0 & 0 & 0 \\
0 & 0 & 0 & -\eta_{SOFC} & 0 & 0 & 0 & 0 & 0 & 1 & 0 & 0 & 0 & 0 & 0 & 0 & 0 & 0 & 0 \\
0 & 0 & 0 & 1 & 0 & 0 & 0 & 0 & 0 & 0 & 0 & 0 & 0 & 0 & 0 & 0 & -1 & 0 & 0 \\
0 & 0 & 0 & 0 & 0 & 0 & 0 & 0 & 0 & 1 & 0 & 0 & 0 & 0 & 0 & 0 & 0 & -1 & 0 \\
0 & 0 & 0 & 0 & 0 & 0 & 1 & 1 & 0 & 0 & 0 & 0 & 0 & 0 & 0 & 1 & 0 & 0 & 0
\end{bmatrix} \cdot \begin{bmatrix} P_{f1} \\ 1/2P_{f2} \\ 1/2P_{f2} \\ 0 \\ 1/2P_{s1} \\ 1/2P_{s1} \\ 1/2P_{p1} \\ 1/2P_{p1} \\ 0 \\ 0 \\ 0 \\ 0 \\ P_{e2} \\ P_{e3} \\ P_{e4} \\ P_{e5} \\ P_{s2} \\ P_{p2} \\ 0 \\ 0 \end{bmatrix} = \begin{bmatrix} 0 \\ 0 \\ 0 \\ 0 \\ 0 \\ 0 \\ 0 \\ 0 \\ 0 \\ 0 \\ 0 \\ 0 \\ 0 \\ 0 \\ 0 \\ 0 \\ 0 \\ P_p \\ 0 \\ 0 \end{bmatrix}$$

- **SOFC failure with discharged battery:** 2 times $\frac{1}{2}P_{f3}$, 2 times $\frac{1}{2}P_{e1}$ P_{e2}, 2 times $\frac{1}{2}P_{b1}$, P_{e3}, P_{e4}, P_{e5}, P_{s2}, P_{p2} are equal to zero.

$$\begin{bmatrix}
-\eta_V & 1 & 1 & 1 & 0 & 0 & 0 & 0 & 0 & 0 & 0 & 0 & 0 & 0 & 0 & 0 & 0 & 0 & 0 \\
0 & 1 & -1 & 0 & 0 & 0 & 0 & 0 & 0 & 0 & 0 & 0 & 0 & 0 & 0 & 0 & 0 & 0 & 0 \\
0 & -\eta_{GT1} & 0 & 0 & 1 & 0 & 1 & 0 & -\eta_{GT2} & 0 & 0 & 0 & 0 & 0 & 0 & 0 & 0 & 0 & 0 \\
0 & 0 & -\eta_{GT1} & 0 & 0 & 1 & 0 & 1 & 0 & -\eta_{GT2} & 0 & 0 & 0 & 0 & 0 & 0 & 0 & 0 & 0 \\
0 & 0 & 0 & 0 & 0 & 0 & -\eta_{p1} & 0 & 1 & 0 & 0 & 0 & 0 & 0 & 0 & 0 & 0 & 0 & 0 \\
0 & 0 & 0 & 0 & 0 & 0 & 0 & 0 & 0 & -\eta_{p1} & 0 & 1 & 0 & 0 & 0 & 0 & 0 & 0 & 0 \\
0 & 0 & 0 & -1 & 0 & 0 & 0 & 0 & 1 & 1 & 1 & 0 & 0 & 0 & 0 & 0 & 0 & 0 & 0 \\
0 & 0 & 0 & 0 & 0 & 0 & 0 & 0 & -1 & 1 & 0 & 0 & 0 & 0 & 0 & 0 & 0 & 0 & 0 \\
0 & 0 & 0 & 0 & 0 & 0 & 0 & 0 & 0 & 0 & -\eta_{PM1} & -\eta_{PM1} & 1 & 0 & 0 & 0 & 0 & 0 & 0 \\
0 & 0 & 0 & 0 & 0 & 0 & 0 & 0 & 0 & 0 & 0 & -\eta_{PM2} & 1 & 1 & 0 & 0 & 0 & 0 & 0 \\
0 & 0 & 0 & 0 & 0 & 0 & 0 & 0 & 0 & 0 & 0 & 0 & -\eta_{EM} & 1 & 0 & 0 & 0 & 0 & 0 \\
0 & 0 & 0 & 0 & 0 & 0 & 0 & 0 & 0 & 0 & 0 & 0 & 0 & -\eta_{P2} & 1 & 0 & 0 & 0 & 0 \\
0 & (1-\Phi) & (1-\Phi) & \Phi & 0 & 0 & 0 & 0 & 0 & 0 & 0 & 0 & 0 & 0 & 0 & 0 & 0 & 0 & 0 \\
0 & 0 & 0 & 0 & 0 & 0 & 0 & 0 & 0 & (1-\Psi) & \Psi & 0 & 0 & 0 & 0 & 0 & 0 & 0 & 0 \\
0 & 0 & 0 & 0 & 0 & 0 & 0 & 0 & 0 & 0 & 0 & 0 & (1-\lambda) & \lambda & 0 & 0 & 0 & 0 & 0 \\
0 & 0 & 0 & -\eta_{SOFC} & 0 & 0 & 0 & 0 & 0 & 1 & 0 & 0 & 0 & 0 & 0 & 0 & 0 & 0 & 0 \\
0 & 0 & 0 & 1 & 0 & 0 & 0 & 0 & 0 & 0 & 0 & 0 & 0 & 0 & 0 & 0 & -1 & 0 & 0 \\
0 & 0 & 0 & 0 & 0 & 0 & 0 & 0 & 0 & 1 & 0 & 0 & 0 & 0 & 0 & 0 & 0 & -1 & 0 \\
0 & 0 & 0 & 0 & 0 & 0 & 1 & 1 & 0 & 0 & 0 & 0 & 0 & 0 & 0 & 1 & 0 & 0 & 0
\end{bmatrix} \cdot \begin{bmatrix} P_{f1} \\ 1/2P_{f2} \\ 1/2P_{f2} \\ 0 \\ 1/2P_{s1} \\ 1/2P_{s1} \\ 1/2P_{p1} \\ 1/2P_{p1} \\ 0 \\ 0 \\ 0 \\ 0 \\ 0 \\ 0 \\ 0 \\ 0 \\ 0 \\ P_p \\ 0 \\ 0 \end{bmatrix} = \begin{bmatrix} 0 \\ 0 \\ 0 \\ 0 \\ 0 \\ 0 \\ 0 \\ 0 \\ 0 \\ 0 \\ 0 \\ 0 \\ 0 \\ 0 \\ 0 \\ 0 \\ 0 \\ P_p \\ 0 \\ 0 \end{bmatrix}$$

- **Battery failure**: $P_{e2} = 0$.

$$\begin{bmatrix}
-\eta_V & 1 & 1 & 1 & 0 & 0 & 0 & 0 & 0 & 0 & 0 & 0 & 0 & 0 & 0 & 0 & 0 & 0 & 0 \\
0 & 1 & -1 & 0 & 0 & 0 & 0 & 0 & 0 & 0 & 0 & 0 & 0 & 0 & 0 & 0 & 0 & 0 & 0 \\
0 & -\eta_{GT1} & 0 & 0 & 1 & 0 & 1 & 0 & -\eta_{GT2} & 0 & 0 & 0 & 0 & 0 & 0 & 0 & 0 & 0 & 0 \\
0 & 0 & -\eta_{GT1} & 0 & 0 & 1 & 0 & 1 & 0 & -\eta_{GT2} & 0 & 0 & 0 & 0 & 0 & 0 & 0 & 0 & 0 \\
0 & 0 & 0 & 0 & 0 & 0 & -\eta_{p1} & 0 & 1 & 0 & 0 & 0 & 0 & 0 & 0 & 0 & 0 & 0 & 0 \\
0 & 0 & 0 & 0 & 0 & 0 & 0 & 0 & 0 & -\eta_{p1} & 0 & 1 & 0 & 0 & 0 & 0 & 0 & 0 & 0 \\
0 & 0 & 0 & -1 & 0 & 0 & 0 & 0 & 1 & 1 & 1 & 0 & 0 & 0 & 0 & 0 & 0 & 0 & 0 \\
0 & 0 & 0 & 0 & 0 & 0 & 0 & 0 & -1 & 1 & 0 & 0 & 0 & 0 & 0 & 0 & 0 & 0 & 0 \\
0 & 0 & 0 & 0 & 0 & 0 & 0 & 0 & 0 & 0 & -\eta_{PM1} & -\eta_{PM1} & 1 & 0 & 0 & 0 & 0 & 0 & 0 \\
0 & 0 & 0 & 0 & 0 & 0 & 0 & 0 & 0 & 0 & 0 & -\eta_{PM2} & 1 & 1 & 0 & 0 & 0 & 0 & 0 \\
0 & 0 & 0 & 0 & 0 & 0 & 0 & 0 & 0 & 0 & 0 & 0 & -\eta_{EM} & 1 & 0 & 0 & 0 & 0 & 0 \\
0 & 0 & 0 & 0 & 0 & 0 & 0 & 0 & 0 & 0 & 0 & 0 & 0 & -\eta_{P2} & 1 & 0 & 0 & 0 & 0 \\
0 & (1-\Phi) & (1-\Phi) & \Phi & 0 & 0 & 0 & 0 & 0 & 0 & 0 & 0 & 0 & 0 & 0 & 0 & 0 & 0 & 0 \\
0 & 0 & 0 & 0 & 0 & 0 & 0 & 0 & 0 & (1-\Psi) & \Psi & 0 & 0 & 0 & 0 & 0 & 0 & 0 & 0 \\
0 & 0 & 0 & 0 & 0 & 0 & 0 & 0 & 0 & 0 & 0 & 0 & (1-\lambda) & \lambda & 0 & 0 & 0 & 0 & 0 \\
0 & 0 & 0 & -\eta_{SOFC} & 0 & 0 & 0 & 0 & 0 & 1 & 0 & 0 & 0 & 0 & 0 & 0 & 0 & 0 & 0 \\
0 & 0 & 0 & 1 & 0 & 0 & 0 & 0 & 0 & 0 & 0 & 0 & 0 & 0 & 0 & 0 & -1 & 0 & 0 \\
0 & 0 & 0 & 0 & 0 & 0 & 0 & 0 & 0 & 1 & 0 & 0 & 0 & 0 & 0 & 0 & 0 & -1 & 0 \\
0 & 0 & 0 & 0 & 0 & 0 & 1 & 1 & 0 & 0 & 0 & 0 & 0 & 0 & 0 & 1 & 0 & 0 & 0
\end{bmatrix} \cdot \begin{bmatrix} P_{f1} \\ 1/2P_{f2} \\ 1/2P_{f2} \\ 1/2P_{f3} \\ 1/2P_{s1} \\ 1/2P_{s1} \\ 1/2P_{p1} \\ 1/2P_{p1} \\ 1/2P_{b1} \\ 1/2P_{b1} \\ 1/2P_{e1} \\ 0 \\ P_{e3} \\ P_{e4} \\ P_{e5} \\ P_{s2} \\ P_{p2} \\ 1/2P_{f3} \\ 1/2P_{e1} \end{bmatrix} = \begin{bmatrix} 0 \\ 0 \\ 0 \\ 0 \\ 0 \\ 0 \\ 0 \\ 0 \\ 0 \\ 0 \\ 0 \\ 0 \\ 0 \\ 0 \\ 0 \\ 0 \\ 0 \\ P_p \\ 0 \\ 0 \end{bmatrix}$$

- **Electric motor failure**: P_{e5}, P_{s2}, P_{p2} are equal to zero.

$$
\begin{bmatrix}
-\eta_V & 1 & 1 & 1 & 0 & 0 & 0 & 0 & 0 & 0 & 0 & 0 & 0 & 0 & 0 & 0 & 0 & 0 & 0 \\
0 & 1 & -1 & 0 & 0 & 0 & 0 & 0 & 0 & 0 & 0 & 0 & 0 & 0 & 0 & 0 & 0 & 0 & 0 \\
0 & -\eta_{GT1} & 0 & 0 & 1 & 0 & 1 & 0 & -\eta_{GT2} & 0 & 0 & 0 & 0 & 0 & 0 & 0 & 0 & 0 & 0 \\
0 & 0 & -\eta_{GT1} & 0 & 0 & 1 & 0 & 1 & 0 & -\eta_{GT2} & 0 & 0 & 0 & 0 & 0 & 0 & 0 & 0 & 0 \\
0 & 0 & 0 & 0 & 0 & 0 & -\eta_{p1} & 0 & 1 & 0 & 0 & 0 & 0 & 0 & 0 & 0 & 0 & 0 & 0 \\
0 & 0 & 0 & 0 & 0 & 0 & 0 & 0 & 0 & -\eta_{p1} & 0 & 1 & 0 & 0 & 0 & 0 & 0 & 0 & 0 \\
0 & 0 & 0 & -1 & 0 & 0 & 0 & 0 & 1 & 1 & 1 & 0 & 0 & 0 & 0 & 0 & 0 & 0 & 0 \\
0 & 0 & 0 & 0 & 0 & 0 & 0 & 0 & -1 & 1 & 0 & 0 & 0 & 0 & 0 & 0 & 0 & 0 & 0 \\
0 & 0 & 0 & 0 & 0 & 0 & 0 & 0 & 0 & 0 & -\eta_{PM1} & -\eta_{PM1} & 1 & 0 & 0 & 0 & 0 & 0 & 0 \\
0 & 0 & 0 & 0 & 0 & 0 & 0 & 0 & 0 & 0 & 0 & 0 & -\eta_{PM2} & 1 & 1 & 0 & 0 & 0 & 0 \\
0 & 0 & 0 & 0 & 0 & 0 & 0 & 0 & 0 & 0 & 0 & 0 & 0 & -\eta_{EM} & 1 & 0 & 0 & 0 & 0 \\
0 & 0 & 0 & 0 & 0 & 0 & 0 & 0 & 0 & 0 & 0 & 0 & 0 & 0 & -\eta_{P2} & 1 & 0 & 0 & 0 \\
0 & (1-\Phi) & (1-\Phi) & \Phi & 0 & 0 & 0 & 0 & 0 & 0 & 0 & 0 & 0 & 0 & 0 & 0 & 0 & 0 & 0 \\
0 & 0 & 0 & 0 & 0 & 0 & 0 & 0 & 0 & 0 & (1-\Psi) & \Psi & 0 & 0 & 0 & 0 & 0 & 0 & 0 \\
0 & 0 & 0 & 0 & 0 & 0 & 0 & 0 & 0 & 0 & 0 & 0 & 0 & (1-\lambda) & \lambda & 0 & 0 & 0 & 0 \\
0 & 0 & 0 & -\eta_{SOFC} & 0 & 0 & 0 & 0 & 0 & 0 & 1 & 0 & 0 & 0 & 0 & 0 & 0 & 0 & 0 \\
0 & 0 & 0 & 1 & 0 & 0 & 0 & 0 & 0 & 0 & 0 & 0 & 0 & 0 & 0 & 0 & 0 & -1 & 0 \\
0 & 0 & 0 & 0 & 0 & 0 & 0 & 0 & 0 & 0 & 1 & 0 & 0 & 0 & 0 & 0 & 0 & 0 & -1 \\
0 & 0 & 0 & 0 & 0 & 0 & 1 & 1 & 0 & 0 & 0 & 0 & 0 & 0 & 0 & 0 & 1 & 0 & 0
\end{bmatrix}
\cdot
\begin{bmatrix}
P_{\mathrm{f1}} \\ 1/2P_{\mathrm{f2}} \\ 1/2P_{\mathrm{f2}} \\ 1/2P_{\mathrm{f3}} \\ 1/2P_{\mathrm{s1}} \\ 1/2P_{\mathrm{s1}} \\ 1/2P_{\mathrm{p1}} \\ 1/2P_{\mathrm{p1}} \\ 1/2P_{\mathrm{b1}} \\ 1/2P_{\mathrm{b1}} \\ 1/2P_{\mathrm{e1}} \\ P_{\mathrm{e2}} \\ P_{\mathrm{e3}} \\ P_{\mathrm{e4}} \\ 0 \\ 0 \\ 0 \\ 1/2P_{\mathrm{f3}} \\ 1/2P_{\mathrm{e1}}
\end{bmatrix}
=
\begin{bmatrix}
0 \\ 0 \\ 0 \\ 0 \\ 0 \\ 0 \\ 0 \\ 0 \\ 0 \\ 0 \\ 0 \\ 0 \\ 0 \\ 0 \\ 0 \\ 0 \\ P_{\mathrm{p}} \\ 0 \\ 0
\end{bmatrix}
$$